BINARY TO TERNARY BLENDS: EFFICIENT AND STABLE ORGANIC SOLAR CELLS FOR VERSATILE APPLICATIONS

Alfonsina Abat Amelenan Torimtubun

ADVERTIMENT. L'accés als continguts d'aquesta tesi doctoral i la seva utilització ha de respectar els drets de la persona autora. Pot ser utilitzada per a consulta o estudi personal, així com en activitats o materials d'investigació i docència en els termes establerts a l'art. 32 del Text Refós de la Llei de Propietat Intel·lectual (RDL 1/1996). Per altres utilitzacions es requereix l'autorització prèvia i expressa de la persona autora. En qualsevol cas, en la utilització dels seus continguts caldrà indicar de forma clara el nom i cognoms de la persona autora i el títol de la tesi doctoral. No s'autoritza la seva reproducció o altres formes d'explotació efectuades amb finalitats de lucre ni la seva comunicació pública des d'un lloc aliè al servei TDX. Tampoc s'autoritza la presentació del seu contingut en una finestra o marc aliè a TDX (framing). Aquesta reserva de drets afecta tant als continguts de la tesi com als seus resums i índexs.

ADVERTENCIA. El acceso a los contenidos de esta tesis doctoral y su utilización debe respetar los derechos de la persona autora. Puede ser utilizada para consulta o estudio personal, así como en actividades o materiales de investigación y docencia en los términos establecidos en el art. 32 del Texto Refundido de la Ley de Propiedad Intelectual (RDL 1/1996). Para otros usos se requiere la autorización previa y expresa de la persona autora. En cualquier caso, en la utilización de sus contenidos se deberá indicar de forma clara el nombre y apellidos de la persona autora y el título de la tesis doctoral. No se autoriza su reproducción u otras formas de explotación efectuadas con fines lucrativos ni su comunicación pública desde un sitio ajeno al servicio TDR. Tampoco se autoriza la presentación de su contenido en una ventana o marco ajeno a TDR (framing). Esta reserva de derechos afecta tanto al contenido de la tesis como a sus resúmenes e índices.

WARNING. Access to the contents of this doctoral thesis and its use must respect the rights of the author. It can be used for reference or private study, as well as research and learning activities or materials in the terms established by the 32nd article of the Spanish Consolidated Copyright Act (RDL 1/1996). Express and previous authorization of the author is required for any other uses. In any case, when using its content, full name of the author and title of the thesis must be clearly indicated. Reproduction or other forms of for profit use or public communication from outside TDX service is not allowed. Presentation of its content in a window or frame external to TDX (framing) is not authorized either. These rights affect both the content of the thesis and its abstracts and indexes.

UNIVERSITAT
ROVIRA i VIRGILI

Binary to Ternary Blends: Efficient and Stable Organic Solar Cells for Versatile Applications

---

ALFONSINA ABAT AMELENAN TORIMTUBUN

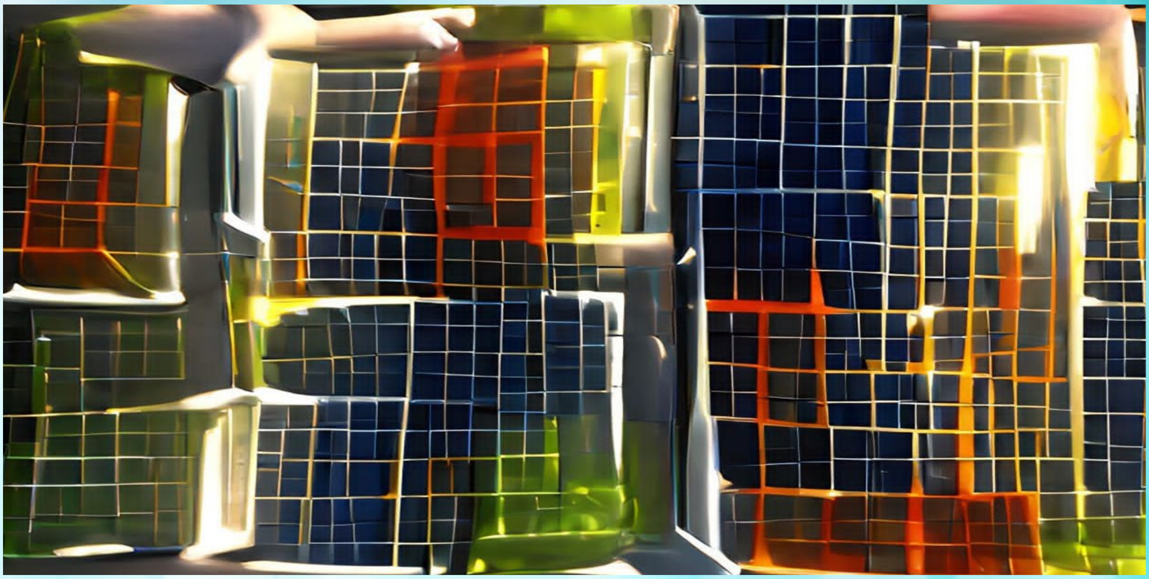

DOCTORAL THESIS

2022

DOCTORAL THESIS

BINARY TO TERNARY BLENDS: EFFICIENT AND STABLE ORGANIC SOLAR CELLS FOR VERSATILE APPLICATIONS

Alfonsina Abat Amelenan Torimtubun

Supervised by Dr. Josep Pallarès Marzal and
Dr. Lluís Francesc Marsal Garví

Departament d'Enginyeria Electrònica, Elèctrica I Automàtica
Nanoelectronic and Photonic Systems (NePhoS)

UNIVERSITAT ROVIRA i VIRGILI

Tarragona
2022

UNIVERSITAT
ROVIRA i VIRGILI

Escola Tècnica Superior D'Enginyeria
Departament d'Enginyeria Electrònica, Elèctrica i Automàtica
Campus Sescelades
Avinguda dels Països
Catalans, 26 43007
Tarragona
Espanya
Tel.: + 34 977 559 610 / 559 728
Fax: + 34 977 559 605

I state that the present study, entitled "**Binary to ternary blends: efficient and stable organic solar cells for versatile applications**" presented by Alfonsina Abat Amelenan Torimtubun for the award of the degree of Doctor, has been carried out under my supervision at the Department of Electrical, Electronic and Automatic Engineering of this University, and that it satisfies all requirements to obtain the doctoral degree with "International Distinction".

Tarragona, April 18th 2022

Doctoral Thesis Supervisor	Doctoral Thesis Co-Supervisor
MARSAL GARVI LUIS FRANCISCO - 39688257D Firmado digitalmente por MARSAL GARVI LUIS FRANCISCO - 39688257D Fecha: 2022.04.18 17:46:12 +02'00'	Josep Pallares Marzal Firmado digitalmente por Josep Pallares Marzal Fecha: 2022.04.18 17:29:11 +02'00'
Dr. Lluis F. Marsal Garví	Dr. Josep Pallarès Marzal

ABSTRACT

High efficiency, stable devices, and low-cost production are key prerequisites for organic photovoltaics technology to enter the niche market. Ternary approach and contacts interface engineering have been reported as effective strategies to overcome the main performance and stability limitations encountered in organic solar cells. However, due to the myriad options of third components and buffer layer materials with various physical and chemical properties, a judicious materials selection that matches certain applications remains a challenge. In this thesis, we combined the interfacial engineering and ternary strategies to improve the device performance and stability of organic solar cells for versatile applications, such as indoor and semitransparent devices. First, a cathode interface engineering using three different electron transport layer materials was comparatively studied under 1 sun and indoor LED illuminations to obtain high efficiency and photostable binary fullerene-based device for indoor application. Then, for traditional outdoor application, we have employed the ternary strategy by adding the novel fluorinated metallophthalocyanines $MPcF_{48}$ and commercial ITIC-M or $PC_{70}BM$ as third components in binary fullerene-based and binary nonfullerene-based blends, respectively, to improve the device efficiency and stability. Likewise, the ternary strategy using the state-of-the-art Y-series nonfullerene acceptors can be applied to obtain an efficient and stable semitransparent nonfullerene-based device. Lastly, we have introduced combined frequency and time-resolved techniques to study in-depth the shelf lifetime degradation of organic solar cells in accordance with the ISOS-D1 protocol.

Acknowledgments

This unforgettable journey began in January 2019 when I first time joined NePhos group, where I met a lot of wonderful people who shaped me both professionally and personally. This thesis would have never been done without the helps and supports from them. Thus, I would like to take this opportunity to do my best to mention all these individuals in the most important section of this thesis (yes, it is right, acknowledgments) to be assured that all help is valued and remembered.

My study has been financed by the European Union's Horizon 2020 research and innovation program under the Marie Skłodowska-Curie grant agreement No. 713679. I also acknowledge the Spanish Ministerio de Ciencia, Innovación y Universidades (MICINN/FEDER) RTI2018-094040-B-I00, the Agency for Management of University and Research Grants (AGAUR) ref. 2017-SGR-1527, the Diputació de Tarragona 2021CM14, the Catalan Institution for Research and Advanced Studies (ICREA) under the ICREA Academia Award, and KAUST Visiting Student Research Program for their financial support.

First and foremost, I would like to thank God for His blessing throughout all the stages of my life, including my PhD journey at the moment. As a human being, I genuinely hope that all the work done in this thesis will benefit many others, practically or theoretically.

I owe my deepest thanks to my supervisors, Prof. Josep Pallarès and Prof. Lluis Marsal, not only for giving me the opportunity to work in an inspiring and challenging environment but also for their knowledge, experience, advice, encouragement, gentleness, and most important for being always supportive for all the challenges met throughout my PhD. It has been a pleasant experience working with them to step one stage higher in my life after PhD. I would also like to thank Dr. José G. Sánchez, for always being patience, helpful, and close to this work,

sharing his knowledge on the technical part of this work, his comments, and suggestions for the scientific articles.

During my PhD, I am very grateful to have a valuable opportunity to collaborate with reputable groups in the field of organic electronics. Prof. Emilio Palomares and his research group members from ICIQ, especially Dr. Maria Méndez, for their tremendous support and excellent collaboration in photophysics characterization and result discussions, Prof. Ángela Sastre-Santos and Dr. Jorge Follana-Berná from Universidad Miguel Hernandez de Elche for their excellent synthetic organic chemistry skill providing some novel organic semiconductor materials, Prof. Derya Baran and her OMEGA Lab research group members in King Abdullah University of Science and Technology for giving me the opportunity to work in their integrated facility as visiting student and learned a lot about semitransparent organic solar cell and its stability. I appreciate her support, guidance, and encouraging discussions during my three months stay.

I would like to take the time to thank Dr. Pilar Formentín, Dr. Carlos Olalla, and Dr. Josep Ferré for their invaluable assistance during this work. I would also like to thank the URV Servei de Recursos Cientifics i Tècnics laboratory staff, especially Dr. Eric Pedrol, Dr. Rita Marimon and Dr. Mariana Stankova, who always being helpful with AFM and TEM technical issues I had encountered. I am also very grateful to the KAUST Solar Center lab operation staff, especially Dr. Abulrahman, Semen, Dr. Craig, and Punita, who always being helpful during my experiment sessions in KAUST. Many thanks to my MFP-COFUND fellowship management team Dr. Oana Moldovan and Dr. Paloma Pontón, who were always helpful, supportive, and informative, big thanks to DEEEA URV Director Dr. Jesus Lecca and the administrative staffs Àngels, Mònica, workshop staffs, cleaning staffs, etc. Thank you very much!

I am very grateful to have a chance to work with wonderful colleagues and

friends from NePhos group both past and current members: Amo, Laura, Pili, Francesc, Elisabet, Jakub, Karen, Pankaj, Anand, Enas, Alejandro, Magaly, Nuria, Akhas, Tabish, and Gohar. I would like to thank OMEGA Lab members who always help me during my research stay, especially Dr. Jianhua, Sri, and Daniel. I would like to express my gratitude to all my friends with whom I shared during these three years: Alejandro Pacheco, Mari Carme, Nancy, Reina, Maricarmen, Francoise, Harold, Angel, Jide, Qasim, Rebecca, Hajar, Aanchal, Ane, Padre Marcelo, Padre Juaqim, Samuel, Daniel and all Indonesian friends in Tarragona, Barcelona, KAUST, Institut Teknologi Kalimantan, Taiwan, and Indonesia.

Last but not least, my family in Indonesia, my lovely sister Angelina Tutulenan Torimtubun and special thanks to René Toro Herrera for all the love, support, encouragement, and prayers during my PhD journey. Thank you for always believing in me when I doubted myself! I love you all.

Terima kasih yang mendalam saya ucapkan untuk kedua orangtua saya Jeremias Torimtubun dan Natalia Prihatin atas cinta, kasih sayang, semangat, didikan, kesabaran dan segala doa yang dipanjatkan untuk keberhasilan anak-anaknya. Terima kasih telah menjadi orang tua yang hebat! Terima kasih telah memberikan kepercayaan kepada anak pertamanya ini hingga ia dapat menyelesaikan studi doktoralnya dan lulus menjadi Dr. Elen! Disertasi ini saya kerjakan dengan sepenuh hati dan sebaik-baiknya agar pantas untuk saya persembahkan khusus kepada Ayah dan Bue sebagai ucapan terima kasih atas cinta dan pengorbanan yang tak akan dapat saya bayar oleh apapun. Elen sayang Ayah dan Bue! Semoga Tuhan selalu melindungi Ayah dan Bue.

Alfonsina A. A. Torimtubun

List of Acronyms

AFM	atomic force microscopy
Ag	silver
AM 1.5G	air mass 1.5 Global
BHJ	bulk heterojunction
BIPVs	building-integrated photovoltaics
BTP-4Cl (or Y7)	2,2'-((2Z,2'Z)-((12,13-bis(2-ethylhexyl)-3,9-diundecyl-12,13-dihydro[1,2,5]thiadiazolo[3,4e]thieno[2",3":4',5']thieno[2',3',:4,5]pyrrolo[3,2-g]thieno[2',3':4,5]thieno[3,2-b]indole-2,10-diyl) bis(methanyly-lidene))bis(5,6-dicholoro-3-oxo-2,3-dihydro-1H-indene-2,1-diylidene))dimalononitrile
BTP-4F (or Y6)	2,2'-((2Z,2'Z)-((12,13-bis(2-ethylhexyl)-3,9-diundecyl-12,13-dihydro-[1,2,5]thiadiazolo[3,4-e]thieno[2",3’’:4’,5']thieno[2',3':4,5]pyrrolo[3,2-g]thieno[2',3':4,5]thieno[3,2-b]indole-2,10-diyl)bis(methanylylidene))bis(5,6-difluoro-3-oxo-2,3-dihydro-1H-indene-2,1-diylidene))dimalononitrile
CB	chlorobenzene
CdTe	cadmium telluride
CE	charge extraction
CIGS	copper indium gallium selenide
CN	1-chloronapthaline
CT-state	charge-transfer state
CuPc	copper phthalocyanine
CuPcF$_{48}$	copper fluorinated phthalocyanine
D/A	donor/acceptor
DC	direct current
DIO	1,8-diiodooctane
DOS	density of states

E_g	energy bandgap
EQE	external quantum efficiency
ETL	electron transport layer
FF	fill factor
h	Planck’s constant
HOMO	highest occupied molecular orbitals
HTL	hole transport layer
IEICO-4F	2,2'-[[4,4,9,9-Tetrakis(4-hexylphenyl)-4,9-dihydro-s-indaceno [1,2-b:5,6-b']dithiophene-2,7-diyl]bis[[4-[(2-ethylhexyl) oxy]-5,2-thiophenediyl]methylidyne(5,6-difluoro-3-oxo-1H-indene-2,1(3H)diylidene)]]bis [propanedinitrile]
iOSCs	inverted organic solar cells
IS	impedance spectroscopy
ITIC-M	3,9-bis(2-methylene-((3-(1,1-dicyanomethylene)-6/7-methyl)-indanone))-5,5,11,11-tetrakis(4-hexylphenyl)-dithieno[2,3-d:2’,3’-d’]-s-indaceno[1,2-b:5,6-b’]dithiophene
ITO	indium tin oxide
J	current density
J_{ph}	photogenerated current
J_{SC}	short-circuit current density
J-V	current density versus voltage
J_0	reverse saturation current density of minority carriers
k_B	Boltzmann constant
LED	light emitting diode
LUMO	lowest unoccupied molecular orbitals
MPP	maximum power point
n	charge carrier density
NMR	nuclear magnetic resonance
NREL	National Renewable Energy Laboratory

OSC	organic solar cell
OPV	organic photovoltaic
PBDB-T	poly[(2,6-(4,8-bis(5-(2-ethylhexyl)thiophen-2-yl) benzo[1,2-b:4,5-b′]dithiophene)-co-(1,3-di(5-thiophene-2-yl)- 5,7-bis(2-ethylhexyl)benzo[1,2-c:4,5-c′]dithiophene-4,8-dione)]
PBDB-T-2F (or PM6)	poly[2,6-(4,8-bis(5-(2-ethylhexyl-3-fluoro)thiophen-2-yl)benzo[1,2-b;4,5-b´]dithiophene))-alt-(5,5-(1',3'-di-2-thienyl-5',7'-bis(2-ethylhexyl)benzo [1',2'-c:4',5'-c']dithiophene-4,8-dione)]
PCE	power conversion efficiency
PC$_{70}$BM	[6,6]-phenyl-C71 butyric acid methyl ester
PDINO	2,9-bis[3-(dimethyloxidoamino)propyl]anthra[2,1,9-def:6,5,10-d'e'f']diisoquinoline-1,3,8,10(2H,9H)-tetrone
PEDOT:PSS	poly(3,4-ethylenedioxythiophene)-polystyrene sulfonate
PFN	poly [(9,9-bis(3'-(N,N-dimethylamino)propyl)-2,7-fluorene)-alt-2,7-(9,9dioctyl-fluorene)]
PL	photoluminescence
PTB7-Th (or PCE10)	(poly[2,6-4,8-di(5-ethyl- hexylthienyl)benzo[1,2-b;3,3-b] dithiophene] [3-fluoro-2[(2-ethylhexyl)- carbonyl]thieno[3,4-b]thiophenediyl]
PTFE	polytetrafluoroethylene
PV	photovoltaic
q	elementary charge
RMS	root-mean-square
R$_S$	series resistance
R$_{Sh}$	shunt resistance
SCLC	space-charge-limited-current
T	temperature
TiO$_x$	titanium dioxide

TPC	transient photocurrent
TPV	transient photovoltage
TW	terawatt
UV-vis	ultraviolet-visible
V	voltage
V_{MPP}	voltage at maximum power point
V_{OC}	open-circuit voltage
VTE	vacuum thermal evaporation
WF	work function
Y5	(2,2’-((2Z,2’Z)-((12,13-bis(2-ethylhexyl)-3,9-diundecyl-12,13-dihydro[1,2,5]thiadiazolo[3,4e]thieno[2’’,3’’:4’,5’] thieno[2’,3’:4,5]pyrrolo[3,2-g] thieno[2’,3’:4,5]thieno[3,2-b]indole-2,10-diyl)bis(methanylylidene))bis(3-oxo-2,3-dihydro1H-indene-2,1-diylidene))dimalononitrile)
ZnO	zinc oxide
ZnPc	zinc phthalocyanine
$ZnPcF_{48}$	zinc fluorinated phthalocyanine
Z’	real impedance
Z”	imaginary impedance
μ	mobility
τ	charge carrier lifetime

List of Figures

List of Tables

List of Scientific Contributions

1. Scientific articles

This thesis is based on some works presented in the following publications:

1. J. G. Sánchez, **A. A. A. Torimtubun**, V. S. Balderrama, M. Estrada, J. Pallarès and Lluis F. Marsal, "Effects of Annealing Temperature on the Performance of Organic Solar Cells Based on Polymer: Non-Fullerene Using V_2O_5 as HTL", *IEEE Journal of the Electron Devices Society,* **2020**, *8,* 421-428. DOI: 10.1109/JEDS.2020.2964634
2. **A. A. A. Torimtubun**, J. G. Sánchez, J. Pallarès and Lluis F. Marsal, "A Cathode Interface Engineering Approach for the Comprehensive Study of Indoor Performance Enhancement in Organic Photovoltaic", *Sustainable Energy & Fuels,* **2021**, *4*, 3378-3387. DOI: 10.1039/D0SE00353K
3. **A. A. A. Torimtubun**, J. G. Sánchez, J. Pallarès and Lluis F. Marsal, "Photostability Study of Inverted Polymer Solar Cells under AM 1.5G and LED Illumination via Impedance Spectroscopy", *IEEE Journal of the Electron Devices Society,* **2021**, *9*, 484-491. DOI: 10.1109/JEDS.2021.3052719
4. **A. A. A. Torimtubun**, J. Follana-Berná, J. G. Sánchez, J. Pallarès, Á. Sastre-Santos and Lluis F. Marsal, "Fluorinated Zinc and Copper Phthalocyanines as Efficient Third Components in Ternary Bulk Heterojunction Solar Cells", *ACS Applied Energy Materials,* **2021**, *4*, 5, 5201-5211. DOI: 10.1021/acsaem.1c00734
5. **A. A. A. Torimtubun**, M. Méndez, J. G. Sánchez, J. Pallarès, E. Palomares and Lluis F. Marsal, "Shelf Lifetime Analysis of Organic Solar Cells Combining Frequency and Time Resolved Techniques", *Sustainable Energy & Fuels,* **2021**, *5,* 6498-6508. DOI: 10.1039/D1SE01107C
6. E. Moustafa‡, **A. A. A. Torimtubun**‡, J. Pallarès and Lluis F. Marsal, "Effect

of Additives and Annealing on the Performance of Nonfullerene-based Binary and Ternary Organic Photovoltaics", *Solar RRL,* **2021**, *2100480,* 1-16. DOI: 10.1002/solr.202100480. (‡ equal contribution)

7. **A. A. A. Torimtubun**, M. Méndez, E. Moustafa, J. Pallarès, E. Palomares and Lluis F. Marsal, "Achieving 17.7% Efficiency of Ternary Organic Solar Cells by Incorporating a High LUMO Level and Miscible Third Component", *submitted*
8. **A. A. A. Torimtubun**, J. Han, S.H.K. Palethi, D. Corzo, J. Pallarès, Lluis F. Marsal and D. Baran, "Efficient and Stable Semitransparent Ternary Organic Solar Cells using Y-series Nonfullerene Acceptor", *will be submitted*
9. **A. A. A. Torimtubun**, M. Ramírez-Como, J. Pallarès and Lluis F. Marsal, "Thermal Stability of PM6:Y7-based Ternary Organic Solar Cells", *will be submitted*

2. Patent

Método de Tratamiento Pre-Térmico para Dispositivos Fotovoltaicos
E. Moustafa, J. Pallarès, L. F. Marsal, J. G. Sánchez and **A. A. A. Torimtubun**
Spanish patent, *submitted*

3. Conference presentations, poster prizes & proceedings

The list of contributed presentations that received the prizes:

1. **A. A. A. Torimtubun**, J. G. Sánchez, V. S. Balderrama, M. Estrada, J. Pallarès and Lluis F. Marsal, "Impact of thermal annealing on the performance of inverted polymer:non-fullerene-based solar cells", *International Conference on NFA-Based Organic Solar Cells: Materials, Mophology and Fundamental (NFASC),* **2021**, Online, **best e-poster prize from ACS Applied Energy Materials**.

2. **A. A. A. Torimtubun**, J. G. Sánchez, J. Pallarès and Lluis F. Marsal, "Shelf lifetime analysis of polymer solar cells combining frequency and time resolved techniques", *NewOPV21. Advances in Organic Photovoltaics Nanoge Fall Meeting 2021*, **2021**, Online, **best e-poster prize from ACS Photonics**.

The list of contributed presentations that had been published in the conference proceedings:

3. **A. A. A. Torimtubun**, J. G. Sánchez, J. Pallarès and Lluis F. Marsal, "Study of the degradation of PTB7-Th:$PC_{70}BM$-based solar cells using TiOx as electron transport layers under ambient environment", *2020 IEEE Latin America Electron Devices Conference (LAEDC)*, **2020**, pp. 1-4.
   DOI: 10.1109/LAEDC49063.2020.9073326 (*oral presentation*)
4. **A. A. A. Torimtubun**, J. Follana-Berná, Á. Sastre-Santos, J. Pallarès and Lluis F. Marsal, "Preliminary study of the role of fluorinated phthalocyanines as non-fullerene acceptors in ternary organic solar cells", *37th European Photovoltaic Solar Energy Conference and Exhibition (EU PVSEC)*, **2020**, pp. 728-731.
   DOI: 10.4229/EUPVSEC20202020-3BV.2.53 (*poster presentation*)
5. **A. A. A. Torimtubun**, J. Pallarès and Lluis F. Marsal, "Analysing the efficiency enhancement of indoor organic photovoltaic using impedance spectroscopy technique", *2021 IEEE Latin America Electron Devices Conference (LAEDC)*, **2021**, pp. 1-4.
   DOI: 10.1109/LAEDC51812.2021.9437965 (*oral presentation*).
6. **A. A. A. Torimtubun**, J. G. Sánchez, J. Ferre-Borrull and Lluis F. Marsal, "(Invited) High performance ternary organic solar cells based on non-fullerene acceptors", *The Electrochemical Society ECS Meeting Abstracts*, **2021**, MA2021-01, 1049.
   DOI: 10.1149/MA2021-01321049mtgabs (*invited talk presentation*).
7. **A. A. A. Torimtubun**, J. Follana-Berná, Á. Sastre-Santos, J. Pallarès and Lluis F. Marsal, "Effect of thermal annealing on the performance of PTB7-

Th:$PC_{70}BM$-based ternary organic solar cells", *2021 13th Spanish Conference on Electron Devices*, **2021**, pp. 45-48.
DOI: 10.1109/CDE52135.2021.9455729 (*oral presentation*).

8. E. Moustafa, **A. A. A. Torimtubun**, J. Pallarès and Lluis F. Marsal, "Effect of additives and annealing on the performance of nonfullerene-based binary and ternary organic photovoltaics", *38th European Photovoltaic Conference and Exhibition (EU PVSEC)*, **2021**, invited paper in Solar RRL with DOI: 10.1002/solr.202100480 (*oral presentation*).

The works in this thesis had been presented in the following conferences:

9. **A. A. A. Torimtubun**, J. G. Sánchez, J. Pallarès and Lluis F. Marsal, "Effect of thermal annealing on the performance of non-fullerene acceptor-based inverted organic solar cells", *Graduate Students Meeting on Electronics Engineering*, **2019**, Tarragona, Spain, *poster presentation*.
10. **A. A. A. Torimtubun**, J. G. Sánchez, J. Pallarès and Lluis F. Marsal, "Impedance spectroscopy analysis on the indoor performance of organic photovoltaics", *12th International Conference on Hybrid and Organic Photovoltaics HOPV20 Online Conference*, **2020**, Online, *poster presentation*.
11. **A. A. A. Torimtubun**, J. Pallarès and Lluis F. Marsal, "Impedance spectroscopy analysis of indoor organic solar cells: a case study", *Graduate Students Meeting on Electronics Engineering*, **2020**, Tarragona, Spain, *oral presentation*.
12. **A. A. A. Torimtubun**, J. G. Sánchez, J. Pallarès and Lluis F. Marsal, "High-performance organic photovoltaic cells for indoor light energy harvesting", *Imaginenano Nano Spain Online Conference (IM2020)*, **2020**, Online, *oral presentation*.
13. **A. A. A. Torimtubun**, J. G. Sánchez, V. S. Balderrama, M. Estrada, J. Pallarès and Lluis F. Marsal, "Thermal annealing effect on the performance of polymer:non-fullerene-based solar cells using V_2O_5 as HTL", *Nanoge Fall Meeting*, **2020**, Online, *poster presentation*.

14. **A. A. A. Torimtubun**, J. Pallarès and Lluis F. Marsal, "Comparative study of photodegradation in organic photovoltaics under 1 sun and LED illumination", *13th International Conference on Hybrid and Organic Photovoltaics HOPV21 Online Conference*, **2021**, Online, *poster presentation.*
15. **A. A. A. Torimtubun**, J. G. Sánchez, J. Pallarès and Lluis F. Marsal, "Impact of annealing temperature on the performance of PBDB-T:ITIC-M – based organic solar cell", *35th Symposium on Microelectronics Technology (SBMicro 2021),* **2021**, Online, *oral presentation.*
16. **A. A. A. Torimtubun**, J. G. Sánchez, J. Pallarès and Lluis F. Marsal, "Simultaneous enhanced efficiency and photostability of indoor organic solar cells", *Nanoge Spring Meeting,* **2022**, Online, *oral presentation.*
17. **A. A. A. Torimtubun**, J. Pallarès and Lluis F. Marsal, "High-performance ternary organic solar cells based on two non-fullerene acceptors working in alloy-like model", *Fundamental Processes in Organic and Inorganic Hybrid Materials and Their Applications Gordon Research Conference,* **2022**, Castelldefels, Spain, *poster presentation.*

4. Scientific dissemination

Besides contributing to the conferences, the author was also contributed to these following outreach activities during the doctoral study:

1. European Researchers´ Night **2019**: "El grafè: un material meravellós", Tarragona, Spain.
2. European Researchers´ Night **2020**: "The solar revolution", Tarragona, Spain.
3. Invited speaker on National Webinar **2021**: "Solar energy utilization potential as a future energy in Indonesia", Balikpapan, Indonesia.
4. Tarragona Radio interview and URV Activa media news **2022**: "Researchers apply a new methodology for the study of organic solar cells shelf-lifetime degradation", Tarragona, Spain.

Dedicated to my parents:

Jeremias Torimtubun and Natalia Prihatin.

"Semangat anak ayah!

Tuhan, doa Ayah & Ibu selalu menyertai setiap langkahmu"

Jeremias Torimtubun

TABLE OF CONTENTS

Chapter 1

Introduction

1.1 Background

One of the largest and most complex challenges confronting the world today is the steady increase in energy consumption driven by population and economic growth. With the improved living standard of people worldwide and a gigantically growing human population that is predicted to exceed 10 billion people, the global energy demand is projected to increase of up to 47% within the next three decades.[1,2] Currently, a huge number of total energy usage about 16 TW is dominated by fossil fuels (natural gas, coal, and oil) as the main energy source.[3,4] However, there are some concerns about using fossil fuels as the main energy source due to their limitation of resources and their negative effects on climate, environment, and health. Renewable energies from wind, solar, biomass, geothermal, and hydropower generation have been considered seriously by the international governments as sustainable energy supplies. Among these natural resources, solar energy has the most potential because it is unlimited and does not depend on climate conditions. Solar irradiance provides the earth with about 120 000 TW, translates to 6-7 thousand times the current world energy consumption.[5] Converting solar energy into electricity was observed for the first time by French physicist Becquerel in 1839, known as the photovoltaic effect, in which the electric current had produced when the sunlight illuminating two connected platinum plates immersed in an electrolyte solution.[6] Then, more than 40 years later, in 1883, the first photovoltaic device based on selenium covered by gold thin-film with power conversion efficiency (PCE) of 1% was discovered.[7,8] It took almost one century for this technology to reach its milestone in 1954 with the discovery of the first practical silicon solar cell with PCE of 6% from the famous Bell Labs, was upgraded up to 14% by Hoffman Electronics.[9] The research efforts drove the PCE of silicon technology even higher, with PCE surpassing 27%, giving the silicon technology as the leader in solar market along with its reasonable stability. Crystalline silicon solar cells along with diverse thin-film technology based on inorganic components such as GaAs, $Cu(In,Ga)Se_2$

(CIGS), CdTe, and amorphous silicon are referred to as first and second generation solar cells, respectively. However, besides their high efficiency and high stability, these inorganic solar cells however have significant drawbacks, such as high material amount and manufacturing costs, complex fabrication process, and time-consuming. Third-generation solar cells have shown high potential for commercial availability of efficient, low-production cost, flexible, and scalable solar cells in the recent decades. Among these photovoltaic technologies, dye-sensitized cells, perovskite cells, and organic solar cells (OSCs) are the most relevant for the future of solar cells. **Figure 1.1** depicts the efficiency records chart from different research solar cell technologies summarized by National Renewable Energy Laboratory (NREL).[10]

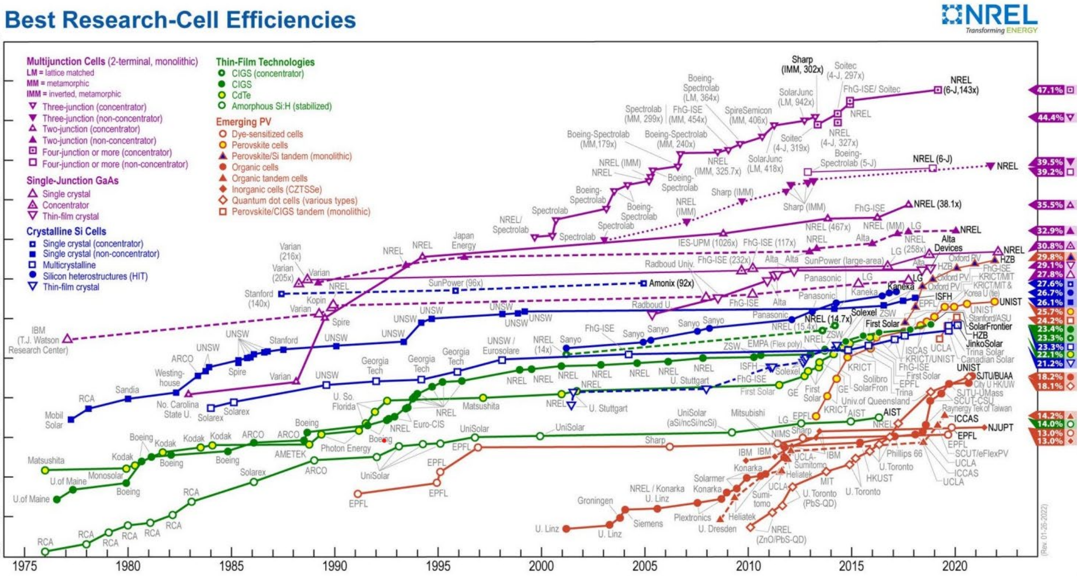

Figure 1.1 Current research-cell efficiency records of different photovoltaic technologies chart summarized by NREL.

In the last few decades, organic photovoltaics (OPVs) – technology based on organic materials – have reached a significant milestone towards commercialization by exceeding the 10% efficiency threshold, which has now been pushed closer to 20% for single-junction cells in lab-scale manufacturing. Even though the efficiency is still lower than inorganic counterparts, the emergence of OSCs has attracted tremendous attention in scientific and industrial communities due to their potential characteristics such as semitransparent, flexible, environmentally friendly, solution-processable, light-weight, low-cost, and scalable for roll-to-roll manufacturing.[11–13] Another essential feature of OSCs is the high absorption coefficient of active layer materials in OSCs (typically 10^5 cm^{-1}, 10^3 higher than silicon) which enables thin films (thickness around 100-300 nm) to absorb a large fraction of the incident solar light due to the lower charge carrier mobility compared to inorganic counterparts.[14] These unique properties of OSCs will lead the revolution in photovoltaic technology, opening a wider variety of advanced applications such as indoor power sources, agrivoltaics, wearable electronics, smart windows, *etc.* for the future OPVs market.

Generally, the Air Mass (AM) 1.5G irradiance (with the light intensity of 100 mW cm^{-1}) is the standard condition used to compare different solar technologies because it resembles the terrestrial sun spectrum of the standard illumination source for measuring PCE, calculated as the ratio of the electrical power output to the optical power input. Therefore, it is assumed implicitly that all photovoltaics are intended to convert solar energy to current rather than photons to current. In fact, recent studies demonstrated that OPVs are not only able to convert solar irradiation to current but also indoor irradiation from light-emitting diode (LED) lamps (with much lower light intensities, typically 0.1-1 mW cm^{-1}) into electricity more efficiently with PCE exceeding 30%, than inorganic solar cells (amorphous silicon and CIGS) with PCE of only 1-2%, as shown in **Figure 1.2**.[15,16] As the light emission spectra and power densities are different for each indoor light sources, the NREL chart will look very different from the latest version of Figure 1.1. This feature of OSCs for indoor power generation will be further discussed in Chapter 3.

Aside from traditional solar cells for power generation, one beauty of OSCs that outshines inorganic solar cells is their ability to be made semitransparent owing to their tunable optical band gap of organic materials to absorb near-infrared light while maintaining visible light transmittance. The semitransparent OSCs (ST-OSCs) can be fabricated by reducing the active layer thickness and using transparent top electrodes, making them appealing for versatile applications such as smart windows in building-integrated photovoltaics (BIPVs), greenhouses, car shelters, wearable electronics, floating photovoltaic, etc.[17] This peculiarity of OSCs for semitransparent application will be explained in Chapter 6.

Kaltenbrunner *et al.* recently took a step further to classify solar technology from regular power conversion efficiency to a power-per-weight (defined as the ratio of the output power per unit area of the solar cell under standard solar irradiation to the weight of the solar cell per unit area) which places OSCs as leading technology with ~10 Wg^{-1}.[18] This comparison is useful in space and aircraft, as well as wearable electronics, where the weight of the devices is just as critical as power output.

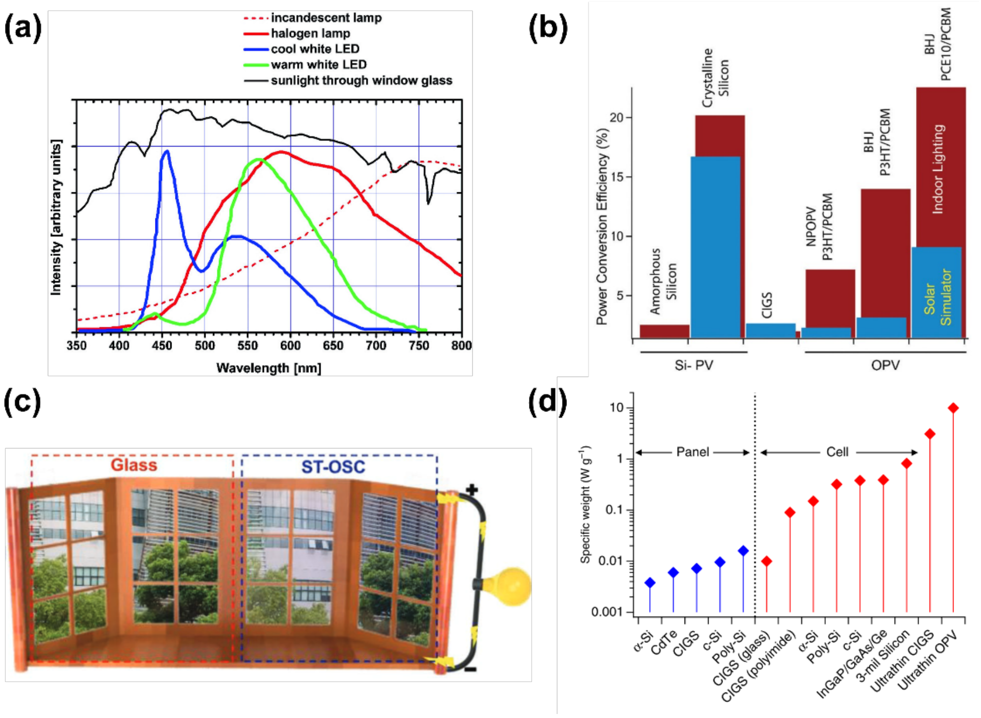

Figure 1.2 (a) Comparison of the indoor light source spectra versus solar spectrum.[15] (b) Corresponding PCEs of silicon and organic solar cells.[16] (c) Semitransparent OSCs as glass applied for smart-window.[19] (d) Power-per-weight for various photovoltaic technologies[11].

1.2 Organic solar cells basic principles

Organic solar cells are devices that use organic semiconductors as photoactive materials or layers that can absorb solar energy (or more broadly photons) and convert it into the current. The invention of OSCs arose from the discovery of the conductivity of conjugated polymers in 1977 by Shirakawa *et al.*, which opened up a new field of organic electronics, leading to the discovery of the first OSCs by Tang in 1987, who combined copper phthalocyanine and a perylene tetracarboxylic derivative with PCE about 1%.[20,21] Although a relatively low PCE was obtained, this discovery is the first demonstration of an organic device with photovoltaic effect. Generally, OSCs consist of the sandwiches of layers that have their own function that will be described in this following section including OSCs device architecture, basic operational principle, and the extracted device performance parameters.

1.2.1 Organic semiconductors

The general term of organic semiconductors refers to a vast group of materials that consists of alternating single and double bonds of carbon atoms (conjugation). The single bonds (σ-bonds) are linked to the localized electrons and double bonds contain both σ and π-bonds. In a conjugated system, carbon atoms are sp^2 hybridized, allowing the p_z orbitals to form π-bonds where π-electrons can be delocalized and travel through the system.[22] The delocalized π-electron is responsible for the semiconducting property similar to the conventional inorganic counterpart. Unlike inorganic semiconductors, where the conduction and valence band expand over the whole crystal and the atoms are bonded together by covalent interactions, the organic molecules on the other side have a weak interaction, typically van der Waals, which regulates the electronic properties of the materials.[23,24] The properties of organic materials are dominated by the molecular orbital of its components: π-bonding orbital interactions yield the valence band known as the highest occupied molecular orbital (HOMO) and π*-antibonding orbital interactions yield the conduction band known as the lowest unoccupied molecular orbital (LUMO). The energy difference between HOMO and LUMO in photoactive materials is generally in the range of 1.1-3.5 eV and is denoted as an energy bandgap (E_g).[25] One of the unique advantages of organic semiconductors compared to their inorganic counterparts is the ability to chemically tune their π-π* transitions (E_g of HOMO-LUMO) which can define the position of their absorption band. As HOMO determines the ionization potential and LUMO the electron affinity, these properties dictate the ability of organic molecules to donate or accept electrons.[26] Therefore, an organic semiconductor with greater HOMO levels commonly works as electron-donor material or so-called *p*-type, semiconductors while those with lower LUMO levels can act as electron-acceptor material or so-called *n*-type semiconductors. **Figure 1.3** illustrates the σ- and π-bonds formed in sp^2 hybridized conjugated molecule and its energy level splitting.

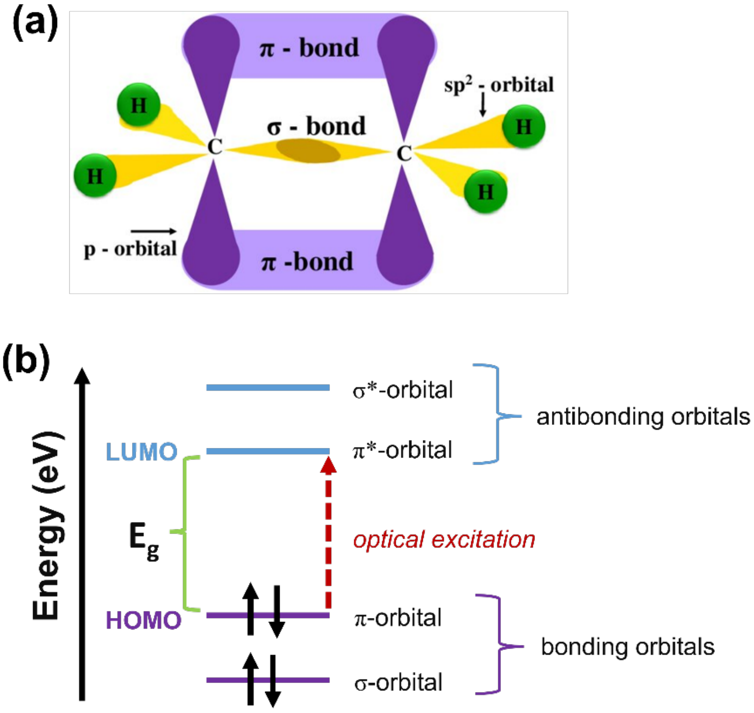

Figure 1.3 (a) Schematic illustration of sp^2 hybridized carbon atoms forming hybridized sp^2-orbitals called σ-bond and overlapped non-hybridized p_z-orbitals called π-bonds. (b) The energy level of orbitals in a π-conjugated molecule.

In contrary to the common inorganic semiconductors where the photons absorbed in the band gap are converted directly into free charge carriers (electrons and holes) at room temperature, organic semiconductors require an additional step because Frenkel excitons (electron-hole pairs) with low dielectric constant (typically 2-4) are generated.[27] Due to this low dielectric constant, strongly bound excitons by Coulomb forces with the binding energy of 0.3-0.5 eV are formed upon light absorption, whereas in inorganic semiconductors, delocalization occurs over multiple atoms, resulting in substantially lower binding energy.[28] The higher exciton binding energy in organic semiconductors results in a lower exciton dissociation rate, thus the probability of forming free charge carriers is low, even at high photon energies applied. Consequently, the charge transport mechanism in organic semiconductors relies on hopping charges between localized states, which results in carrier mobilities rarely exceeding 10 $cm^2 V^{-1} s^{-1}$.

1.2.2 Device architectures

The geometries of organic solar cells can be classified into several categories: (1) single-junction based on the photoactive materials morphology – single layer, bilayer heterojunction, and bulk heterojunction; (2) single-junction based on the buffer layers position – inverted structure; and (3) multi-junction device – tandem structure. **Figure 1.4** depicts each type of OSCs architecture and its energy band diagram. Among those categories, the simplest OSCs architecture is single layer OSCs in which the work function difference of two electrodes sandwiching an organic layer (typically *p*-type) creates an electric field that promotes the exciton dissociation in the depletion layer so that free charges can be collected at the respective electrodes, as shown in **Figure 1.4a**. As the electric field is not sufficient enough to split the excitons, only excitons generated in the depletion region contribute to the photocurrent, resulting in low quantum efficiencies (< 1%) and very low PCE (< 1%).[29] Thus, to obtain a large enough local electric fields to split the excitons, two layers of the highest electron affinity (electron acceptor material, A) and ionization potential (electron-donor material, D) are stacked together between conductive electrodes, known as bilayer heterojunction structure in which the photo-generated charges are created at the planar interface (see **Figure 1.4b**). Nevertheless, the PCE of this bilayer OSCs was still low due to the short exciton diffusion length (<10 nm), while D layer needs a thickness of around 80-100 nm to absorb the light, leaving all the rest of the exciton decay before reaching the interface to dissociate. As the photoactive layer thickness should have been similar to or less than the diffusion length of organic materials, the bulk heterojunction (BHJ) structure was designed by mixing together the donor and acceptor materials, where the interfacial D/A area was dramatically increased and the travel distance of a photogenerated exciton to dissociate was reduced due to the formation of interpenetrated networks (see **Figure 1.4c**). These BHJ OSCs are still the most popular and high-performing architecture until now with PCE exceeding 18%.[30]

In addition to the organic semiconductor layers and the cathode/anode electrodes, OSCs feature thin layers placed between the electrodes and the organic photoactive layer that are able to improve the charge collection and extraction, known as buffer layers or interfacial layers or interlayers. The effectivity of these layers is based on their ability to improve the energy-level alignment between HOMO and LUMO levels of organic materials with the work function of electrodes. There are two types of buffer layers that generally used in OSCs: (1) buffer layer placed between the cathode and the acceptor materials to improve the electron transporting and collection, known as electron transport layer (ETL) and (2) buffer layer between the anode and the donor materials to improve the hole transporting and collection, known as hole transport layer (HTL). Unlike the conventional architecture that is illuminated through a transparent anode electrode and reaches an opaque cathode electrode, the inverted OSCs reverse the buffer layer sequence to improve device stability and performance. As a result, the charges are collected in the opposite electrodes, as shown in **Figure 1.4d**.

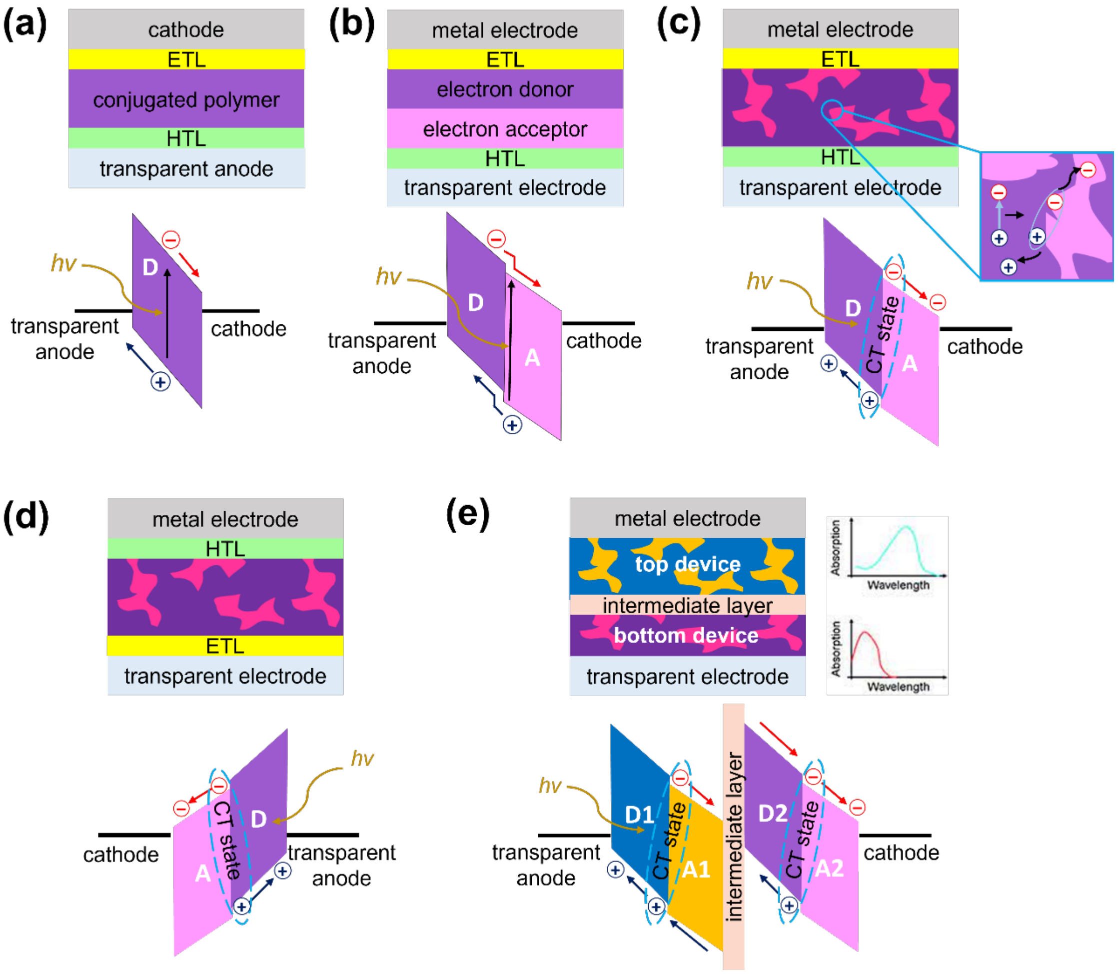

Figure 1.4 The device architecture of (a) single-layer semiconductor in single-junction, (b) bilayer heterojunction, and (c) bulk heterojunction with a conventional structure; (d) inverted structure; and (3) multi-junction device with tandem structure along with each energy alignment.

Tandem solar cells are more complex device architectures consisting of two distinct sub-cells with different bandgaps layered on top of each other, as depicted in **Figure 1.4e**. The first cell absorbs the higher-energy portion of the solar spectrum while remaining transparent to the lower-energy photons transmitted to and absorbed by the second cell. The intermediate layer should ensure the alignment of the quasi-Fermi level of the acceptor of the first cell with the quasi-Fermi level of the donor of the second cell or vice-versa. Due to the combination of two different bandgap materials, thermalization losses are reduced and large portion of the solar spectrum can be covered more efficiently.[31]

1.2.3 Working principles of bulk heterojunction solar cells

A better understanding of the fundamental process of converting light into electricity in BHJ OSCs is important to further enhance the device performance. Generally, the photocurrent generation in BHJ OSCs is composed of four consecutive steps: exciton generation, exciton dissociation, charge transport, and charge collection. **Figure 1.5** explains the events happening in a bulk heterojunction OSC from photon absorption to charge collection upon light illumination.

(i) Photon absorption and exciton generation

First, photons are absorbed by the donor or the acceptor within the active layer in which the energy of photon is transferred to an electron, resulting in the electron excitation from HOMO to LUMO ($\pi - \pi^*$ transition). As aforementioned, instead of the direct free charge carrier formations in inorganic materials upon photon absorption, the charge carriers in organic materials form an electrostatic attraction among them, leading to high binding energy due to their low dielectric constant, resulting in a coulombically bounded Frenkel excitons generation within the active layer. Without external perturbations, these excitons can relax to the ground state within hundreds of picoseconds, leading to the exciton recombination. The number of photons absorbed in the active layer is highly influenced by the absorption coefficient of the material and the film thickness of the active layer.[32,33]

(ii) Exciton diffusion and dissociation

Once an exciton is generated, excitons diffuse from one site to another within the condensed phase-form via energy transfer before decaying to the ground state. The energy transfer can occur through Förster (via space) or Dexter (via bond).

Excitons in this stage have a finite lifespan to reach the D/A interface, and the distance traveled during that time is referred to as exciton diffusion length, L_D, typically between 5-15 nm for amorphous π-conjugated polymers and in the range of 20-47 nm for non-fullerene acceptors.[34,35] If the lifetimes of the carriers are very short, they recombine before reaching the D/A interface. At the D/A interface, the exciton from a donor unit dissociates via electron transfer to the acceptor unit and subsequently forms a charge transfer (CT) state exciton. A similar step may happen for an acceptor exciton via hole transfer. Thus, the donor or acceptor phase must be small enough for excitons to reach the D/A interfaces before decaying to guarantee effective charge transfer in D/A blend, that is why phase separation is critical for optimal device performance.

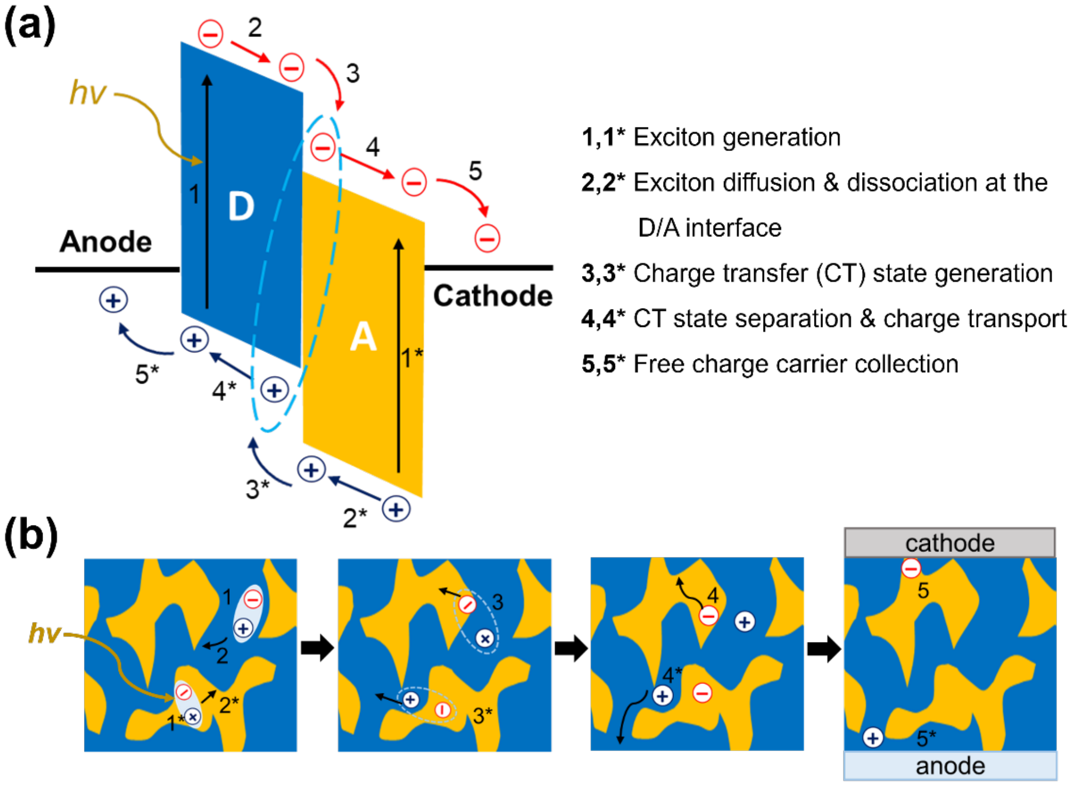

Figure 1.5 The working principle of BHJ solar cells from the perspective of (a) energy level alignment and (b) device layer structure.

(iii) Charge transfer state separation and charge transport

As the thermal energy of OSCs at room temperature is insufficient to separate the charges directly after absorption, therefore the energy difference of either the LUMO of D and A for electron transfer and the HOMO for hole transfer is required to separate the excitons in organic solar cells.[36] As aforementioned, LUMO and HOMO, which are often approximated by the electron affinity and ionization potential in molecular solid must be higher than the exciton binding energy, so that the charge separation becomes energetically favorable, where a free electron is on the electron-acceptor bulk and free hole on the electron-donor bulk. Free carriers in this stage are formed as polaron distortions in organic semiconductors and they are no longer in π or π^* orbitals but rather on polaron energy levels with slightly less energy. Depending on the type of polymer semiconductor used, this process takes an ultra-short time interval of within 100 fs.[37,38]

The transportation of free charge carriers to their respective electrodes can be driven by the built-in electric fields (drift) or a charge-concentration gradient (diffusion). In amorphous organic semiconductors, the charge transport mechanism is mainly performed by the hopping transport. Since the localization of amorphous semiconductors is strong, the density of states (DOS) which describes the energetic distribution of electronic states within energy bands is typically approximated with a Gaussian distribution. This mechanism is less efficient than band transport because amorphous organic semiconductors exhibit high trap concentrations resulting in low charge carrier mobility and charge recombination.

(iv) Charge carrier collection

Finally, at the electrodes, the free charges are collected and contributed to the photocurrent. The electrons are collected at the low work function electrode (cathode) and holes at the high work function electrode (anode). To realize an efficient charge carrier extraction, the LUMO of the acceptor should be higher than the work-function of the cathode, while the HOMO of the donor should be lower than the work-function of the anode. The difference between those energies offset determines the ohmic or Schottky contacts between organic material/electrode interface, whereas the ohmic contact is the most preferable for a highly efficient charge collection. A Schottky contact, on the other hand, might cause electrical losses and inefficient charge injection. The charge collection efficiency is affected by several factors such as charge transfer, dipole formation, chemical reactions, traps within the organic material, and charge recombination.[39]

1.2.4 Recombination processes

Several charge loss mechanisms affecting the photovoltaic performance of OSCs can take place in all the processes from light absorption to the free charge collection: exciton recombination, geminate recombination, and non-geminate recombination. **Figure 1.6** illustrates the recombination process in BHJ solar cells with the corresponding Jablonski diagram. When the excitons are formed upon light illumination in the photoactive layer, it is possible that excitons can recombine before reaching the D/A interface in their diffusion process, known as exciton recombination. Another loss mechanism that can take place during exciton dissociation is the so-called *geminate or monomolecular recombination*. The name 'geminate' is derived from the Latin word *gemini* which means twins, in this context the electron-hole pair is twins that create the absorption of a single photon. The geminate recombination occurs because the excited electron-hole pairs or CT state turn back to the ground state before dissociating into free charge carriers. Thus, the electron-hole pairs remain bound at the interface due to the electron-hole Coulombic attraction. Since each absorbed photon yields one electron-hole pair, the geminate recombination scales linearly with the number of absorbed photons. However, it is worth noting that the likelihood of any given geminate pair recombining is independent of the total density of geminate pairs at light intensities similar to one sun. As a result, the proportion of geminate pairs lost to geminate recombination at low light intensities is the same as it is at higher light intensities.

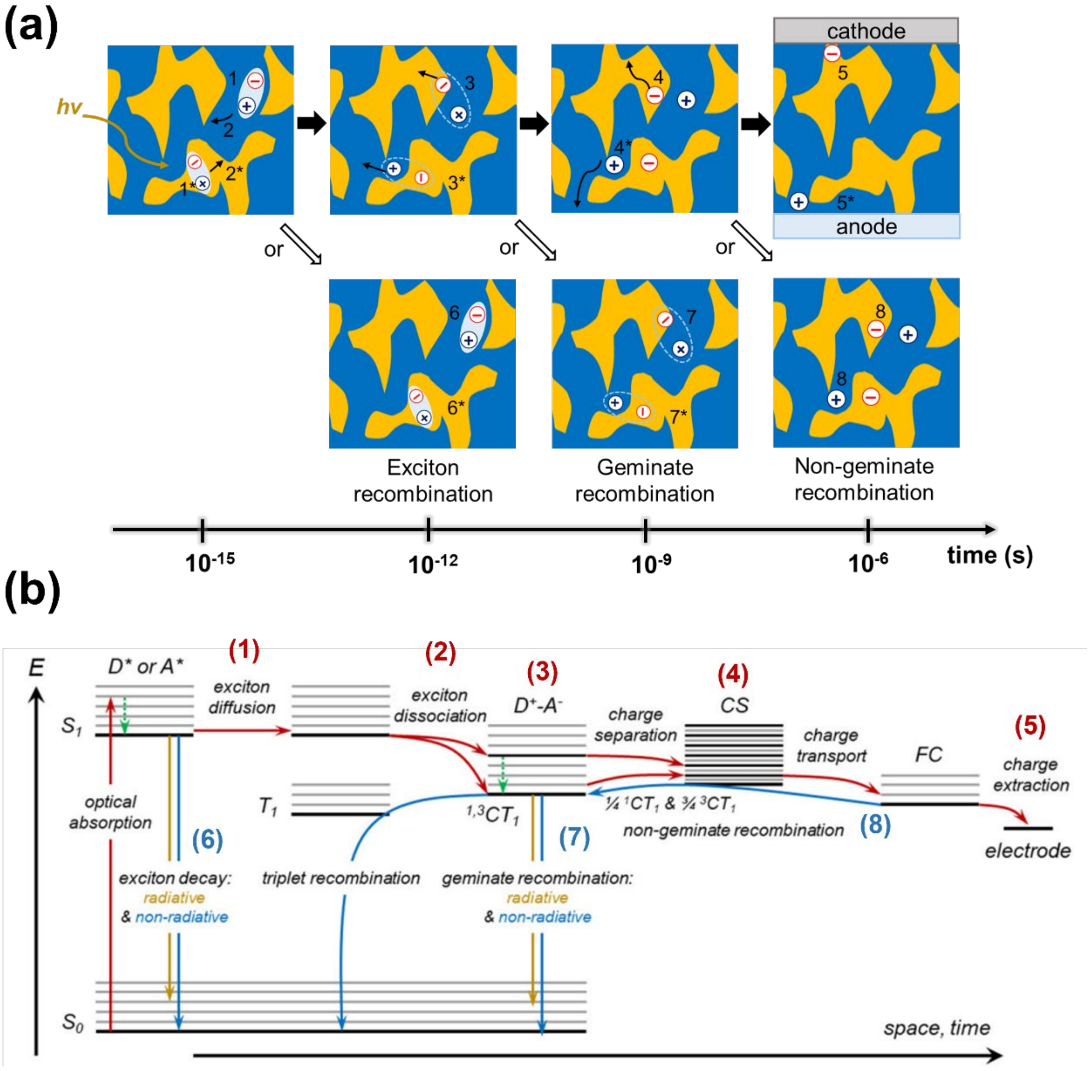

Figure 1.6 Recombination processes in organic BHJ solar cells from the perspective of (a) active layer and (b) Jablonski diagram as a function of time. Figures are modified from[40,41].

After CT states excitons are successfully dissociated into free carriers, the free electrons and holes have to diffuse to their selective electrode, otherwise they may recombine back to the ground state via *nongeminate recombination*. Nongeminate recombination differs from geminate recombination in that the hole and electron in nongeminate recombination do not originate from the same photon.

Figure 1.7 depicts the nongeminate recombination mechanisms that occurred in solar cells. Recombination resulting from these non-geminate charge carriers may be recognized as three distinct mechanisms: bimolecular (Langevin), trap-assisted (Shockley-Read-Hall / SRH), and auger recombination. Bimolecular recombination is the recombination of a free electron with a free hole that is commonly linked to the asymmetric charge carrier mobility of holes/electrons in bulk, which leads to the space charge formation, reduced charge carrier lifetime and carrier density, as shown in **Figure 1.7a**. This type of recombination is the primary loss mechanism in most efficient OSCs, and it is generally described by Langevin recombination coefficient R_L following equation 1.1:

$$R_L = \frac{q}{\varepsilon_r \varepsilon_0} \mu_e + \mu_h \tag{1.1}$$

where q is the elementary charge, ε_r is the relative permittivity, ε_0 is the vacuum permittivity, and μ_e and μ_h are the mobilities of electrons and holes, respectively. Langevin-type implies that the rate-limiting step is the diffusion of two mobile opposing charges attracted to each other in their mutual Coulomb field.[42,43]

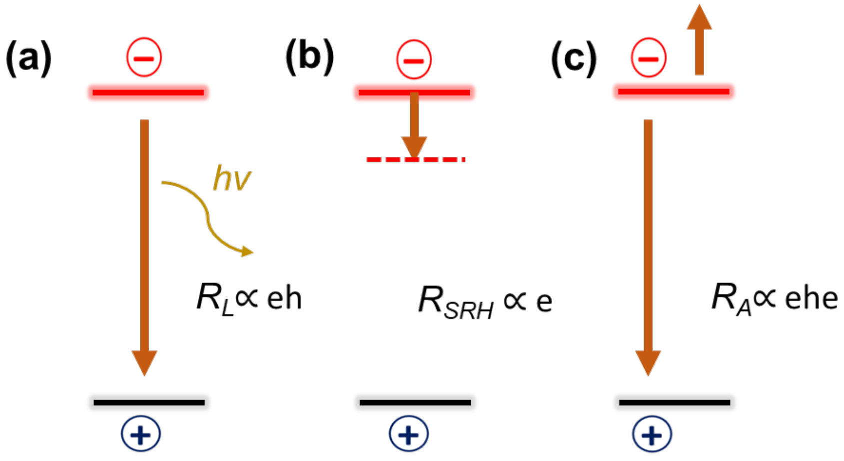

Figure 1.7 Non-geminate recombination mechanisms: (a) bimolecular Langevin recombination where the rate is dependent on both electron and hole mobilities and densities; (b) trap-assisted Shockley-Read-Hall recombination where the rate depends on electron (hole) mobility and density combined with amount of electron (hole) traps; and (c) Auger recombination where the rate has third order of dependence on carrier density.

As depicted in **Figure 1.7b**, free charge carriers can also be lost by first-order process of trap-assisted recombination in which one electron and one hole recombine through a localized energetic trap. This recombination is commonly modeled in inorganic semiconductors by the SRH recombination process which involves two carriers, the first one carrier is trapped and the second one is the free charge with the opposite sign. The rate-limiting step in the SRH process is the diffusion of the mobile carrier toward the trapped one in their mutual Coulomb field. The analysis of current-voltage (*J-V*) characteristics as a function of the light intensity (P_{light}) is a particularly effective method for estimating which type of nongeminate recombination. Information on the trap-assisted recombination can be assessed by studying the light intensity dependence of the open-circuit voltage (V_{OC}) as described in equation 1.2:

$$V_{OC} = \frac{E_g}{q} - \frac{kT}{q} \ln \left[\frac{(1-P)\gamma N_c^2}{PG} \right] \tag{1.2}$$

where E_g is the energy difference between the HOMO of the donor and the LUMO of the acceptor, q is the elementary charge, k is the Boltzmann constant, T is the temperature in Kelvin, P is the dissociation probability of the electron-hole pairs into free carriers, γ is the recombination constant, N_c is the density of states in the conduction band, and G is the photogeneration rate.[44,45] Since G is the only term directly proportional to light intensity (with P and γ independent on it), a slope of V_{OC} vs $\ln(P_{light})$ should equal kT/q in the case of bimolecular recombination. On the other hand, in the presence of trap-assisted recombination losses, a stronger dependency of V_{OC} versus light intensity is typically observed with the slope of V_{OC} *vs.* $\ln(P_{light})$ being closer to 2 kT/q.

In addition, the third possible nongeminate recombination mechanism is Auger recombination, also known as trimolecular recombination, which has a recombination order of 3, as exhibited in **Figure 1.7c**. Auger recombination occurs when an electron in the LUMO recombines with a hole in the HOMO, transferring energy to a third electron, which is subsequently stimulated to a higher energetic state. Since AM 1.5G illumination is generally not enough to provide high charge carrier densities for Auger recombination, this type of recombination is less likely to be present in OSCs.

1.2.5 Photovoltaic performance parameters

The photovoltaic performance of a solar cell is typically evaluated by measuring the current density (J) as a function of applied voltage (V) in the dark and under illumination conditions. The curve generated from this measurement is widely known as *J-V* curves or *J-V* characteristics, as depicted in **Figure 1.8**. Although a solar cell produces no photocurrent in the dark, it should follow diode behavior that allows current to flow in one direction when polarized properly. In an ideal solar cell, when the series and shunt resistances are negligible, the *J-V* characteristic of the diode can be expressed according to Shockley's equation 1.3:

$$J = J_0 \left[\exp\left(\frac{qV}{kT}\right) - 1\right] \tag{1.3}$$

where J_0 is the reverse saturation current density, q the elementary charge, k Boltzmann constant, T the temperature, and V the output voltage. It is worth noting that the meaning of J_0 is linked to the number of charges capable of overcoming the energetic barrier in the reverse direction, which represents the minority charge density in the vicinity of the barrier.[46] The farther from the ideal solar cell, the greater J_0 value will be. In the case when a solar cell is illuminated, a photocurrent J_{ph} is generated, thus resulting in a downward shift of the *J-V* curve, as shown in **Figure 1.8a** and equation 1.4:

$$J = J_0 \left[\exp\left(\frac{qV}{kT}\right) - 1\right] - J_{ph} \tag{1.4}$$

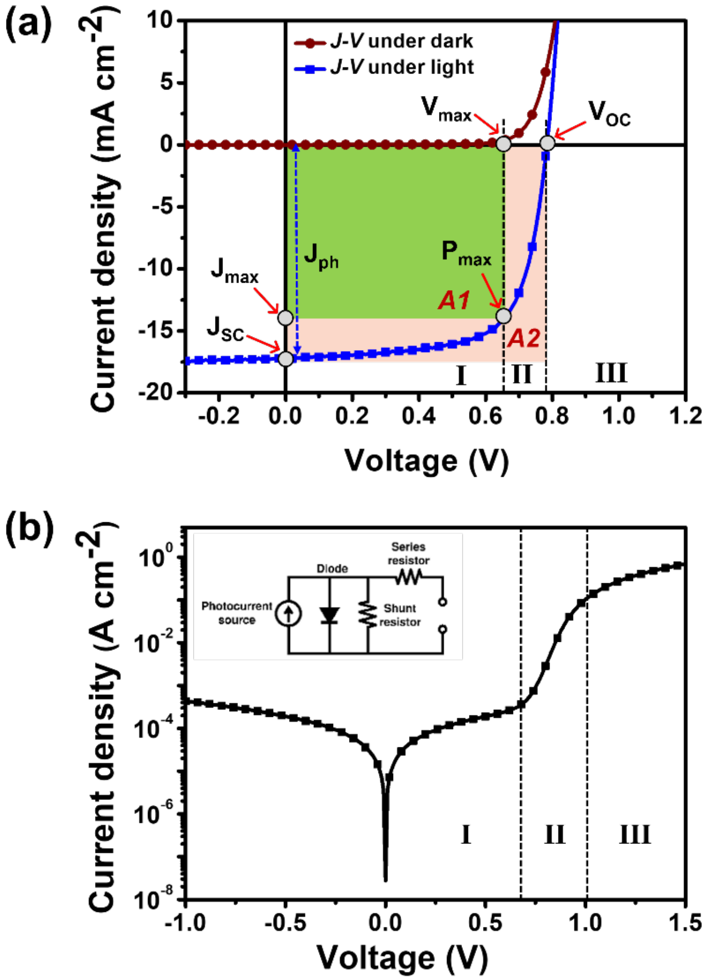

Figure 1.8 Typical current density versus applied bias of a solar cell under (a) 1 sun illumination and (b) in the dark. Inset figure b is the equivalent circuit for practical solar cell. The three regions account for where the different effects dominate: Region I accounts for leakage (shunt) current, Region II recombination currents, and Region III series resistance.

As aforementioned, the typical standard test condition of Air Mass 1.5 Global spectrum (AM 1.5G) at cell temperature of 25° C has generally been used as P_{light} an incident light intensity of 100 mW cm^{-2} in the illuminated *J-V* measurement in order to do an accurate and comparable characterization. “Air Mass 1.5” denotes 1.5 atmosphere thickness, corresponding to 48.2° solar zenith angle while the term “Global” refers to both direct and diffuse radiation.[47] Therefore, to evaluate the performance of OSCs, a parameter of PCE is used, which is calculated as the ratio of maximum power output to the incident power of the light source. The maximum power output (P_{max}) of the device is the point at which the product of the current density and applied bias is maximum (J_{max} and V_{max}) – this is known as the maximum power point (MPP). In other words, P_{out} can be calculated from the product of the short circuit current (J_{SC}), V_{OC} and the fill factor (FF) as expressed in equation 1.5:

$$PCE = \frac{P_{max}}{P_{light}} = \frac{J_{max} \times V_{max}}{P_{light}} = \frac{J_{SC} \times V_{OC} \times FF}{P_{light}} \qquad (1.5)$$

The J_{SC} is the current output when the maximum photocurrent density (J_{ph}) is recorded at the short-circuit condition, i.e. the condition where the output voltage bias is zero, the external load has zero or negligible resistance. As V=0, equation 1.4 becomes:

$$J(V = 0) = J_{ph} = J_{SC} \qquad (1.6)$$

J_{SC} depends on the area of the whole layer of solar cells that intersect with the active layer, thus in order for the J_{SC} of OSCs can be compared with the other device with similar structures, J_{SC} is obtained by dividing by the area with the unit of mA cm^{-2}. Moreover, J_{SC} can be influenced by the number of incident photons, the thickness of the active layer, the spectrum of the incident light, the morphology of the organic semiconductor layer, and the efficient exciton generation and dissociation.

The V_{OC} is the maximum voltage a solar cell can provide to an external circuit, which measured at open-circuit condition where no net current flows out of the device (J=0). The V_{OC} depends on the energy gap between the LUMO level of the acceptor and the HOMO level of the donor. Some factors that are of crucial importance in determining V_{OC} of OSCs are density of states or energetic disorder, charge transfer states, D/A interface, microstructure, recombination, temperature, light intensity, and charge carrier density.[48] Equation 1.7 describes the V_{OC} with $J(V=0)$ and $J_{ph} >> J_0$:

$$V_{OC} = n_{id}\frac{kT}{q}\ln\left(\frac{J_{ph}}{J_0} + 1\right) \tag{1.7}$$

The FF is a parameter that measures the quality of OSCs in terms of power. FF describes how "square" the *J-V* curve is and it indicates how "difficult" or "easy" it is to extract photogenerated carriers from a photovoltaic device. Thus, FF can be defined in equation 1.8 as:

$$FF = \frac{A1}{A2} = \frac{J_{max} \times V_{max}}{J_{SC} \times V_{OC}} \tag{1.8}$$

where $J_{max} \times V_{max}$ represents the green rectangle A1 and $J_{SC} \times V_{OC}$ represents the beige rectangle A2. The ideal value for FF is 1 (A1=A2) when the *J-V* curve is a rectangle (with no parasitic resistance). Nevertheless, in practical solar cells, the FF is always lower than 1 due to the presence of parasitic resistance effect and the fact that photovoltaic devices are composed of *p-n* junction diodes, and thus *J-V* curve behaves more like exponential functions rather than step functions.[49]

In the case of practical solar cells, parasite resistances (series and shunt resistance) are non-negligible. Thus, the series resistance R_S and shunt resistance R_{Sh} are counted into the equivalent model for energy losses, as shown in inset **Figure 1.8b**, where the solar cell *J-V* behavior can be divided into four constituent parts: a photocurrent source, diode, series resistor, and shunt resistor. Note that the diode represents electron-hole recombination at *p-n* junction. R_S is derived from the bulk resistance of the active layer and electrodes and also the interfacial contact resistance between the active layer and electrodes. The main effect of high R_S on the OSCs performance is the less voltage drop in the diode, resulting in the reduction of FF. On the other hand, R_{Sh} arises from several kinds of leakage currents originating from the pinhole in the cell, the edge of the device, or from localized defects due to the imperfections of the manufacturing process. R_{Sh} has the effect of dividing current from diode, opposite to the effect of R_S, the low R_{Sh} in OSCs reduces V_{OC} and FF, resulting in the decrease of P_{out}. Considering the parasitic resistance, the equivalent circuit in equation 1.4 can be expressed by:

$$J = J_0 \left[\exp\left(\frac{q(V-JR_S)}{nkT}\right) - 1\right] + \frac{V-JR_S}{R_{Sh}} - J_{ph} \tag{1.9}$$

According to equation 1.8, the *J-V* curve is generally divided into three regions, as shown in Figure 1.8b. At reverse bias or negative voltages and low positive voltages (Region I), the drift of charge carriers to respective electrodes is high, so no current can flow, the *J-V* curve is determined by $1/R_{Sh}$. As the voltage increases, at the intermediate positive voltage (Region II), the *J-V* curve is an exponential line and its characteristic is defined by the diode (n) where the diffusion current overcomes the drift current. At high positive voltages (Region III), the *J-V* curve is a second straight line with the slope controlled by $1/R_S$ where the charges start to accumulate and modify the electric field in the medium.[50,51]

1.3 Ternary organic solar cells

As aforementioned in the previous section, the development and basic concept of binary OSCs that bulk heterojunction architecture can facilitate the improvement of PCE by over 18% in single-junction devices to date, however, despite the significant advancement achieved, the PCE of OSCs has to be boosted to compete with commercial inorganic solar cells. The main limitation in OSCs is due to the intrinsic narrow absorption bands of organic semiconductor materials, making it challenging to fully utilize the energy from the solar spectrum with a single-junction binary device. To overcome the absorption limitation, ternary (multicomponent) and tandem (multijunction) OSCs have become two main strategies employed in the last decade (**Figure 1.9**).

Tandem OSCs, despite an improved light absorption as well as reduced thermalization photonic energy loss leading to a recorded PCE of over 20% reported,[52] the fabrication of tandem OSCs require complicated preparation processes, which is particularly challenging for all solution-processed BHJ OSCs and may impede their commercial applications. Alternatively, the ternary strategy is not only a simple yet effective approach that can combine each merit of binary and tandem OSCs by incorporating a third component (either D or A) to improve the photon harvesting capability in a single-junction device, but also it can maintain the simplicity of single-step layer processing fabrication rather than the more complex tandem OSCs. Here, the fundamental mechanism in ternary OSCs (TOSCs), the role of third component addition in the ternary blend as well as the state-of-the-art ternary systems will be further discussed.

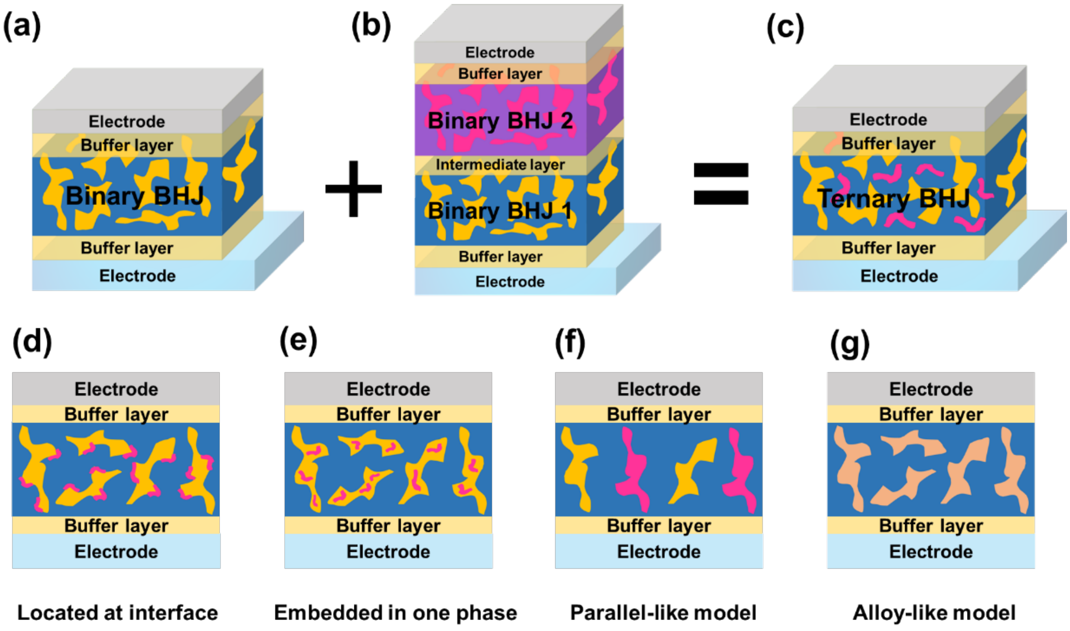

Figure 1.9 Schematic of (a) bulk-heterojunction, (b) tandem, and (c) ternary OSCs. (d) – (g) Possible ternary morphologies based on the location of the third component in ternary OSCs.

1.3.1 Working mechanism of TOSCs

In principle, a ternary blend is composed of three components in a single photoactive layer: two host components consist of a primary electron donor (D or D1) and a primary electron acceptor (A or A1), together with the third guest component that is the minority addition of secondary donor, D2 or secondary acceptor, A2 into the host system. Depending on the position of the third component in the blend, it may determine the primary working mechanism of TOSCs based on the energetic and phase structure of the third component, as shown in **Figure 1.9d-g.**[53] That is, the third component can be (d) embedded in either the host donor or host acceptor phase, (e) located at the host donor/acceptor interfaces, (f) creates its own phase separated from the host donor and acceptor phases forming the so-called parallel-linkage, and (g) alloyed with the host donor or host acceptor to display collective electrical properties. However, in practice, depending on the ratio of D2 or A2 to the binary host system, the BHJ of ternary blends can feature one or more of these BHJs, and hence more than one working mechanism could be adopted. As depicted in **Figure 1.10**, there are four main TOSCs working mechanisms proposed in the literature, (i) charge transfer and (ii) energy transfer operating mechanism governed by the energetics, whereas (iii) parallel-linkage model, and (iv) alloy model operating mechanism governed by the blend phase structure.

(i) Charge transfer

To obtain an efficient charge transfer, the HOMO and LUMO energy levels of the third component should be located between those of the host donor and host acceptor, forming a cascade energy alignment. This cascade energy level can avoid energy traps and can facilitate the charge separation and charge transfer at the D/A interface due to the functionality of the third component as a charge relay for electron and hole transport.[54] In the charge transfer mechanism, the third component will directly generate free charge carriers, and the charge transport channels strongly depend on the existing host domains, indicating the location of the guest component is at the interfaces between the host donor and acceptor. As illustrated in **Figure 1.10a**, in the case of D1/D2/A ternary system, the exciton generated in the donor matrix (D1 and D2) could be dissociated into the charge carriers at the D1/A and D2/A interfaces. The electrons are primarily transferred to D2 through D1 before being transferred to A. Through the transport channel of A, the electrons can be effectively collected by the cathode; additionally, the holes are first transferred to D1 through D2 and then transported to the anode via the transport channel of D1, where they are efficiently gathered by the anode. Typically, the V_{OC} of the charge transfer dominant TOSCs tends to be pinned to the smaller one of the corresponding binary OSC devices, which may be explained by the fact that almost all the holes can reach the anode through the transport channel of the donor with a higher HOMO level.

The charge transfer mechanism was first introduced and explained by Koppe *et al.*[55] in 2010 by adding C-PCPDTBT or Si-PCPDTBT as a third component in the host P3HT:PC$_{61}$BM blend with a PCE of 2.8% probed by photoluminescence (PL) spectroscopy and transient absorption spectroscopy (TAS). It was observed by PL that the emission intensity of host donor P3HT was quenched, without increased emission intensity of third component PCPDTBT, indicating that the charge transfer occurred in the corresponding ternary system. On the other hand, the TAS results suggested that by selectively photoexcited the third component, the steady state concentration of third component polarons was negligible when it was blended with host matrix. The current-voltage measurement could be employed for assessing the charge transfer mechanism in ternary blend. An *et al.*[56] studied the charge transfer between D1 and D2 (without A) with *J-V* characteristics, obtaining higher current density in the D1:D2 blend than those of single donors.

(ii) Energy transfer

In a ternary blend, the other mechanism governed by the energetics of three materials is the so-called energy transfer mechanism, which sometimes can simultaneously exist with the charge transfer process. Thus, the dominant mechanism will be dependent on the kinetically competitive relationship between them. In the energy transfer mechanism (see **Figure 1.10b** for D1/D2/A example structure), the third component (D2) does not directly generate free carriers. Instead, D2 acts as the energy absorber to harvest energy photons from the excited energy state in D1 through Förster resonance energy transfer (FRET) or Dexter energy transfer. Then, the generated exciton in D2 dissociates at the interfaces between D2 and A, which can form free electrons and holes. The free electrons are transferred to the cathode via A's transmission channel, while the free holes in D2 can either be transferred directly to the anode or transported to D1 and subsequently to the anode via D1's transmission channel.

To realize an effective energy transfer, the emission spectrum of the energy donor (D1) should overlap with the absorption spectrum of the energy acceptor (D2). Depending on the spectral gap between absorption and emission, the energy transfer mechanism mainly includes two forms: FRET (long-range and based on resonance) of electrofluorescence and Dexter energy transfer (short-range and based on electron exchange) of electro-phosphorescence. The former occurs through the long-range dipole-induced Coulomb interaction between the energy donor and energy acceptor materials. Meanwhile, the latter primarily occurs through the electron-exchange interaction between the energy donor and energy acceptor materials. Since the radius of the energy transfer is limited, the distribution position of the energy donor and energy acceptor should be relatively near (<10 nm), which is equivalent to the distribution requirements of the third component in the charge transfer mechanism.[57]

Recently, a high PCE of 17.4% for the energy transfer dominant device was achieved by Ma *et al.*[58] for integrating reduced miscibility and the higher LUMO level of ITCPTC third component into PM6:Y6 blend (D/A1/A2 system). They used PL measurement to discriminate between charge and energy transfer, in which the PL intensity of the third component ITCPTC increase when blended with the host acceptor (Y6) with respect its pristine film. In addition, the overlapping spectra between emission of ITCPTC and the absorption of Y6 were observed, strongly indicating the energy transfer between A1 and A2, which contributed to the enhancement of J_{SC}. Moreover, they also fabricated the single-component device and obtained the current density in the corresponding J-V characteristic of the A1/A2 blend is not significantly increase with the respect to the A1 and A2 neat films, implying that no significant charge transfer occurs between A1 and A2.

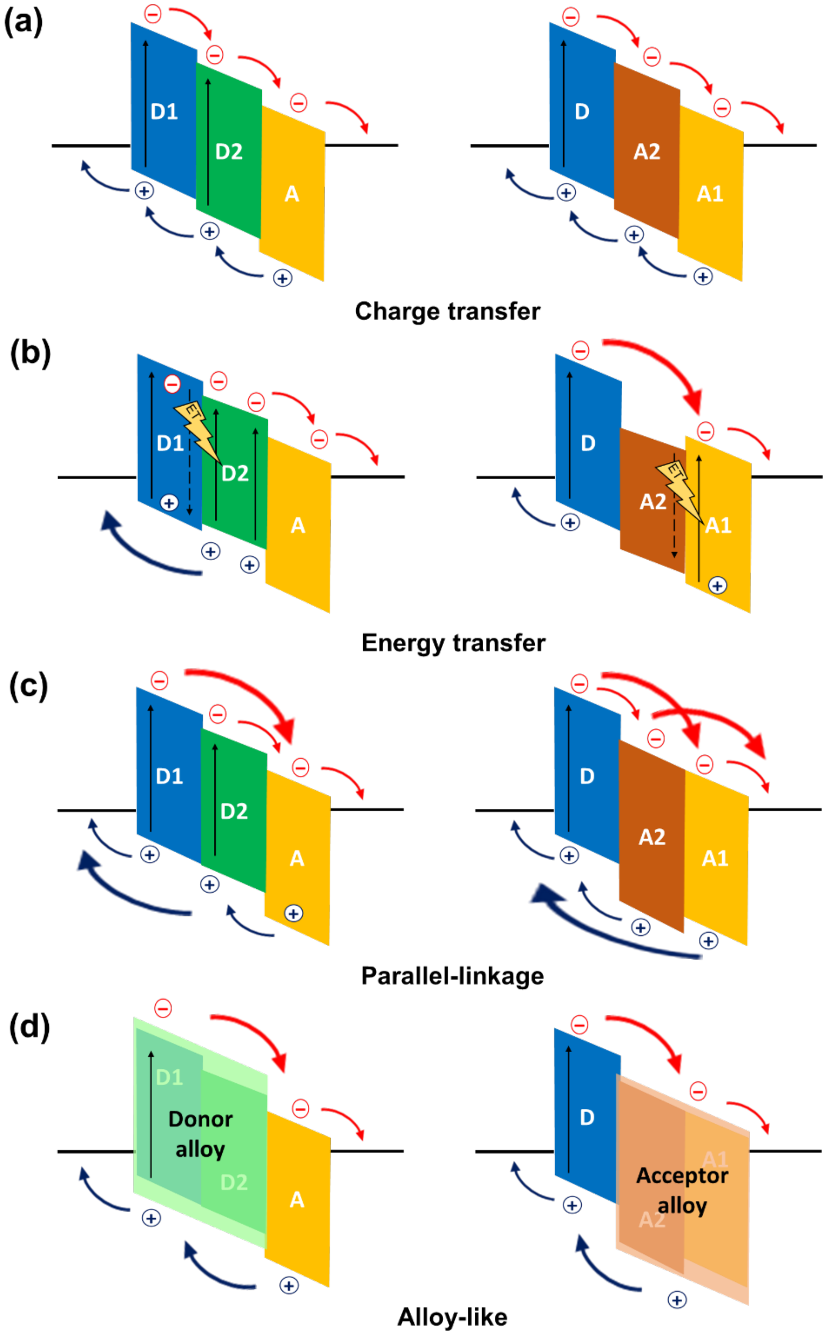

Figure 1.10 Schematic diagram of four working mechanisms of TOSCs: (a) charge transfer mechanism, (b) energy transfer mechanism, (c) parallel-linkage model, and (d) alloy-like model. The left-hand side figures are D1:D2:A systems and the right-hand side figures are D:A1:A2 systems.

(iii) Parallel-linkage model

Different from the charge transfer and energy transfer mechanisms that are governed by the energy alignment, the parallel-linkage model is one of the TOSCs fundamental mechanisms governed by the nanomorphology of the blend. This model does not necessitate complicated conditions to occur, which means that the absorption spectra, the energy levels, and miscibility between the third component and the host system do not need to be perfectly matched. In parallel-linkage model, by considering the example of TOSCs with the D1/D2/A structure, the excitons generated in each individual donor (D1 and D2) diffuse to the corresponding donor/acceptor interfaces and then dissociate into the free electrons and holes (see **Figure 1.10c**). It is worth noting that there is no energy transfer and charge transfer between D1 and D2 because the device works independently as two subcells (D1/A device and D2/A device) connecting in parallel, analogous to a tandem architecture. As a result, the J_{SC} of this TOSC can be equivalent to the sum of the J_{SC} values of the two individual subcells, whereas the V_{OC} of the ternary blend lies between the V_{OC} values of two subcells. Apart from conventional composition-dependent multiblend systems, which only employ a limited quantity of the third component, parallel-linkage model has relatively high tolerance to third component composition ratios.

Yang *et al.* were the first to propose and introduce the concept of parallel linkage mechanism using DTffBT:DTPyT:$PC_{61}BM$ blend (D1/D2/A structure) with the best PCE of >7%.[59] At first, they fabricate two binary devices with each active layer thickness of 50 nm, then they combined the two 50 nm-subcells into so-called parallel-like bulk heterojunction (PBHJ) ternary solar cell with a total active layer thickness of 100 nm. The two subcells with 50 nm-thick active layers contain approximately the same quantity of individual components as that in the corresponding PBHJ cells with 100 nm-thick active layers. The result revealed that the external quantum efficiency (EQE) of the TOSCs is close to that of the sum of each subcell, indicating that the free electrons and holes generated in each subcell were transported via their respective transfer channels and gathered by the electrodes. As a result, the J_{SC} of the TOSCs is nearly identical to the sum of the two subcells with half the thickness of the active layer. The current record PCEs for parallel-linkage dominant TOSCs were achieved by Zhang *et al.*[60] in 2020 using Phi-Se as third component added into PM6:Y6 binary blend with 16.4% PCE.

(iv) Alloy-like model

In contrast with the parallel-linkage model, the alloy-like model usually requires the third component that has excellent compatibility with the donor or acceptor of the host system. The good miscibility between A1/A2 or D1/D2 and their similar structural backbones along with their similar electrical properties are reported to facilitate a better-intermixed phase, forming either A1/A2 or D1/D2 electronic alloy. A new charge-transfer state with a new mutual HOMO energy level and a new LUMO energy level of a new single phase of two or multiple components is formed, as shown in **Figure 1.10d**. As a result, the energy level changes with a variation of the third component ratio, leading to the evolution of V_{OC} in TOSCs.

The alloy model mechanism was first proposed by Thompson *et al.*[61] using a P3HTT-DPP:P3HT-co-EHT:$PC_{61}BM$ blend in D1/D2/A configuration with PCE of 5.51%. Recently, Zhan *et al.*[62] investigated an alloy-like model TOSCs by adding BTP-M (A2) into a PM6:Y6 binary system. Different from Y6, BTP-M replaced the electron-pulling F atom of Y6 with the electron-pushing methyl group to afford higher energy levels and lower crystallinity. Because of the similar chemical structure, BTP-M showed excellent compatibility with Y6 and had higher HOMO and LUMO energy levels in contrast to Y6. The compatible and similar electrical characteristics resulted in the formation of alloy-like models. Owing to the appropriate energy levels of the alloy, the energy loss was effectively reduced from 0.49 to 0.45 eV. Besides, the morphology of the TOSC was considerably optimized by the alloy model formed by Y6 and BTP-M and the slightly lower crystallinity of BTP-M resulted in achieving an excellent PCE of 17.03% with a J_{SC} of 26.56 mA cm^{-2} and V_{OC} of 0.875 V. The significant improvement in the photovoltaic performance could be mainly attributed to the enhancement in the EQE and the reduction in energy loss.

1.3.2 The role of the third component

The judicious selection of the third component and optimization of weight ratio in ternary blend can play various roles in improving TOSC performance, mostly from an electrical and/or morphological standpoint. Electrically, the third component can serve as a charge-relay bridge and/or an energy transfer sensitizer for high-energy region. Morphologically, it can induce enhanced crystallinity while maintaining the appropriate phase domain size, which is predicted to facilitate the balanced of charge dissociation and charge transport.

(i) Spectral and energetic modulation

The first consideration in selecting the third component in TOSCs is guided by the requirement of extending or enhancing light absorption of the active layer, usually into near-infrared (NIR) regions or covering strong absorption in most regions of the solar spectrum. Therefore, it is a straightforward strategy to introduce a third component with complementary absorption to its host binary blend. A common method to enhance optical absorption is by synthesizing or selecting the third component material based on their optical band gap, E_g^{opt} that can extend or complement those of host system. Generally, the organic semiconductor materials can be classified into wide-, medium-, narrow-, and ultranarrow-E_g^{opt} materials, proportionate to a progressive redshift of light absorption region. The wide-E_g^{opt} materials have a light absorption in the range of 350–550 nm, like polymer donor P3HT and fullerene derivative acceptors. The medium-E_g^{opt} materials such as PDBDB-T and PBDB-TF donors can cover the spectra at 400–650 nm, while the narrow-E_g^{opt} materials such as PTB7-Th donor and ITIC acceptor have the optical absorption regions at 550–750 nm. For the ultranarrow E_g^{opt} materials like IEICO and

Y-series nonfullerene acceptors, they have a low-bandgap that indicates strong optical absorptions in the NIR region.

As the excitons dissociation primarily occurs at the D/A interfaces in the OSCs, it is necessary to choose the third component material carefully in ternary blend to enhance charge transfer efficiency. Therefore, the third component should have an appropriate energy level alignment and offset between HOMO and LUMO of host system to form a cascade-energy-level alignment or act as a sensitizer via an energy transfer mechanism that can enhance solar energy utilization. The small energy offset cannot offer an adequate driving force for effective charge transfer. In contrast, if the offset is too large, it can cause unnecessary energy loss, leading to a low V_{OC}. After the excitons dissociate from the D/A interfaces, the free charge carriers are formed and transported through electron transfer channel and hole transfer channel to the corresponding electrodes. Thus, to balance the charge transfer in the blend, a higher mobility material as an additive to the binary blend has been proposed by Liu *et al.*[63] The more balanced electron and hole mobility of the device is favorable for charge transfer and collection and the utilization of excitons, thereby contributing to the improvement in the PCE of TOSCs.

(ii) Morphological regulator

It is well known that the photovoltaic processes of the OSCs are strongly correlated with the microstructure morphology of the active layer and thus play a critical role in determining the performance of TOSCs. An appropriate design and selection of the material of the third component can effectively adjust the phase separation scale, phase purity, and molecular packing arrangement of the different components inside the active layer. Meanwhile, the active layer with multiple subphase separations is more beneficial to the efficient separation of excitons, charge transfer, and charge collection. By fine tuning the aggregation of molecules, the charge transfer of the TOSCs can be strongly improved, thereby enhancing the PCE of the device. Mixing a new component makes the BHJ nanostructure more complicated due to the higher complexity of the multimaterials interplay (e.g., miscibility). From the thermodynamic point of view, miscibility is a critical factor for determining the degree of phase separation in a BHJ active layer. To be specific, materials with better miscibility facilitate smaller and impure phase domains, while limited intermixing between materials tends to create a relatively purer phase with larger phase domains. The miscibility between multiple components can be quantitively evaluated by the Flory – Huggins interaction parameters (χ) or interfacial tension (γ) between the third component and the hosts.

(iii) Energy loss management

The V_{OC} is an important device parameter to consider when evaluating the performance of solar cells. In ternary OSCs, the selection of third component with complementary absorption and suitable energy levels with respect to the host binary system is critical factor for improving J_{SC} and V_{OC}. Then, the total energy loss (E_{loss}) of photo-generated currents in devices is highly important. The E_{loss} is calculated as the difference between the minimal E_g of the materials in the blend and the qV_{OC} of the device ($E_{loss}= E_g - qV_{OC}$), where q is the elementary charge. Shockley and Quisser developed a thermodynamic detailed balance theory approach for solar cells which gives the universal V_{OC} loss. The reduced energy loss in OSCs devices based on Shockley–Quisser theory considers two main recombination losses: (1) the radiative recombination losses that are caused by the unavoidable energy losses for any solar cells ($E_g - qV_{OC}^{\mathrm{rSQ}}$) and additional radiative recombination from absorption below the bandgap ($q\Delta V_{OC}^{\mathrm{rad,\ belowgap}}$), and the other is (2) the nonradiative recombination loss ($q\Delta V_{OC}^{nonrad}$) is ascribed to any type of nonradiative recombination such as trap-assisted recombination. Recently, it was reported that NFA-based OSCs exhibit efficient charge separation even though the driving force approaches zero, resulting in small $q\Delta V_{OC}^{\mathrm{rad,belowgap}}$, encouraging us to employ the ternary strategy, especially in the case of parallel or alloy model dominant systems, where V_{OC} would be tuned with the composition loading of the third component.[64,65]

(iv) Enhanced stability

Generally, the stability of OSCs is affected by various factors, such as exposure to humidity and oxygen, thermal-stress-induced materials aggregation, photooxidation of BHJ active layer, and the intrinsic microstructural instability due to the spinodal demixing and/or crystallization of small molecular acceptors.[53] The morphological instability, including so-called "burn-in", is introduced to denote the degradation process in which the efficiencies of OSCs decline rapidly at the initial stage of the operation and then become stable afterward. The burn-in process arises from quenching of the active layer into a non-equilibrium nanostructure during the kinetically driven solution deposition process.[66,67] Severe fullerene dimerization via photoinduced free radicals often occurs in polymer–fullerene based OSCs, resulting in trap-assisted recombination due to increased photoinduced trap states and thus significantly reducing the efficiency by 25 – 50%.[53] In addition, fullerenes tend to self-aggregate upon thermal stress leading to degradation and thus poor thermal stability, while for NFA-based OSCs, negligible light-induced burn-in degradations have been reported for some specific polymer-molecule systems via replacing fullerenes by O-IDTBR and ITIC-series based small molecular acceptors.[68] These encouraging results point to the possibility of constructing stable ternary OSCs containing NFAs. According to recent studies, the microstructural stability of NFA-based OSCs is strongly influenced by the materials combination. Interactions among components, such as miscibility, are critical in driving microstructural degradation at thermodynamic equilibrium state. More specifically, the poor miscibility between donor and acceptor (below the percolation threshold) would necessitate the use of additional processing optimization methods (such as thermal annealing, solvent annealing, or additives) to assist the D/A system in reaching a state above the percolation threshold that is required for efficient charge transport, despite the fact that this state is far from the metastable morphology state. This kinetically quenched microstructure, however, would cause morphological deterioration, which originated from the demixing of the mixed phases toward equilibrium state, limiting the long-term stability of OSCs devices. Furthermore, the strong crystallization of NFAs may also thermodynamically deteriorate morphological stability. Therefore, to establish stable morphology, material composites need to have a reasonable balance between miscibility and suppressed crystallization of the small molecular acceptors, which could be facilitated by adding a third component.

1.3.3 State-of-the-art ternary BHJ systems

According to the possible combinations of three components, all the TOSCs can be classified into four categories, including polymer/polymer/small molecule, polymer/small molecule/small molecule, all-polymer, and all-small molecule types. **Table 1.1** presents the development of the state-of-the art ternary BHJ system from the first-time ternary strategy was introduced in 2009 to date.

1.4 Aims and outline of the thesis

High efficiency along with high stability and low-cost production are the essential requirements for OPVs technology to reach the mature market. To meet those requirements, the ternary approach and the contacts interface engineering have been the most frequently used as the effective strategies to overcome the main performance and stability limitations encountered in the active layer and the interfaces between active layer/contacts, in which they play critical roles in one/more photogenerated current processes. Ternary device can feature the combined merits of extended light absorption of tandem device while maintaining the simplification of device fabrication in single-junction BHJ architecture. In addition, with a judicious selection of third component material, ternary device enables an efficient exciton dissociation, improves the charge transport properties, reduced the non-radiative recombination, and optimises the nanomorphology of the blend. As the morphology of active layer is critically affected by the properties

Table 1.1 Non-exhaustive data of over a decade of research into organic ternary solar cells. Pacesetter, pivotal, record blends, *J-V* parameters, and respective working mechanism models. Each year, only data presenting higher efficiencies than the previous year is included, and the trend is consistent. Table is reproduced from Ref[69]

Ternary blend	Configuration	Weight ratio	V_{OC} (V)	J_{SC} (mA cm^{-2})	FF (%)	PCE (%)	Model	Year
P3HT/ F8BT/ PC$_{61}$BM	D1/D2/A	1/1.4/0.6	0.670	3.2	45.2	1.9	–	2009
P3HT/ PCPDTBT/ PC$_{61}$BM	D1/D2/A	0.8/0.2/1	0.620	8.0	55.4	2.8	CTM*	2010
P3HT/ PC$_{61}$BM/ ICBA	D/A1/A2	1/0.1/0.9	0.804	8.2	60.0	3.9	AM*	2011
P3HT/ CuMePc/ PC$_{61}$BM	D1/D2/A	1/1/2	0.580	16.3	56.0	5.3	AM	2011
DTffBT/ DTPyT/ PC$_{61}$BM	D1/D2/A	0.5/0.5/1	0.870	13.7	58.9	7.0	PM*	2012
P3HT/ aza-BODIPY/ PC$_{61}$BM	D1/D2/A	0.9/0.1/1	0.560	7.9	64.7	2.8	ETM*	2013
PTB7/ PID2/ PC$_{71}$BM	D1/D2/A	0.9/0.1/1.5	0.720	16.8	68.7	8.2	CTM	2014
PTB7-Th/ PID2/ PC$_{71}$BM	D1/D2/A	0.8/0.2/1.5	0.780	16.7	70.8	9.2	CT/ET-M	2015
PTB7-Th/ P(NDI2OD-T2)/ PC$_{71}$BM	D1/D2/A	0.99/0.01/1.67	0.810	23.0	61.0	11.6	ET/PM	2016
PBDB-T/ IT-M/ Bis-PC$_{61}$BM	D/A1/A2	1/1/0.2	0.952	17.4	73.7	12.2	PM	2017
PTB7-Th/ COi8DFIC/ PC$_{71}$BM	D/A1/A2	1/1.05/0.45	0.727	27.4	73.4	14.6	AM/PM	2018
PM6/ IT-4F/ Y6	D/A1/A2	1/0.24/0.96	0.844	25.4	75.9	16.3	AM	2019
PM6/ 3TP3T-4F/ Y6	D/A1/A2	1/0.18/1.02	0.850	26.1	75.4	16.7	CTM	2019
PM6/ PC$_{71}$BM/ Y6	D/A1/A2	1/0.2/1.2	0.852	25.5	76.9	16.7	PM	2020
PM6/ BTP-M/ Y6	D/A1/A2	1/0.24/0.96	0.875	26.6	73.5	17.0	AM	2020
PM6/ DRTB-T-C4/ Y6	D/A1/A2	1/0.15/1.2	0.850	24.8	**81.3**	17.1	CTM	2020
PM6/ MF1/ Y6	D/A1/A2	1.2/0.1/0.9	0.853	25.7	78.6	17.2	AM	2020
PM6/ MeIC/ BTP-4F-12	D/A1/A2	1/0.12/1.08	0.863	25.4	79.2	17.4	CTM	2020

Table 1.1 (*cont.*) Non-exhaustive data of over a decade of research into organic ternary solar cells. Pacesetter, pivotal, record blends, *J-V* parameters, and respective working mechanism models. Each year, only data presenting higher efficiencies than the previous year is included, and the trend is consistent. Table is reproduced from Ref[69]

Ternary blend	Configuration	Weight ratio	V_{OC} (V)	J_{SC} (mA cm^{-2})	FF (%)	PCE (%)	Model	Year
PM6/ ITCPTC/ Y6	D/A1/A2	1/0.06/1.14	0.861	25.7	78.8	17.4	ETM	2020
PM6/ $PC_{71}BM$/ BTP-eC9	D/A1/A2	1/0.2/1	0.855	26.2	77.7	17.4	CTM	2020
PM6/ C8-DTC/ Y6	D/A1/A2	1/0.12/1.08	0.873	26.5	75.6	17.5	CTM	2020
PM6/ S3/ Y6	D1/D2/A	0.8/0.2/1.2	0.856	25.9	79.2	17.5	AM	2020
PM6/ Y6-1O/ BTP-BO-4F	D/A1/A2	1/0.18/1.02	0.860	26.1	78.3	17.6	AM	2021
PM6/ BTTzR/ Y6	D1/D2/1	0.8/0.2/1.2	0.870	26.2	77.7	17.7	CTM/AM	2021
D18-Cl/ Y6-1O/ Y6	D/A1/A2	1/0.48/1.12	0.900	25.9	76.9	17.9	AM	2021
PM6/ AQx-3/ Y6	D/A1/A2	1/0.4/0.8	0.870	26.8	77.2	18.0	CTM/AM	2021
PM6/ BTP-S2/ BO-4Cl	D/A1/A2	1/0.3/0.9	0.861	27.1	78.0	18.2	–	2021
PBDB-TF/ PB2F/ BTP-eC9	D1/D2/A	0.8/0.2/1.2	0.863	26.8	80.4	18.6	CTM	2021
D18-Cl/ $PC_{61}BM$/ N3	D/A1/A2	1/0.1/1.4	0.849	28.2	78.0	18.7	–	2021
PBDB-TF/ HDO-4Cl/ eC9	D/A1/A2	1/0.2/1	0.866	27.1	80.5	18.9	AM	2021

[*] Introduction of the working mechanism. CTM is the abbreviation of charge transfer mechanism, ETM is electron transfer mechanism, AM is alloy-like model, and PLM is parallel-linkage model.

of underlying interfacial layer, therefore engineering and optimization of the buffer layers, especially the cathode interface of the device has been demonstrated to improve the device performance and stability. However, due to the myriad options of third component and buffer layer materials with varied physical and chemical properties, a proper selection of the materials that match certain applications and are able to show a simultaneous improvement in device performance and stability remains a challenge.

The scientific community has made this significant progress in understanding the underlying mechanism that occurs by the addition of a third component in ternary OSCs as well as by engineering the cathode interface in BHJ OSCs, however those advances are mostly investigated under 1 sun condition and for a conventional solar module application. Owing to the aforementioned unique properties of OSCs over their inorganic counterparts, the OSCs have a great potential to create their specific market as indoor OSCs and semitransparent OSCs. Different from conventional OSCs modules under 1 sun condition, indoor and semitransparent OSCs have their own challenges, so different strategies should be taken into account for their performance and stability optimization. The poor absorption mismatching between the active layer and light sources spectra, high energy-loss, and unexpected recombination are key limitations in indoor OSCs; whereas the compromise between PCE and average visible transmittance (AVT) is a critical issue in semitransparent OSCs. Inspired by the efforts to develop high-performance traditional outdoor OSCs, interfacial engineering and ternary strategies should be good approaches to overcome those issues in indoor and semitransparent OSCs.

In this thesis, combining the interfacial engineering and ternary strategies to improve the device performance and stability of OSCs for versatile applications, we conducted research, and the work done is summarized in this study. First, we have investigated the performance and photostability of binary fullerene-based OSCs using an interface engineering strategy under 1 sun condition and under indoor LED illumination. Then, for traditional outdoor application, we have employed the ternary strategy by adding the novel fluorinated metallophthalocyanines $MPcF_{48}$ and commercial ITIC-M or $PC_{70}BM$ as third components in binary fullerene-based and binary nonfullerene-based blends, respectively, to improve the device efficiency and stability. Yet, a ternary strategy using the state-of-the-art Y-series nonfullerene acceptors can be applied to obtain efficient and stable semitransparent nonfullerene-based OSCs. As of last, we have introduced combined frequency and time-resolved techniques to study in-depth the shelf lifetime degradation of OSCs in accordance with the ISOS-D1 protocol. The whole study is organized into eight chapters.

Chapter 1 introduces the background introduction to the development of organic semiconductors and organic photovoltaics. The basic photo-electric conversion, working principles, and photovoltaic performance parameters of organic solar cells are explained in detail afterward. A particular focus on basic physics of ternary organic solar cells is elaborated. Finally, the state-of-the-art of ternary OSC systems are described.

Chapter 2 is devoted to experimental methods and materials used in this thesis to elucidate the theoretical background given in Chapter 1. Chemical structures of photoactive materials will be provided, as well as detailed instructions on how to conduct the experiments. Working principles of spectroscopic techniques (absorption, PL, IS, TPV/TPC) and characterization setup will be introduced, along with its specifications.

Chapter 3 will discuss the forthcoming application of organic solar cells as indoor energy harvesters under artificial light illumination. The device performance and stability of fullerene-based OSCs under indoor 2700 K LED light versus standard 1 Sun illumination will be comparatively studied. A cathode interface engineering using three different ETL materials will be discussed comprehensively as a strategy to improve the indoor OSCs performance. Finally, to further accelerate the commercialization of OSCs in the Internet of Things (IoT) market, the photostability study and degradation mechanism of highly efficient indoor OSCs will be analysed along with the photoaged OSC under 1 sunlight.

Chapter 4 will expand the work of the optimized fullerene-based binary BHJ OSCs from Chapter 3 with the addition of novel organic semiconductor materials as third components to construct an efficient ternary BHJ OSCs. The effect of different central metal atom from fluorinated zinc and copper metallophthalocyanine $MPcF_{48}$ as third component on the performance of ternary OSCs will be investigated. The materials and device characterizations will be discussed in order to gain more understanding of the influence of metal atom substitution on the photovoltaic properties, blend surface morphology, and device photostability.

In contrast to the widely used fullerene acceptors in Chapter 4, **Chapter 5** introduces nonfullerene acceptors that have propelled OSCs efficiencies in binary BHJ or ternary BHJ OSCs. High performance of state-of-the-art PM6:Y7 blend OSCs will be optimized to enhance its device performance and photostability by a ternary strategy. Herein, two different acceptor materials systems, such as nonfullerene ITIC-M and fullerene $PC_{70}BM$ will be incorporated into the PM6:Y7-blend. Although the studied third component materials have a distinctly different chemical structure, they possess high-lying lowest unoccupied molecular orbital (LUMO) and good miscibility with nonfullerene acceptor Y7 that may affect the performance of the studied ternary OSCs. The optical, morphological, electrical, transient and time-resolved measurements will be carried out to elaborate on the effect of the third components on the device performance and photostability of ternary nonfullerene OSCs.

Benefiting from the NIR spectrum from most nonfullerene acceptors, **Chapter 6** presents the advanced technology application of OSCs from its semitransparent properties using a nonfullerene-based ternary strategy. Thanks to the nature of NIR absorption and tunable energy alignment, the rising star of Y-series acceptors is chosen and will be added into the state-of-the-art PTB7-Th:IEICO-4F semitransparent binary blend to investigate their roles in the device performance, the transparency properties, and the operational stability (thermal- and photo-stability) of TOSCs. Some electrical, optical, and morphological characterization will be further discussed to gain perspective on balancing the trade-off between PCE, AVT, and stability, which are the main challenges for efficient semitransparent OSCs.

To be able to enter the mature market, understanding the degradation mechanism in OSC is as important as fabricating high-performance and multi-functional devices. **Chapter 7** will focus on the stability study of OSCs, specifically on the shelf lifetime analysis of PTB7-Th:$PC_{70}BM$-based OSCs using combined frequency and time-resolved techniques. Following the ISOS-D1 protocol, we further observe the whole degradation process of each layer with the aid of advanced photophysics techniques, impedance spectroscopy (IS), and photovoltage/photocurrent transient (TPV/TPC). The observed degradation mechanism detected by each technique and the combination of both will be elaborated on.

In the last chapter, **Chapter 8** summarizes the main results obtained from the appended papers of this thesis. The short outlook for future research using interface engineering and ternary blend approaches in organic solar cells for versatile applications such as indoor, flexible, and semitransparent OSCs will be further presented.

Chapter 2

Materials and experimental section

2.1 Materials

The materials used in this thesis are either commercially available or supplied by our collaborator. In the organic BHJ solar cells, the absorption takes place in the active layer, which consists of the electron donor and the electron acceptor organic semiconductor materials. **Figure 2.1** shows the molecular structures of the conjugated polymer donors and small molecule acceptors studied in this work. The donor polymers purchased by chemical companies are PTB7-Th (1-Material), PBDB-T (1-Material), and PBDB-TF (known as PM6, 1-Material). The small molecule acceptor material of the fullerene derivative $PC_{70}BM$ was purchased from Solenne B.V., and the nonfullerene materials ITIC-M, Y1, Y5, Y6, and Y7 were provided by 1-Material, while $ZnPcF_{48}$ and $CuPcF_{48}$ were synthesized by Prof. Ángela Sastre-Santos (Universidad Miguel Hernández de Elche, Spain). The corresponding HOMO and LUMO energy levels of all photoactive materials studied are shown in **Figure 2.2**. The addition of solvent additives in a photoactive BHJ blend aids in improving the device performance, therefore 1,8-diiodooctane (Alfa Aesar) and 1-chloronapthalene (Sigma-Aldrich) were used in this thesis.

The buffer layers are sandwiched between the active layer and the electrodes. These interlayers have a function to reduce interface barriers and selectively transport the hole and electron carriers from active layer to the electrodes. Based on their function, the buffer layers are classified as hole transporting layer (HTL) and electron transport layer (ETL). Without further purification and pretreatment, we directly used commercially available PEDOT:PSS (Clevios TM) solution, vanadium oxide (V_2O_5) and molybdenum oxide (MoOx) powders (Sigma-Aldrich) as HTL materials. For metal-oxide ETL materials, we used pre-treated zinc oxide (ZnO) and titanium dioxide (TiOx). The ZnO-solution precursor was prepared by sol-gel process, dissolving zinc acetate dehydrate in 2-methoxylethanol and ethanolamine. The sol-gel method was also employed to prepare TiOx-solution by dissolving titanium isopropoxide, 2-methoxylethanol and ethanolamine. The materials to prepare ZnO and TiOx solution were purchased from Sigma-Aldrich. For the organic ETL materials, we purchased polymer PFN and small-molecule PDINO from 1-Material and we carried out a pre-treatment by dissolving them in methanol. **Figure 2.3** depicts the chemical structures of the buffer materials used in this thesis.

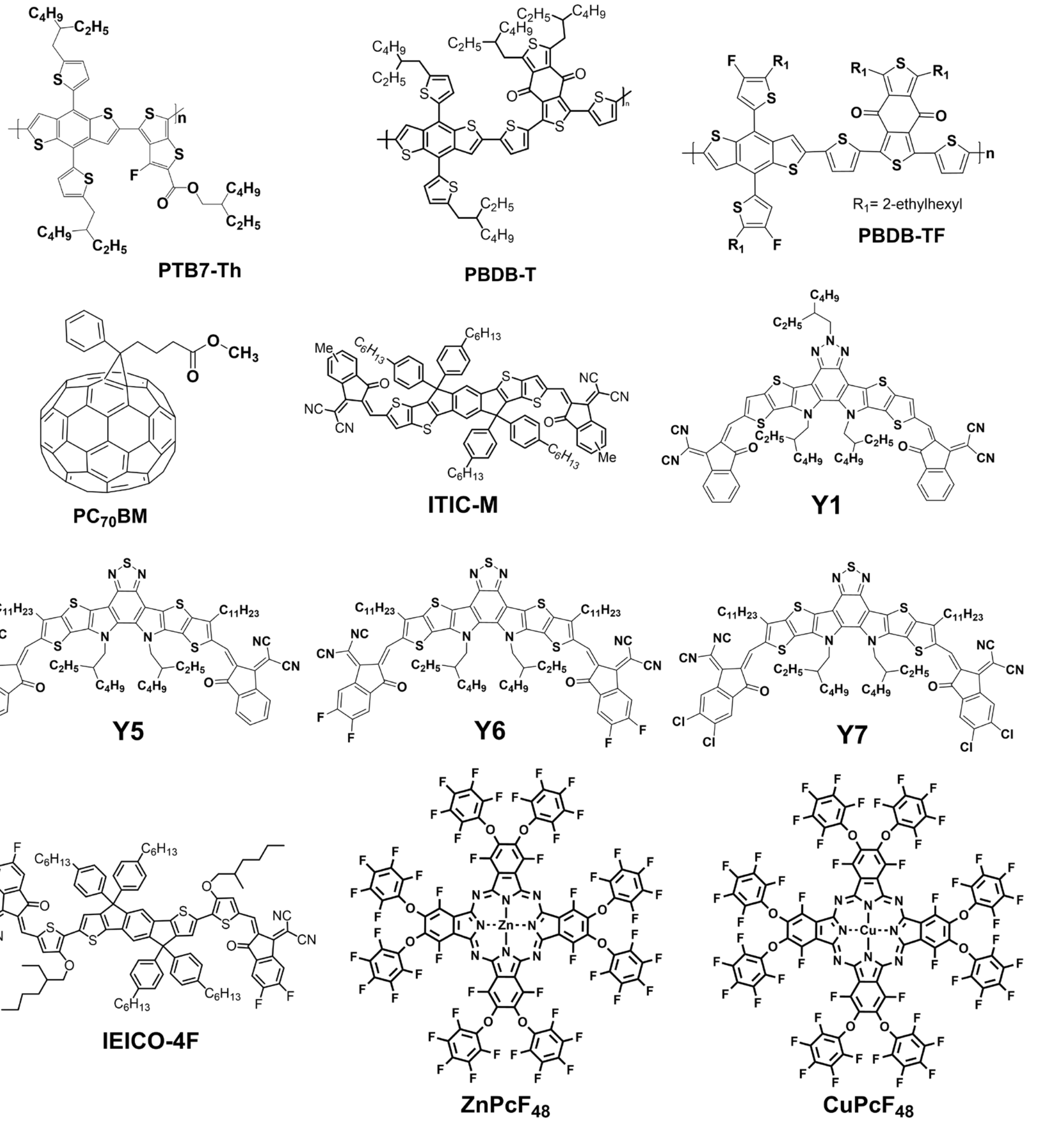

Figure 2.1 Chemical structure of the organic semiconductors used as photoactive layer in this thesis.

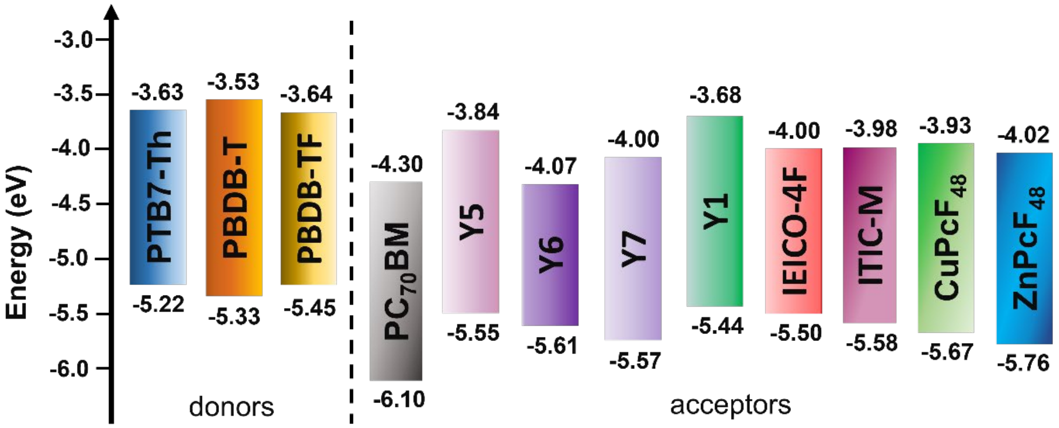

Figure 2.2 HOMO and LUMO energy levels according to the literature for the organic semiconductor materials used in this thesis.

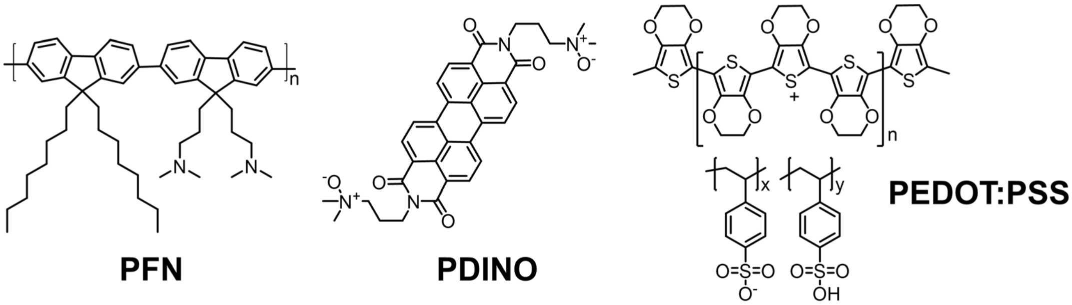

Figure 2.3 Chemical structure of the polymer and small molecule buffer layers used in this thesis.

The transparent electrode used was Indium Tin Oxide (ITO) patterned glass substrates which were purchased from PsiOTec Ltd. As back contact electrodes, high purity of 99.99% for silver wire and gold each were purchased from Testbourne Ltd. and thermally evaporated under vacuum conditions. A quart crystal thickness analyzer within the evaporator chamber was employed to measure the thickness of the back electrodes.

2.2 Deposition techniques

The deposition of the solution-processed layers, such as active layers and the buffer layers in this thesis was mainly using the spin-coating method. In addition, the vacuum thermal evaporation method was used to deposit the powdered buffer layers or metal top electrodes.

2.2.1 Spin-coating

Spin-coating is a commonly used solution method in lab-based scale fabrication to form a thin-film of effectively uniform thickness from solution-processed materials. Spin-coating is carried out in four steps, deposition, spin-up, spin-off, and evaporation. A few amounts of solution are dropped onto the center of a substrate, and the substrate is accelerated to a high angular velocity to simultaneously spin-up and spin-off the solution and evaporate the solvent. This stage is followed by drying of the coated film, forming a thin film of the material on the surface of the substrate. In general, the material efficiency is quite low, approximately 2-5% of materials are dispensed onto the substrate, while 95-98% of material is flung off and discarded throughout the process. Although spin-coating is not a compatible method with large-scale continuous in roll-to-roll (R2R) manufacturing, relatively high uniformity and well-controlled thickness can be acquired by this deposition technique. The thickness of the wet film is inversely related to the spin speed and depends on the properties of the solution (concentration, viscosity, surface tension, drying rate, etc.). The spin-speed unit of this method is revolutions per minute (rpm) which signifies the number of turns in one minute.[70]

In this thesis, all photoactive layers, PFN, TiOx, ZnO, PDINO, and PEDOT:PSS layers were deposited by spin-coating method using a spin-coater machine model WS-400B-6NPP/LITE from Laurell Technologies Corporation. **Figure 2.4** shows the spin-coater machine and the illustration of spin-coating working principle.

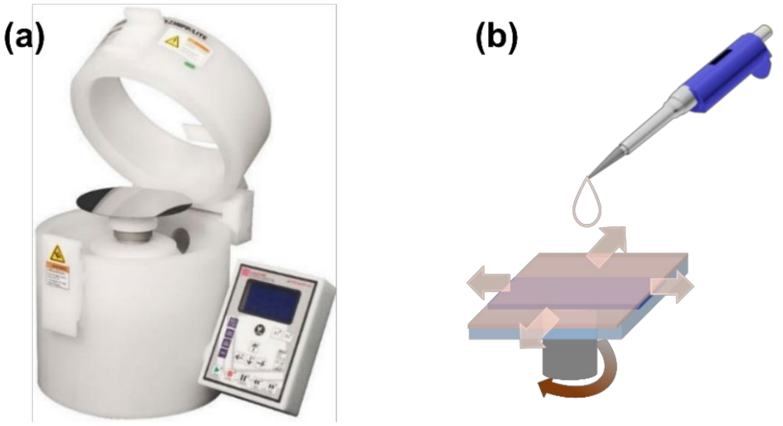

Figure 2.4 (a) The picture of spin-coater machine used in this thesis and (b) the illustration of spin-coating working principle.

2.2.2 Vacuum thermal evaporation

Vacuum thermal evaporation (VTE) is a well-known vacuum deposition technique for coating thin films of pure solid materials such as metals, non-metals, oxides, nitrides, and organic materials. The coated films are usually in the thickness range of angstroms to microns and can be a single material or multiple materials in a layered structure. The VTE technique is advantageous for its simplicity (evaporation of numerous layers or co-evaporation of various compounds), its high precisely film-thickness control (±0.5 nm), and its high homogenous of the deposited films.[71] However, the wasteful consumption of the material and non-uniformity of the deposition rate are the main drawbacks that made it unsuitable for the R2R process. The VTE process involves heating a solid material until overcome its melting point, then evaporates and facilitates the vapor particles moving and directly reaching a cold substrate surface where these vapors again change to a solid-state. To get high melting points of source materials, a large direct current (DC) passes through a resistive boat/crucible (made of a high melting point metal such as tungsten, molybdenum, or tantalum), where the ultra-high vacuum condition ($<1\times10^{-6}$ mbar) supports the evaporation of the metal and further carrying it to the substrate.

The substrates are placed upside down (toward the direction of evaporation) in a substrate holder and protected by a deposition shutter that is in the open position during evaporation process, as shown in **Figure 2.5a**. In this thesis, the V_2O_5, MoO_x, Au, and Ag layers were thermally evaporated under high vacuum by an evaporator located in a glove-box model MB20/MB200 from MBRAUN. The metals can be evaporated by manual deposition controller that is shown in **Figure 2.5b** and the working principle of thermal evaporation is depicted in **Figure 2.5c**.

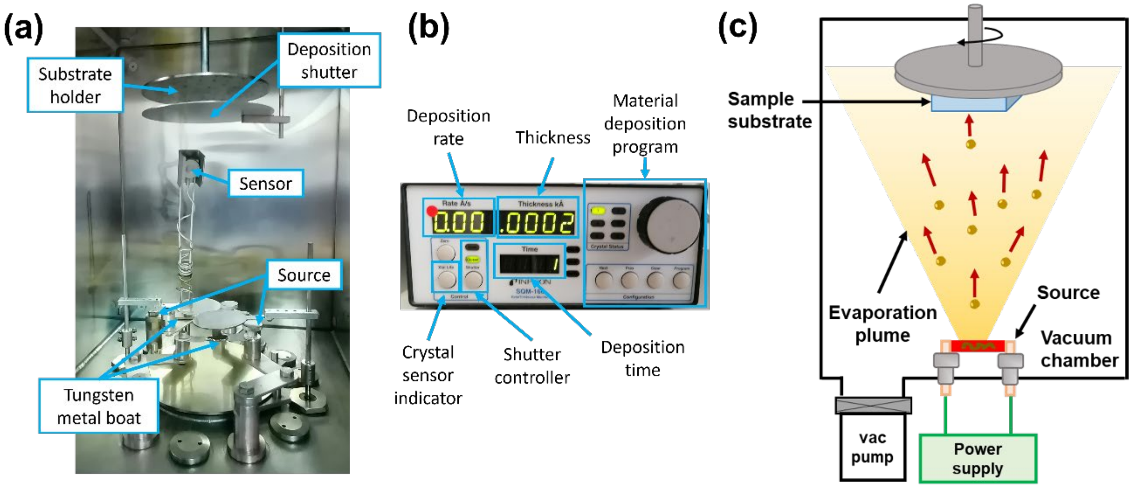

Figure 2.5 Picture of (a) different parts of vacuum thermal evaporator and (b) manual deposition controller used in this thesis, (c) the illustration of VTE working principle.

2.3 Device fabrication

The OSCs cells fabricated in this thesis were based on conventional and inverted device architectures, as shown schematically in **Figure 2.6**. For both types of OSCs, the general cleaning method for ITO-patterned glass substrates was used. The first step of the substrate cleaning is critical to avoid any impurities and dust contaminants that might affect the final performance of the OSCs. Before the deposition of the buffer and active layers, ITO-patterned glass substrates with a sheet resistance of 10 Ω cm^{-2} were cleaned using a surface-active cleaning detergent diluted in deionized water. Afterward, the substrates were rinsed using deionized water and blow-dried with a nitrogen air gun. Subsequently, the substrates were sonicated in acetone, methanol and isopropanol anhydrous solvents in a sequence for 10 min each. The cleaned ITO-glass substrates were blow-dried under nitrogen stream and transferred to an oven at 100ºC for 10 min to remove any residual solvents. Then, the cleaned ITO substrates were placed in ultraviolet-ozone chamber for 15 min to activate the ITO surfaces and to further remove any organic residues from their surfaces.

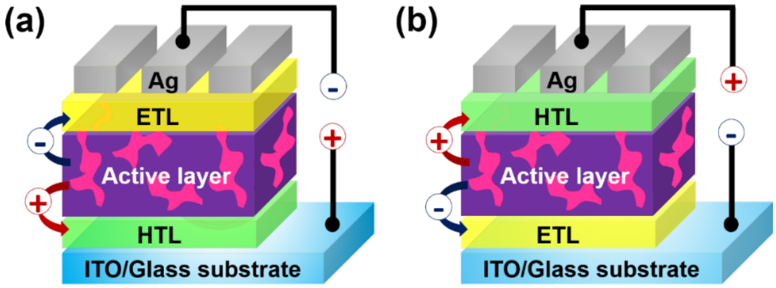

Figure 2.6 Device architecture of organic solar cells with (a) conventional and (b) inverted structure.

(i) Conventional structure

As shown in **Figure 2.6a**, the conventional structure of BHJ solar cells studied in this work consists of ITO/HTL/active layer/ETL/Ag. PEDOT:PSS was used as HTL to improve hole collection by the ITO. A 30 nm thin-film of PEDOT:PSS was obtained by spin-coated the filtered PEDOT:PSS solution through a 0.2 μm PTFE filter on ITO substrates at 4000 rpm for 40 sec, then annealed at 150°C for 15 min in atmospheric air. The PEDOT:PSS-coated substrates were transferred to a high-purity nitrogen-filled glove box for further processing. The active layer was deposited on the top of HTL by spin-coating method. In this thesis, donor polymers PBDB-TF (PM6) and seven acceptors (Y1, Y5, Y6, Y7, ITIC-M, IEICO-4F, and PC$_{70}$BM) were investigated in the conventional geometry of the studied devices. The details of active layer preparation and deposition are listed in **Table 2.1**. As the ETL material in the conventional structure, PDINO was used and dissolved using methanol with the concentration of 1.5 mg mL^{-1} and its solution was spin-coated on the active layer at 3000 rpm for 30 sec to obtain 15 nm thickness.

(ii) Inverted structure

The inverted architecture of OSC devices was fabricated with the structure of ITO/ETL/active layer/HTL/Ag schematically depicted in **Figure 2.6b**. PFN, TiOx, and ZnO were employed as ETL materials for the studied inverted OSCs in this thesis. As organic ETL, PFN precursor solution was prepared by dissolving PFN powder in methanol with the presence of a small amount of acetic acid (1.84 µL mL^{-1}), giving a total concentration of 1.84 mg mL^{-1}. A thin layer of PFN was spin-coated on ITO glass substrate at 4000 rpm for 60 sec to obtain 10 nm thickness. On the other hand, the inorganic metal oxide ETL of ZnO was prepared by sol-gel process, dissolving 150 mg of zinc acetate dehydrate in 1 mL of 2-metoxylethanol with 30 µL ethanolamine as a stabilizer, then the mixture was left for 1 h under vigorous stirring at 70°C and was diluted by methanol 1:1 (v/v) ratio to obtain ZnO-precursor solution. Afterward, to obtain 15 nm ZnO thin film, the ZnO-precursor solution was deposited on the top of precleaned ITO substrates by spin-coating at 4000 rpm for 40 sec and then was annealed at 200°C for 1 h under ambient environment. In addition, TiOx as another metal oxide ETL was also prepared by sol-gel process, in which 1 mL of 2-methoxyethanool, 0.1 mL ethanolamine, and 0.2 mL titanium isopropoxide were stirred at 120°C for 3 h and then was diluted with methanol 1:6 (v/v) ratio to acquire TiOx precursor solution. A 15 nm thickness layer of TiOx was obtained by spin-cast the TiOx at 6000 rpm for 45 sec and then annealed at 400°C for 5 min. Before the deposition of active layer, the deposited layer of ZnO and TiOx were exposed under UV illumination for 10 min while the deposited PFN layer substrate was illuminated with UV light for 30 sec to fill the light traps within the ETL, thus reducing the light-soaking effect. Then, the donor polymers of PTB7-Th or PBDB-T and small molecule acceptors of PC$_{70}$BM or ITIC-M were employed as the active layer studied in the inverted structure. The details of the corresponding active layer preparation and deposition are summarized in Table 2.1. As HTL in the inverted structure, a very thin layer of V_2O_5 (5 nm) or MoOx (10 nm) was deposited at rate of 0.05 kÅ s^{-1} on the top of active layer by VTE under high vacuum conditions ($\leq 1 \times 10^{-6}$ mbar).

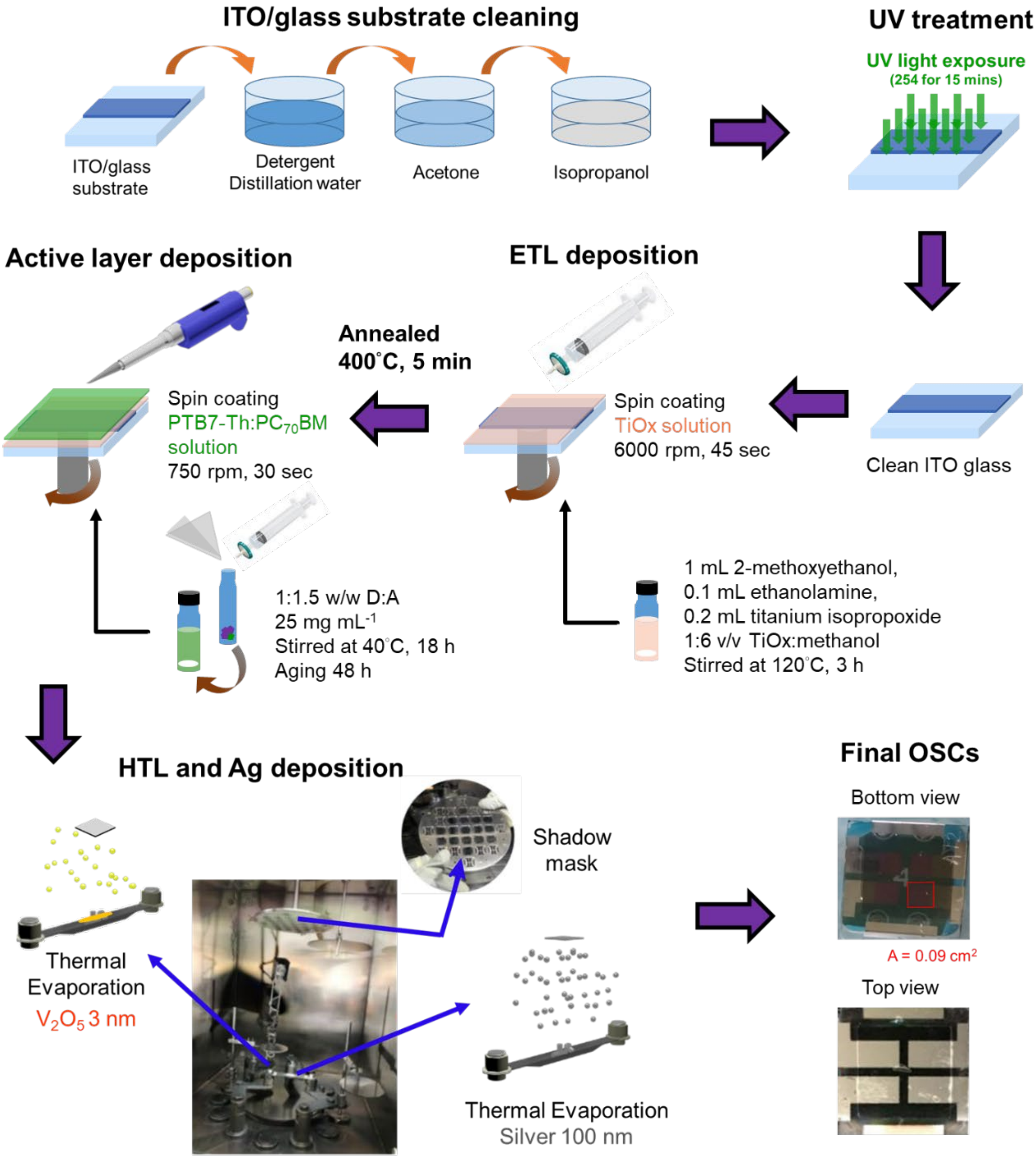

Figure 2.7 Inverted OSC step-by-step fabrication procedure.

Table 2.1 Details of active layer preparation and deposition conditions for the fabricated devices in this thesis.

Blend	D:A weight ratio	Total concentration [mg mL^{-1}]	Solvent	Solutions pretreatment	Aging	Spin speed [rpm]	Post-deposition annealing
PTB7-Th:PC$_{70}$BM	1:1.5	25	97 vol% CB, 3 vol% DIO	stir 40°C, 18 h	48 h	750	None
PTB7-Th:PC$_{70}$BM:CuPcF$_{48}$	1:1.5:0.03	25	97 vol% CB, 3 vol% DIO	stir 40°C, 18 h	48 h	750	None
PTB7-Th:PC$_{70}$BM:ZnPcF$_{48}$	1:1.5:0.03	25	97 vol% CB, 3 vol% DIO	stir 40°C, 18 h	48 h	750	None
PTB7-Th:CuPcF$_{48}$	1:1	20	97 vol% CB, 3 vol% DIO	stir 40°C, 18 h	48 h	750	None
PTB7-Th:ZnPcF$_{48}$	1:1	20	97 vol% CB, 3 vol% DIO	stir 40°C, 18 h	48 h	750	None
PTB7-Th:IEICO-4F	1:1.5	20	96 vol% CB, 4 vol% CN	stir RT, 18 h	None	1500	100°C, 5 min
PTB7-Th:IEICO-4F:Y5	1:1.3:0.2	20	96 vol% CB, 4 vol% CN	stir RT, 18 h	None	1000	100°C, 5 min
PTB7-Th:IEICO-4F:Y6	1:1.4:0.1	20	96 vol% CB, 4 vol% CN	stir RT, 18 h	None	1500	80°C, 5 min
PTB7-Th:IEICO-4F:Y7	1:1.3:0.2	20	96 vol% CB, 4 vol% CN	stir RT, 18 h	None	1500	100°C, 5 min
PTB7-Th:IEICO-4F:Y1	1:1.3:0.2	20	96 vol% CB, 4 vol% CN	stir RT, 18 h	None	1000	100°C, 5 min
PTB7-Th:Y6	1:1.5	25	96 vol% CB, 4 vol% CN	stir RT, 18 h	None	1000	100°C, 5 min
PBDB-T:ITIC-M	1:1	20	96 vol% CB, 4 vol% CN	stir 80°C, 3 h	None	1000	80°C, 5 min
PM6:Y6	1:1.2	18	99.5 vol% CF, 0.5% CN	stir 80°C, 3 h	None	1500	90°C, 5 min
PM6:Y7	1:1	20	99.5 vol% CB, 0.5 vol% CN	stir 80°C, 3 h	None	4000	90°C, 5 min
PM6:Y7:ITIC-M	1:1:0.1	20	99.5 vol% CB, 0.5 vol% CN	stir 80°C, 3 h	None	4000	90°C, 5 min
PM6:Y7:PC$_{70}$BM	1:1:0.1	20	99.5 vol% CB, 0.5 vol% CN	stir 80°C, 3 h	None	4000	90°C, 5 min
PM6:ITIC-M	1:1	20	99.5 vol% CB, 0.5 vol% CN	stir 80°C, 3 h	None	4000	90°C, 5 min
PM6:PC$_{70}$BM	1:1	20	99.5 vol% CB, 0.5 vol% CN	stir 80°C, 3 h	None	4000	90°C, 5 min

As top electrodes in either inverted or conventional structures, silver (Ag) wire or gold (Au) with high purity of 99.99% was evaporated under high vacuum conditions ($\leq 1 \times 10^{-6}$ mbar) and the deposition rate of 0.1 – 0.4 kÅ s^{-1} was set to form a 100 nm Ag or Au thickness using a patterned mask. The effective area of the cell was 0.09 cm^2, which was determined by an optical microscope. **Figure 2.7** illustrates the step-by-step procedure for device fabrication in an inverted structure.

2.4 Characterization techniques

Before going into details of each characterization technique used within this thesis, it is worth acknowledging some collaborators who helped to measure and analyze the experimental results of the studied devices in this thesis. The charge extraction (CE) and transient photocurrent/photovoltage (TPC/TPV) characterization were carried out with the help of Dr. Maria Méndez under the supervision of Prof. Emilio Palomares from the Institute of Chemical Research of Catalonia (ICIQ-BIST). Transmission electron microscopy (TEM) analyses were performed with the help of Dr. Rita Marimon from the URV Microscopia laboratory center.

Excluding some ambient degradation analysis measurements, all the electrical and photophysics characterizations were carried out under nitrogen environment ($H_2O < 0.1$ ppm and $O_2 < 0.1$ ppm). To protect the devices from degradation since all the characterization systems work under environmental conditions, the devices were put inside a samples-holder from Ikerlan Ltd. (see **Figure 2.8**) sealed under nitrogen conditions inside the glovebox. On the other hand, for the ambient degradation measurement, the devices were set in the samples-holder under environmental conditions.

Figure 2.8 Sample-holder used to place the studied devices for the transportation and measurements outside the glovebox.

2.4.1 Photovoltaic device characterizations

Current density – voltage characteristics

The current density – voltage (*J-V*) characteristics of the studied devices were measured by a computer-controlled Keithley 2400 source measure unit in the dark and under illumination. The AM 1.5G simulated solar simulator (Abet Technologies model 11000 class type A, Xenon arc) was employed as the light source to measure *J-V* characteristic of the cells under standard illumination at a light intensity of 100 mW cm^{-2}. The light intensity was calibrated by using an NREL-certified monocrystalline photodiode cell. For the indoor light application measurement, a commercial LED lamp (warm white lamp with a color temperature of 2700 K Philips A60 13W E27) was used as an artificial indoor light source with the different illuminances of the LED light measured by a digital light meter (Spectra Cine, Candela II-A, Model C-2010 EL). The distance between the artificial light source and the devices were kept constant. The incident LED light intensities were obtained by adjusting the power supply calibrated by a silicon-cell pyranometer (calibration factor of 5.0 W m^{-2} mV^{-1}, model MP-100, Apogee Instruments, Inc.). All the *J-V* characteristics were carried out at room temperature. The *J-V* curves were measured in the forward direction with a scan step of 0.01 V and a dwell time of 2 ms. The experimental setup for *J-V* measurement in the dark or under AM 1.5G is shown in **Figure 2.9**.

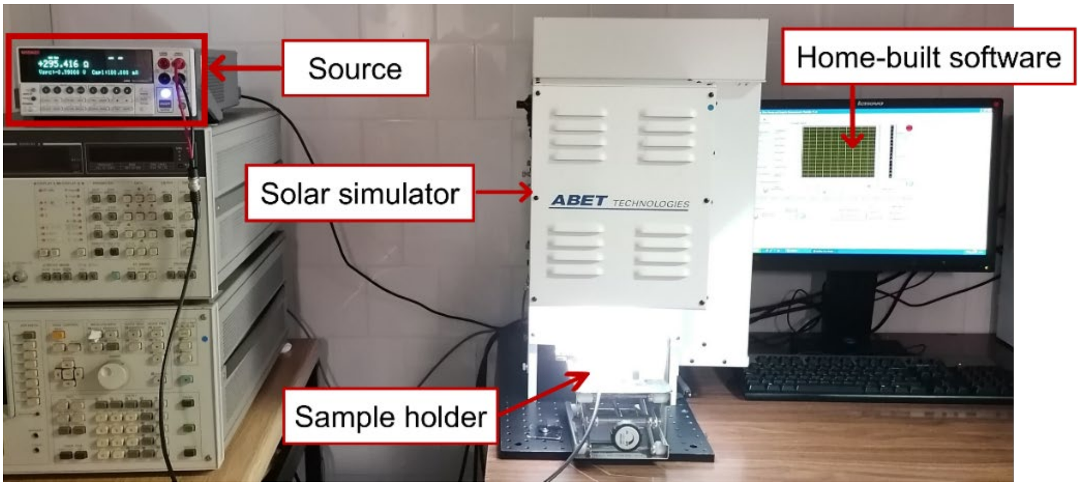

Figure 2.9 The experimental setup for *J-V* characteristics measurements under AM 1.5G illumination or in the dark.

Short-circuit current density and open-circuit voltage dependency on light intensity

The *J-V* characteristics dependence over different light intensity measurement using a set of optical density filters has proven to be a powerful tool for determining the dominant recombination loss mechanism in OSC devices.[42] These optical filters help to fix the intensity of the AM 1.5G light passing through to the devices from the light source. **Figure 2.10** shows the *J-V* curves obtained from the same device under different light intensities. The J_{SC} and V_{OC} values from the measured *J-V* curves of the device were extracted at each light intensity and then plotted it in a log-log scale for J_{SC} *vs.* light intensity curve and in a semi-log scale for V_{OC} *vs.* light intensity curve, as displayed in **Figure 2.11**. From the J_{SC} *vs.* light intensity curve, a power law dependence of S1 from equation $J_{SC} \propto P_{light}^{S1}$ can be extracted, and it is possible to predict if there are photocurrent losses under short-circuit conditions. In an ideal case, photocurrent loss is negligible under short-circuit condition if S1 value close to 1 (see **Figure 2.11a**). On the other hand, the ideality factor *n* value can be extracted from V_{OC} vs light intensity curve from equation 1.2. The working OSCs devices usually have *n* values between 1 and 2, where the *n* value equal to 1 signifies band-to-band recombination while the *n* value close to 2 means the trap-assisted recombination or SRH recombination is dominant.

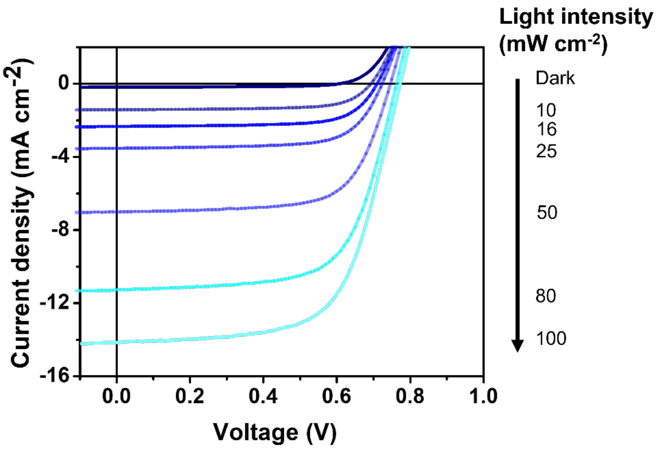

Figure 2.10 The *J*-*V* characteristic dependency of PTB7-Th:PC$_{70}$BM device over different light intensities.

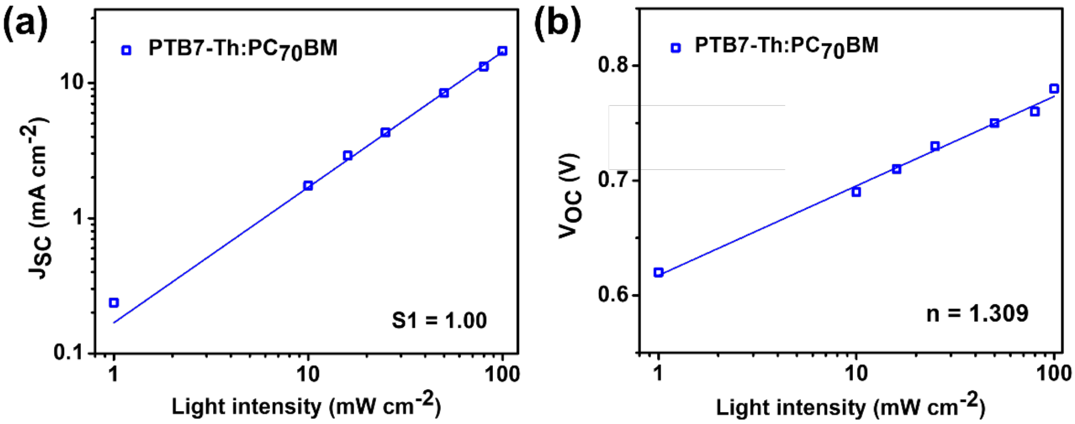

Figure 2.11 The estimated S1 and *n* values from the plot of (a) log-log J_{SC} *vs.* light intensity curve (b) semi-log V_{OC} *vs.* light intensity curve obtained from the *JV* curve in Figure 2.10.

Photocurrent density versus effective voltage measurement

Photocurrent density (J_{ph}) as a function of the effective voltage (V_{eff}) was measured to investigate the photocarrier dynamic process. The J_{ph} is defined as $J_{ph} = J_L - J_D$, where J_L and J_D represent the current densities under illumination and in the dark, respectively. From the resulting J_{ph}-V characteristics, the compensation voltage (V_0) at $J_{ph} = 0$ was defined, as shown in inset **Figure 2.12**. In Figure 2.12 the J_{ph} vs V_{eff} is plotted on log-log scale, where the V_{eff} is defined by $V_0 - V_{app}$ (applied voltage).

It is demonstrated that at small effective voltage ($V_0 - V_{app} < 0.1$V) the photocurrent increases linearly with the V_{eff} and at $V_0 - V_{app} > 0.1$V the photocurrent enters the saturation regime in which the photocurrent is governed by the field- and temperature-dependent dissociation of e-h pairs.[72] At higher reverse voltage $V_0 - V_{app} > 1$ V, J_{ph} value comes into the saturated state (J_{sat}) and becomes field and temperature independent, indicating that almost all excitons can be effectively dissociated into free charge carriers and then extracted by two separate electrodes by the applied field. The exciton dissociation efficiency (P_{diss}) and charge collection efficiency (P_{coll}) can be calculated by J_{ph}/J_{sat} values under short-circuit and maximal power output conditions, respectively.

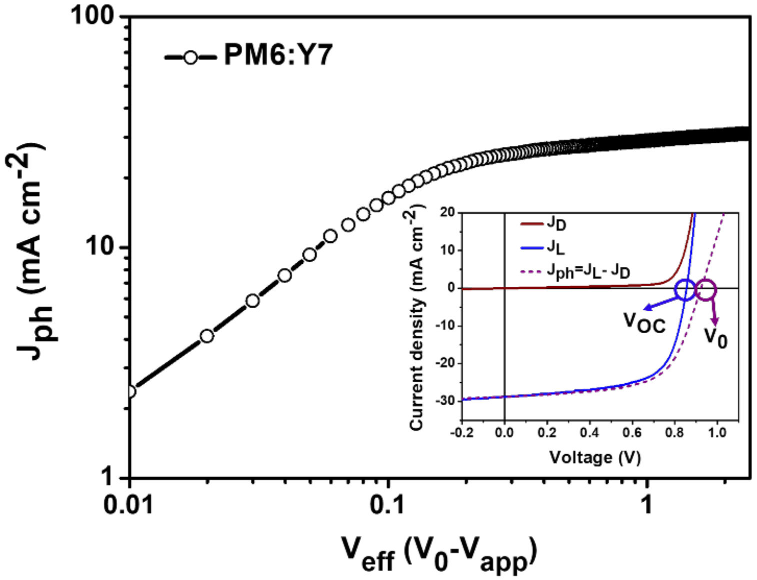

Figure 2.12 The J_{ph} versus V_{eff} characteristic of PM6:Y7 device. The inset shows the J_L, J_D, and J_{ph} as a function of applied voltage, whereas the blue arrow indicates the V_{OC} and the purple arrow the compensation voltage (V_0), respectively.

2.4.2 Space charge limited current method

The hole and electron mobilities were measured by adopting the space charge limited current (SCLC) method for electron-only and hole-only devices. The configuration of hole-only and electron-only devices was ITO/PEDOT:PSS/BHJ active layer/MoO_x/Au and ITO/ZnO/BHJ active layer/PDINO/Ag, respectively. According to the Mott-Gurney equation, the measured dark current was fitted to the SCLC model to determine the charge carrier mobility:[73]

$$J_{SCLC} = \frac{9}{8}\varepsilon_0\varepsilon_r\mu\frac{V^2}{d^3} \tag{2.1}$$

where J is the measured current density, ε_0 is the permittivity of vacuum (8.85 x 10^{-14} F cm^{-1}), ε_r is the relative dielectric constant of the materials (estimated to be 3 for organic semiconductors),[74] μ is the charge carrier mobility, d is the thickness of the films (~100 nm). V is the difference of applied voltage (V_{app}) and offset voltage (V_{bi}). The data are recorded with a Keithley 2400 by sweeping from 1 to 9 V at a scan rate of 40 mV s^{-1}. The carrier mobility can be calculated from the slope of 2 in the log-log dark *J-V* curve, as shown in **Figure 2.13**.

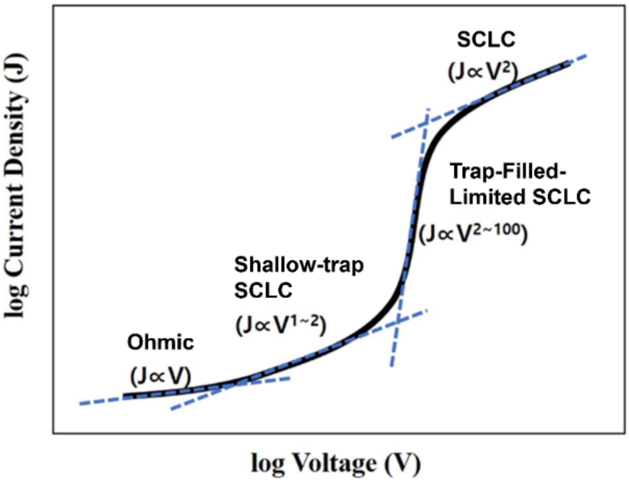

Figure 2.13 The log-log dark *J-V* characteristic showing the current limited by Ohmic, shallow-trap SCLC, trap-filled-limited SCLC, and SCLC.

2.4.3 Steady-state spectroscopy

UV-Vis Spectroscopy. The ultraviolet-visible (UV-vis) spectroscopy is employed to get any information about the absorbance / reflectance / transmittance spectra of a compound in a solution or a thin-film state. To perform solution absorption measurement, the sample was diluted in chloroform or chlorobenzene (analytical grade) which used as the solvent in the quartz cuvette at room temperature. For thin-film state, the sample was prepared in the quartz glass by using the same treatment as depositing the layer in a device. In principle, the UV-vis region is in the wavelength range from 300 to 900 nm. The different absorption spectra observed in different wavelength is due to the different chromophore responses to different electrons excitation behaviour of the material by the absorbance of light energy or electromagnetic radiation. The UV-vis spectra were recorded on Perkin Elmer Lambda 950 UV/Vis/NIR spectrometer using an integrated sphere at room temperature. **Figure 2.14a** shows the UV-vis spectrophotometer used for the absorbance and transmittance spectra analysis in this thesis.

The energy of the optical bandgap (E_g^{opt}) can be calculated accordingly to the equation 2.2:

$$E_g^{opt}(eV) = h\, x \frac{c}{\lambda} \approx \frac{1240}{\lambda} \tag{2.2}$$

where λ denotes the absorption edge wavelength onset expressed in nm, obtained from the offset wavelength derived from the low energy absorption band as represented in **Figure 2.14b**.

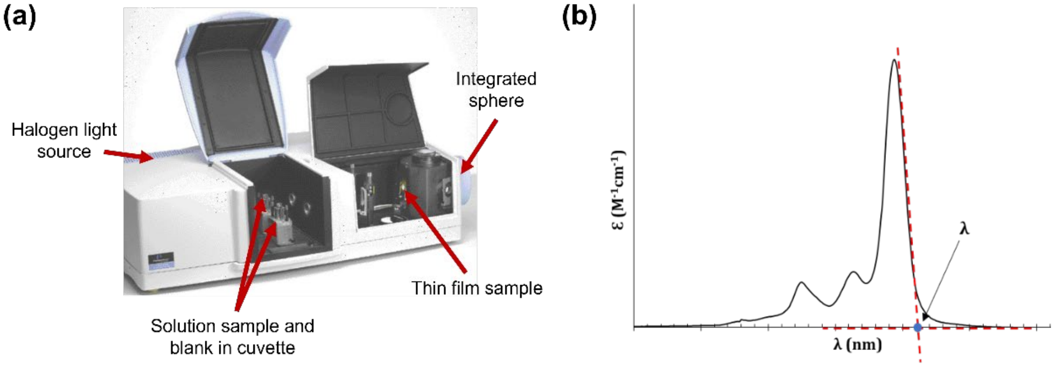

Figure 2.14 (a) The experimental setup of UV-vis spectrophotometer and (b) schematic representation of a UV-Vis spectrum and the respective optical band gap energy estimation in this thesis.

Photoluminescence spectroscopy. Photoluminescence (PL) measurements were carried out on active layers, which were recorded on fluorolog Horiba Jobin Yvon Lrd. steady state spectrofluorometer with a PMT (UV-vis) detector that allows fluorescence measurements in the wavelength range from 250 to 850 nm at room temperature. The fluorescence spectrum was corrected for the optical density of the sample at the excitation wavelength and for the detection sensitivity of the detector. The thin-film sample was prepared by spin-coating the sample under the same condition as the active layer deposition condition. The excitation wavelength was determined in the lower energy of the absorption peak.

External quantum efficiency measurement. The external quantum efficiency (EQE), alternatively so-called the incident-photon-to-current (IPCE) is defined as the ratio of the number of incident photons to the number of charge carriers extracted by a photovoltaic device. The EQE is related to the combination of five fundamental processes, as described by equation 2.3:

$$\eta_{EQE} = \eta_A \times \eta_{ED} \times \eta_{CD} \times \eta_{CT} \times \eta_{CC} \tag{2.3}$$

in which each term has the name of light absorption (η_A), exciton migration (η_{ED}), exciton dissociation or charge separation (η_{CD}), charge transport (η_{CT}), and charge collection to the electrodes (η_{CC}).[75] In this thesis, the EQE spectra were recorded by quantum efficiency measurement system from Lasing, S.A. (IPCE-DC model, LS1109-232) equipped with a Newport 2936-R power-meter unit, a Xenon lamp power supply, and a monochromator. All the EQE measurement were performed under forwarding wavelength sweep direction from 300 nm to 1000 nm. The experimental setup for EQE measurement is shown in **Figure 2.15**. Experimentally, the light from a broadband light source such as a Xenon lamp is sliced and filtered through a monochromator to create a single wavelength source. Each wavelength records the number of generated electrons. The equation 2.4 can be used to determine the calculated EQE value:

$$EQE = \frac{h\nu\, J_{SC}}{P_{in} q} \tag{2.4}$$

where $h\nu$ is the photon energy, P_{in} is the incident light intensity, and q is the absolute value of electron charge. Since the EQE is the spectral response of the cell, the integrated $J_{SC,EQE}$ of the cell under illumination can be calculated by:

$$J_{SC,EQE} = \int qEQE(\lambda)S(\lambda)d\lambda \tag{2.5}$$

where $S(\lambda)$ is photons per second. The $J_{SC,JV}$ is generally measured from the J-V characteristic under the solar simulator and the calculated $J_{SC,EQE}$ is typically lower than the $J_{SC,JV}$ for OSCs with a small deviation (<10%).

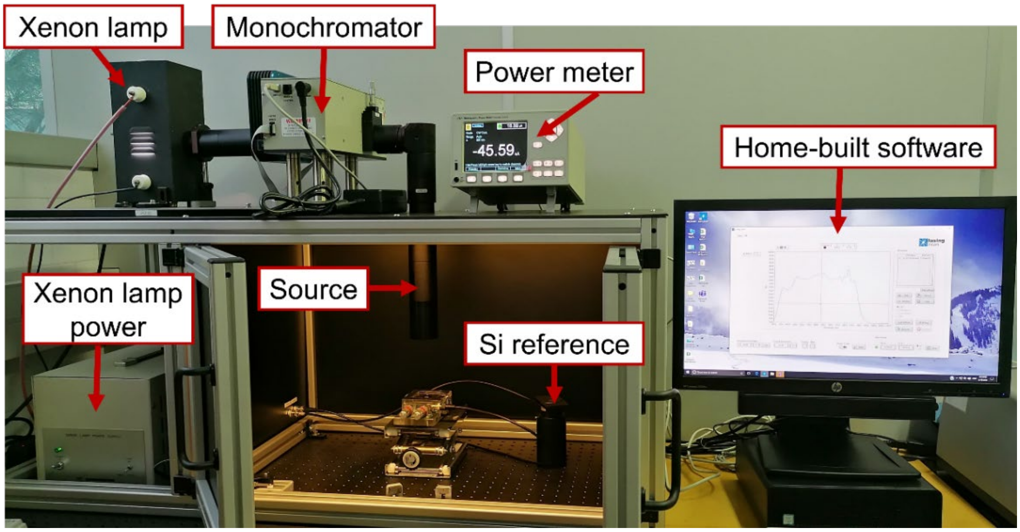

Figure 2.15 The EQE measurement experimental setup.

2.4.4 Time-resolved spectroscopy

Charge extraction. Charge extraction (CE) is a large modulation technique that measures the amount of stored charge present in the solar cell. **Figure 2.16** illustrates the CE measurement and its corresponding process. Here, the solar cell is positioned in front of a white LED array (LED from LUXEON Lumileds and powered by an Aim-TTi PLH120-P power supply), where the light intensities of white LED can be modulated to stabilise the V_{OC} of the solar cell at some point of *J-V* curve. After the V_{OC} is balanced, the solar cell is short-circuited ($V = 0$V) through a circuit containing a small resistance (50 Ω) whilst the light source is simultaneously switched off. When short circuited, most of the free charges in the solar cell flow through the resistor to create a current transient due to the solar cell discharged through the contacts. It is important to note that CE extracts all the kinds of charges like carries and the geometrical charges presented at the cell at a given voltage. Thus, charge extraction must be faster than the carrier recombination to prevent the charge losses before the cell is short-circuited.[76]

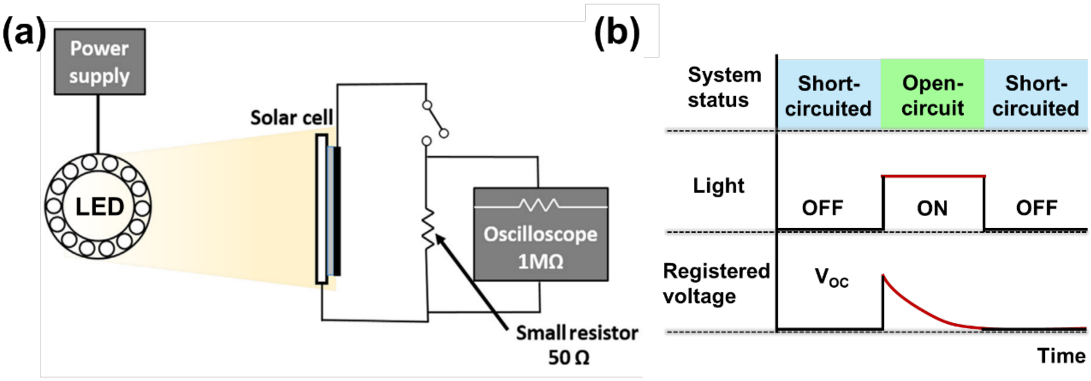

Figure 2.16 (a) The charge extraction measurement and (b) its corresponding process. The figure is modified from Ref [76].

Transient photovoltage/photocurrent. The transient photovoltage/photocurrent (TPV/TPC) is the time-resolved technique employed to calculate the charge carrier lifetime of organic solar cells. Both techniques are based on the excitation of the device by a fast and small perturbation of the incident light perturbing the solar cell. In particular, TPV technique is leveraged to study the carrier recombination process in solar cell device by perturbing the solar cell V_{OC} under illumination in open-circuit condition, which can be directly associated with a small perturbation of the quasi-Fermi level.[77] On the other hand, TPC through the Differential Capacitance (DC) analysis is used to measure the extra carriers in the solar cell generated by laser pulse-induced perturbation in short-circuit conditions. Unlike the CE method, an advantage of the DC method is that it can be employed in a system with high recombination rates, in which the CE decay and the TPV decay have similar kinetics.

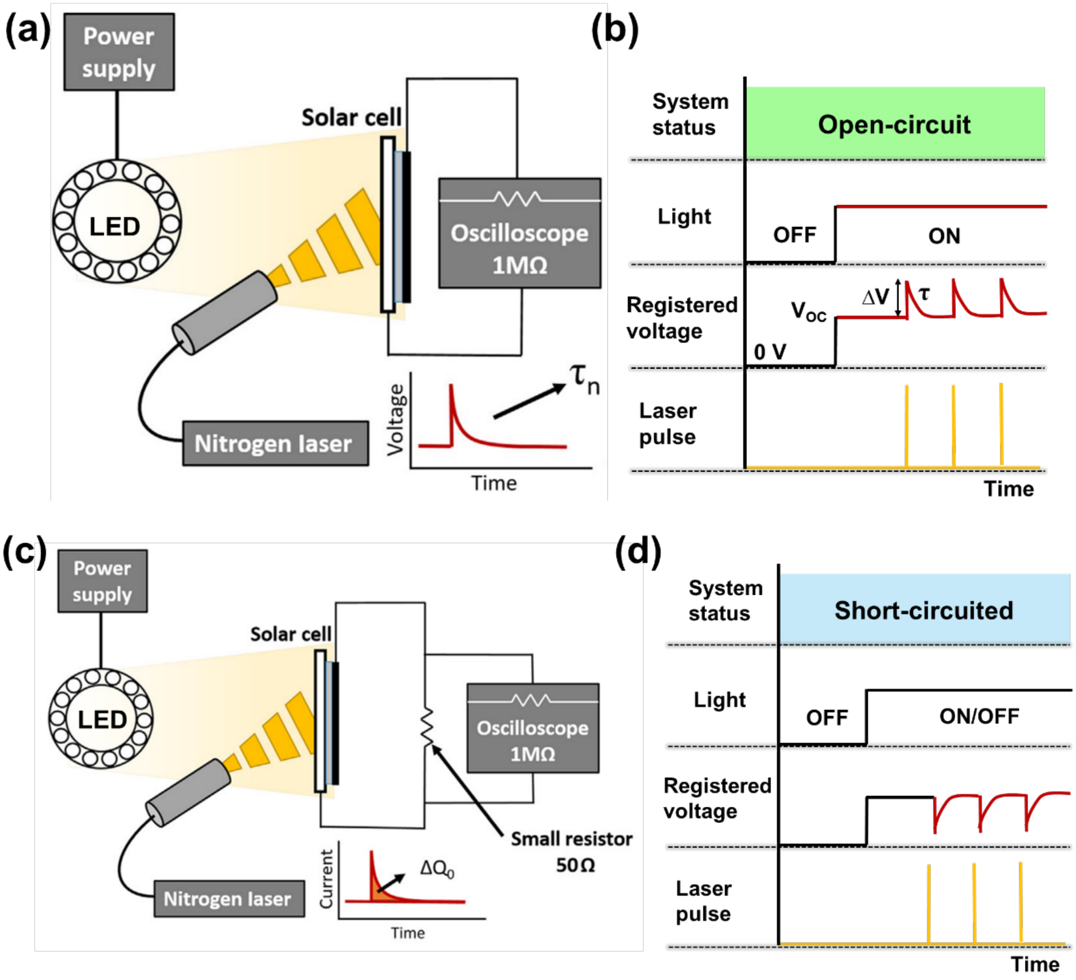

Figure 2.17 Schematic illustration of (a) transient photovoltage measurement with (b) TPV corresponding TPV process and (b) transient photocurrent measurement with (d) its corresponding TPC process. The figure is modified from Ref [76].

Figures 2.17a and **b** illustrate the TPV measurement setup and its corresponding signals that can be monitored at the oscilloscope. To perform TPV, the photovoltaic device is kept at an open-circuit and irradiated under a continuous light source to promote a constant and stable V_{OC}. The device is held at open-circuit condition, so the current cannot flow through the contacts while it is connected to an oscilloscope that can register the changes in voltage over time. After the V_{OC} is stabilised, the device is excited with a short-lived laser pulse that generates a small perturbation of the V_{OC}. A nanosecond nitrogen laser (PTI GL-3300) has been used to control the 590 nm excitation wavelength (the emission of Rhodamine 6G dye) in order to hold the solar cells in approximately V_{OC} condition. To trigger the laser pulse, an analogue function generator (Aim-TTi TG330) has been used to generate a square wave pulse with a duration of 1.5 ns. A semitransparent optical filer was utilized to adjust the laser pulse intensity. The extra charge carriers produced by the laser pulse are forced to recombine and cannot be extracted since the device is in open-circuit condition, leading to the registration of the transient to the initial V_{OC}.

Figures 2.17c and **d** illustrate the TPC measurement setup and its current response that can be monitored at the oscilloscope. The TPC measurement setup is quite similar to the TPV measurement setup, with the exception that the solar cell is connected to a small resistance (50 Ω) whilst kept in short-circuit condition. To perform TPC, a small perturbation in the solar cell current generated by the laser pulse is measured on the oscilloscope as a voltage drop across the resistor that can easily be converted into a transient current by using Ohm's law. The transient current generated by the nitrogen laser pulse is measured and integrated over time so that the amount of the photo-generated charges (ΔQ) can be calculated.

Impedance spectroscopy. The impedance spectroscopy (IS) is a versatile characterization technique used to study the kinetic and energetic processes, profile the electronic structure, and observe bulk and interfacial electrical properties within OSCs devices that cannot be observed in a direct current regime.[78–80] Moreover, capacitance-frequency (*C-f*) or known as one of the defect spectroscopy technique can be performed using IS measurements. In IS technique, the OSC device is measured at a relevant operational DC offset bias (typically at open-circuit condition) in order to quantify electrical or electrochemical dynamics that define the device performance. Defect spectroscopy, on the other hand, determines the energy distribution of traps by recording the change in the capacitance of the depleted semiconductor as a function of temperature, voltage, and/or frequency.[81–83] In this thesis, IS measurement was employed to observe the formation of the traps during loss mechanism, which takes place at the interfaces. The energy distribution of the traps was also observed by *C-f* measurement. The data obtained from IS and *C-f* measurements were recorded using HP-4192A impedance analyser. In an IS measurement, the sample response to a small-signal, sinusoidal electrical stimulus is measured as a function of frequency. Several voltage perturbations were applied at a frequency range from 1 kHz to 1 MHz with an AC signal and 5 mV amplitude. The IS measurement was carried out in dark and under AM 1.5G or LED illumination calibrated by a certified monocrystalline silicon photodiode. The corresponding information was extracted and quantified from the spectrum using an equivalent circuit model. On the other side, to be able to calculate the density of states (DOS) by *C-f* measurement, the capacitance-voltage (*C-V*) measurement should be performed in dark conditions at a frequency 1 MHz, 5mV amplitude and voltage scan from -6V to 6 V to get the value of built-in voltage (V_{bi}). **Figure 2.18** shows the experimental setup for IS measurements under AM 1.5G illumination.

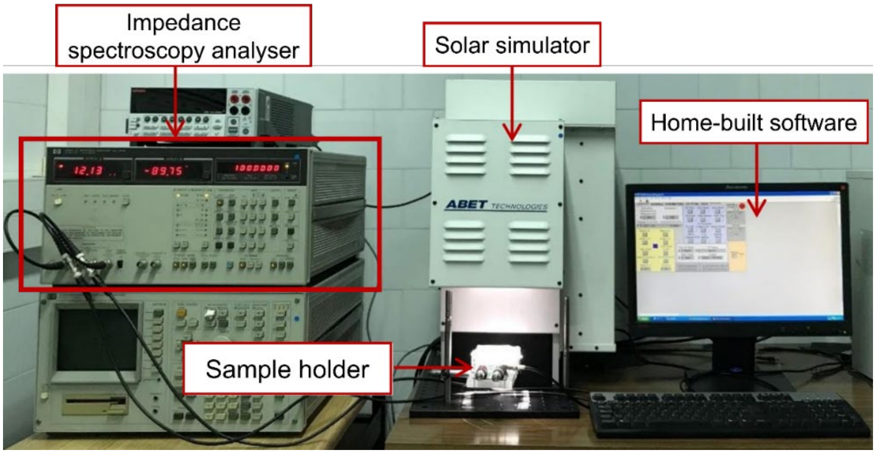

Figure 2.18 The experimental setup of impedance spectroscopy measurement.

2.4.5 Thin-film characterization

Atomic force microscopy. Atomic force microscopy (AFM) is the common technique to probe the surface morphology and the roughness of thin films. Mainly, AFM has three differing operation modes which are contact mode, tapping mode and non-contact mode. In this thesis, AFM measurements were carried out in tapping mode, where the tip lightly taps on the surface of the specimen during scanning. The cantilever in tapping mode oscillates at its resonant frequency and the changes in the oscillation amplitude can be used to measure the distance between the tip and the specimen surface. The specimens for AFM characterization were prepared under the same condition compared with the active layer deposition of the OSCs devices. The cantilever used was silicon probes with a typical spring constant of 1 – 5 N m^{-1} and a resonant frequency of 75 kHz operated under ambient conditions. The images were processed using a Molecular Imaging Pico SPM II instrument (pico +) software.

Transmission electron microscopy. The transmission electron microscopy (TEM) method investigates the blend microstructure in transmission mode and can provide elemental map distribution of the material presented in the blend. The active layers for the TEM investigations were prepared as plan view specimens in the same condition as the active layers of the OSC devices. To get the specimen for TEM analysis, first the film layers of PEDOT:PSS and blends with a thickness of 100 nm were deposited on glass. Then, the sample was put into a petri dish with distilled water to dissolve PEDOT:PSS layer, whereas the active layer was floated off and transferred to a 400-mesh copper TEM supporting grid. The TEM images of the active layer were obtained by using a JEOL model 1011 operated at 80 kV.

Contact angle measurements. Contact angle measurements were performed by an optical tensiometer (Attention Theta Flex, Biolin Scientific, Sweden) using liquid drops of water and ethylene glycol (EG) by sessile drop analysis. Experimentally, a thin film specimen-coated glass substrate was set below the syringe containing water or EG solvent. Then, a water or EG droplet (~15 mL) formed at the end of a syringe by turning clockwise the base of the syringe until a droplet was dropped on the specimen. Then, the contact angle image analysis was recorded by video recorder, where each image of this video is later analysed to determine the contact angle at the moment the image was captured.[84] Basically, the contact angle is determined by measuring the angle between the surface and the tangent of the drop surface at the contact. **Figure 2.19** depicts the contact angle measurement performed in this thesis.

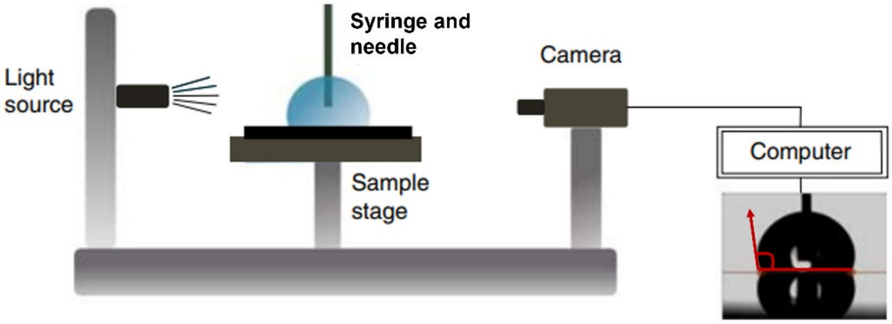

Figure 2.19 The contact angle measurement experimental setup, modified from Ref [84].

To measure the miscibility between the materials in ternary blend, the surface tension value can be further calculated from contact angle measurement according to Wu's equation:[85]

$$\gamma_{A-B} = \gamma_A + \gamma_B - 4\left(\frac{\gamma_A^d \gamma_B^d}{\gamma_A^d + \gamma_B^d} + \frac{\gamma_A^p \gamma_B^p}{\gamma_A^p + \gamma_B^p}\right) \tag{2.6}$$

where $\gamma_{A\text{-}B}$ represents interfacial tension between material A and B, γ_A and γ_B are the surface tension of A and B, respectively. The superscript *d* and *p* represent the dispersion and polar components calculated using the contact angle with water and ethylene glycol.

2.5 Dark *J-V* modeling

The equivalent circuit device models operated in MATLAB software were employed to fit the experimental data obtained from the dark *J-V* characteristics of the corresponding devices. The equivalent circuit models are useful for understanding the electrical behavior of semiconductor devices, considering the dominant effect of the diode, shunt and series resistance for a given voltage on the generated photocurrent of the device. For ideal solar cells, the equivalent circuit models are represented in inset Figure 1.8b. As in many case that the loss mechanisms are commonly contributed to the dark mechanism, the cells behaviour may deviate from the ideal condition. **Figure 2.20** depicts the two-diode model we used to fit the non-ideal dark *J-V* characteristics of crystalline or amorphous photovoltaic heterojunction.[82] The SCLC mechanism may present in high resistance materials such as organic semiconductors. Two diodes are employed to check whether one or two different mechanisms are observed in the structure.

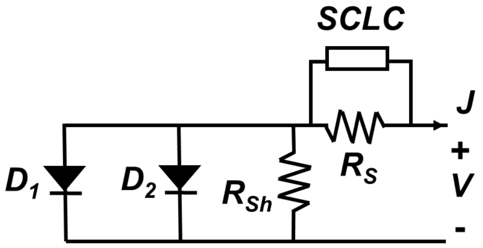

Figure 2.20 Non-ideal equivalent circuit model for an arbitrary heterojunction.

Chapter 3

Binary bulk heterojunction solar cells based on fullerene acceptor for indoor application

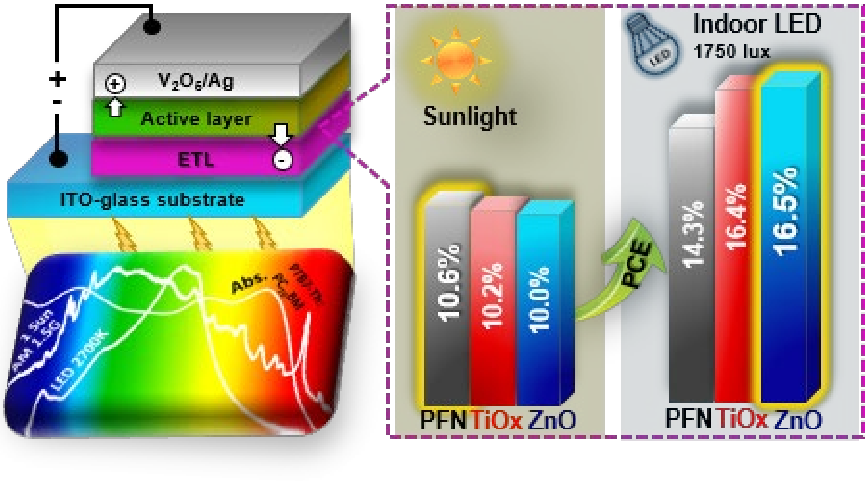

This chapter is based on the published work: Torimtubun, A.A.A. *et al.*, "A Cathode Interface Engineering Approach for the Comprehensive Study of Indoor Performance Enhancement in Organic Photovoltaic," *Sustain. Energy Fuels*, **2021**, *4*, 3378-3387 and Torimtubun, A.A.A. *et al.* "Photostability Study of Inverted Polymer Solar Cells under AM 1.5G and LED Illumination via Impedance Spectroscopy", *IEEE J. Electron Devices Soc.*, **2020**, *9*, 484-491.

3.1 Introduction to indoor low-light application

The potential application of photovoltaics (PV) for indoor energy harvesting has attracted considerable attention providing off-grid energy sources for tens of billion low power consumption devices used for Internet of Things (IoT).[86–90] IoT enables a communication system between wireless electronic devices such as sensors, displays, actuators, etc. through the internet, in which these devices are essential to lead the future generation of smart buildings, factories, and retail sectors.[91–94] Such low power consumption devices are usually operated under an indoor environment, in which the light intensity ranging from 0.5 – 1 mW cm^{-2} for a well-lit room.[16,95–98] Therefore, a self-sustainable power source that operates with high power densities and high efficiency is required.[92,99]

PV cells offer great promise to efficiently convert low light levels under indoor light conditions due to their high output voltage and good spectral response in the visible region.[86,92,100–102] The emission spectra of the common indoor sources, such as incandescent light bulbs, fluorescent lamps and light-emitting diodes (LEDs) have a range from 400 to 800 nm, which are narrower than spectral irradiance of an AM 1.5G light source with the range from 400 to 2000 nm.[99,103,104] In consequence, PV cells developed for outdoor applications such as crystalline silicon (c-Si) solar cells show high power conversion efficiency (PCE) under 1 sun, but it shows low PCE under indoor illumination due to their mismatch spectrum range and decreased photovoltage.[16,86,103,105] Unlike the c-Si solar cells, several emerging photovoltaic technologies, including organic photovoltaic (OPV) cells, dye-sensitized cells and perovskite solar cells, show remarkable performance under room lighting illumination due to their highly tunable light-absorption photoactive material properties (~390 – 760 nm)[88], and well-matched spectral response in the visible light region; thus, making them an efficient energy sources for low-power indoor applications.[86,95] OPV cells are taking more steps forward the commercialization of indoor PVs than the dye-sensitized and perovskite counterparts due to their low cost, light weight, and large-area module fabricated by solution-based technologies.[106,107]

Recent studies of OPV devices under different incident light illumination conditions and different indoor artificial light sources have been reported. Mori *et al.*[103] found that the PCE of PTB7-Th:$PC_{70}BM$ based devices (8.43%) is lower than PCE of the c-Si solar cells (13.49%) under 1 sun; however, when illuminated under LEDs light at 890 lux (0.4 mW cm^{-2}), their PCE of 11.63% is higher than that of c-Si solar cells (9.65%). Using the same photoactive materials, Cutting *et al.*[16] achieved a PCE of up to 21.04% under 20.5 mW cm^{-2} of LED illumination. On the other hand, Aoki[108] and Minnaert *et al.*[109] studied the performance of OPVs for indoor applications under artificial light sources: fluorescent light, sodium lamp, metal halide lamp, cool LED light, and warm LED light. They suggested that it is unnecessary to test the devices under all artificial light sources to demonstrate their potential indoor application. Depending on the active material, a good match of the absorbance spectrum of the OPV device with the emission spectrum of the indoor light source is important to characterize the suitability of an OPV for indoor energy harvesting.[110] The following characteristics are required to obtain efficient indoor PV devices: (i) well-matched photo-response spectrum with indoor light and high EQE, (ii) suppressed trap-mediated recombination and (iii) high V_{OC}.[86,91,111–113]

Several strategies to improve OPV performance under indoor light illumination have been investigated by several research groups. Lee *et al.*[91] optimized the photoactive layer (BTR:$PC_{71}BM$) and improved the PCE of over 28% under fluorescent lamps using the solvent vapor annealing technique. Another group, Cui *et al.*[86] using a material design engineering approach to synthesize photoactive materials whose absorption spectra match those of indoor light sources; the devices fabricated from those materials showed low energy loss, resulting in high V_{OC} of 1.10 V and high PCE of 26.1% under LEDs illumination. Yin *et al.*[88] and Nam *et al.*[114] have adopted ternary blend approaches to improve the overall performance of OPV by enhancing carrier mobilities to improve the fill factor (*FF*), complementing the optical absorption to escalate short circuit current density (J_{SC}) and matching energy level of the photoactive materials to enlarge V_{OC}.[88,114] Interface engineering was another strategy employed by Goo *et al.*[115] and Shin *et al.*[116] to improve the shunt resistance and reduce the work function of ethoxylated polyethylenimine (PEIE) and zinc oxide nanoparticle (ZnO NPs)/PEIE modification as electron transport layer (ETL), respectively.

Besides some efforts to achieve high PCE of indoor OPV cells, stability is another vital factor for achieving commercial application of OPVs technology.[117–120] Extrinsic degradation in the presence of water and oxygen, intrinsic degradation in the dark, and intrinsic photo-induced degradation are dynamic aging mechanisms that may affect the stability of OPVs.[121–123] The development of encapsulation technologies makes it now possible to control the extrinsic degradation.[124] However, the cells are still degraded intrinsically over time, even with perfect encapsulation. In OPVs, semiconductor polymers are generally degraded under sunlight irradiation in the absence of oxygen and moisture.[125,126] Hence, studying the intrinsic photostability of OPVs under an inert atmosphere is particularly interesting, as it provides a more solid understanding of the process involved in the absence of a substance that could chemically alter the photoactive materials.[127] Doumon *et al.* showed that the solar irradiation-induced degradation of polymer:fullerene solar cells in the inert condition is mainly due to the ultraviolet (UV) components of the solar spectrum affecting the operational lifetime of polymers with different chemical structure.[126] A recent study by Gasparini *et al.* also suggested that the full sun illumination light-induced trap formation may cause V_{OC} losses.[128] In addition, severe burn-in phenomenon has been widely observed at the beginning of the photodegradation under sunlight and inert environment in OPVs, which lead the PCE drops exponentially.[66,129,130] Although the photostability of PSCs under 1 sun illumination has been reported in several studies, the photodegradation mechanism of OPVs under LED light as a common artificial indoor light source has rarely been studied, which is worth noting that the application of indoor OPVs in IoT is surging. Therefore, a rigorous understanding of the photostability of PSCs under LED illumination is urgently needed.

In this chapter 3, we employ the interface engineering approach to improve the indoor performance of PTB7-Th:$PC_{70}BM$ inverted OPV cells using three different commonly used ETL materials, *i.e.*, poly [(9,9-bis(3'-(N,N-dimethylamino)propyl)-2,7-fluorene)-alt-2,7-(9,9–dioctylfluorene)] (PFN), titanium sub-oxide (TiO_x), and zinc oxide (ZnO). These ETL materials are chosen due to their reported success under 1 sun to reduce the electron extract barrier from the active layer to the cathode and modify the surface of ITO.[82,131–136] However, their performances under indoor illumination have not been studied in depth. Here, using AFM, UV-Vis spectroscopy, EQE, *J–V* measurement and impedance spectroscopy (IS), we found that by expediently optimizing the materials and deposition condition of the ETLs, the OPV cells performance could be enhanced under both outdoor and indoor illumination. However, it performs opposingly under different lighting conditions. PCE of up to 16.49% under LED illumination at 200-2000 lux, together with an attractive PCE of up to 10.55% under 1 sun illumination, is presented. The effect of the choice of ETL in the device performance is agreed well with the parasitic resistance effect, the charge recombination, and the trend of charge collection efficiency. Besides, the indoor champion device was further investigated by IS analysis to study and compare its photostability under the exposure of standard 1 Sun illumination and 1000 lux artificial LED 2700 K light over aging time. Standard procedures of ISOS L-1 and low-light measurement protocols were used for an accurate lifetime determination.[137] The OPV cells under LED light showed about 12 times prolonged lifetimes (3060 min) relative to the cells illuminated under full sunlight. The photodegradation behaviors of the devices studied by IS analysis reveal that the main cause behind the instability is the electron transport layer.

3.2 Controlling the charge extraction in indoor OPVs

Figure 3.1a shows the chemical structure of the donor polymer PTB7-Th and the fullerene acceptor $PC_{70}BM$. Polymer donor PTB7-Th is chosen due to high V_{OC} (~0.80 V).[103] The binary BHJs of PTB7-Th:$PC_{70}BM$ solar cells were fabricated using an inverted structure ITO/ETL/PTB7-Th:$PC_{70}BM$/V_2O_5/Ag, as illustrated in **Figure 3.1b**. An inverted structure device was employed because this is a preferred architecture for indoor performance, and it provides vertical phase separation and concentration gradient in the active layer.[138] The PFN layer, TiO_x layer, or ZnO layer was used as ETL. **Figure 3.1c** displays the energy level diagram of each material in the inverted OPV (iOPV). The HOMO and LUMO levels of the donor PTB7-Th are –5.22 and –3.63 eV, while the HOMO and LUMO of the acceptor $PC_{70}BM$ are –6.10 and –4.30 eV, respectively.[139] A large energy offset between HOMO of the donor and the LUMO of the acceptor is needed to obtain a high V_{OC}. A higher V_{OC} under 1 sun illumination is more favorable for the indoor light application of iOPVs due to the extra voltage loss when the light intensity is reduced. A minimum $LUMO_{donor}$ – $LUMO_{acceptor}$ difference of around 0.3 eV is preferred to ensure an efficient electron separation of excitons at the donor-acceptor interfaces.[103,140,141]

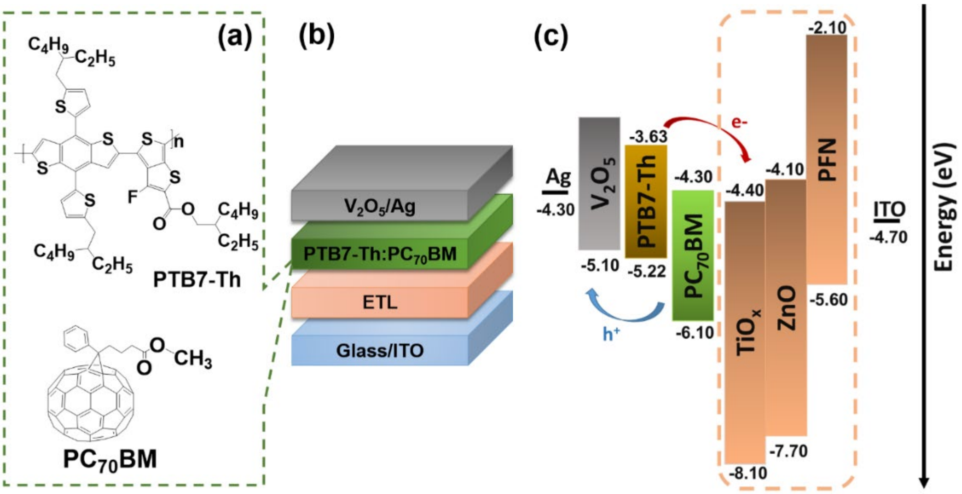

Figure 3.1 (a) Chemical structures of PTB7-Th and $PC_{70}BM$; schematics illustration of (b) the device architecture and (c) the energy level alignment.

The evolution of the surface morphologies of the three different ETLs on the glass/substrate was carried out by atomic force microscopy (AFM) analysis. **Figure 3.2a–d** display the surface topologies of the bare ITO and ITO modified with the three different ETLs. The root-mean-squared (RMS) roughness values estimated from the AFM height profiles in an area of 5 μm x 5 μm were 3.67 nm (bare ITO), 2.52 nm (ITO/PFN), 2.50 nm (ITO/TiO_x), and 2.47 nm (ITO/ZnO). The bare ITO showed the highest RMS values, while a smooth surface was observed for the ITO modified by ETLs. However, the latter samples showed no significant differences in their RMS roughness. The smooth surfaces observed for all ETLs-modified ITO are believed to aid the formation of the photoactive layer, leading to effective electron collection.[115] The optical effect is another essential factor for effective ETL. **Figure 3.2e** shows the optical transmittance spectra of the different ETLs, measured with UV-vis spectrometer. In the spectral range of around 400 – 500 nm, all the samples, including the reference ITO had transmittance above 75%. Therefore, ZnO-based ETLs which had the highest transmittance would be preferable as a highly transparent cathode that can allow the max photon flux to reach the active layer for generating photocurrents.[114]

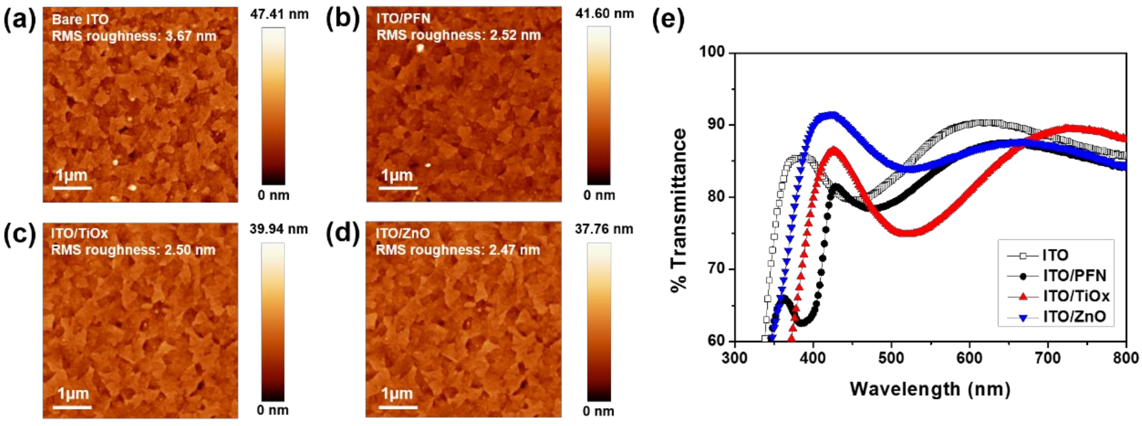

Figure 3.2 AFM topographical images acquired from tapping mode of (a) bare ITO, (b) ITO/PFN, (c) ITO/TiOx, and (d) ITO/ZnO and (e) their transmittance spectra.

3.2.1 Device performance under outdoor illumination

Figure 3.3a shows the best *J–V* characteristics of PTB7-Th:PC$_{70}$BM iOPV with PFN, TiO$_x$, or ZnO film as ETL under 1 sun simulated solar illumination (100 mW cm^{-2} of AM 1.5G solar irradiation). The detailed photovoltaic parameters, such as J_{SC}, V_{OC}, *FF*, PCE, and parasitic resistances (R_S and R_{Sh}) measured under AM 1.5G illumination are summarized in **Table 3.1**. For the reliable data and reasonable comparison, the average and standard deviation values were measured from more than 12 devices. It can be seen that the device performance is improved by using PFN as the ETL. All of the PTB7-Th:PC$_{70}$BM cells with different ETL show the same high V_{OC} values (0.79 V) due to the deep HOMO energy level of the donor PTB7-Th (5.22 eV). This indicates that V_{OC} values do not depend on the choice of ETL materials. The V_{OC} values is proportional to the difference between HOMO and LUMO levels of active layer materials.[142] It is also shown that both types of devices have an outstanding *FF* (> 70%) as the high V_{OC} values lead to the high *FF* values.[143] It is worth mentioning that the highest *FF* of 75.00% obtained by PFN-ETL is the best-reported values for PTB7-Th:PC$_{70}$BM–based organic photovoltaic (see **Table 3.2**). The device with ZnO as an ETL exhibits a J_{SC} of 16.63 mA cm^{-2}, *FF* of 72.85%, and V_{OC} of 0.79 V, resulting in an average PCE of 9.57 ± 0.29% (with a maximum of 10.03%). With the TiO$_x$ as an ETL, the J_{SC} increases to 17.06 mA cm^{-2}, *FF* decreases slightly to 72.03%, and V_{OC} remains at 0.79 V, leading to an average PCE of 9.71 ± 0.24% (maximum PCE of 10.20%). By replacing ZnO and TiO$_x$ with PFN, the device performance was improved, giving the highest PCE of 10.55% and the highest *FF* of 75.00% (with an average PCE value of 10.04 ± 0.31%, J_{SC} of 17 mA cm^{-2}, and V_{OC} of 0.79 V). In the outdoor condition, the device performance (J_{SC}, *FF*, and PCE) under 1 sun illumination could be improved by using PFN as ETL; meanwhile, the V_{OC} values were similar, indicating that PCE was mostly determined by photon absorption yield.[114] This result is in good agreement with the result obtained by He *et al.*[131] using PFN as the ETL in a PTB7:PC$_{71}$BM BHJ system. In addition, the calculated values of R_S and R_{Sh} from Figure 3.3a at open-circuit and short-circuit voltage, respectively, exhibit similar values for all devices. A slightly higher R_S value for the device with TiO_x-ETL was observed. Meanwhile, the highest R_{Sh} value belongs to the PFN-based device. In general, the values of R_S and R_{Sh} for the three types of devices are lower than 3 Ω cm^2 and around or more than 1 kΩ cm^2, respectively; these are preferable values to operate in both indoor and outdoor illumination.[144]

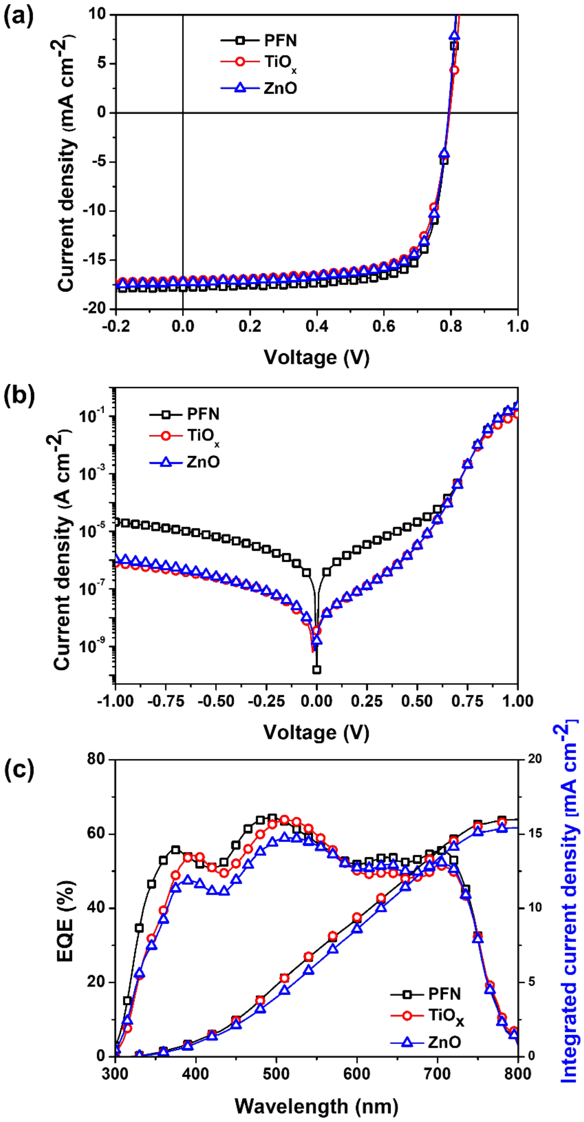

Figure 3.3 *J-V* characteristics of the different ETLs measured under (a) one sun illumination and (b) in the dark; (c) EQE spectra of the devices with different ETLs.

Table 3.1 Device performance parameters for different ETLs (PFN, TiOx, and ZnO) measured under AM 1.5G with 100 mW cm^{-2} intensity. The first row displays the average and the standard deviation of photovoltaic parameters obtained from over 12 devices, and the second row shows the parameters obtained for the best device.

Electron transport layer		**J_{SC} / J_{calc}[a] (mA cm^{-2})**	**V_{OC} (V)**	**FF (%)**	**PCE$_{avg}$ (%)**	**R_S (Ω cm^2)**	**R_{Sh} (Ω cm^2)**
PFN	Average	17.00 ± 0.56 (16.00)	0.794 ± 0.006	74.32 ± 1.22	10.04 ± 0.31	0.90 ± 0.04	1.60 ± 0.56
	Best	17.81	0.789	75.00	10.55	0.87	1.25
TiO$_x$	Average	17.06 ± 0.39 (15.86)	0.790 ± 0.003	72.03 ± 0.78	9.71 ± 0.24	1.66 ± 0.05	1.08 ± 0.22
	Best	17.74	0.799	71.86	10.20	1.62	1.18
ZnO	Average	16.63 ± 0.52 (15.43)	0.790 ± 0.003	72.85 ± 0.40	9.57 ± 0.29	0.88 ± 0.04	0.98 ± 0.35
	Best	17.26	0.789	73.61	10.03	0.83	1.14

[a] The J_{calc} is the integrated current density calculated from the EQE spectrum.

Table 3.2 Device performance summary of the PTB7-Th:PC$_{70}$BM-based OPV devices under AM 1.5G condition reported in the literature with the average device area ≤ 16 mm^2.

	Device architecture	**Type**	**J_{SC} (mA cm^{-2})**	**V_{OC} (V)**	**FF (%)**	**PCE (%)**	**Ref.**
A	ITO/PEDOT:PSS/PTB7-Th:PC$_{70}$BM/Al	Std	19.80	0.79	65.00	10.12	145
B	ITO/PEDOT:PSS/PTB7-Th:PC$_{70}$BM/Ca/Al	Std	16.86	0.78	68.16	9.00	146
C	ITO/PEDOT:PSS/PTB7-Th:PC$_{70}$BM/C$_{60}$/Al	Std	19.01	0.82	69.10	10.80	147
D	ITO/PEDOT:PSS/PTB7-Th:PC$_{70}$BM/LiF/Al	Std	14.88	0.79	64.50	7.58	148
E	ITO/PEDOT:PSS/PTB7-Th:PC$_{70}$BM/LiF/Al	Std	17.11	0.80	55.20	7.60	149
F	ITO/PEDOT:PSS/PTB7-Th:PC$_{70}$BM/BCP/Ag	Std	17.74	0.78	64.11	8.95	150
G	ITO/PEIE/PTB7-Th:PC$_{70}$BM/MoO$_3$/Ag	Inv	18.10	0.79	66.00	9.50	151
H	ITO/TiOx/PTB7-Th:PC$_{70}$BM/MoO$_3$/Ag	Inv	15.10	0.79	50.00	6.00	135
I	ITO/PFN/PTB7-Th:PC$_{70}$BM/MoO$_3$/Ag	Inv	17.43	0.83	73.78	10.61	152
J	ITO/PFN/PTB7-Th:PC$_{70}$BM/MoO$_3$/Ag	Inv	16.01	0.80	72.28	9.59	153
K	ITO/PEIE/PTB7-Th:PC$_{70}$BM/MoO$_3$/Ag	Inv	18.30	0.79	62.00	9.00	154
L	ITO/ZnO/PF$_{EO}$SO$_3$Na/PTB7-Th:PC$_{70}$BM/MoO$_3$/Al	Inv	17.79	0.78	67.80	9.41	155
M	ITO/patterned ZnO/PTB7-Th:PC$_{70}$BM/MoO$_x$/Al	Inv	19.47	0.78	66.90	10.10	156
N	ITO/amorphous ZnO/PTB7-Th:PC$_{70}$BM/MoO$_x$/Ag	Inv	16.60	0.77	71.50	9.10	133
O	ITO/ZnO:PBI-H/PTB7-Th:PC$_{70}$BM/MoO$_3$/Al	Inv	17.69	0.82	72.90	10.59	157
P	ITO/ ZnO-C$_{60}$/PTB7-Th:PC$_{70}$BM/MoO$_3$/Ag	Inv	15.73	0.80	74.30	9.35	158
Q	ITO/ZnO/PTB7-Th:PC$_{70}$BM/MoO$_3$/Ag	Inv	19.30	0.81	70.00	10.95	159
R	ITO/PFN/LiF/PTB7-Th:PC$_{70}$BM/V$_2$O$_5$/Ag	Inv	19.05	0.79	73.50	11.00	139
S	ITO/PFN/PTB7-Th:PC$_{70}$BM/V$_2$O$_5$/Ag	Inv	17.81	0.79	**75.00**	10.55	

[S] Result from this contribution, obtained from the *J-V* measurement of the best device.

Figure 3.3b depicts the *J-V* characteristics of the devices based on PFN, TiO_x, and ZnO ETLs measured in the dark, which gives a better understanding of the performance of the devices (leakage current, ideality factor, series and shunt resistances) under low light conditions. A single diode equivalent model shown in **Figure 3.4a** was used to fit the experimental dark *J-V* curves to elucidate the dominating effect of the diode, R_S or R_{Sh} on the three regions of *J-V* characteristic. Considering the drop voltage in the junction which is due to the exponential terms of J_D and the shunt resistance J_{RSh}, the dark current can be expressed as:[160]

$$J + J_{ph} = J_D + J_{Rsh} = \sum_{i=1}^{2} J_{Si}\left[\exp(A_i V_J) - 1\right] + \frac{V_J}{R_{Sh}} \tag{3.1}$$

Using equation 3.1, the experimental dark *J-V* characteristics shown in Figure 3.3b has been fitted using 2 diodes. Then for each sample, two ideality factor (n) and two saturation current (J_0) have been obtained. **Figure 3.4b** shows only the ZnO-based device for an example, the other samples show similar behavior. **Table 3.3** summarizes the extracted device performance parameters from the experimental and fitted *J-V* dark curves. From the fitting data at high forward *J-V* region ($V > 0.6$ V), it is shown that all samples are dominated by diode 1 (J_{01} in the range of pA cm^{-2}) under 1 sun condition (V_{OC} close to 0.8 V), however for indoor condition (V_{OC} close to 0.6 V), all samples are dominated by diode 2 (J_{02} in the range of nA cm^{-2}). We also noticed that PFN-based device has the highest J_0 values under outdoor conditions but the lowest J_0 values under indoor conditions, which is in good agreement with the measured efficiency values. To fit the medium forward *J-V* region at $0.2 < V\text{ (V)} < 0.6$, another diode with an ideality factor close to 2 can be defined. This is typical for trap assisted recombination processes. At the low forward dark *J-V* region ($0 < V\text{ (V)} < 0.2$), the *J-V* characteristics were fitted considering the shunt resistance effect. The R_{Sh} value of PFN-ETL device is one order magnitude lower than R_{Sh} values of the TiO_x- and ZnO-ETL devices. As a result, the PFN-based device has the highest leakage current. Hence, a high leakage current can dominate the photocurrent when the incident light intensity is low.[87,99,161] Although the PFN

ETL has the highest leakage current, the three types of the devices show leakage current below 10^{-3} mA cm^{-2}; this is still suitable for devices operating under typical indoor illumination, as reported by Lee *et al.*[87]

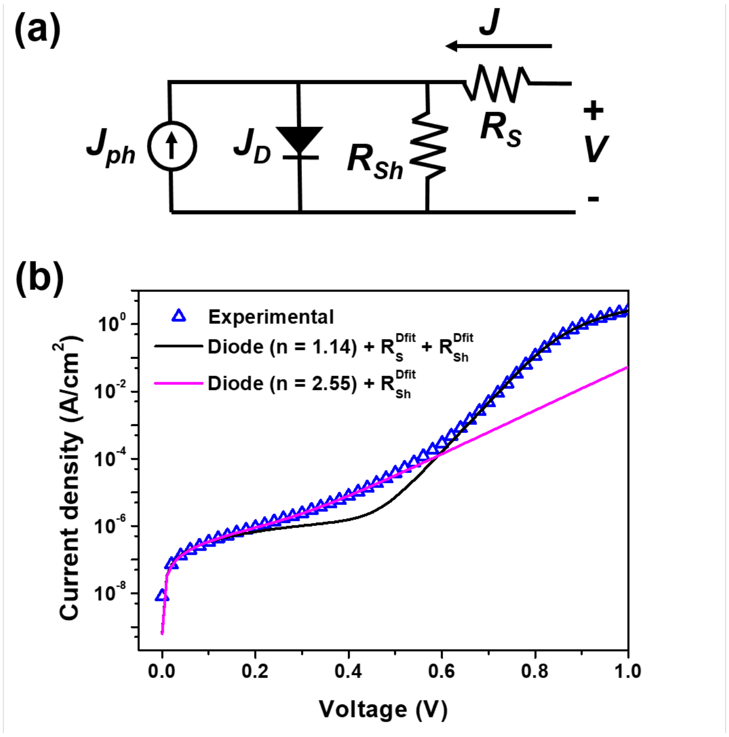

Figure 3.4 (a) Single-diode equivalent circuit model under dark (J_{ph} = 0) and illumination, (b) experimental (symbol), and modeled (line) *J*-*V* curves of ZnO-based device under darkness using a single diode equivalent model with two different ideality factor (*n*).

Table 3.3 Extracted device performance parameters from an experimental (D_{exp}) and a fitting (D_{fit}) model of *J*-*V* dark measurement (Figure 3.4b) for PFN-, TiO_x-, and ZnO-based devices.

Device parameters	PFN	TiO_x	ZnO
Rs^{Dexp} (Ω cm^2)	9.47	16.88	9.55
Rs^{Dfit} (Ω)	0.50	1.20	0.50
Rsh^{Dexp} (Ω cm^2)	1.24 x 10^5	4.28 x 10^6	4.03 x 10^6
Rsh^{Dfit} (Ω)	2.35 x 10^5	4.08 x 10^6	3.85 x 10^6
J_{01}^{Dfit} (A cm^{-2})	3.75 x 10^{-14}	1.28 x 10^{-14}	2.23 x 10^{-14}
n_1	1.16	1.11	1.14
J_{02}^{Dfit} (A cm^{-2})	3.80 x 10^{-7}	1.82 x 10^{-9}	1.35 x 10^{-9}
n_2	5.1	2.64	2.55

Figure 3.3c displays the external quantum efficiency (EQE) spectra of the iOPV with different ETL materials. All of the devices displays photoresponse spectrum in the range of 300 to 800 nm, which well matches with the absorption spectra of PTB7-Th:PC$_{70}$BM and AM 1.5G solar irradiation (**Figure 3.5**). The devices based on PFN-, TiO$_x$-, and ZnO-ETLs show photoresponses with maximum EQE values of 68%, 64%, and 59% at the wavelength of 485, 510, and 515 nm, respectively. Table 3.1 also shows the calculated J_{SC} values of the devices based on the PFN-, TiO$_x$-, and ZnO-ETLs obtained by integrating the EQE spectra in Figure 3.3c with the AM 1.5G solar spectrum are 16.00, 15.86, and 15.43 mA cm^{-2}, respectively, which are in good agreement to the measured values of *J-V* characteristics with the maximum error less than 8%.

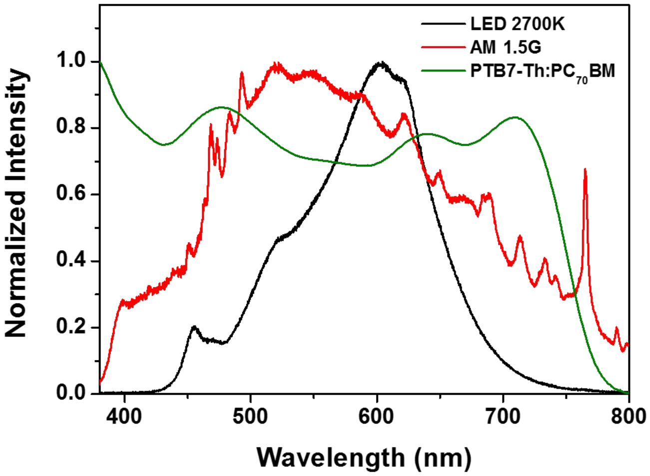

Figure 3.5 Absorption spectra of PTB7-Th:PC$_{70}$BM and light spectra of LED 2700K and AM 1.5G illumination.

3.2.2 Device performance under artificial indoor light

Figure 3.5 also presents the normalized absorption spectra of PTB7-Th:PC$_{70}$BM along with 1 sun illumination (AM 1.5G, 100 mW cm^{-2}) in comparison with the illumination spectrum of LED 2700K light source in the wavelength range of 400 – 800 nm. With the optical band gap of 1.37 eV,[139] their optical response nicely cover the entire LED emission, which could be better suited for indoor application. **Figure 3.6** displays the *J-V* characteristics for the best performing devices with the different ETLs under 1000 lux LED illumination (measured light power irradiance: 0.415 mW cm^{-2}). In this work, the devices were investigated under a 2700K LED lamp with the luminance of 250 – 2000 lux, which are corresponding to the intensity of the indoor lighting sources that typically in the ranges of < 1 mW cm^{-2}.[16,92,132] LED light was employed due to its low power consumption as a versatile light source; it is expected to become widespread for residential and office use.[162] Moreover, LED light offers a deduction of up to 58.4% of the Shockley-Queisser limit on photovoltaic performance.[96,100]

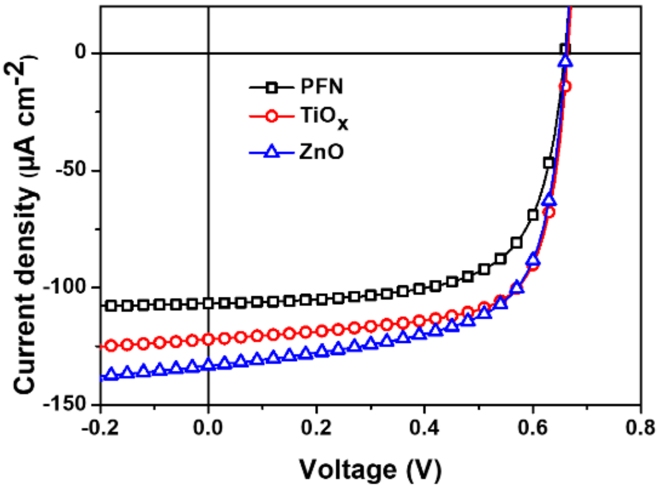

Figure 3.6 *J-V* characteristics of different ETLs measured under a 1000 lux LED light with a color temperature of 2700 K.

We tested the best devices with each ETL under 1 sun conditions to determine their indoor performance under a 2700 K LED lamp. **Table 3.4** shows that unlike the outdoor performance, the ZnO-based device exhibits the best performance among the three ETLs under the luminance of 1000 lux LED light, with a PCE of 13.94%, a J_{SC} of 133.31 µA cm^{-2}, a V_{OC} of 0.66 V, an *FF* of 65.83%, an R_S of 1.94 Ω cm^2, and an R_{Sh} of 40.94 kΩ cm^2. The TiO$_x$-based iOPV shows a slightly decrease indoor performance with a PCE of 13.83%, a J_{SC} of 122.10 µA cm^{-2}, a V_{OC} of 0.66 V, a *FF*

Table 3.4 Device performance parameters for the best OPV cells with each ETLs (PFN, TiOx, and ZnO) measured under different lux intensities of a 2700 K LED.

ETL	**Lux**	J_{SC} **(mA cm^{-2})**	V_{OC} **(V)**	**FF (%)**	P_{in} **(mW cm^{-2})**	P_{out} **(mW cm^{-2})**	**PCE (%)**	R_S **(Ω cm^2)**	R_{Sh} **(Ω cm^2)**
PFN	250	27.52	0.56	50.92	120	7.87	6.56	2.75	160.49
	500	53.3	0.63	62.63	215	21.07	9.8	2.14	244.67
	750	82.33	0.65	65.23	315	34.97	11.1	1.95	183
	1000	**107**	**0.66**	**67.13**	**415**	**47.31**	**11.4**	**1.85**	**158**
	1250	134.79	0.67	68.76	520	62.14	11.95	1.84	133.56
	1500	166.37	0.68	69.65	620	78.86	12.72	1.76	116.79
	1750	212.43	0.69	70.56	725	103.48	14.27	1.69	94.96
	2000	214.67	0.69	70.70	825	104.78	12.7	1.69	93.24
TiOx	250	31.88	0.62	64.64	120	12.78	10.65	4	134.64
	500	62.57	0.64	68.73	215	27.52	12.8	3.66	93.74
	750	95.35	0.66	69.94	315	44.1	13.97	3.34	75.28
	1000	**122.1**	**0.66**	**71.21**	**415**	**57.39**	**13.83**	**3.31**	**63.21**
	1250	149.86	0.68	72.44	520	73.84	14.2	3.18	72.87
	1500	183.08	0.68	73.82	620	91.88	14.82	3.17	66.87
	1750	232.51	0.69	74.16	725	118.97	16.41	3.06	59.57
	2000	242.9	0.69	74.44	825	124.74	15.12	3.05	58.89
ZnO	250	33.81	0.61	59.55	120	12.29	10.24	2.45	100.6
	500	69.63	0.64	63.13	215	28.12	13.08	2.15	63.62
	750	104.06	0.65	65.78	315	44.38	14.09	2.05	48.95
	1000	**133.31**	**0.66**	**65.83**	**415**	**57.85**	**13.94**	**1.94**	**40.94**
	1250	163.6	0.67	67.83	520	74.36	14.3	1.94	38.41
	1500	198.11	0.68	68.21	620	91.88	14.82	1.87	34.15
	1750	251.53	0.69	68.90	725	119.55	16.49	1.8	29.49
	2000	247.42	0.69	68.83	825	117.56	14.25	1.79	29.93

of 71.21%, an R_S of 3.31 Ω cm^2, and an R_{Sh} of 63.21 kΩ cm^2. Unexpectedly, PFN-based device, which showed the highest performance under outdoor illumination, exhibited the lowest performance under indoor illumination, with a PCE of 11.40%, a J_{SC} of 107 µA cm^{-2}, a V_{OC} of 0.66 V, a FF of 67.13%, an R_S of 1.85 Ω cm^2 and an R_{Sh} of 158 kΩ cm^2. For the indoor illumination with different lux intensities ranging from 250 to 2000 lux, it can be observed that all of the devices possess varying values of V_{OC}, J_{SC}, FF, R_S, and R_{Sh} for different ETLs used, indicating that indoor

performance shows a dependency on the choice of ETLs.

Figure 3.7a-b show the power-law dependence of J_{SC} and V_{OC} values on the incident light intensity (P_{light}), which can give recombination information within the devices. As displayed in Figure 3.7a, the values of J_{SC} is proportional to the light intensity according to the relationship $J_{SC} \propto P_{light}^{S1}$, where $S1$ is the determined exponential factor. The fitted $S1$ value for the PFN-, TiO_x-, and ZnO-based devices were 0.95, 0.94, and 0.92, respectively, under solar irradiation at strong light intensities (> 10 mW cm^{-2}) and they both increased up to unity when exposed to LED light at weak light intensities (< 1 mW cm^{-2}). The $S1$ values close to unity (i.e., $S1 \approx 1$) for devices illuminated under both indoor and 1 sun conditions suggest the low levels of the non-geminate charge recombination and limited space charge effects due to the low photogenerated carrier density in these OPVs under LED and 1 sun lighting conditions.[163] In another word, it can be inferred that the ratio of photons to electrons remained constant with decreasing light intensity.[86] It is worth noting that J_{SC} of ZnO-based devices under indoor performance showed the highest J_{SC} due to the higher transmission of ZnO ETL in the LED spectra wavelength which allowing maximum photon flux of LED emission absorbed by the active layer to generate more photocurrent. This result is in good agreement with the transmission spectra analysis (*vide supra*) and its high output power density (P_{out}) of 57.85 μW cm^{-2}.

The V_{OC} is a key parameter to gain more insight into the recombination kinetics. Figure 3.7b shows the logarithmic dependence of the V_{OC} values upon the light intensity for illumination under 1 sun and LED light, which can be expressed using the equation derived from the Shockley diode equation below:

$$V_{OC} \propto S2\frac{k_B T}{q}\ln\left(P_{opt}\right) \propto n\frac{k_B T}{q}\ln\left(J_{SC}\right) \tag{3.2}$$

where n is the recombination ideality factor of the diode ($n=S2/S1$), k_B is the Boltzmann constant, T is the cell temperature, and q is the electron charge. As shown in Figure 3.7b, the obtained $S2$ values of 1.12, 1.00, and 1.09 lead to the obtained n

values of 1.18, 1.05, and 1.18, for devices with PFN, TiO_x, and ZnO under 1 sun illumination (> 10 mW cm^{-2}), respectively. These values are close to 1 and similar to the ones obtained from the dark fitting model (see Table S2), indicating that these devices may act as an ideal diode under 1 sun due to the absence of trap-assisted recombination. Besides, the *S2* values of 1.99, 1.44, and 1.55 lead to the *n* values of 1.83, 1.40, and 1.49 for the PFN-, TiO_x-, and ZnO-based devices under indoor illumination (< 1 mW cm^{-2}), respectively. These fitted slopes under indoor illumination are higher than those under 1 sun illumination, indicating the trap-assisted recombination enhance under indoor light intensity.[132] This trend is coherent with the presence of the second exponential region at medium-dark bias, as stated before. Thus, the photovoltage loss of ~0.2 V is observed due to the significantly reduced the light intensity and enhance the trap-mediated charge recombination.[88]

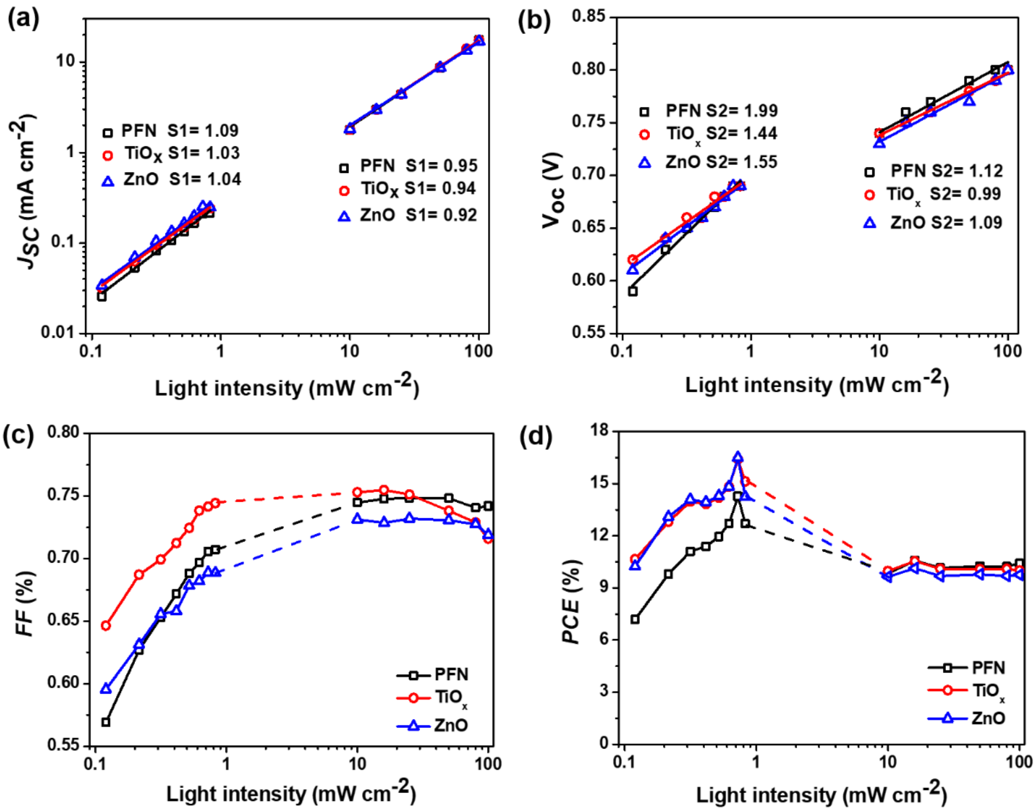

Figure 3.7 Device performance parameters: (a) J_{SC}, (b) V_{OC}, (c) FF, and (d) PCE of the best OPV cells with each ETL *versus* light intensity. The dotted lines are given to guide the eye.

The result obtained from the V_{OC} vs. light intensity corroborates the dark J-V experiment and modeling results (Figure 3.3b, Figure 3.4 and Table 3.3) in which the current density of the diode (J_D) for all ETLs shows the same exponential dependency on the applied voltage at $V_{OC} \approx 0.8$ V, and it shows a leakage region at $V_{OC} \approx 0.6$ V. It is worth noting that at low illumination level, the PFN-based device has the highest leakage current and n value closes to 2 than the other two ETLs. As a result, the overall current within the device could be dominated by leakage current and the trap-assisted recombination process may enhance. This may explain why PFN ETLs perform opposingly and show poor device performance under artificial light conditions.

As shown in **Figure 3.7c**, the influence of leakage current may appear in the dependence of *FF* on incident light intensity. When the light intensity strengthens from 10 to 100 mW cm^{-2} (under simulated solar irradiation), the *FF* appears steady and then shows a decreasing trend. The decrease of *FF* as light intensity increase can result from two origins, that are bimolecular recombination and series resistance.[42,164] Based on J_{SC} vs. incident light intensity fitting, see Figure 3.7a, slopes of ≈1 for all ETLs are observed, indicating the suppressed bimolecular recombination. Thus, bimolecular recombination may not play a significant role in the *FF* decreasing trend at the strong light intensity within these devices. From the J-V dark measurement, Figure 3.3b, TiO_x ETL exhibits the highest R_S values, which can explain the sharp decrease of *FF* for TiO_x compare to the other two ETLs, as shown in Figure 3.7c. Thus, probably the series resistance has an influence for the decreased *FF* at the strong light intensity (>10 mW cm^{-2}) for these iOPVs. On the other side, the reverse trend at the weak light intensity (<1 mW cm^{-2}, under LED 2700K illumination) is observed. The low light intensity in which *FF* decreases is determined by the shunt resistance.[132,164] As shown in Table S3, PFN ETL has the lowest R_{Sh} value, which may explain a steeper *FF* decay at weak light intensity than TiO_x- and ZnO-ETLs based devices.

This *FF* behavior depending on the ETLs type under indoor illumination, can also be explained within the context of a single diode-based equivalent circuit model (Figure 3.4a). The expression to calculate *FF* $((J_{max} \text{ x } V_{max})/(J_{SC} \text{ x } V_{OC})$ can be defined using the normalized R_S ($r_s = R_S \text{ x } (J_{SC}/V_{OC})$), normalized R_{Sh} ($r_{sh} = R_{Sh} \text{ x } (J_{SC}/V_{OC})$), and normalized V_{OC} ($v_{OC} = eV_{OC}/nkT$), where the characteristic resistance (R_{CH}) is defined as $R_{CH} = V_{OC}/(J_{SC}\text{A})$. When $R_S = 0$ and $R_{Sh} = \infty$, the ideal *FF* of OPVs can be expressed as follows:

$$FF_O = \frac{v_{oc} - \ln\left(v_{oc} + 0.72\right)}{v_{oc} + 1} \qquad (3.3)$$

As shown in **Table 3.5**, the calculated *FFo* is higher than those of the experimental *FF* values for all of the samples under both outdoor and indoor conditions. Put PFN-iOPV under 1 sun as an example; the V_{OC} is about 0.79 V, then the normalized v_{OC} is 28.07. According to equation 3.3, the calculated *FFo* is 83.01%, while the experimental *FF* value of PFN under 1 sun is 75.00%. The difference between the experimental value and the calculated value from an ideal solar cell model suggests that there should be other losses in the practical OPVs.[143]

Table 3.5 Parameters used to predict the FF for all device structures manufactured.

ETL	Illuminance	r_S	r_{Sh}	v_{OC}	FF_{RS}	FF_0	FF_{Rs+Rsh}
PFN	1 sun	0.0196	28.0747	23.6883	0.8139	0.8301	0.7903
TiOx	1 sun	0.0359	26.1514	21.1954	0.7865	0.8159	0.7629
ZnO	1 sun	0.0182	24.9295	23.8732	0.8159	0.8310	0.7892
PFN	1000 lux	0.0003	26.1015	12.8291	0.7390	0.7392	0.7181
TiO_x	1000 lux	0.0006	11.6980	17.7278	0.7905	0.7910	0.7371
ZnO	1000 lux	0.0004	8.2491	16.4696	0.7796	0.7799	0.7060

In the real case of OPVs, parasitic resistances are inevitable factors. Thus, the effects of R_S and R_{Sh} are introduced to the equivalent circuit model to consider these energy losses.[143] A semi-empirical and approximated expression for *FF* incorporating the effects of R_S and R_{Sh} are shown as follow:

$$FF_{R_S+R_{Sh}} = FF_{R_S}\left[1-\frac{v_{oc}+0.7}{v_{oc}}\times\frac{FF_{R_S}}{r_{Sh}}\right] \tag{3.4}$$

where FF_{Rs} is the fill factor influenced by series resistance. The calculated fill factor values from Equation 3 are summarized in Table 3.5 and **Figure 3.8**. It can be seen that the experimental (*FF*) and predicted values (FF_{Rs+Rsh}) have the same trend, indicating that *FF* within these devices were influenced by parasitic resistance effects due to the type ETL used. In the case of device performance for all devices, the R_{CH} values under LED lamp were larger than those under AM 1.5G illumination. It is due to the J_{SC} values decrease by two orders magnitude under LED lamp. Moreover, the values of R_S (in ideal OPVs, $R_S = 0$) were theoretically small compare to the values of R_{Sh} (in ideal OPVs, $R_{Sh} = \infty$). For this reason, the calculated r_s values (< 0.01) appeared to be too negligible to give an influence on the indoor performance, while the effects of r_{sh} were more significant to reduce *FF* under dim light condition. In this case, the PFN-based device has the highest r_{sh} value under indoor illumination, which is expected to increase *FF* and PCE. However, its low FF_0 value derived from the lowest value of normalized V_{OC} (v_{oc}), leads the PCE to decrease more sharply than the other two ETLs, see **Figure 3.7d**. This low v_{oc} is associated with the presence of trap-assisted recombination in PFN-iOPVs due to their ideality factor (*n*) value close to 2 (Figure 3.7b).

The presence of the trap-assisted recombination in PFN is coherent with the alignment of the work function (WF), as shown in Table 3.6. A larger energy mismatch between the WF of PFN (4.08 eV) and LUMO of the PC$_{70}$BM (4.30 eV) which induces a higher level of recombination and limits the electron selectivity at the interface, leading to lower *FF* and PCE.[139,162] Interestingly, ZnO-iOPVs have the lowest *FF*, the highest PCE and the highest max output power (P_{max}) under LED light. Their high performance under indoor illumination was mainly affected by the photon absorption yield (the highest photocurrent generated), which is in good agreement with AFM and transmittance optical analysis (Figure 3.2).

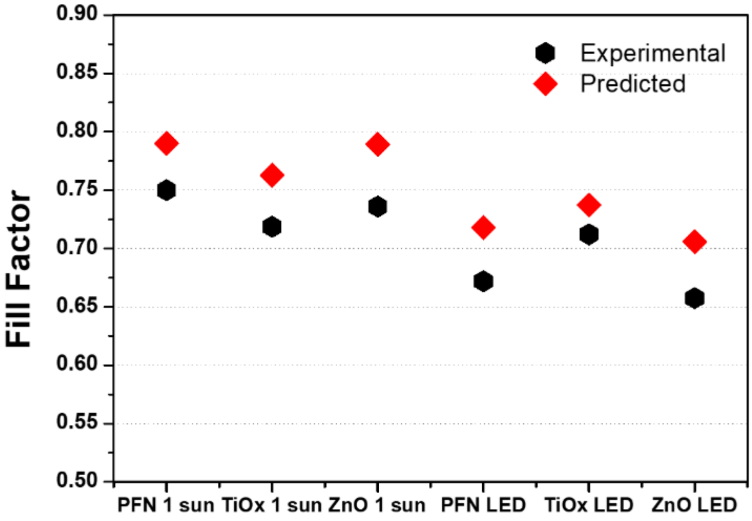

Figure 3.8 Experimental and predicted fill factor values for each ETL of the PTB7-Th:$PC_{70}BM$-based devices under AM 1.5G and 1000 lux 2700 K LED illumination.

Table 3.6 Parameters used to predict the FF for all device structures manufactured.

Layers	WF (eV)	Contact type
ITO	4.45 [139]	Schottky contact
ITO/PFN	4.08 [139]	Ohmic contact
ITO/TiO_x	4.25 [165]	Ohmic contact
ITO/ZnO	4.20 [166]	Ohmic contact

The electron affinity (EA) of the acceptor $PC_{70}BM$ is 4.3 eV. It can be seen that all of ETL had lower work function values than the EA of the acceptor. It indicates that a desirable Ohmic contact between $PC_{70}BM$ and the ITO electrode is formed, facilitating an efficient electron transport and collection.[167] The WF of metal oxide ETLs (TiO_x and ZnO) is altered due to the UV-induced oxygen adsorption/desorption processes in the metal oxide ETLs.[168] Meanwhile, the organic ETLs (PFN) can effectively reduce the work function of bare ITO by forming a permanent dipole on the ITO surfaces in an inverted OPV.[167]

To gain more insight into the effect of the different ETL materials on charge transport properties under outdoor and indoor performances, impedance spectroscopy (IS) measurements were performed at open-circuit voltage. IS is an effective tool to gain information about carrier accumulation at open circuits, rapid extraction at short circuits, and carrier transport mechanism within each layer of the organic photovoltaic.[169,170] **Figure 3.9a-b** display the Cole-Cole plots of the impedance spectra for PFN, TiO_x, and ZnO as ETL taken near V_{OC} under AM 1.5G and LED 2700K illumination, respectively. All plots under outdoor or indoor illumination show typical arc behavior for all applied voltages, which is correlated with the carrier transfer at the active layer/electrode interface.[163,169] The observed radius of the semicircles varies with altering ETLs, both under 1 sun and LED illumination, which usually associated with different charge injection or charge extraction process within these devices.[170] To understand this behavior, we have fitted the experimental data with the equivalent circuit model shown in **Figure 3.10**, which consists of one series resistance connected to three resistor capacitance ladder (RC) in series. The series resistance takes into account the ITO layer. Each element of the 3RC circuit is correlated to the capacitance and resistance of ETL, the bulk active layer, and the hole transport layer (HTL). Using the proposed electrical equivalent circuit to fit the experimental impedance spectroscopy data, we were able to observe a different behavior for outdoor and indoor performance. Moreover, we are also able to identify the impact of each interlayer on device performance.[171] The calculated geometrical capacitance values of each layer are displayed in **Table 3.7**, which can be described by equation 3.5:

$$C = \varepsilon_0 \varepsilon_{layer} \frac{A}{d_{layer}} \qquad (3.5)$$

where ε_0 is the vacuum dielectric permittivity, the ε_{layer} is the relative dielectric permittivities (ε_{bulk}, ε_{ETL}, and ε_{V2O5}), d_{layer} is the thickness of each layer (d_{bulk}, d_{ETL}, and d_{V2O5}) and A is the active area. The different expected capacitance values for each layer allows us to assume the correlation between each layer-RC ladder.

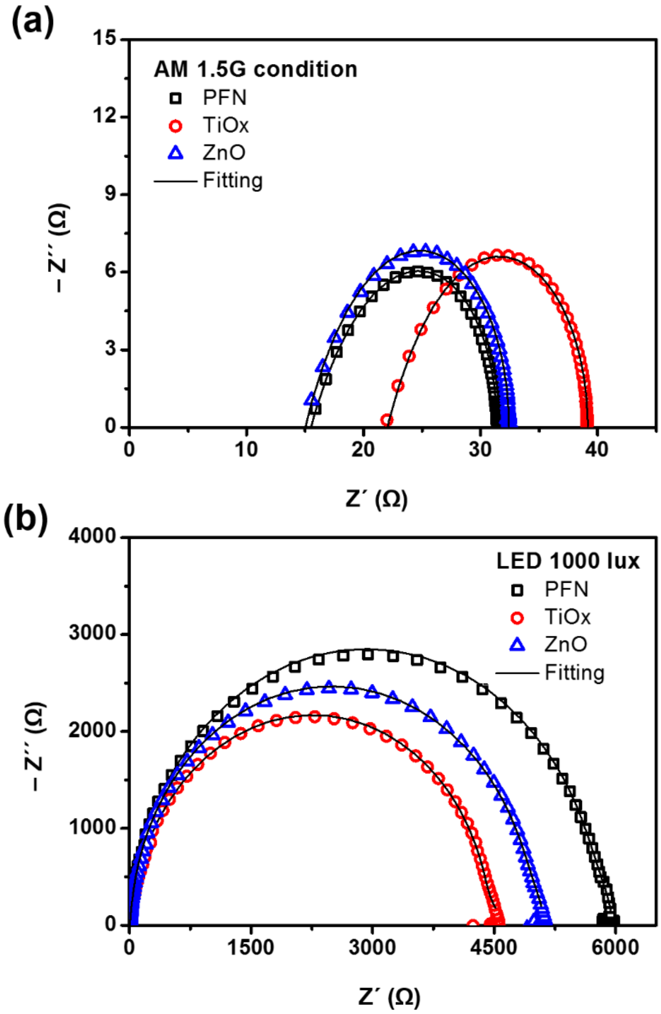

Figure 3.9 Cole-Cole plots of PTB7-Th:PC$_{70}$BM-based iOPVs using PFN, TiOx, and ZnO as the ETL, measured under 1 Sun condition (a) and indoor illumination (b) at open-circuit voltage. The solid lines are the fitted experimental data using the three-RC circuit model.

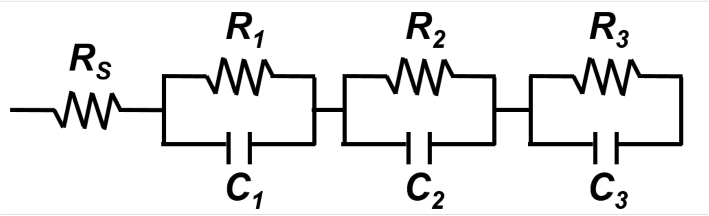

Figure 3.10 The schematic illustration of three resistor capacitance equivalent circuit model used for the fitting of impedance spectra.

Table 3.7 Parameters used to predict the FF for all device structures manufactured.

Layer	ε_{layer}	d_{layer} (nm)	Capacitance (nF)
Bulk	3.9 [163]	100	3
V_2O_5	5 [172]	5	78
PFN	3.5 [173]	10	28
TiO_x	50 [170]	15	200
ZnO	4 [163]	15	21

Table 3.8 Capacitance and resistance values of each layer for different ETLs used under AM 1.5G illumination. The values were extracted by modeling the IS measurements at open-circuit voltage.

ETL	Layer	Capacitance (nF)	Resistance (Ω)
PFN	R_s	-	4
	PFN	28	10
	Bulk	5	6
	V_2O_5	78	11
TiO_x	R_s	-	8
	TiO_x	200	3
	Bulk	4	16
	V_2O_5	75	12
ZnO	R_s	-	10
	ZnO	21	15
	Bulk	3	1
	V_2O_5	74	6

On one hand, the outdoor fitting values do not show a dominant RC ladder for applied voltages close to open-circuit conditions, as displayed in **Table 3.8**. The measurement is strongly affected by the ITO series resistance. Thus, the low resistance values signify the smooth charge transport at the interface between each layer.[104] On the other hand, the indoor fitting values are mainly due to the bulk RC ladder because the resistance of the bulk is orders of magnitude higher than the others resistances used for the fitting, see **Table 3.9**. As shown in **Figure 3.11**, the bulk resistance values decrease exponentially with the applied voltage. This is typical for

Table 3.9 Capacitance and resistance values of each layer of different ETLs under 1000 lux LED illumination. The values were extracted by modeling the IS measurements at various applied voltages.

ETL	**Layer**	**V_{bias} = 0V**		**V_{bias} = 0.2V**		**V_{bias} = 0.4V**		**V_{bias} = V_{OC}**		**V_{bias} = 0.8V**	
		C (nF)	**R (Ω)**	**C (nF)**	**R (Ω)**	**C (nF)**	**R (Ω)**	**C (nF)**	**R (Ω)**	**C (nF)**	**R (Ω)**
PFN	R_s	-	4	-	4	-	4	-	8	-	9
	PFN	28	2	28	2	28	3	28	10	28	11
	Bulk	3.3	1 x 10^6	3.5	4.4 x 10^5	4.0	1.03 x 10^5	5.0	5700	7.5	440
	V_2O_5	80	150	80	150	80	100	80	70	80	90
TiO_x	R_s	-	14	-	12	-	14	-	15	-	15
	TiO_x	266	2	266	1	266	3	266	10	266	10
	Bulk	3.0	3.7 x 10^5	3.2	3.0 x 10^5	3.5	1.2 x 10^5	4.5	4450	6.0	500
	V_2O_5	78	200	78	200	78	130	78	10	78	10
ZnO	R_s	-	4	-	4	-	4	-	5	-	8
	ZnO	21	2	21	3	21	3	21	7	21	12
	Bulk	3.5	5.4 x 10^5	3.5	4.2 x 10^5	4.0	1.5 x 10^5	4.5	4900	6.0	470
	V_2O_5	80	130	80	150	80	130	80	60	80	65

the recombination resistance:[174]

$$R_{rec} = \left(\frac{\partial J_{rec}}{\partial V}\right)^{-1} = R_{00} \exp\left(-\frac{qV}{nk_B T}\right) \tag{3.5}$$

where R_{00} is the pre-exponential factor, and the other parameters are the same as in equation 3.2. As expected from recombination resistance, the slope is related to the ideality factor, n. From the fitting, a similar value close to 2.5 were obtained for all the samples, with is in good agreement with the ideality factors values obtained not only in dark current density-voltage (exponential region for medium voltage bias) but also incident light intensity-V_{OC} measurements. In all the analysis, the results can be explained when we assume that the currents are limited by trap-assisted recombination for indoor illumination conditions. In addition, the charge collection efficiency (CCE)[174] can be defined following equation 3.6:

$$CCE \approx 1 - \frac{R_{rec(OC)}}{R_{rec(NOC)}} \tag{3.6}$$

where R_{rec} is the recombination resistance in open circuit (OC) or non-open circuit (NOC) conditions used in equation 3.5. As shown in Figure 3.12, the values obtained from CCE at the maximum power bias point, V_m ~ 0,4 V, follows the same trend as the indoor PCE (CCE_{ZnO} = 96.7% > CCE_{TiOx} = 96.1% > CCE_{PFN} = 94.5%).

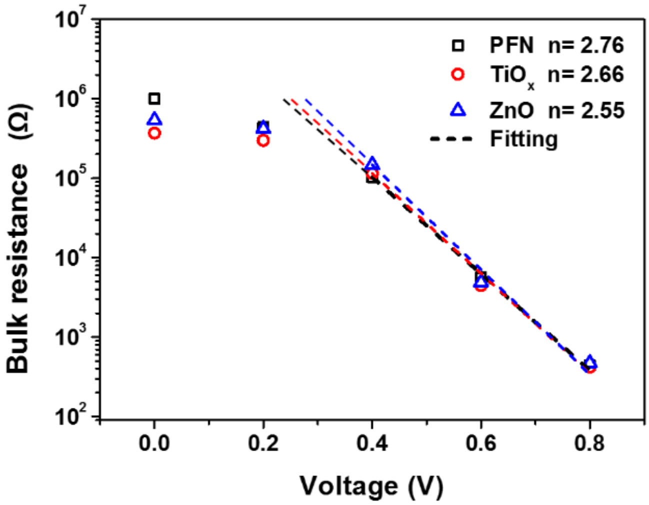

Figure 3.11 The bulk resistance obtained from IS measurements of each layer *vs.* the applied voltage measured under 1000 lux LED illumination.

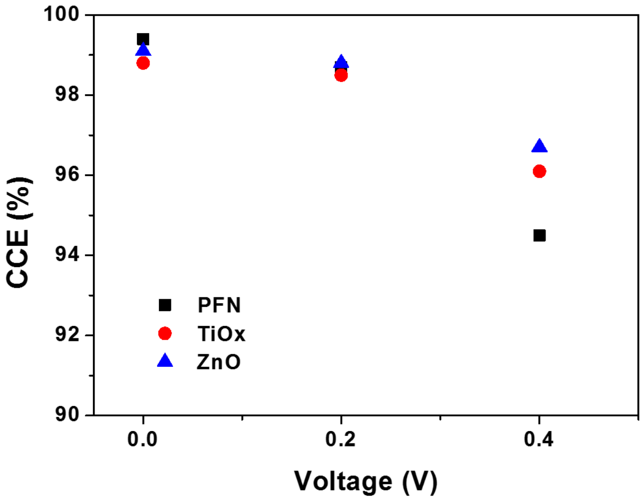

Figure 3.12 The charge carrier extraction of the PFN-, TiOx-, and ZnO-ETL iOPV obtained from IS measurement at applied voltage measured under 1000 lux LED illumination.

3.3 Photostability study under outdoor and artificial indoor light illumination

Beside the device performance investigation, we further study the photostability lifetime and degradation behavior of the best indoor cell under continuous illumination of two different light sources, standard reference AM 1.5G (100 mW cm^{-2}) and 1000 lux LED 2700 K lamp (0.35 mW cm^{-2}) in inert atmosphere. **Figure 3.13** shows the illuminated *J-V* characteristics of the studied devices before and after the photo-aging test. It can be observed that the *J-V* curve for the degraded cell under AM 1.5G illumination (**Figure 3.13a**) was shifted to lower V_{OC}, while the degraded cell under LED illumination (**Figure 3.1b**) shows a more pronounced shift to the lower J_{SC} with respect to the fresh cells. More detailed photovoltaic parameters values are summarized in **Table 3.10**, where all numbers represent the average and standard deviation values from four cells in each group. The dark *J-V* characteristics of these devices are displayed in **Figure 3.14** and **Table 3.11**.

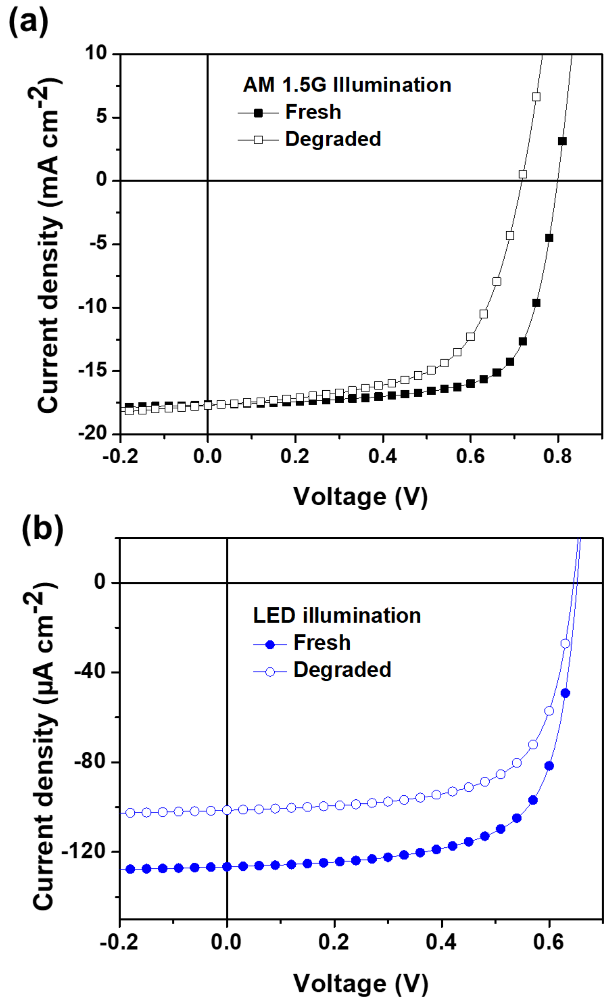

Figure 3.13 Illuminated *J-V* characteristics of fresh (solid symbol) and degraded (open symbol) cells exposed under (a) AM 1.5G and (b) 1000 lux LED 2700 K irradiation. The light intensity of AM 1.5G spectrum is 100 mW cm^{-2} and 1000 lux LED 2700 K spectrum is 0.35 mW cm^{-2}.

Table 3.10 Photovoltaic parameters of PTB7-Th:PC$_{70}$BM–based solar cells just after fabrication under different light sources illumination.

Light sources	V_{OC} **(V)**	**J$_{SC}$ (mA cm^{-2})**	**FF (%)**	**PCE (%)**	**Standard lifetime**
AM 1.5G T_0	0.79 ± 0.01	17.13 ± 0.40	71.40 ± 0.42	9.64 ± 0.20	-
AM 1.5G T_{80}	0.72 ± 0.01	17.88 ± 0.35	59.74 ± 3.03	7.70 ± 0.52	260 min
LED 1000 lux T_0	0.65 ± 0.01	0.13 ± 0.01	65.60 ± 2.94	15.70 ± 0.40	-
LED 1000 lux T_{80}	0.65 ± 0.01	0.10 ± 0.01	66.59 ± 0.47	12.53 ± 0.34	3060 min

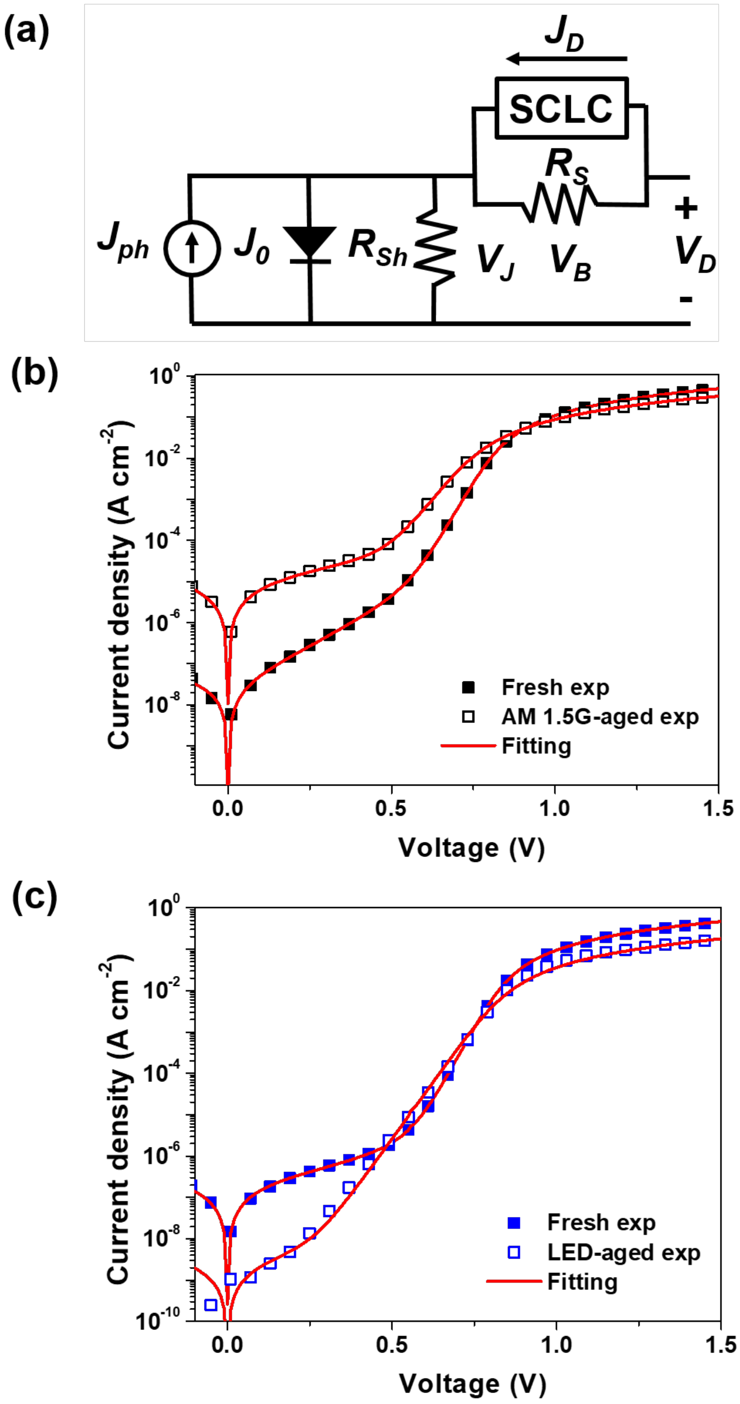

Figure 3.14 (a) Single-diode equivalent circuit model under dark ($J_{ph} = 0$) and illumination. Experimental (symbol) and modeled (line) *J-V* curves of (b) the fresh and AM 1.5G-aged PSCs and (c) the fresh and LED-aged OPVs under darkness using a single diode equivalent model with two different ideality factor (n).

Table 3.11 Extracted device performance parameters from an experimental (D_{exp}) and a fitting (D_{fit}) model of *J-V* dark measurement (Figure 3.4b) for PFN-, TiO_x-, and ZnO-based devices.

Device parameters	**Fresh AM1.5G**	**Degraded AM1.5G**	**Fresh LED 1000 lux**	**Degraded LED 1000 lux**
R_S^{Dexp} (Ω cm^2)	2.1	3.1	2.2	5.8
R_S^{Dfit} (Ω)	1.2	2.2	1.3	3.5
R_{Sh}^{Dexp} (Ω cm^2)	2.5 x 10^6	1.54 x 10^4	6.6 x 10^5	1.2 x 10^8
R_{Sh}^{Dfit} (Ω)	4.6 x 10^6	1.7 x 10^4	7.3 x 10^5	5.2 x 10^7
J_0^{Dfit} (A cm^{-2})	9.2 x 10^{-14}	2.9 x 10^{-10}	1.4 x 10^{-14}	8.3 x 10^{-12}
n	1.2	1.6	1.2	1.5
k_{SCLC} (A cm^{-2})	15	11	15	16
m_{SCLC}	2	2	2	2

In the meantime, by using an equivalent circuit model shown in **Figure 3.14a**, the total current J_D can be divided into two terms as the bulk voltage drop due to the parallel combination of the series resistance and the SCLC term, as follow

$$J_D = J_{RS} + J_{SCLC} = \frac{V_B}{R_S} + V_B^m \tag{3.7}$$

Using equation 3.1 and equation 3.7, the experimental dark *J-V* characteristics shown in **Figure 3.14b** had been fitted using a single diode. Then for each sample, the *n*, J_0, and SCLC parameters (k and m) have been obtained, as shown in **Table 3.11**.

In agreement with the device performance study in section 3.1 and 3.2, a max PCE of the fresh device under 1 sun illumination was 10% with the average PCE of 9.64%, a V_{OC} of 0.79 V, a J_{SC} of 17.13 mA cm^{-2}, and a FF of 71.4%. On the other hand, the fresh cells illuminated under LED light have a PCE about 1.6 times higher than that of 1 sun-illuminated cells, showing the highest PCE of 16.19% with an average PCE of 15.7%, a V_{OC} of 0.65 V, a J_{SC} of 0.13 mA cm^{-2}, and an FF of 65.6%. The PCE enhancement of the PSCs cells illuminated under LED light is in good agreement with the related studies using PTB7-Th:$PC_{70}BM$ as the photoactive materials.[16,103,175] It may be due to the well-match between the absorption photoactive spectra of OPVs with the emission spectra of the LED spectrum.

To investigate the effect of different light source illumination on the photodegradation mechanism of the studied devices, the photo-aging test was conducted in an inert atmosphere (<0.1 ppm O_2 and <0.1 ppm H_2O) under continuous illumination of standard 1 sun and 1000 lux LED light. In an inert environment, the degradation due to ambient moisture and oxygen can be avoided, giving a less significant effect on the studied photostability mechanism. **Figure 3.15** shows the performance parameters of the devices: PCE, J_{SC}, V_{OC}, and FF over the aging time, normalized to their initial values. Following the ISOS-L-1 and low light measurement protocols, the device lifetimes are listed in **Table 3.12**. The photo-aging test was carried out until the PCE of the cells decays 20% from its initial value, known as E_{80}, T_{80}. The initial PCE (E_0) and the times T_{95}, T_{90}, and T_{85} defined in the protocols[137] are also shown in the table. After reaching T_{80}, we found that the

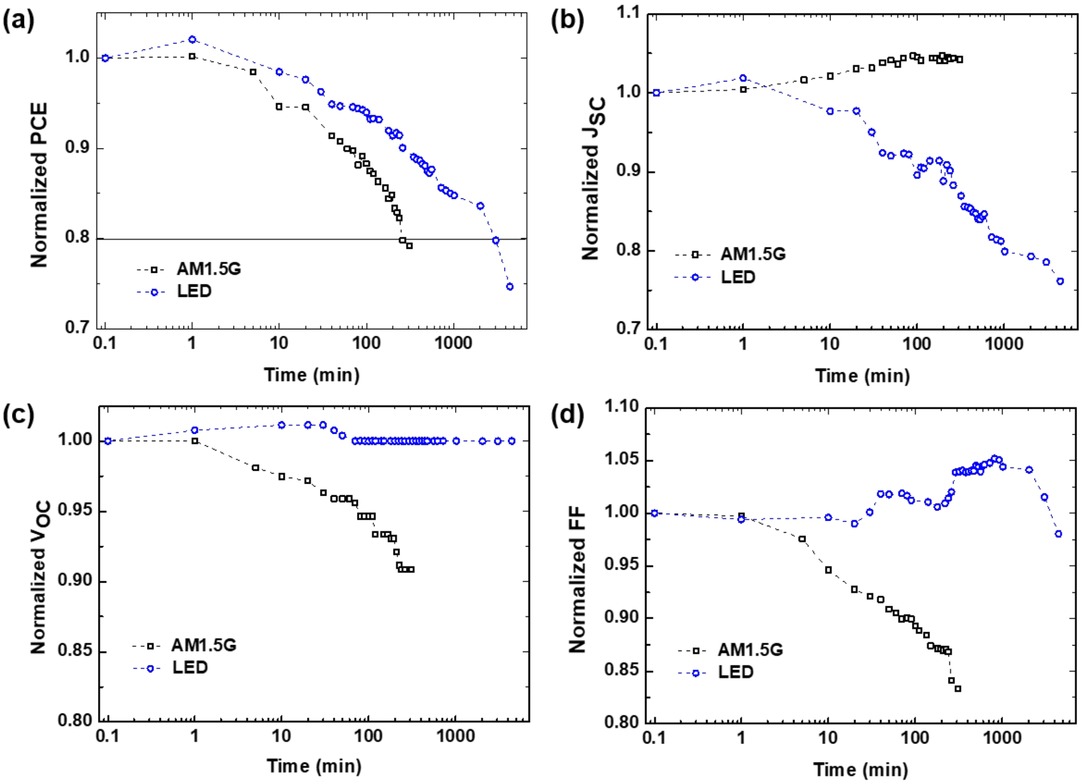

Figure 3.15 Normalized device performance parameters (a) PCE, (b) J_{SC}, (c) V_{OC}, and (d) FF of inverted PTB7-Th:$PC_{70}BM$-based device under two light sources exposure: AM 1.5G solar simulator (black squares) and 1000 lux LED lamp (blue circle).

Table 3.12 Summary of photostability lifetime of the fabricated cells degraded under AM 1.5G and 1000 lux LED light illumination.

Standard lifetime	AM 1.5G	LED 1000 lux
E_0, T_0 (PCE, %)	9.98	16.19
T_{95} (min)	3001	40
T_{90} (min)	60	260
T_{85} (min)	180	1020
T_{80} (min)	260	3060

lifetimes of the cells aged under LED illumination are almost 12 times longer than under AM 1.5G solar simulator. It indicates a vivid effect of different light source illumination on the photodegradation pathways of PSCs.

As presented in **Figure 3.15a**, the PCEs for all cells decrease exponentially over the degradation time. The PCE of LED-aged cells dropped 20% after 3,060 min of continuous illumination, while those of 1 sun-aged cell reaches its T_{80} only in 260 min. Rapid decay of all of the studied OPVs devices in the first few minutes are observed in **Figure 3.16**. This phenomenon is often reported as a "burn-in loss" degradation mechanism due to the photochemical reaction within the device layers and the presence of processing additive 1,8-diiodooctane as photo-acid.[176–178]

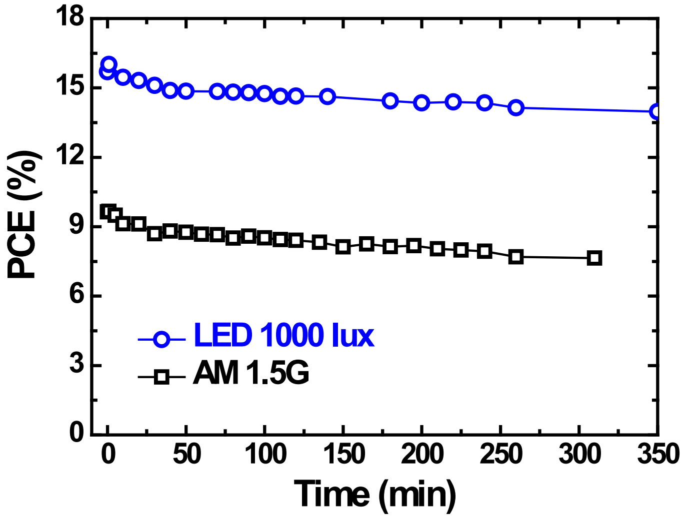

Figure 3.16 Burn in loss observed in a few minutes of the aging test.

Figure 3.15b presents the normalized J_{SC} values for two different light sources photo-aging over the degradation time. At T_{80}, the devices illuminated under AM 1.5G solar simulator show an increasing J_{SC} 4% higher in respect of its initial value. That increment may arrive from the UV-irradiation dependence, known as light-soaking effect, when the UV components from the solar simulator spectrum irradiate the cells. The light-soaking phenomenon in inverted PSCs employing TiOx or the other metal-oxides materials as ETL has been widely observed.[179] It may originate from the photoinduced rearrangement of the Fermi levels at indium tin oxide/TiOx interface, as reported elsewhere.[165,180] On the contrary, the J_{SC} of LED-aged cells fell 21% at T_{80}. The J_{SC} decay under LED illumination originates from the absence of UV components in the LED spectrum. This behavior correlates well with the PCE behavior over the photo-aging time.

The normalized V_{OC} over the photo-aging time is presented in **Figure 3.15c**. The sun-aged cells show decreased values of around 10% after they reached T_{80}. V_{OC} losses may arise from light-induced trap states/defects, as described elsewhere.[128] Different behavior was observed in LED-aged cells, and their V_{OC} start to increase slightly until 30 min and remain stable after 50 min. The other performance parameters that need to take into account is FF, as shown in **Figure 3.15d**. Normalized FF of sun-aged devices decreases abruptly around 16% of its initial value until T_{80}. On the other hand, the FF values of LED-aged cell have followed the trend: stable for a long time, decrease for a short time, suddenly increased, and continue following the same trend until it has decreased up to its initial value at T_{80}.

To examine the charge carrier recombination mechanisms within the devices, the dependency of the J_{SC} and V_{OC} on light intensity (P_{light}) was measured and the results are shown in **Figure 3.17**. The J_{SC} generally follows a power-law dependence upon P_{light}, as described by the expression:

$$J_{SC} \propto {P_{light}}^{S1} \tag{3.7}$$

where *S1* represents a power-law exponent. For bulk heterojunction polymer/fullerene-based solar cells, *S1* ranges typically from 0.85 to 1.[181] A linear dependence was observed when the value of *S1* close to 1 indicates weak bimolecular recombination. Conversely, a value of *S1* smaller than 1 suggests that bimolecular recombination of free charge carriers can limit the photocurrent devices.[182] **Figure 3.17a,b** show the plots of J_{SC} vs P_{light} for the cells illuminated under solar irradiation (10 – 100 mW cm^{-2}) and 1000 lux LED light intensity (<1 mW cm^{-2}). It is apparent that the slope is unity and is not influenced by different light sources exposure. All plots were fitted using equation 3.7. The similar fitted *S1* values for the fresh (0.98) and aged (0.94) cells illuminated under AM 1.5G and LED irradiation suggest that there is neither bimolecular recombination nor a build-up of space charge in all devices for both fresh and aged cells.

To gain more insight into recombination kinetics between the fresh and photo-aged PSCs, the logarithmic dependence of V_{OC} vs. P_{light} can be expressed using equation 3.2. **Figure 3.17c,d** show semilogarithmic plots of V_{OC} versus P_{light} for fresh and aged-PSCs under both illumination. The fitted *S2* values were obtained from equation 3.2. The obtained *S2* values of 0.99 and 1.26 lead to obtained *n* values of 1.01 and 1.28 for the fresh cells under 1 sun and 1000 lux LED light illumination, respectively. Furthermore, the increasing *S2* values were expected when we carried out the photoaging test. The solar-aged cells have *S2* values of 1.75 and the LED-aged cells of 1.47, resulting in *n* values of 1.86 and 1.38, respectively. This trend is coherent with the ideality factor of the diode obtained from the dark *J-V* fitting model (*n* value in Table 3.11). These results are in the range of expected values since the ideality factor for PSCs ranges between 1 and 2 ($1 \leq n \leq 2$).[183] Following theoretical considerations, the condition of *n* equal to 1 indicates the bimolecular recombination mechanism governs the charge recombination in PSCs, whereas when *n* near to 2, it is dominated by trap-assisted recombination mechanism.[177] In addition, the increase from $n = 1$ to $n = 2$ indicates the increasing trap density, as observed in the solar-aged cells. A higher increased of *n* values of solar-aged cells ($n = 1.86$) from its fresh sample suggest the recombination losses in solar-aged cells are mainly due to band-tail trap states in bulk. It can explain a rapid decay of V_{OC} over the AM 1.5G aging time, that is due to the light-induced trap formation, as shown in Figure 3.15c. On the other hand, the lower *n* values for LED-aged cells compare to their solar-aged counterpart can be attributed to low concentration traps in bulk under low-light illumination, resulting in the most stable V_{OC} values over the LED aging time (Figure 3.15c).

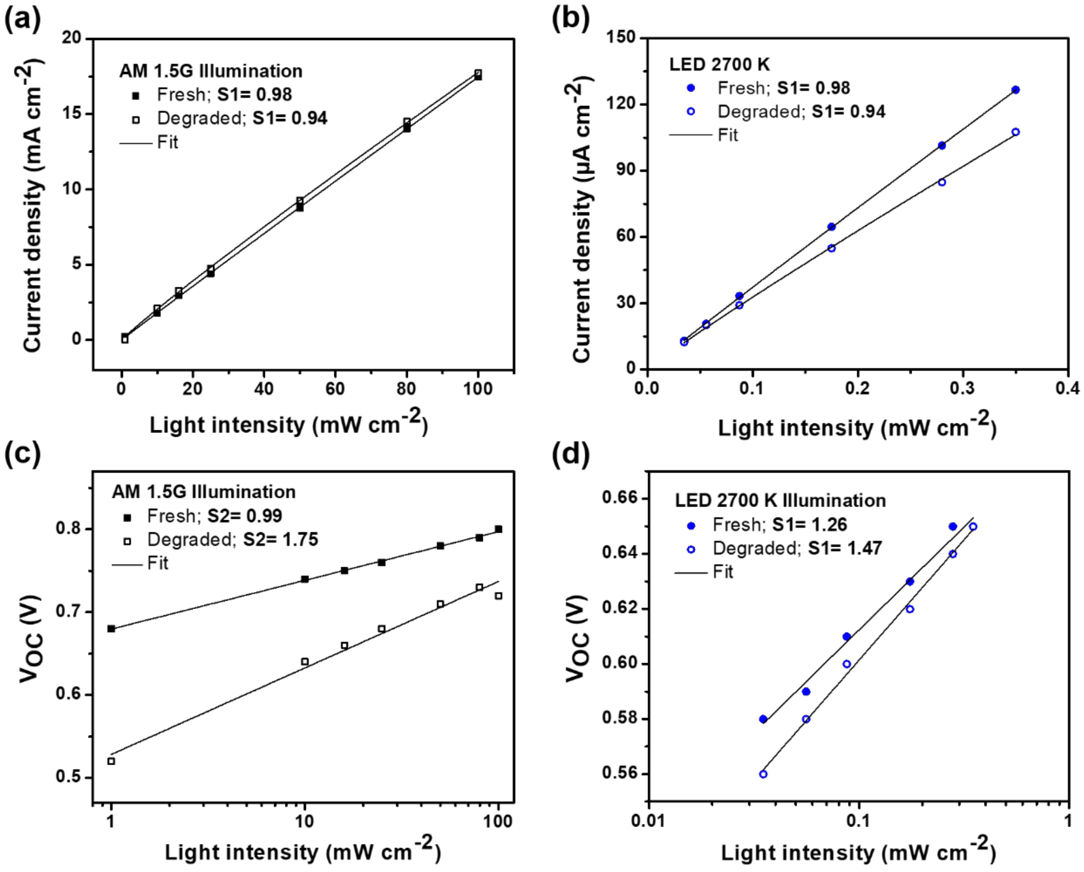

Figure 3.17 (a,b) J_{SC} and (c,d) V_{OC} dependence on light intensity over aging time of inverted PTB7-Th:PC$_{70}$BM-based device under (a,c) AM 1.5G and (b) 1000 lux LED light illumination. All measurements were carried out in an inert atmosphere.

In spite of the fact that *J-V* curves could provide the information in which performance parameters were affected by photodegradation, they could not give concrete evidence to understand the detrimental cause of PSCs performance deterioration. It is because of the complexity of the photodegradation mechanism. Hence, impedance spectroscopy (IS) measurements were carried out under solar simulator and LED irradiation aging condition to gain more information on the photostability of PTB7-Th:PC$_{70}$BM-based devices. The IS measurements were performed under the frequency sweep from 1 Hz to 10 MHz over the aging time from T$_0$ up to T$_{80}$ at the open-circuit voltage bias, superimposing an AC signal with 50 mV amplitude. The experimental data were fitted by an equivalent electrical model using three resistor/capacitor (3RC) circuits in series, as shown in Figure 3.10. These elements are related to the series resistance of ITO and the resistance and capacitance of TiO$_x$, active layer, and V$_2$O$_5$. The geometrical capacitance values of each layer can be calculated using equation 3.5 and their values shown in Table 3.7.

Figure 3.18 shows the Cole-Cole (Nyquist) plots of the impedance spectra of solar-aged and LED-aged PSCs measured at the open-circuit condition with their corresponding Bode plots in **Figure 3.19**. It is observed that a single process represented by one arc behavior in the Cole-Cole plot and one maximum in the real and imaginary components of the Bode plots depend on the illumination condition given, high-frequency features under AM 1.5G illumination and low-frequency features under LED 1000 lux illumination. The important parameters that can be extracted from the Cole-Cole plots after fitting with the 3RC circuit model are the capacitance (C), resistance (R), and time constant (τ). It can be seen that all plots over the degradation time show typical arc behavior, indicates that the equivalent 3RC circuit model is suitable for these spectra. Moreover, the diameter of arc increases as the aging time increases, suggesting an increased bulk resistance of PTB7-Th:PC$_{70}$BM devices.[170] It is worth noting that the diameter of the arc is directly related to the value of the resistance. The extracted resistance values of the fitted data from solar-aged and LED-aged cells over the lifetime stability are listed in **Table 3.14** and **3.15**, respectively. It is observed that the LED-aged cells have orders of magnitude higher resistance than that of solar-aged cells. The higher resistances of LED-illuminated fresh and aged cells were mainly due to the bulk RC ladder under low-light conditions, as we report elsewhere.[175] Moreover, the fitting values of solar-illuminated fresh cells are dominated by ITO series resistance. Nevertheless, as the aging time increase, the measurement is strongly affected by TiO_x resistance.

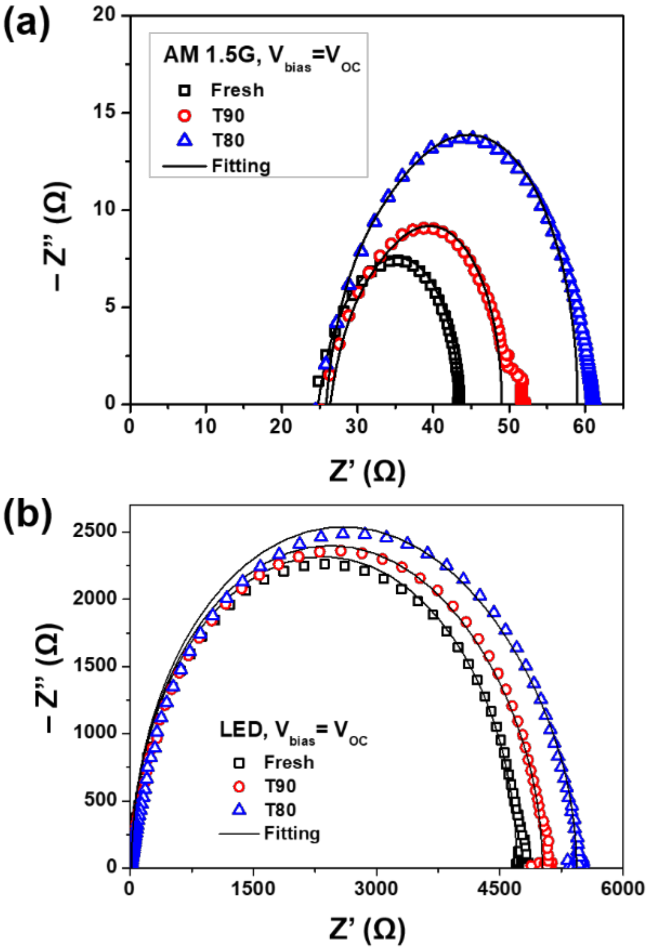

Figure 3.18 Cole-Cole plots at open-circuit voltage bias over aging time of PTB7-Th:$PC_{70}BM$-based devices under (a) AM 1.5G and (b) 1000 lux LED illumination. The experimental results were fitted using the 3RC circuit model (solid lines).

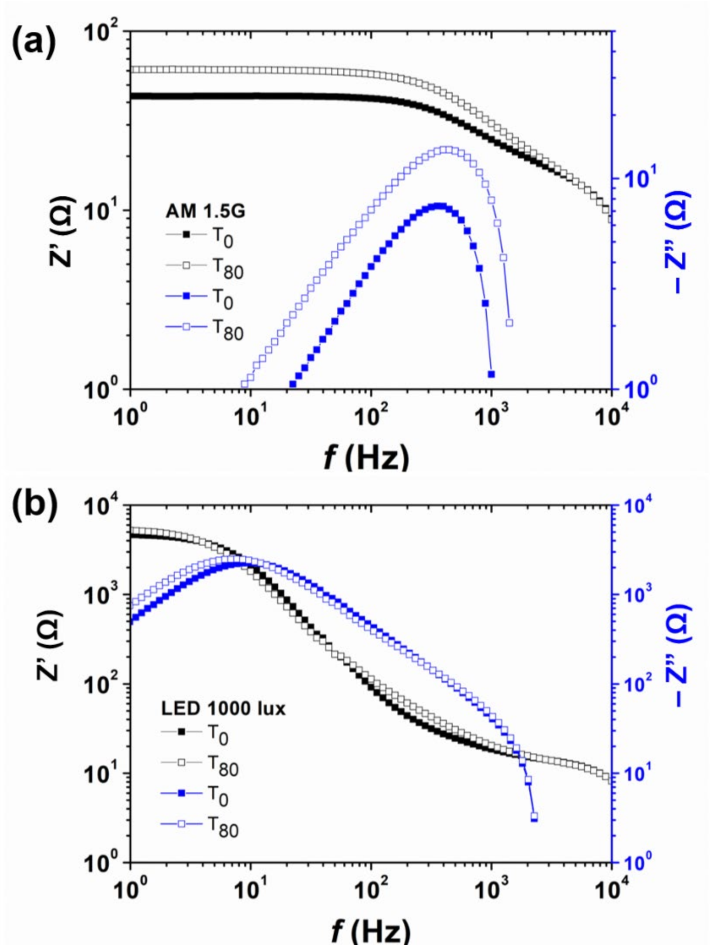

Figure 3.19 Bode plots, Z' and Z'' versus frequency, of the cells under (a) AM 1.5G and (b) LED 1000 lux illumination at open-circuit voltage condition.

To further analyze in which layer affects most the photodegradation under different light sources illumination, the percentage contribution of each layer resistance to the total resistance ($R_{tot} = R_S + R_{ETL} + R_{bulk} + R_{HTL}$) was investigated, as shown in **Figure 3.20**. We found the $\Delta R_{layer}/R_{total}$ (R_{layer}/R_{total} of aged – R_{layer}/R_{total} of fresh) of TiO_x is the highest among the other layers under both AM 1.5G and LED illumination. This result suggests that the performance deterioration of OPVs under both AM 1.5G and LED illumination is mainly due to the degradation of TiO_x layer. Such degradation may arise due to the photochemical activation under operation.[184]

Table 3.13 Capacitance and resistance values of each layer of different ETLs under standard AM 1.5G illumination (100 mW cm^{-2}) at various applied voltages bias.

ETL	**Layer**	**V_{bias} = 0.6V**				**V_{bias} = V_{OC}**			
		C (nF)	**R (Ω)**	**τ (μs)**	**ρ (MΩ cm)**	**C (nF)**	**R (Ω)**	**τ (μs)**	**ρ (MΩ cm)**
Fresh	ITO	-	15	-	-	-	16	-	-
	TiOx	200	6	1.20	0.36	200	12	2.40	0.72
	Bulk	3.5	8	0.03	0.07	3.5	7	0.03	0.07
	V2O5	78	19	1.48	3.42	78	8	0.62	1.44
T_{90}	ITO	-	15	-	-	-	17	-	-
	TiOx	200	12	2.40	0.72	200	16	3.20	0.96
	Bulk	3.9	8	0.03	0.07	3.5	8	0.03	0.07
	V2O5	78	19	1.48	3.42	78	8	0.62	1.44
T_{80}	ITO	-	15	-	-	-	17	-	-
	TiOx	200	22	4.40	1.32	200	24	4.56	1.44
	Bulk	3.9	10	0.04	0.09	3.5	8	0.03	0.07
	V2O5	78	20	1.56	3.60	97	10	0.97	1.80

Table 3.14 Capacitance and resistance values of each layer of different ETLs under 1000 lux LED illumination (0.35 mW cm^{-2}) at various applied voltages bias.

ETL	**Layer**	**V_{bias} = 0.6V**				**V_{bias} = V_{OC}**			
		C (nF)	**R (Ω)**	**τ (μs)**	**ρ (MΩ cm)**	**C (nF)**	**R (Ω)**	**τ (μs)**	**ρ (MΩ cm)**
Fresh	ITO	-	16	-	-	-	16	-	-
	TiOx	200	124	24.80	7	200	50	10	9
	Bulk	3.0	21625	64.88	185	3.5	4250	14.88	36
	V2O5	78	300	23.40	51	78	270	21.06	48
T_{90}	ITO	-	16	-	-	-	16	-	-
	TiOx	200	500	100	28	150	400	60	23
	Bulk	3.5	23000	89.70	197	3.9	4300	16.77	37
	V2O5	78	320	24.96	55	78	300	23.40	51
T_{80}	ITO	-	16	-	-	-	16	-	-
	TiOx	200	2500	500	143	150	515	77.25	29
	Bulk	3.5	24000	93.60	205	3.9	4500	17.55	38
	V2O5	78	600	46.80	103	78	400	31.2	68

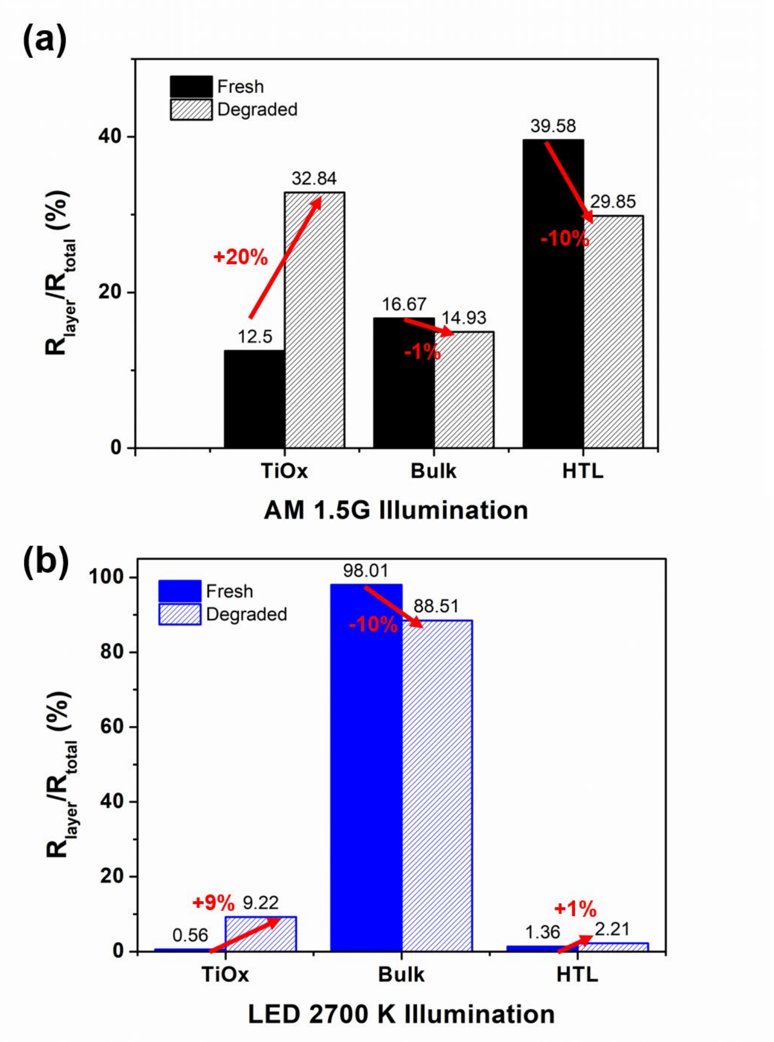

Figure 3.20 The percentage contribution of each layer resistance to the total resistance of the cellsfor fresh and degraded devices photodegraded under (a) standard AM 1.5G and (b) 1000 lux LED 2700K irradiation. The values were extracted by modeling the IS measurements at open-circuit conditions.

3.4 Conclusions

In conclusion, the photovoltaic performance of OPV devices based on PTB7-Th:$PC_{70}BM$ using different types of ETL materials had been studied under one sun AM 1.5G and indoor light illumination of warm light color (2700 K LED). The results showed significant difference in the performance of the OPV devices depending on the ETL used. The PFN-iOPV displayed a superior performance under 1 sun, with a higher PCE compare to TiO_x- and ZnO-iOPV and the best reported *FF* of 75.00% among the studied PTB7-Th:$PC_{70}BM$-based devices. Unexpectedly, PFN-iOPV showed the lowest performance when it exposed to indoor illumination under 250–2000 lux illumination. The highest PCE values are obtained from the ZnO-ETL with a PCE of up to 16.49%. The changes in the *FF* values observed in indoor and outdoor conditions can be estimated by incorporating the parasitic series and shunt resistances effect due to the type ETL used. These results correlate well with the leakage current and the presence of trap-assisted recombination under low light intensity. In addition, the indoor PCEs for the different ETLs agreed well with the trend of the charge collection efficiency. On the other side, a long operational lifetime T_{80} of 3,060 min were achieved by LED-irradiated devices, higher and more stable than that of AM 1.5G-irradiated devices with T_{80} of only 260 min. Using impedance spectroscopy and three resistive-capacitive equivalent circuit models, we were able to reveal that the main source of the photodegradation in the PTB7-Th:$PC_{70}BM$-based device is the electron transport layer. Our findings suggest that the proper considerations should be taken into account for better design and optimize an effective ETL for high performance and photostable OPVs for indoor applications.

Chapter 4

Ternary bulk heterojunction solar cells based on fullerene acceptor

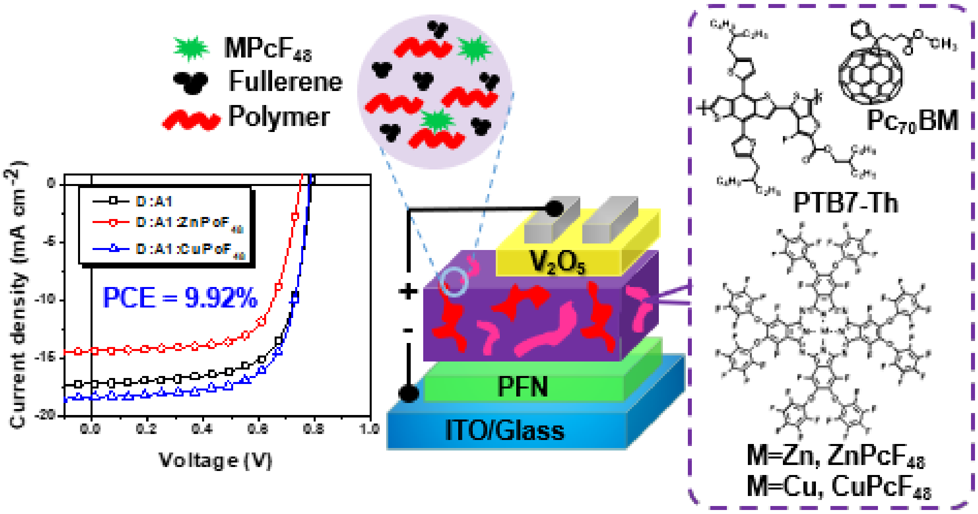

This chapter is based on the published work: Torimtubun, A.A.A. *et al.* Fluorinated Zinc and Copper Phthalocyanines as Efficient Third Components in Ternary Bulk Heterojunction Solar Cells. *ACS Appl. Energy Mater.*, **2021**, *4*, 5201-5211.

4.1 Introduction and the aim of the work

Bulk heterojunction OSCs featuring properties of low-cost, light-weight, solution-processed, large-area, semi-transparency, and flexible substrates have attracted great interest for decades.[163,185–189] OSCs are typically composed of the active layer consists of electron donor (D) and electron acceptor (A) materials in the blends of single-junction OSCs or tandem cells.[139,175,190,191] However, due to low charge carrier mobility, limited spectral absorption, and high thermal loss in organic materials, the tandem cell strategy is preferred as an effective way to address these issues.[192,193] Tandem cell can suppress the thickness constraint due to low mobility of organic materials in a single-junction cell, providing a wide and efficient optical absorption spectrum.[194] Meanwhile, thermalization losses in a single-junction cell can also be avoided thanks to the tunability band structure of the active organic materials in tandem cell.[195] Nevertheless, the complex fabrication process and high upfront cost limit the practical application of tandem cells.[196] In recent years, ternary organic solar cells (TOSCs) have been proved to be one of the most promising methods to improve device performance by adding a third component into a binary system, resulting in a single three-component photoactive layer.[67,197,198] TOSCs could combine each merit of binary and tandem solar cells to extend light absorption, simplify device fabrication, and increase device efficiency in a single-junction device.[197,199–202]

In a ternary blend, the addition of the third components (secondary donor D_2, or secondary acceptor A_2) does not only provides a broadened light-harvesting and optimizing the film morphology, but also facilitating better charge transport and exciton dissociation.[203–205] The dominant fullerene derivatives have been widely used in OSCs as a primary electron acceptor (A_1) or A_2. However, fullerene acceptors showed a weak light absorption, difficult energetic tunability and thermal instability.[201,206] Recently, non-fullerene acceptors (NFAs) have been synthesized to overcome the disadvantages of FAs. The rapid progress of highly efficient NFAs materials has offered a new opportunity for studying ternary OSCs due to the great tunability of chemical structures, optical properties and electronic properties of NFAs, and their ability to phase separate into nanoscopic domains in blended thin films.[113,133,207–210]

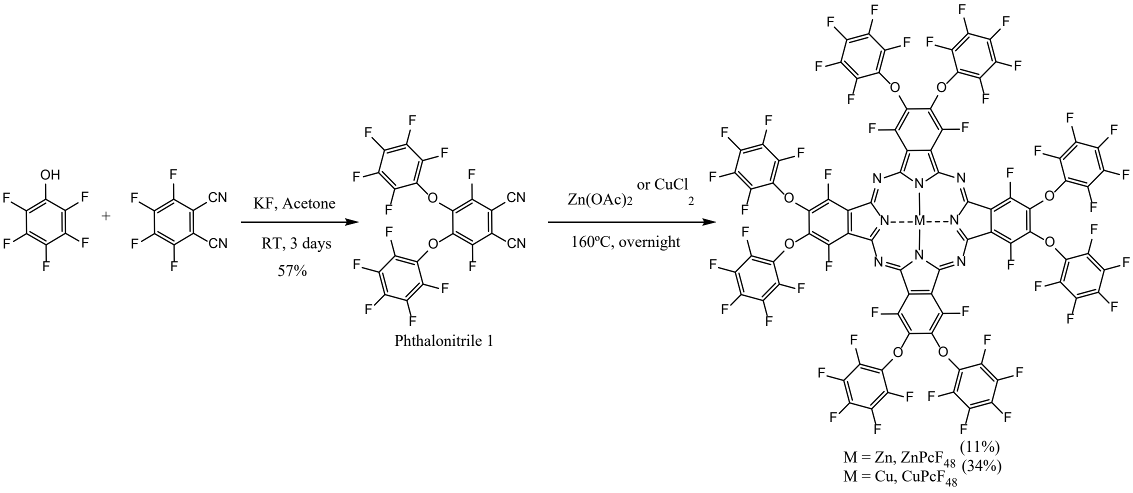

Figure 4.1 Synthetic route of $ZnPcF_{48}$ and $CuPcF_{48}$.

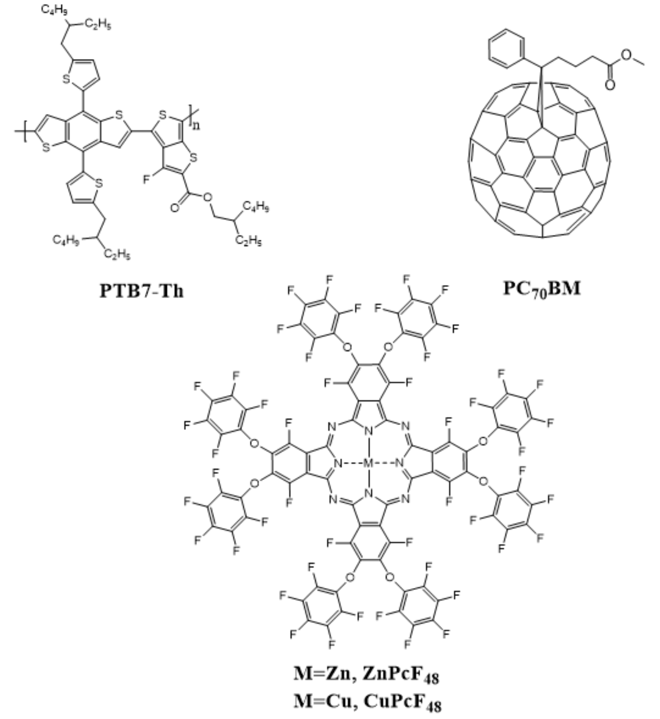

Figure 4.2 Chemical structures of PTB7-Th, $PC_{70}BM$, $ZnPcF_{48}$, and $CuPcF_{48}$ in the ternary bulk heterojunction solar cells.

Different small molecules from the phthalocyanines (Pc) derivatives have been described to provide alternative photovoltaic semiconductor materials for OSC applications.[211–214] Pcs play an important role as NFAs due to their high molar extinction coefficients, stability, and the highest occupied molecular orbital (HOMO)/the lowest unoccupied molecular orbital (LUMO) energy levels complementary with the energy levels of the other two components.[215,216] However, Pcs have poor solubility in organic solvents and most of the Pcs used to date in ternary solar cells have been SiPcs thanks to the functionalization of the axial positions that avoid aggregation processes.[217–221] Due to this problem, to date, not too many Pcs have been incorporated in ternary solar cells. Different studies have been performed using CuPc [222] and ZnPc [223] as third components and in all the cases resulted in an efficiency improvement compared to its two-component counterpart. In all these studies, Pcs acts as efficient transporter between a fullerene derivative and a polymer. For this reason, a deeper study should be done studying the influence of the substituents and the metal of the Pcs on the PV performance. In this work, we have prepared two new zinc and copper phthalocyanines substituted with electronegative fluorine atoms in benzene rings to enhance their solubility and their electron acceptor capability. Hence, $ZnPcF_{48}$ and $CuPcF_{48}$ (**Figure 4.1**) have been synthesized and incorporated into the ternary system based on PTB7-Th:PC70BM (**Figure 4.2**) to understand their influence on the OSC device performance.

4.2 Results and discussion

4.2.1 Synthesis and materials properties

The synthesis of $ZnPcF_{48}$ and $CuPcF_{48}$ was accomplished by statistical cyclotetramerization of 3,6-difluoro-4,5-bis(pentafluorophenoxy)phthalonitrile **1** using $Zn(OAc)_2$ or $CuCl_2$ as a template, respectively (Figure 4.1). Phthalonitrile **1** was synthesized by nucleophilic aromatic substitution of pentafluorophenol to tetrafluorophthalonitrile and characterized by FT-IR, ^{13}C NMR, and MALDI-ToF-MS. The ^{13}C NMR spectrum was performed without fluoride decoupling and showed several multiplets due to coupling of the ^{13}C with the ^{19}F. The ^{13}C signal assignments of the phthalonitrile **1** were performed by a comparative study between pentafluorophenol and tetrafluorophthalonitrile ^{13}C NMR spectra (see **Figure A1** and **A2** in the Appendix section).

Just like phthalonitrile **1**, ZnPcF$_{48}$ was not possible to characterize using ^{1}H NMR because of the absence of proton signals but was characterized using ^{19}F NMR, ^{13}C NMR, and 2D NMR experiments using THF-d_8 as solvent. The ^{19}F NMR spectrum shows four different signals, and their assignment was made thanks to the different multiplicities and the 2D experiment (see **Figure A3** and **A4**). The ^{13}C-NMR of ZnPcF$_{48}$ was performed with and without fluoride decoupling, as shown in **Figure A5** and **A6**. The carbons most affected by the formation of the phthalocyanine ring are the A and the H, which appear more deshielded than in the case of phthalonitrile **1** (see **Figure A7**). The remaining carbons are not as affected. The existence of fluorine atoms in the non-peripheral positions of phthalocyanine ring is also demonstrated by signal B in the ^{13}C NMR experiment with fluoride coupling (see Figure A6). This signal appears as a doublet of doublets with coupling constants of 4 Hz and 266 Hz, being the latter characteristic of ^{13}C–^{19}F couplings. In the case of CuPcF$_{48}$, due to the paramagnetic character of copper, there was not possible to characterize by NMR experiments. Both phthalocyanines were further characterized by FT-IR, HR-MALDI-TOF, and UV-vis experiments. The FT-IR for both phthalocyanines shows the absence of the characteristic peak of C≡N around 2200 cm^{-1}, which appears in the FT-IR of phthalonitrile **1** (see **Figure A8**–**A10**). The mass experiments show the expected molecular peaks with an isotopic distribution that exactly matched the simulated isotopic patterns (see **Figure A11**–**A13**). The UV-vis spectra of the individual thin film and CHCl$_3$ solution of PTB7-Th, ZnPcF$_{48}$, CuPcF$_{48}$, and PC$_{70}$BM are shown in **Figure 4.3a**. In solution, ZnPcF$_{48}$ and CuPcF$_{48}$

exhibit the Soret band around 360 nm and the Q band around 694 nm, which are the characteristic of nonaggregated phthalocyanines. Compared with solution absorption spectra, $ZnPcF_{48}$ and $CuPcF_{48}$ films show a broader absorption range and, respectively, perform a red-shift to the near IR absorption spectra of 822 nm and 806 nm, which suggests the presence of ordered *J*-aggregations in the film.[224] Beside near IR absorption peak, another strong absorption peak of $ZnPcF_{48}$ and $CuPcF_{48}$ films appear at visible range (378 and 652 nm, 382 and 648), which is complementary to both PTB7-Th and $PC_{70}BM$. The complementary absorption should be beneficial to aid the photon harvesting efficiency, resulting in high short-circuit current density (J_{SC}) and further improve the efficiency of ternary devices. The complementary absorption spectra of the binary and ternary thin films are displayed in **Figure A1** and **A15**.

Due to the π-π stacking of the molecules in the solution, the oxidation and reduction potentials were not able to measure by cyclic voltammetry. These values were obtained from the differential pulse voltammetry (DPVs) in DCM and dry THF as solvent, for $ZnPcF_{48}$ and $CuPcF_{48}$, respectively, containing 0.1 M $TBAPF_6$ as the supporting electrolyte. As shown in **Figure 4.3b**, $ZnPcF_{48}$ has two oxidation potentials at 0.57 and 0.79 V and two reduction potentials at –0.78 and –1.13 V *vs.* Fc/Fc^+. Meanwhile, $CuPcF_{48}$ shows one oxidation potential at 1.05 V and two reduction potentials at –0.87 and –1.30 V *vs* Fc/Fc^+. The estimated LUMO energy levels were calculated according to equation $E_{LUMO} = -4.8 - E_{red}$, where E_{red} is the first reduction potential. For $ZnPcF_{48}$ and $CuPcF_{48}$, E_{LUMO} are –4.02 and –3.93 eV, respectively. As a consequence of the difficulty to obtain the first oxidation potential of $CuPcF_{48}$, the HOMO energy levels for $ZnPcF_{48}$ and $CuPcF_{48}$ were determined, adding the absorption onset to E_{LUMO} value. These values for $ZnPcF_{48}$ and $CuPcF_{48}$ are –5.76 and –5.67 eV, respectively, as shown in Figure 4.3b. The energy bandgap from absorption onset was obtained from the equation 2.2 as represented in Figure 2.14.

The HOMO and LUMO energy offset of PTB7-Th and PC$_{70}$BM is reduced by the addition of ZnPcF$_{48}$ and CuPcF$_{48}$ as third components in a ternary blend, which provides more pathways to enhance the charge transfer of both electrons and holes by forming a cascade energy transfer.[203,225] By using photoluminescence instrument (see **Figure A16**), the emission of MPcF$_{48}$ is moderately overlapped the absorption of PTB7-Th, suggest the presence of energy transfer *via* Forster resonance energy transfer (FRET).[225] Hence, these results suggest that the subtle change in metal atom in MPcF$_{48}$ can significantly influence the photophysical and electrochemical properties.

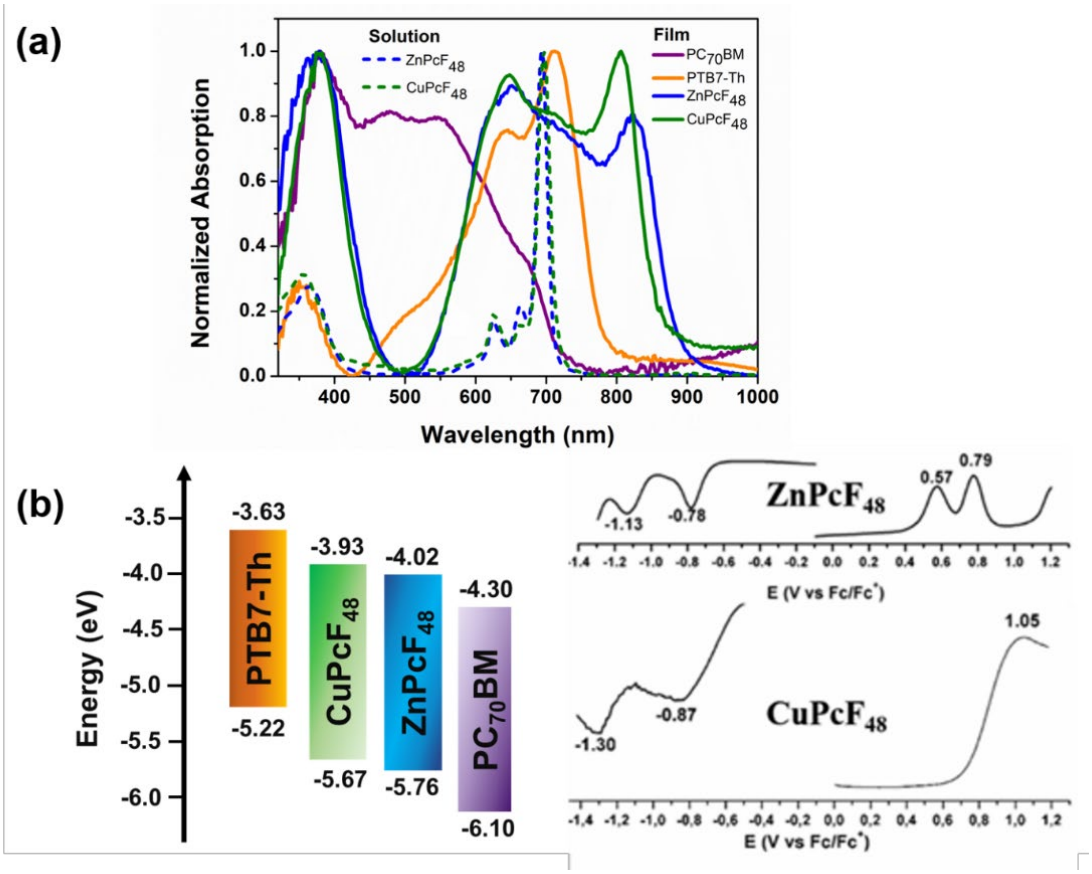

Figure 4.3 (a) Normalized UV-vis spectra of individual solutions (dashed lines) and thin films (solid lines) and (b) diagram representation of the estimated energy levels for PTB7-Th, CuPcF$_{48}$, ZnPcF$_{48}$, and PC$_{70}$BM (left), calculated from differential pulse voltammetry in DCM (ZnPcF$_{48}$) and THF (CuPcF$_{48}$) using 0.1 M TBAPF6 as supporting electrolyte (right).

4.2.2 Photovoltaic properties

The device performance of binary and ternary OSCs with different fluorinated phthalocyanines small molecules is thoroughly studied. The OSCs devices were fabricated with an inverted configuration of ITO/PFN/active layer/V_2O_5/Ag. The ratio of $MPcF_{48}$ in the ternary devices was optimized, as summarized in **Table A1** – **A3**. The ratio of $MPcF_{48}$ to PTB7-Th:$PC_{70}BM$ blend ratio in the active layer was varied from 0% to 12% while keeping the ratio of the donor to acceptor weight ratio constant of 1:1.5. The binary PTB7-Th:$MPcF_{48}$ blend was performed with the donor to acceptor weight ratio of 1:1 for further investigation. The *J-V* characteristics of the optimized OSCs devices based on the PTB7-Th:$PC_{70}BM$ (1:1.5), PTB7-Th:$PC_{70}BM$:$ZnPcF_{48}$ (1:1.47:0.03), PTB7-Th:$PC_{70}BM$:$CuPcF_{48}$ (1:1.47:0.03), PTB7-Th:$ZnPcF_{48}$ (1:1), and PTB7-Th:$CuPcF_{48}$ (1:1) bulk heterojunction blends under AM 1.5G illumination (100 $mW\cdot cm^{-2}$) and dark illumination are shown in **Figure 4.4**. The device parameters such as J_{SC}, V_{OC}, FF, and PCE are summarized in **Table 4.1**. To make a good data statistic, the extracted data were obtained from over 10 devices. As shown in **Figure 4.4a** and Table 1, the $PC_{70}BM$-based binary reference OSCs show a max PCE of 9.23% with J_{SC} of 16.82 $mA\cdot cm^{-2}$, a V_{OC} of 0.78 V, and a FF of 68.22%. Both $MPcF_{48}$–based binary OSCs show poor device performance compared to $PC_{70}BM$-based binary devices. $CuPcF_{48}$–based binary OSCs show a max PCE of 0.01% with a J_{SC} of 0.06 $mA\cdot cm^{-2}$, a V_{OC} of 0.32 V, and an FF of 0.24%. Despite having low performance, $ZnPcF_{48}$–based binary OSCs have one order magnitude higher PCE than those of $CuPcF_{48}$–based binary OSCs with a max PCE of 0.07%, a J_{SC} of 0.27 $mA\cdot cm^{-2}$, a V_{OC} of 0.33 V, and an FF of 0.50%. This may arise from a larger ΔHOMO of PTB7-Th / $ZnPcF_{48}$ (0.54 eV) than that of PTB7-Th/$CuPcF_{48}$ (0.45 eV). As reported by Yang *et al.*, minimizing energy level-offset between a donor and non-fullerene acceptor may provide sufficient driving force for more efficient exciton dissociation, and thus increasing the PCE.[226] On the other hand, $ZnPcF_{48}$ TOSCs show a max PCE

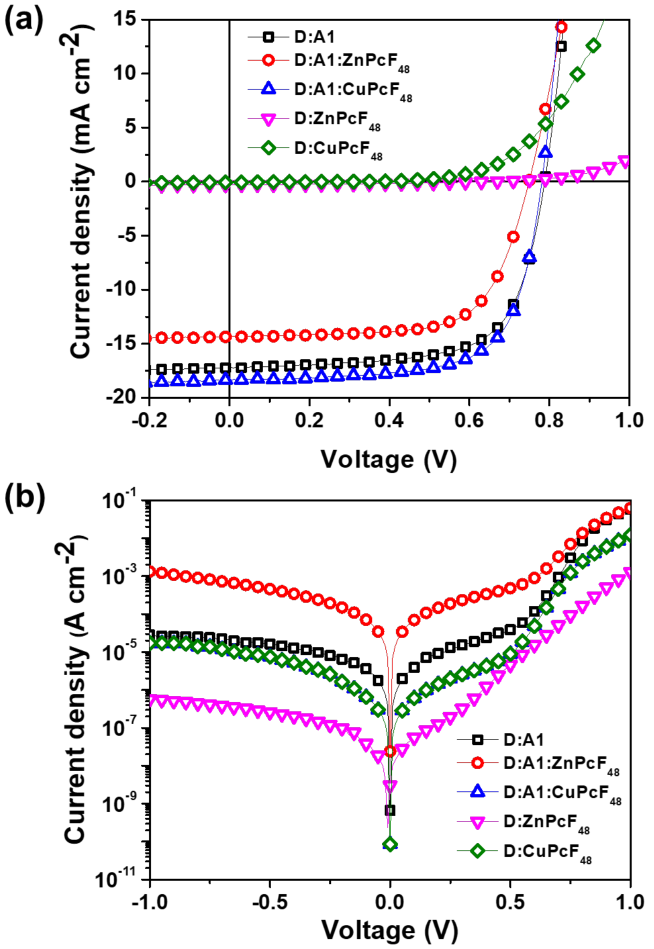

Figure 4.4 *J-V* characteristics of the binary and ternary solar cells devices under (a) AM 1.5G illumination and (b) dark condition.

Table 4.1 Summary of the device performance parameters of ternary organic solar cells with different fluorinated phthalocyanines small molecules.[a)]

D:A$_1$:A$_2$	J_{SC} (avg) / $J_{calc.}$ [b)] [mA·cm-2]	V$_{OC}$ (avg) [V]	FF (avg) [%]	PCE (avg/best) [%]
D:A$_1$	16.82 (16.00)	0.78	68.22	9.01 (9.23)
D:A$_1$:ZnPcF$_{48}$	14.25 (13.88)	0.77	64.47	7.12 (7.21)
D:A$_1$:CuPcF$_{48}$	17.90 (17.31)	0.78	68.54	9.57 (9.92)
D:ZnPcF$_{48}$	0.27 (0.25)	0.33	0.50	0.03 (0.07)
D:CuPcF$_{48}$	0.06 (0.06)	0.32	0.24	0.005 (0.006)

[a)] Average values were calculated from over 10 devices; [b)] $J_{calc.}$ values in parentheses are the integrated current densities calculated from EQE curves.

of 7.21% with a J_{SC} of 14.25 mA·cm^{-2}, a V_{OC} of 0.78 V, and a FF of 64.47%. Even though ZnPcF$_{48}$ exhibits complementary absorption and energy cascade transfer for PTB7-Th and PC$_{70}$BM, its lower device performance than those of PC$_{70}$BM-binary reference devices may be attributed to the tendency of ZnPcF$_{48}$ to solubilize in either PTB7-Th and PC$_{70}$BM phase rather than at PTB7-Th:PC$_{70}$BM interface.[227] By using contact angle measurement, we found that ZnPcF$_{48}$ materials are likely to be miscible in the acceptor phase (see **Table 4.2**). It can be seen from the Table 4.2 that the χ values for the PTB7-Th:ZnPcF48 (0.38) is much higher than those of PC$_{70}$BM:ZnPcF$_{48}$ (0.28), suggesting much lower miscibility or weaker interaction between ZnPcF$_{48}$ and PTB7-Th while a better mixed-phase between PC$_{70}$BM and ZnPcF$_{48}$ is found. On the other hand, the χ values for the binary reference PTB7-Th: PC$_{70}$BM (0.01) is much lower than the ZnPcF$_{48}$-based blend, indicating a better miscibility and well mixed-phase in its blend. This result is in good agreement with the morphology characterization and device performance parameter.

We then explored CuPcF$_{48}$ as the third component in TOSCs. A max PCE of 9.92% with J_{SC} of 17.90 mA·cm^{-2}, a V_{OC} of 0.78 V, and a FF of 68.54% was achieved. It is demonstrated that their J_{SC} and FF are higher than those of reference binary devices. The enhancement in the J_{SC} is attributed to the complementary absorption profile of the ternary active layer (Figure A14–A15). A slightly higher value of FF for the CuPcF$_{48}$-TOSCs as compared to PC$_{70}$BM-binary OSCs may be related to the fact that CuPcF$_{48}$ improves electron transport.

Table 4.2 Key parameters of contact angle measurements using water and ethlyene glycol droplets.

Samples	θ_{water} (°)	θ_{EG} (°)	γ^p (mN m^{-1})	γ^d (mN m^{-1})	Surface tension (mN m^{-1})	χ with D	χ with A1
PTB7-Th	91.59	72.29	22.49	6.56	29.06	-	0.01
PC$_{70}$BM	90.60	65.54	17.34	10.86	28.21	0.01	-
ZnPcF$_{48}$	93.84	74.49	13.64	9.70	23.34	0.38	0.28

Figure 4.4b depicts the *J-V* characteristic measured in the dark, which gives a further understanding of leakage current, series and shunt resistance in the device performance. The extracted device performance parameters are summarized in **Table 4.3**. At the reverse and low forward voltages, the R_{Sh} was dominated, which is correlated with the leakage current of the devices. The value of R_{Sh} for $ZnPcF_{48}$ TOSCs is the lowest among other binary and $CuPcF_{48}$ TOSCs. As a result, $ZnPcF_{48}$ TOSCs have the highest leakage current, which can dominate the photocurrent and thereby reduce the light current. On the other hand, upon adding $CuPcF_{48}$ in the TOSCs, the leakage current greatly decreases at negative voltages in compared to those of binary OSCs. At a region of the applied voltage around 0.5–1.0 V, $CuPcF_{48}$ TOSCs and $PC_{70}BM$ binary devices have similar R_S values, and lower than that of $ZnPcF_{48}$ TOSCs. Similar R_{Sh} values are also observed in $CuPcF_{48}$ TOSCs and $PC_{70}BM$ binary devices, resulting in their similar FF values. A lower FF value of $ZnPcF_{48}$ TOSCs is observed with its much lower R_{Sh} value. It suggests that the parasitic series and shunt resistance effect may contribute to the change of FF in TOSCs.

Table 4.3 Extracted devices parameters from *J-V* dark measurements.

$D:A_1:A_2$ [%w/w]	**R_S [Ω·cm²]**	**R_{Sh} [Ω·cm²]**	**J_0 [A·cm⁻²]**
$D:A_1$	3.85	1.15×10^6	2×10^{-11}
$D:A_1:ZnPcF_{48}$	2.60	1.46×10^3	3×10^{-8}
$D:A_1:CuPcF_{48}$	3.77	1.86×10^6	1×10^{-11}
$D:ZnPcF_{48}$	112.48	2.13×10^6	1×10^{-7}
$D:CuPcF_{48}$	30.71	6.82×10^5	1×10^{-11}

To gain further insight into enhanced J_{SC} values for $CuPcF_{48}$-based ternary systems, the external quantum efficiency (EQE) spectra were measured, as shown in **Figure 4.5a**. Binary of PTB7-Th:$PC_{70}BM$, PTB7-Th:$ZnPcF_{48}$, and PTB7-Th:$CuPcF_{48}$ bulk heterojunction solar cells show maximum EQE values of 68.93%, 1.93%, and 0.71% at the wavelengths of 470 nm, 370 nm, and 340 nm, respectively.

Meanwhile, the maximum EQE value of 66.68% for $ZnPcF_{48}$ TOSCs is lower than binary PTB7-Th:$PC_{70}BM$, and the EQE peak is shifted to the lower wavelength at 430 nm. It indicates that the addition of $ZnPcF_{48}$ as a third component in PTB7-Th:$PC_{70}BM$-based OSCs contributes to the deterioration of the device performance, as shown clearly in **Figure 4.5b**, by taking the ΔEQE (defined as $EQE_{ternary} - EQE_{binary}$). The contribution of $ZnPcF_{48}$ as third component in the photon-to-electron conversion capability is only can be seen in the wavelength range at 370 nm to 450 nm. On the contrary, the $CuPcF_{48}$ TOSCs show an enhanced EQE response in the whole wavelength range at 300–800 nm. The highest value of the EQE response of corresponding $CuPcF_{48}$ TOSCs reaches 74.64% at 470 nm. The escalation of the EQE values for $CuPcF_{48}$ TOSCs together with the increased J_{SC} contributes to the FRET effects, which signify that more excitons are generated due to the enhanced absorbed photons in ternary photoactive layer. These results suggest that the central metal atom substitution in fluorinated phthalocyanines for the third component in TOSCs apparently affects the photon harvesting efficiency. It is worth mentioning that the integrated current density J_{SC} for binary and ternary devices are in good agreement with the measured J_{SC} values from J-V curves with a maximum error of less than 8%.

The effects of fluorinated zinc and copper phthalocyanines on the charge recombination dynamics were extracted by analyzing V_{OC} and J_{SC} as a function of light intensity (P_{light}). The plot V_{OC} versus the natural logarithm of P_{light} provides information on the degree of trap-assisted recombination under V_{OC} conditions. Typically, a slope (S) equal to 1 kT/q suggests the presence of bimolecular recombination, whereas an S ranged between 1 and 2 ($1\ kT/q \leq S \leq 2\ kT/q$) indicates the presence of monomolecular recombination and trap-assisted recombination losses. **Figure 4.6a** shows the plot V_{OC} versus ln P_{light} for binary devices based on PTB7-Th:$PC_{70}BM$, PTB7-Th:$ZnPcF_{48}$, and PTB7-Th:$CuPcF_{48}$, and ternary OSCs based on PTB7-Th:$PC_{70}BM$:$ZnPcF_{48}$ and PTB7-Th:$PC_{70}BM$:$CuPcF_{48}$. The slope values were calculated to be 1.31 *kT*/*q*, 1.74 *kT*/*q*, 1.92 *kT*/*q*, 1.34 *kT*/*q*, and 1.25 *kT*/*q*, respectively. These results suggest that the trap-assisted recombination losses can be suppressed by adding a small amount of $CuPcF_{48}$ in TOSCs. Consequently, the J_{SC} and FF of ternary OSC PTB7-Th:$PC_{70}BM$:$CuPcF_{48}$ are simultaneously increased as compared to those of the binary system made of PTB7-Th:$PC_{70}BM$. However, the higher *S* value of PTB7-Th:$PC_{70}BM$:$ZnPcF_{48}$ OSC indicates that adding a small concentration of $ZnPcF_{48}$ results in a higher trap-assisted recombination degree, resulting in lower J_{SC} and FF as compared to the binary system (see Table 4.1).

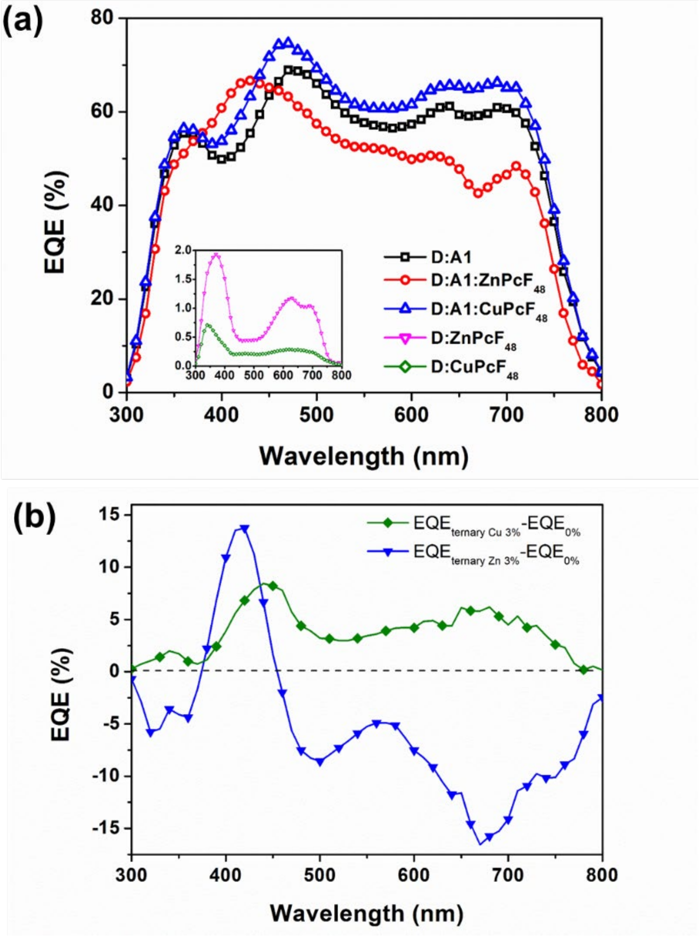

Figure 4.5 (a) EQE spectra of binary bulk heterojunction OSC and ternary bulk heterojunction OSCs with two different third components and (b) The ΔEQE values (*y*-axis) of ternary devices with respect to $PC_{70}BM$-binary device.

Figure 4.6b shows the power-law function Jsc ∝ P_{light}^{α}, where α represents the bimolecular recombination intensity. An α value equal to unity (α =1) indicates that bimolecular recombination does not take place within the devices.[228,229] The calculated α values are 1 for all devices, excluding the device PTB7-Th:CuPcF$_{48}$ with α = 1.1. The results indicate there is no bimolecular recombination in all devices.

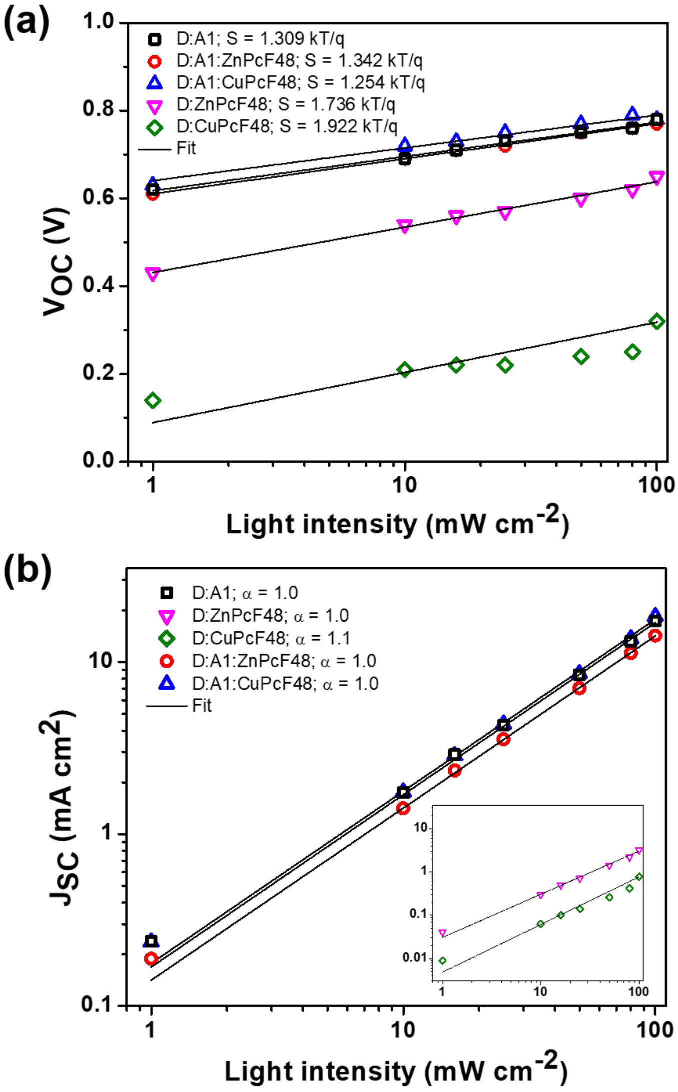

Figure 4.6 (a) V_{OC} and (b) J_{SC} vs light intensity of binary and ternary films.

To gain insight into the influence of zinc and copper phthalocyanines on the charge dynamics, we measured the photocurrent (J_{Ph}) as a function of the effective voltage (V_{eff}). The J_{Ph} is defined as the difference between the current-density measured under 1 sun illumination and measured under dark conditions ($J_{Ph} = J_L - J_D$). On the other hand, V_{eff} is defined as $V_{eff} = V_0 - V_{app}$, where V_0 is the voltage at $J_{Ph} = 0$, and V_{app} is the applied voltage. **Figure 4.7** shows the J_{Ph} versus V_{eff} plot for the binary OSC based on PTB7-Th:$PC_{70}BM$, and the ternary OSCs PTB7-Th:$PC_{70}BM$:$ZnPcF_{48}$ and PTB7-Th:$PC_{70}BM$:$CuPcF_{48}$. For PTB7-Th:$ZnPcF_{48}$ and PTB7-Th:$CuPcF_{48}$-based devices, the saturation current could not be reached even at bias >1 V, suggesting severe charge recombination phenomena. The saturation current density (J_{sat}) is extracted from Figure 4.3a, where the J_{Ph} saturates at a high V_{eff} of over 1.5V for binary and ternary devices. The maximum charge generation rate (G_{max}) is defined as $J_{sat} = qLG_{max}$, where q is the elementary charge, and L is the thickness of the binary or ternary organic layer. Besides, the exciton dissociation efficiency (η_{diss}) is calculated by J_{Ph}/J_{sat} value under the short-circuit condition, whereas the charge carrier collection efficiency (η_{coll}) is defined by J_{Ph}/J_{sat} under the maximal power-point condition. **Table 4.4** summarizes the values of G_{max}, η_{diss}, and, η_{coll} for binary OSC PTB7-Th:$PC_{70}BM$ and the ternary OSCs PTB7-Th:$PC_{70}BM$:$ZnPcF_{48}$ and PTB7-Th:$PC_{70}BM$:$CuPcF_{48}$. In ternary OSC PTB7-Th:$PC_{70}BM$:$CuPcF_{48}$ the G_{max} is slightly higher than that of the binary devices, while the G_{max} of PTB7-Th:$PC_{70}BM$:$ZnPcF_{48}$ is lower than that of the binary system, however G_{max} for binary-ternary OSCs are almost in the same order of magnitude. Moreover, the PTB7-Th:$PC_{70}BM$:$CuPcF_{48}$ OSC exhibited the highest values of η_{diss} and η_{coll}, indicating that adding a 3% of $CuPCF_{48}$ into a PTB7-Th:$PC_{70}BM$ system allows improving the charge dynamics of the ternary system. These results agree with the improved J_{SC} and FF of the PTB7-Th:$PC_{70}BM$:$CuPcF_{48}$ OSC in comparison to those of PTB7-Th:$PC_{70}BM$.

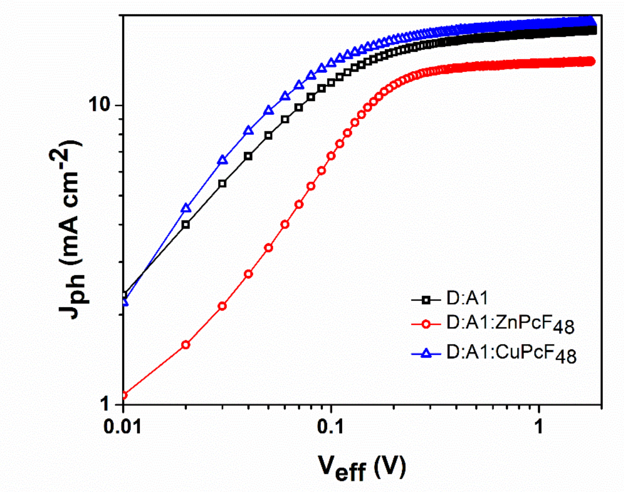

Figure 4.7 Variation of photocurrent (J_{Ph}) with effective voltage (V_{eff}) in PC$_{70}$BM-binary and ternary solar cells devices.

Table 4.4 The values G$_{max}$, η_{diss}, and, η_{coll} for binary OSC PTB7-Th:PC$_{70}$BM and the ternary OSCs PTB7-Th:PC$_{70}$BM:**ZnPcF$_{48}$** and PTB7-Th:PC$_{70}$BM:**CuPcF$_{48}$**.

Device	**G$_{max}$ [m^{-3} s^{-1}]**	**η_{diss} [%]**	**η_{coll} [%]**
D:A$_1$	1.11x10^{28}	97.23	83.90
D:A$_1$:ZnPcF$_{48}$	8.71x10^{27}	97.98	83.63
D:A$_1$:CuPcF$_{48}$	1.16x10^{28}	98.89	84.01

4.2.3 Thin-film surface properties

Even though ZnPcF$_{48}$ and CuPcF$_{48}$ have the same value of the energy bandgap ($E_g = E_{HOMO} - E_{LUMO}$) of 1.74 eV and similar HOMO and LUMO values, ZnPcF$_{48}$-based binary OSC showed an order magnitude higher efficiency when paired with PTB7-Th than those of CuPcF$_{48}$. The reason behind this may correlate with the different morphology of the bulk film, as shown in **Figure 7**. The tapping-mode atomic force microscopy (AFM) measurements were performed to investigate the bulk surface morphology changes by introducing MPcF$_{48}$ to binary reference blend. The corresponding AFM height and phase images for PTB7-Th:MPcF$_{48}$ blend

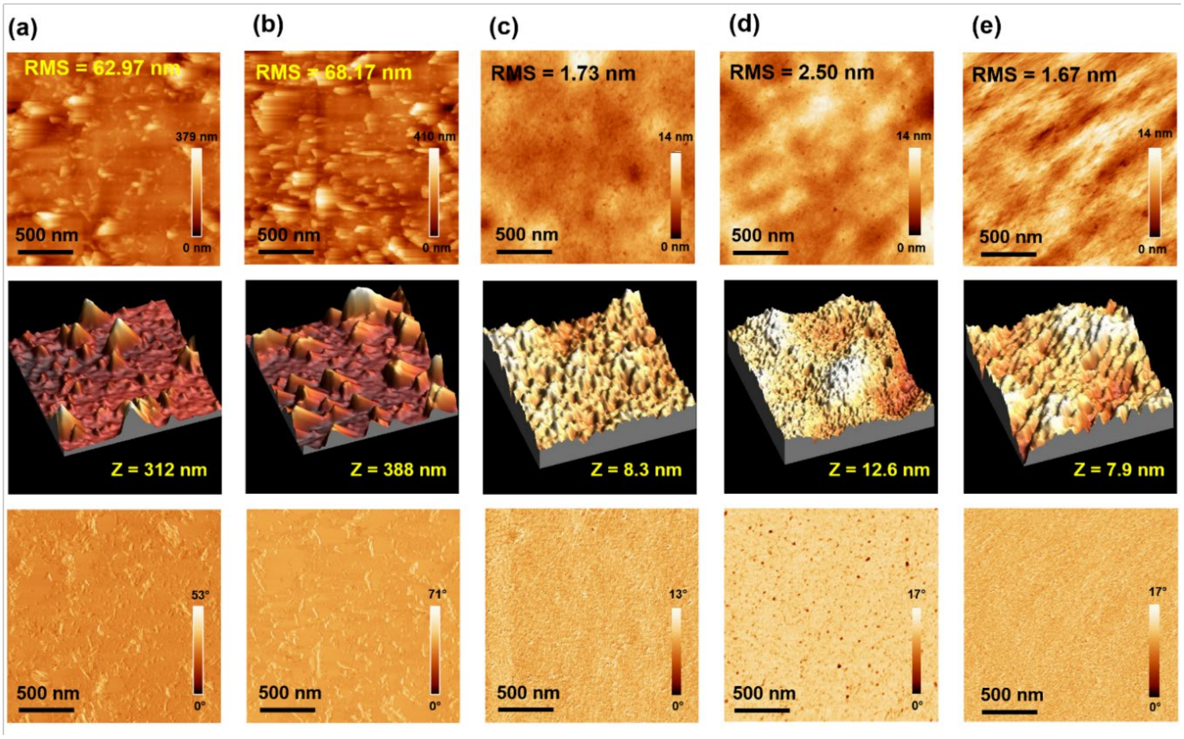

Figure 4.8 AFM height images (top), AFM 3-dimensional height images (middle) and AFM phase images (bottom) (2 x 2 μm) of binary (a) D:ZnPcF$_{48}$, (b) D:CuPcF$_{48}$ and (c) D:A$_1$; ternary (d) D:A$_1$:ZnPcF$_{48}$ and (e) D:A$_1$:CuPcF$_{48}$.

are shown in **Figure 7a** and **b** (top part is 2-dimensional images, middle part is 3-dimensional images, while bottom part is the phase images). Both MPcF$_{48}$-based binary blends show a coarse, distinctive phase-separated morphology with large island-like domain. Larger domain sizes on the photoactive layer of OSCs are not favorable for charge transport or exciton diffusion, thus explaining why MPcF$_{48}$-binarsy OSCs have inferior device performance (see Table 1). Even though both MPcF$_{48}$-binary blends have a large domain and very rough surfaces, the ZnPcF$_{48}$-based binary blend shows clearly less aggregation because ZnPcs are known to disperse better in solution than CuPcs.[230] Compare to PTB7-Th:CuPc$_{F48}$ blend, PTB7-Th:ZnPc$_{F48}$ blend shows a lower root-mean-square (RMS) roughness of ~63 nm, less aggregation with smaller hills, and smaller height difference, as shown in its corresponding 3-D height and phase images. This result is in good agreement with the higher performance of $ZnPcF_{48}$-based binary OSC than $CuPcF_{48}$-based binary OSC. Due to $MPcF_{48}$-binary poor film morphology, they are likely to play a bigger role than small energetic differences.

Figure 7c displays the morphology of binary reference PTB7-Th:$PC_{70}BM$ blend film featuring smooth crystallized like domain with RMS roughness of 1.72 nm. In the case of ternary system, the 3% addition of $ZnPcF_{48}$ as third component in PTB7-Th:$PC_{70}BM$ blend results in increasing RMS roughness of 2.5 nm and a larger height difference of 12.6 nm, as shown in **Figure 7d**. Moreover, the formation of homogeneous dispersity of pinholes on $ZnPcF_{48}$-ternary blend film is clearly observed in the phase image, which is not beneficial to facilitate charge transport. On the other hand, the incorporation of 3% $CuPcF_{48}$ in PTB7-Th:$PC_{70}BM$ blend effectively decreases RMS to 1.67 nm and results in a finer interpenetrating bulk heterojunction morphology relative to the $PC_{70}BM$-binary blend, as shown in **Figure 7e**. The smoother morphology of PTB7-Th:$PC_{70}BM$:$CuPcF_{48}$ ternary blend compared to $PC_{70}BM$-binary blend may explain the reduced recombination losses and better charge dynamics of $CuPcF_{48}$-based ternary compared to the binary blend, which has been reflected in the higher value of FF and J_{SC} in the incorporation of $CuPcF_{48}$ third component in TOSCs devices.

4.2.4 Photostability study

In addition to high device performance, the information about ambient stability is necessarily important for the future commercialization of OSCs. Generally, the ambient photostability of OSCs depends on several factors, such as exposure to humidity and oxygen, intrinsic properties of the organic materials, fullerene dimerization in FA-based OSCs, microstructural stability of NFA-based OSCs, etc. Recent studies about the photostability investigation of ternary OSCs showed that the incorporation of third component might enhance the ternary system photostability by minimizing the molecular structural changes, preserving the crystallinity, deactivate light-induced trap formation, and balancing the charge carriers mobilities in their active layers upon photodegradation exposure.[128,231] We believe that the incorporation of $MPcF_{48}$ as third component in TOSCs may affect the device photostability. Thus, we performed the photostability study of nonencapsulated binary and ternary devices exposed under continuous AM 1.5G illumination at open-circuit condition in an ambient atmosphere (room temperature, relative humidity = 50 – 60%).

The evolution results of photovoltaic parameters for all devices under the ambient photodegradation test are presented in **Figure 4.9**. The $ZnPcF_{48}$-TOSCs suffer the most in degradation with more than 95% efficiency loss after 40 min of illumination, as shown in **Figure 4.9a**. On the other hand, the PCE of $PC_{70}BM$-binary OSCs is reduced by 90% from its original value. The most stable device is the $CuPcF_{48}$-TOSCs, with a PCE decay of almost 85%. Reasonable photoaging decay was noticed for all photovoltaic parameters in all devices, as shown in **Figure 4.9b–d**. It is obvious to see that J_{SC} decay in all photodegraded devices has similar behavior with PCE decay behavior, suggesting that J_{SC} is the main contributor to the observed PCE loss. Moreover, it is observed that FF decay also contributes to the PCE loss after J_{SC} decay. A relatively higher J_{SC} and FF loss in photodegraded $ZnPcF_{48}$-TOSCs may be attributed to the morphological instabilities of bulk heterojunction.[232] On the other hand, the addition of 3% CuPcF48 in binary PTB7-Th:$PC_{70}BM$ blend can moderately enhance the ambient photostability, verified by the relatively the lowest V_{OC} and FF loss. This result indicates that the metal atom substitution strategy in the third component of TOSC affects the photostability of OSCs. Further study needs to be carefully carried out to go more in-depth into the main degradation mechanism caused by the metal atom substitution of $MPcF_{48}$ third component in TOSCs for a full application of ternary strategy in the future.

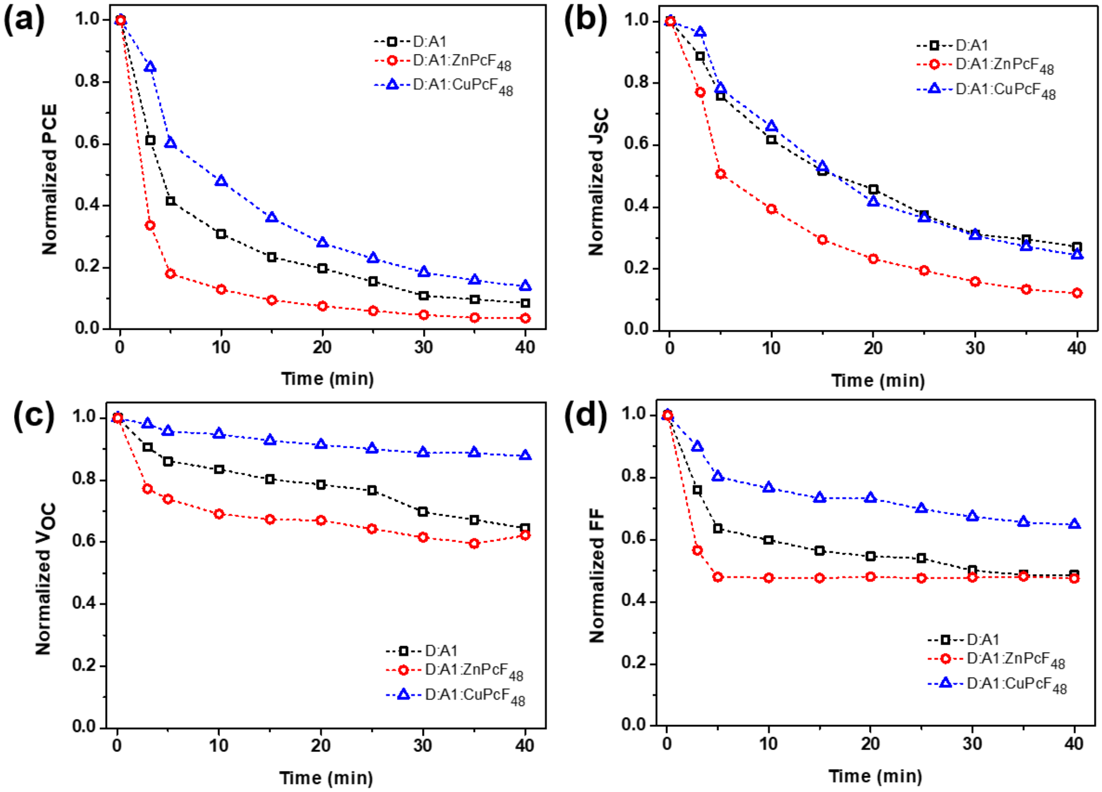

Figure 4.9 Normalized (a) PCE, (b) J_{SC}, (c) V_{OC}, and (d) FF of PC$_{70}$BM-binary, ZnPcF$_{48}$-ternary and CuPcF$_{48}$-ternary devices over photoaging time.

4.3 Conclusions

In summary, we have successfully synthesized fluorinated zinc and copper phthalocyanines (ZnPcF$_{48}$ and CuPcF$_{48}$) as new third components in ternary OSCs with a device architecture of ITO/PFN/PTB7-Th:PC$_{70}$BM:MPcF$_{48}$/V$_2$O$_5$/Ag. The introduction of MPcF$_{48}$ with different central atoms have an influence on the electronic structure, optical absorption, energy level alignment, charge transport and recombination, and blend film morphology of TOSCs. Among MPcF$_{48}$ derivatives, CuPcF$_{48}$ has the highest PCE of up to 9.92%, due to their better morphology, improved exciton dissociation, better charge carrier collection efficiency, and more suppressed trap-assisted recombination, thus making it a promising new NFA material for OSCs applications. Further studies are in progress in order to optimize the devices using new CuPcs as TOSC third component to increase PV performance and stability.

Chapter 5

Ternary bulk heterojunction solar cells based on nonfullerene acceptors

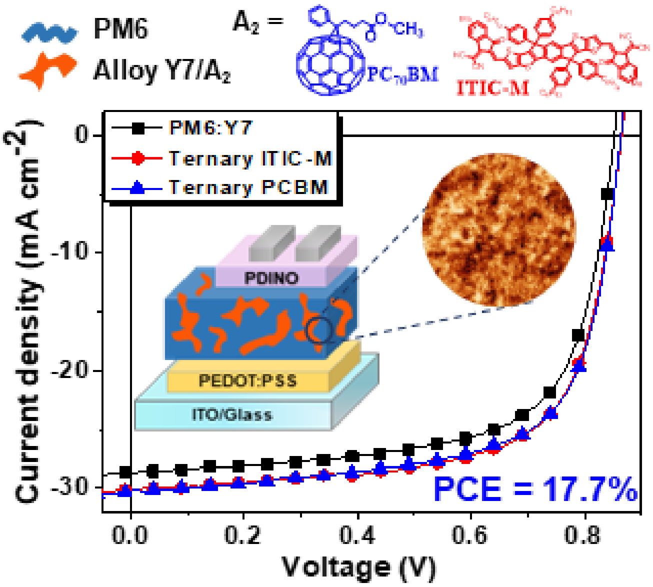

This chapter is based on the submitted work: Torimtubun, A.A.A. *et al.* Achieving 17.7% Efficiency of Ternary Organic Solar Cells by Incorporating a High LUMO Level and Miscible Third Component. *submitted*.

5.1 Introduction and aim of the work

The bulk-heterojunction organic solar cells (OSCs) have made significant progress thanks to the synergistic advances in materials design and device engineering, boosting the power conversion efficiency (PCE) to over 18% in single-junction OSCs.[233–236] The recent emergence of high-performance Y-series nonfullerene acceptors (NFA) paired with polymer donor PM6 has motivated a major revolution in OSCs field. To further boost PCE of OSCs, constructing ternary organic solar cells (TOSCs) is a facile and effective approach *via* introducing third component, either a secondary donor or a secondary acceptor, in binary host blend. The third component in TOSCs can have various functions for successfully constructing the efficient and stable TOSCs such as widening the absorption spectra, modulating the energetics, regulating morphology, and enhancing stability,[53,69,237–240] making a rational selection of third component material, is of urgent and fundamental importance.

To choose a compatible third component, some key factors must be considered, mainly from the electrical and morphological perspectives. Considering the energetic perspective, a higher-energy lowest unoccupied molecular orbital (LUMO) material for a two acceptors system or a deeper highest occupied molecular orbital (HOMO) material for a two donors system was selected as third component to increase simultaneously the open-circuit voltage (V_{OC}) and short-circuit current density (J_{SC}) values of ternary device.[224,241–243] In the case of two acceptors system, either fullerene acceptor (FA) or NFA can be selected as a good ternary composite in the state-of-the-art PM6:Y-derivative binary blend system, depending on its compatibility with Y-derivative host acceptor. For example, Zhang and coworkers introduced an amorphous ICBA into PM6:Y7 binary blend, which helps improve the V_{OC} by elevating the LUMO energy levels and concurrently increase J_{SC} by extending the absorption in a short wavelength band, thus boosting the PCEs of the corresponding TOSCs to 16.76%.[232] In fact, employing a NFA as third component with a smaller band gap and a higher LUMO energy level than the acceptor host can achieve simultaneously enhancement in both V_{OC} and J_{SC}, as demonstrated by An's group by adding MF1 in PM6:Y6 binary system achieving a high PCE of 17.22%.[244]

On the morphological perspective, from the thermodynamics point of view, it has been demonstrated that a third component with suitable miscibility with host acceptor is more likely to form a mixed acceptor phase, resulting in quasilinear relationship between open-circuit voltage (V_{OC}) and weight ratio of third component. Jia *et al.* found that by adding ITIC as third component into PM6:Y6 binary blend, the variations of ITIC content in acceptor domain can linearly tunable V_{OC}, which was modulated by the interplay between CT states and nonradiative recombination rates.[64] Furthermore, structural similarities between two nonfullerene acceptors allows them to form an alloy-like composite with homogeneous acceptor phases, leading to optimize energy-level alignment and maintain the blend morphology, thus maintaining the device fill factor (FF).[245] Apart from the performance enhancement, achieving stable TOSCs is critical for commercialization, thus Dong and co-workers reported this similar structure of two NFAs could facilitate better thermal and photostability of TOSCs, which might be associated with suppressed aggregation tendency by alloy-formation.[246] These studies highlight the synergizing use of third component that has a higher LUMO level and a relatively low miscibility with the host acceptor for obtaining highly efficient and photostable NFA-based TOSCs. However, reports of highly efficient and stable TOSCs with acceptor alloy-like formation are still rare, especially for Y7-based systems.

In this contribution, two distinct categories of acceptor materials – the classic fullerene derivative PC70BM and the classic nonfullerene ITIC-M are employed as the third components in the state-of-the-art PM6:Y7 host binary system. Despite the fact that the two acceptor guests $PC_{70}BM$ and ITIC-M possess completely different chemical structures, we notice a PCE enhancement of over 7% in the ternary devices due to their good miscibility and higher LUMO energy level relative to the host acceptor Y7. Compared to the champion PCE of the PM6:Y7 binary OSCs (PCE = 16.46%), the champion PCEs of the ternary OSCs as high as 17.73% and 17.67% for PM6:Y7:ITIC-M and PM6:Y7:$PC_{70}BM$ devices, respectively, are demonstrated. Due to the good compatibility between ITIC-M or $PC_{70}BM$ and Y7, an acceptor alloy-like state was formed, showing a nondisrupted bicontinous film morphology in ternary blends, which is favorable for charge dissociation, charge collection and transport properties with suppressed bimolecular and trap-assisted charge recombination. The higher LUMO levels of the third components helps the ternary OSCs elevates the V_{OC} by reducing energy-loss and reverse saturation current, creating less-localized shallow trap sites along with suppressing charge recombination and Urbach energy. Furthermore, photoluminescence and single material device investigations demonstrate energy transfer between the two well-mixed acceptors, contributing to the increased current. The combination of these improvements leads in a simultaneously enhanced V_{OC}, J_{SC} and FF with respect to those of binary host. The findings imply that one of the keys to obtain high efficiency ternary OSCs is establishing good morphological compatibility with host materials with suitable energy levels and complementary absorption.

5.2 Results and discussion

Figure 5.1a depicts the chemical structures of host donor PM6, host NFA-based Y7, and third components ITIC-M NFA and $PC_{70}BM$ FA, as well as the schematic illustration of the device structure used in this work. **Figure 5.1b** shows the HOMO and LUMO energy levels of PM6, Y7, ITIC-M, and $PC_{70}BM$, which are consistent with previous studies.[208,245,247,248] Both of secondary acceptors $PC_{70}BM$ and ITIC-M have LUMO levels higher than those of host acceptor Y7, which is expected that the ternary OSCs may yield higher V_{OC} values. **Figure 5.1c** presents the normalized UV-vis absorption spectra of the used materials in their neat-film states. The maximum absorption peaks of ITIC-M (703 nm) lie between those of

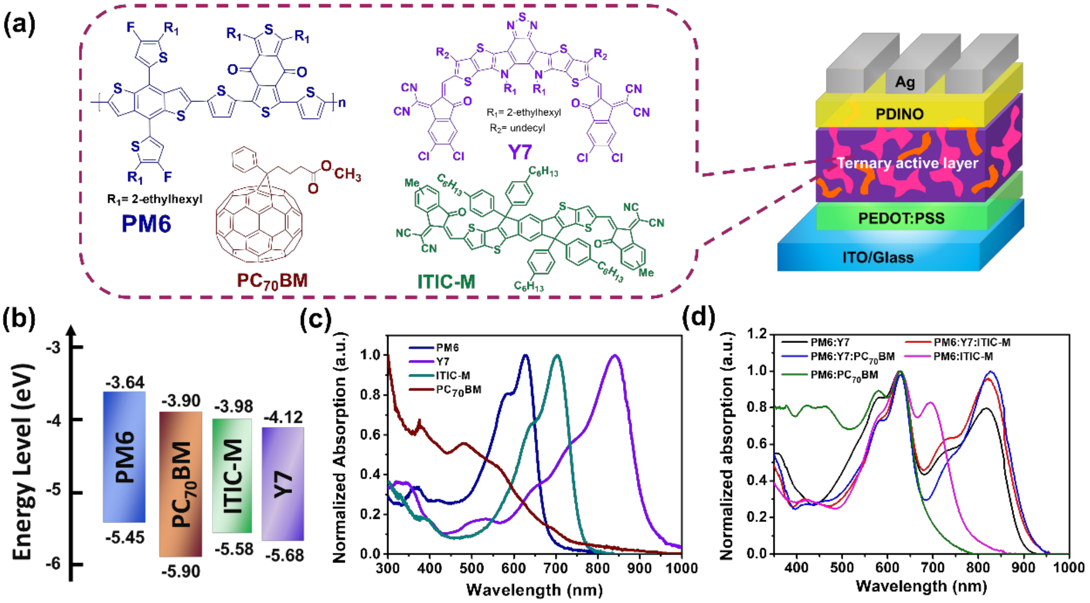

Figure 5.1 (a) Chemical structures of photoactive materials and schematic diagram of device architecture used in this study, (b) energy level diagrams of PM6, Y7, ITIC-M and $PC_{70}BM$, (c) normalized UV-Vis absorption spectra of neat PM6, Y7, ITIC-M and $PC_{70}BM$ films; and (d) normalized absorption spectra of the binary and ternary blend films.

PM6 (626 nm) and Y7 (841 nm) whereas $PC_{70}BM$ have a strong light absorption in the wavelength range from 300 nm to 700 nm, indicating the formation of a complementary and broaden absorption spectrum by third components. In addition to the pristine materials, the normalized UV-vis absorption spectra of the blend films are exhibited in **Figure 5.1d**. It is observed that the binary films of PM6:Y7 host system, PM6:ITIC-M, and PM6:$PC_{70}BM$ have absorption peaks (λ_{max}) at 817 nm, 694 nm and 427 nm, respectively, implying that adding $PC_{70}BM$ and ITIC-M as third components may compensate for the absorption of host system. In ternary PM6:Y7:ITIC-M blend film, a slightly redshifted and increased absorption peak intensity at ~821 nm is observed, along with an increase shoulder near 730 nm, indicating the contribution from ITIC-M. On the other hand, due to the 10 nm redshifted and increased Y7 absorption peak position in ternary PM6:Y7:$PC_{70}BM$, along with a decrease shoulder near 684 nm, thus we suspected that $PC_{70}BM$ would have a good compatibility with Y7 to provide more photon absorption which induce a higher short-circuit current density (J_{SC}) values in ternary OSCs.[249]

To confirm the good compatibility of the two acceptors, the contact angle measurements of neat films were performed to study the surface tension of materials and thus to estimate the strength interaction between them and their effect on the phase segregation and blend morphology. **Figure 5.2** presents the contact angle images based on liquid drops of water and ethylene glycol (EG), while **Table 5.1** lists the surface tension (γ) values of the materials calculated according to Wu's equation and the Flory–Huggins interaction parameter (χ).[85,250] As a result, the surface energies for PM6, Y7, ITIC-M, and $PC_{70}BM$ pristine films are 23.98 mN m^{-1}, 27.23 mN m^{-1}, 28.31 mN m^{-1}, and 28.21 mN m^{-1}, respectively. Accordingly, the interaction parameter χ values between PM6 and Y7 ($\chi_{\mathrm{PM6,Y7}} = 0.103$) is relatively small, suggesting a good miscibility between them. In contrast, the $\chi_{\mathrm{PM6,ITIC\text{-}M}} = 0.180$ and $\chi_{\mathrm{PM6,PCBM}} = 0.171$ are higher than those of $\chi_{\mathrm{PM6,Y7}}$ values, indicating a lower miscibility (i.e., weaker interactions) between PM6 host donor and the third components. Interestingly, the interaction parameter between Y7 and the third components are extremely low ($\chi_{\mathrm{Y7,ITIC\text{-}M}} = 0.011$ and $\chi_{\mathrm{Y7,PCBM}} = 0.009$), indicating a good compatibility between host and guest acceptors which could form an alloy-like composite, supporting our hypothesis. From thermodynamic point of view, therefore, the addition of a less miscible third component (larger value of χ) relative to the donor effectively increase the pure phase domain sizes, which is favorable for charge dissociation and charge collection.[58]

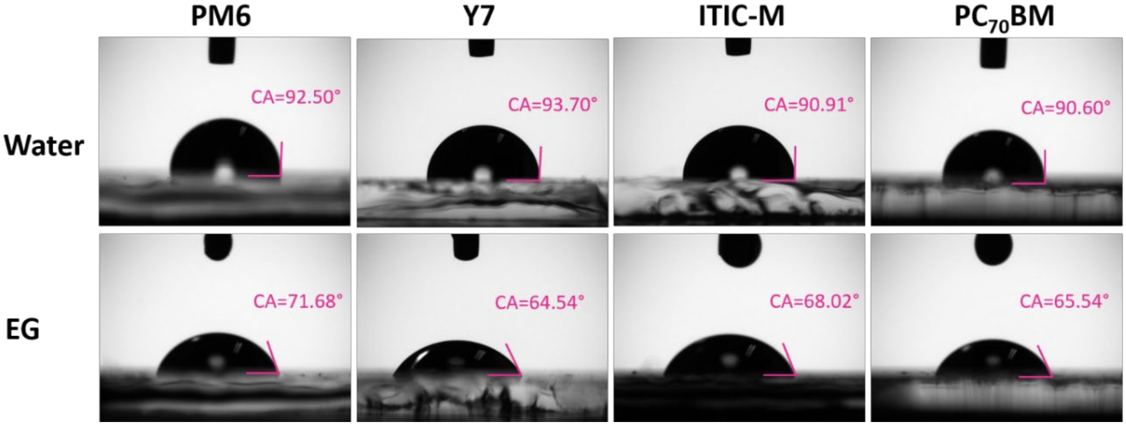

Figure 5.2 Contact angle images of the neat films of PM6, Y7, ITIC-M, and PC$_{70}$BM. The values of the images are the average contact angle from nine tests of different part in the same film.

Table 5.1 Contact angles, surface tension, and interaction parameters.

Materials	**θ$_{water}$ (°)**	**θ$_{EG}$ (°)**	**γ^p (mN m^{-1})**	**γ^p (mN m^{-1})**	**Surface tension (mN m^{-1})**	**$\chi^{a)}$ with PM6**	**$\chi^{a)}$ with Y7**
PM6	92.50	71.68	12.46	11.53	23.98	N/A	0.103
Y7	93.70	64.54	7.77	19.46	27.23	0.103	N/A
ITIC-M	90.91	68.02	19.17	9.14	28.31	0.180	0.011
PC$_{70}$BM	90.60	65.54	17.34	10.86	28.21	0.171	0.009

$^{a)}$ The Flory-Huggins interaction parameter based on the surface tension data formula between the donor (D) and the acceptor (A) calculated using $\chi = (\sqrt{\gamma D} - \sqrt{\gamma A})^2$.

To investigate the performance of ternary OSC with different third component materials addition, PC$_{70}$BM FA and ITIC-M NFA, a series of binary and ternary OSCs were fabricated with a conventional device architecture of ITO/PEDOT:PSS/active layer/PDINO/Ag. The host donor to acceptor weight ratio was fixed at 1:1, following the optimized conditions for PM6:Y7, and the contents of the third components changes proportionally to determine the optimal composition. The detailed fabrication and characterization of OSCs are described in the Supporting Information. The current density-voltage (*J-V*) curves for the optimal binary and ternary devices measured under AM 1.5G illumination with 100 mW cm^{-2} light intensity are plotted in **Figure 5.3a**. The detailed photovoltaic parameters are listed in **Table 5.2**. The average performance parameters are obtained from at least twenty individual OSC devices. The PM6:Y7 binary OSCs deliver a PCE_{max} of 16.46% (average PCE of 16.37 ± 0.39%) with a V_{OC} of 0.845 ± 0.008 V, an impressive J_{SC} of 28.02 ± 0.74 mA cm^{-2}, and an FF of 66.56 ± 1.28%. In contrast, the PM6:ITIC-M binary OSCs show a lower PCE_{max} of 9.22% (average PCE of 8.86 ± 0.25%) with a significantly enhanced V_{OC} of 1.019 ± 0.006 V but reduced values of J_{SC} (15.86 ± 0.47 mA cm^{-2}) and FF of (54.86 ± 1.24%). Moreover, the PM6:PC_{70}BM binary OSCs exhibit PCE_{max} of 9.43% (average PCE of 8.88 ± 0.32%) with a reduced J_{SC} of 13.51 ± 0.38 mA cm^{-2} but an increased V_{OC} (0.960 ± 0.007 V) and FF (68.33 ± 1.13%). It should be noted that the PM6:Y7 showed the highest efficiency for binary system, which is worth investigated as the high-performing host binary in ternary system. With a minute addition of ITIC-M (10 wt%), the ternary PM6:Y7:ITIC-M OSCs achieved an impressive PCE_{max} of 17.73% (average PCE of 17.15 ± 0.33%) with V_{OC} of 0.868 ± 0.004 V, J_{SC} of 29.27 ± 0.57 mA cm^{-2}, and FF of 67.58 ± 0.89%, outperforming the binary host device. The champion ternary device with the addition of ITIC-M benefits from the significant increase of V_{OC} and J_{SC} and slightly improved average FF, mainly related to the up-shifted LUMO energy level and complementary absorption of ITIC-M with respect to that of Y7. Besides, loading a small amount of blue-shifted absorption third component material, PC_{70}BM (10 wt%), into PM6:Y7 host blend had successfully enhanced the device performance for ternary PM6:Y7:PC_{70}BM device due to the concurrent increase in V_{OC} (0.856 ± 0.006 V), J_{SC} (29.38 ± 0.83 mA cm^{-2}), and FF (68.39 ± 1.34%), leads to the high PCE_{max} of 17.67% (average PCE of 17.12 ± 0.34%). The significant increase of J_{SC} and FF in PM6:Y7:PC_{70}BM device should be attributed to the two factors. First, the enhanced photon harvesting of ternary blend due to the broader absorption window that cover the light spectrum from ultraviolet to near-infrared (NIR) regions, and the second, the well-developed morphology of ternary blend

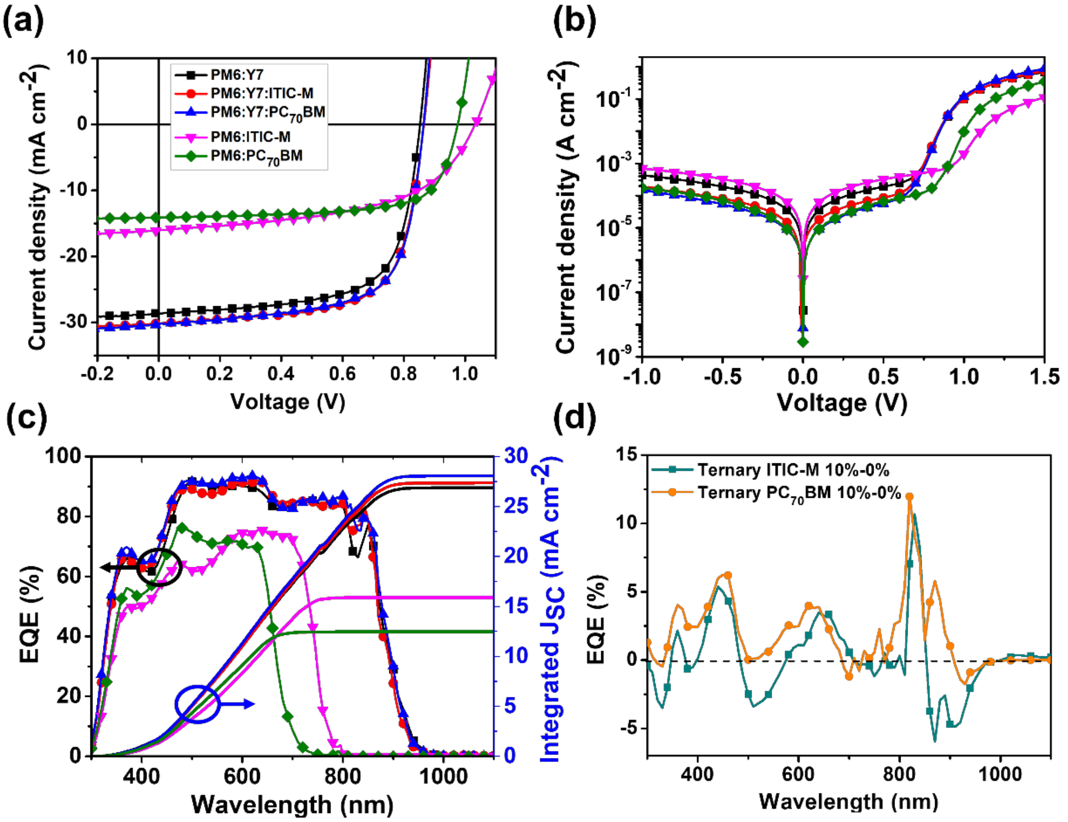

Figure 5.3 Current density-voltage (J-V) characteristic curves measured under (a) AM 1.5G illumination and (b) in dark condition; (c) EQE curves of the corresponding OSCs and (d) the ΔEQE values of 10% addition of either ITIC-M or $PC_{70}BM$ with respect to the 0% device.

films with $PC_{70}BM$ addition. As both ternary ITIC-M and ternary $PC_{70}BM$ have similar average PCEs, the V_{OC} and J_{SC} are the main parameters that improve substantially with the addition of third component, which should be benefited from the lower LUMO levels and an alloy-like acceptor phase formation due to good compatibility between the host and guest acceptors. In light of the higher lying LUMO energies in both ITIC-M and ternary $PC_{70}BM$ with regard to Y7, we believe that the energy loss (E_{loss}) can be regulated in the ternary cells. The E_{loss} of OSCs can be determined according to $E_{loss} = E_{gap} - qV_{OC}$ with E_{gap} is the optical energy gap calculated from Tauc's method from the absorption spectra of the blends.[251] As listed in Table 5.2, the PM6:Y7 binary host OSCs shows a E_{loss} of 0.539 eV, consistent to the values in recent study.[208] The E_{loss} of the optimized ternary ITIC-M- and $PC_{70}BM$-based OSCs are 0.49 eV and 0.484 eV, respectively, which are lower compared to their binary counterparts. The reduced E_{loss} by incorporating appropriate third components are critical in improving performance of ternary OSCs.

Table 5.2 Device performance parameters of optimized binary and ternary OSCs measured under AM 1.5G with 100 mW cm^{-2} intensity.

Blend	**V_{OC} (V)**	**J_{SC} (mA cm^{-2})**	**J_{SC}^{EQE} (mA cm^{-2})**	**FF (%)**	**PCE $^{a)}$ (%)**	**E_{loss} (eV)**
Binary PM6:Y7	(0.845 ± 0.008) 0.850	(28.02 ± 0.74) 28.65	26.87	(66.56 ± 1.28) 67.57	(16.37 ± 0.39) 16.46	0.539
Ternary PM6:Y7:ITIC-M	(0.868 ± 0.004) 0.870	(29.27 ± 0.57) 30.16	27.36	(67.58 ± 0.89) 67.57	(17.15 ± 0.33) 17.73	0.490
Ternary PM6:Y7:$PC_{70}BM$	(0.856 ± 0.006) 0.860	(29.38 ± 0.83) 30.22	28.05	(68.39 ± 1.34) 67.98	(17.12 ± 0.34) 17.67	0.484
Binary PM6:ITIC-M	(1.019 ± 0.006) 1.030	(15.86 ± 0.47) 16.27	15.87	(54.86 ± 1.24) 57.20	(8.86 ± 0.25) 9.22	0.581
Binary PM6:$PC_{70}BM$	(0.960 ± 0.007) 0.970	(13.51 ± 0.38) 13.91	12.46	(68.33 ± 1.13) 69.93	(8.88 ± 0.32) 9.43	0.801

$^{a)}$ The maximum device parameters values are shown outside of parentheses. The statistical values are listed in parentheses, obtained from over 20 devices.

Figure 5.3b presents the dark *J-V* characteristics of binary and ternary OSCs, which provide an information regarding their bulk and interfacial resistance (R_S), ideality factor along with the leakage current and charge carrier recombination (R_{Sh}) of the devices. The R_S and R_{Sh} (parasitic resistance) values of the optimized devices are listed in **Table 5.3**. At reverse voltage bias without illumination (V < 0V), the drift of charge carriers is determined by R_{Sh}, which is correlated with the current loss such as leakage current. The ideal R_{Sh} should be very high, resulting in zero current flows through R_{Sh}, *i.e.* no current leakage in the device. The R_{Sh} values are 2.75×10^3, 6.20×10^3, and 1.59×10^3 Ω cm^2 for PM6:Y7, PM6:Y7:ITIC-M, and PM6:ITIC-M devices, respectively, implying that the leakage current and higher degree of charge carrier recombination in the ternary device can be restrained by incorporating appropriate ITIC-M. The similar tendency to suppress leakage current and lowering the degree of charge carrier recombination can be regulated by adding a proper amount of $PC_{70}BM$ in ternary device, demonstrating by the higher R_{Sh} value of 1.13×10^4 Ω cm^2 observed for ternary PM6:Y7:$PC_{70}BM$ device than those of binary host and binary PM6:$PC_{70}BM$ device (1.07×10^4 Ω cm^2). It is worth noting that the high leakage current in ITIC-M-based OSCs leads to a significant reduction about one-order magnitude lower in R_{Sh} values with respect to those of $PC_{70}BM$-based OSCs, which indicates that $PC_{70}BM$ could provide a good interfacial morphology by suppressing the leakage current and morphological traps on the PM6-donor system, better than those of ITIC-M, as discussed later. At high voltages ($V > 1V$), the charges start to accumulate and are limited by R_S. R_S values are 1.29, 1.41, and 1.19 Ω cm^2 for PM6:Y7, PM6:Y7:ITIC-M, and PM6:Y7:$PC_{70}BM$ devices, lower than those R_S values of 4.07 and 1.77 Ω cm^2 for PM6:ITIC-M and PM6:$PC_{70}BM$ binary devices, respectively, indicating fewer defects at the Y7-based BHJ blend and/or at the interfaces within the corresponding devices, which should be beneficial for an efficient charge carrier collection and better charge carrier mobility.[242,252] It has been demonstrated that the parasitic resistances effect might contribute to the change of FF in TOSCs, thus we calculated the ideal FF (FF_0) values of all devices along with the FF affected by R_S (FF_{Rs}) and R_{Sh} (FF_{Rsh}), as summarized in **Table 5.4**. In ideal condition, FF_0s are expected to be improved by the addition of third components, however the observed experimental FFs are much lower than the calculated ideal FF_0, emphasizing the significant effect of R_S and R_{Sh} on the studied devices.

The other parameter that can be extracted by dark J-V characteristics is the dark reverse saturation current density (J_0) which represent the current density of minority carriers. Suppressing J_0 is an important strategy to increase V_{OC} as V_{OC} is strongly related to J_{ph}/J_0 as described by equation 5.1:

$$V_{OC} = \frac{kT}{q} \ln\left(\frac{J_{ph}}{J_0} + 1\right) \tag{5.1}$$

where n_{id} is the ideality factor that can be extracted from either light dependency measurement and transient techniques as mentioned later, k is the Boltzmann constant, T is the temperature, and q is the elementary charge. The extracted J_0 values are 37.00, 7.36, 9.98, 2.03, and 3.96×10^{-9} A cm^{-2} for binary host, ITIC-M ternary, PC$_{70}$BM ternary, ITIC-M binary, and PC$_{70}$BM binary devices, respectively. The gradually decreased J_0 values in the studied devices is in an excellent agreement with the increased V_{OC} values of ternary OSCs, implying that the J_0 values can be restrained according to the slightly enhanced LUMO levels of alloyed acceptors along with the increased ITIC-M and PC$_{70}$BM content.

Table 5.3 Extracted series resistance and shunt resistance values from dark *J-V* curves for all devices.

Blend system	***R$_S$*** **(Ω cm^2)**	***R$_{Sh}$*** **(Ω cm^2)**	**J$_{leakage}$ at -0.5V (A cm^{-2})**	**J$_0$ (A cm^{-2})**
Binary PM6:Y7	1.29	2.75×10^{3}	1.90×10^{-4}	3.70×10^{-8}
Ternary PM6:Y7:ITIC-M	1.41	6.20×10^{3}	8.10×10^{-5}	7.36×10^{-9}
Ternary PM6:Y7:PC$_{70}$BM	1.19	1.13×10^{4}	5.60×10^{-5}	9.98×10^{-9}
Binary PM6:ITIC-M	4.07	1.59×10^{3}	3.30×10^{-4}	2.03×10^{-7}
Binary PM6:PC$_{70}$BM	1.77	1.07×10^{4}	7.10×10^{-5}	3.96×10^{-9}

To investigate the underlying reason of the enhanced J_{SC} values, the corresponding external quantum efficiency (EQE) spectra of the relevant OSCs were measured, as presented in **Figure 5.3c**. It is observed that the host binary PM6:Y7 has a broad photon response in the wavelength region of 300 – 950nm, whereas the binary PM6:ITIC-M and binary PM6:PC$_{70}$BM show the EQE response in the wavelength of 300 – 780nm and 300 – 730nm, respectively, which are in good agreement with UV-vis profile. In comparison with binary host device, the optimized ITIC-M-based ternary device exhibits an enhanced EQE responses in the whole wavelength range of 300 – 830nm and finely increase in the range of 1000 – 1100nm (see **Figure 5.3d**), whereas the optimized $PC_{70}BM$-based ternary device shows an enhanced EQE responses in the whole wavelength of 300 – 900 nm with a higher response at NIR wavelength (>800nm). The increased EQE responses for both ternary devices are in good agreement with the simultaneously red-shifted λ_{max} of PM6 and Y7 moieties in the ternary blends compared to the corresponding neat films, suggesting a better molecular orientation of PM6 and Y7 moieties after loading a small amount of compatible third components, thus provide more efficient photo-current generation. A good agreement between UV-vis and EQE results corroborates the increment in the J_{SC} values of ternary devices with respect to the binary counterparts. In addition, the calculated J_{SC} values from the integrating EQE spectra conforms the J_{SC} values measured from the J-V curves with deviations of less than 10%.

Table 5.4 Parameters used to predict the fill factor for all studied devices.

Blend system	r_s	r_{sh}	v_{OC}	FF_O	FF_{Rs}	FF_{Rs+Rsh}	FF_{exp}
Binary PM6:Y7	0.043	16.414	23.347	0.828	0.793	0.753	0.676
Ternary PM6:Y7:ITIC-M	0.050	10.920	26.540	0.843	0.802	0.741	0.676
Ternary PM6:Y7:$PC_{70}BM$	0.040	10.753	25.908	0.840	0.807	0.744	0.680
Binary PM6:ITIC-M	0.064	5.971	28.237	0.850	0.796	0.687	0.572
Binary PM6:$PC_{70}BM$	0.058	16.018	27.348	0.847	0.797	0.756	0.699

To analyze the effect of the third components addition on the surface morphology of the corresponding blends, we performed the atomic force microscopy (AFM) and transmission electron microscopy (TEM) measurements. The AFM topographic and phase images of binary and ternary blends are presented in **Figure 5.4a** and **5.4b**. In the topographic images, the blend films of Y7-, ITIC-M-, and $PC_{70}BM$-based binary blends displayed the root-mean-square (RMS) surface

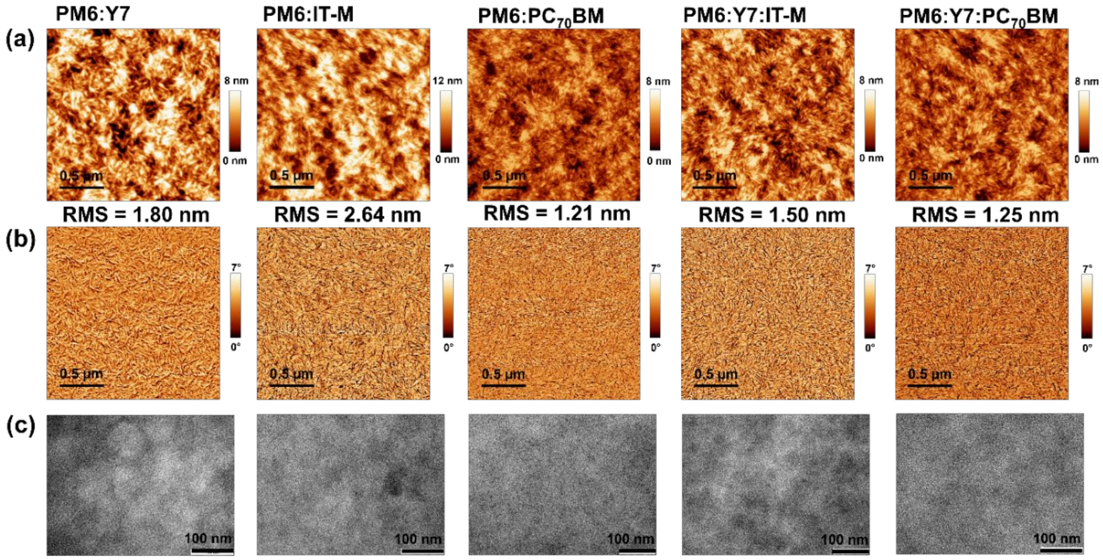

Figure 5.4 AFM (a) topographic and (b) phase images and (c) TEM images of binary and ternary blend films.

roughness of 1.80, 2.64, and 1.21 nm, respectively. The rougher surfaces of PM6:ITIC-M is undesirable for charge collection by the electrodes, which can be correlated to the larger $\chi_{\text{PM6,ITIC-M}}$ values than that of $\chi_{\text{PM6,PCBM}}$ and $\chi_{\text{PM6,Y7}}$ from the surface tension measurement. Thus, PM6:ITIC-M OSCs exhibited the lowest FF value in the *J-V* characteristic. After loading a small amount of ITIC-M/PC$_{70}$BM, the ternary blend films of PM6:Y7:ITIC-M and PM6:Y7:PC$_{70}$BM were modified with an optimized RMS roughness of 1.50 and 1.25 nm. As a result, a better dispersity of interpenetrating nanostructure with the favorable shape of the domains in ternary blend films interposed between those of Y7- and ITIC-M/PC$_{70}$BM-based binary blends is observed in the AFM phase images. It is worth noting the smaller RMS and homogeneous nanostructure of PC$_{70}$BM-based binary and ternary blends than those of either Y7-based binary or ITIC-M-based binary and ternary blends may facilitate good interfacial morphology, which in accordance with the lower leakage current observed in dark *J-V* characteristics. Moreover, the size of the nanofibril structures become smaller with increasing ITIC-M contents. The TEM images further corroborate the changes of dispersity in nanoscale blend morphology between binary and ternary blends, as shown in **Figure 5.4c**. The homogeneous small domain size and nanofibrous structures can be observed in binary blend films. The fine variation of nanofibrous structures observed from TEM images of the ternary blend suggests the good compatibility among the used materials. In good agreement with the surface tension calculation, the good compatibility between Y7 and third component ITIC-M/$PC_{70}BM$ is favorable for the acceptor alloy state formation, leading to more efficient electron transport channel.[253]

As widely known in OSCs community, three different fundamental mechanisms are mainly occurred in ternary BHJ: 1) charge-transfer mechanism, where a cascading energy alignment is formed among three components for efficient charge transport and dissociation; 2) energy-transfer mechanism, where the third component with a different bandgap performs as an energy donor, absorbing more photons and inducing long-distance or short-distance energy transfer to the energy acceptor; 3) parallel or alloy mechanism, where the third component either creates additional pathways or mix with the host component and behaves like one tunable material to facilitate charge process.[254] The photoluminescence (PL) measurement can be used as a technique to disregard the charge or energy transfer within the ternary systems. PL spectra of the neat (PM6), binary host (PM6:Y7) and ternary (PM6:Y7:ITIC-M and PM6:Y7: $PC_{70}BM$) films were measured under an excitation wavelength of 600 nm. As plotted in **Figure 5.5a**, the neat PM6 film exhibits the strongest PL emission. The emission peak at 665 nm of PM6 can be completely quenched in all blend films and in the meantime PL emission peaks of blend films are blue-shifted, indicating the presence of an electron transfer between PM6 and the acceptors. The two ternary blend films were more efficiently quenched than the PM6:Y7 binary blend, suggesting the addition of ITIC-M or $PC_{70}BM$ as third component indeed promote electron transfer from PM6 to the mixed acceptor phase. Considering that the overlap between the UV-vis spectral absorption of Y7 and the PL emission of third components ITIC-M or $PC_{70}BM$ (see **Figure 5.6**), this strongly indicates energy transfer between ITIC-M or $PC_{70}BM$ and Y7, which could contribute to the slightly increased J_{SC} values and enhanced EQE spectra of ternary OSC devices. Additionally, we fabricated a series of devices with the active layer containing the acceptors only to give further insight on the intermolecular dynamics process between Y7 and the secondary acceptors (ITIC-M or $PC_{70}BM$). **Figure 5.5b** shows the *J-V* characteristics of the corresponding devices under AM 1.5G illumination with 100 mW cm^{-2} light intensity, J_{SC}s of the devices is rather low due to the absence of PM6 donor in the active layer. The J_{SC} values are 1.874, 0.257, 0.285, 0.358 and 1.658 mA cm^{-2} for Y7, ITIC-M, $PC_{70}BM$, Y7:ITIC-M (1:0.1), and Y7:$PC_{70}BM$ (1:0.1) based devices, respectively, suggesting that the charge transfer occurs between either Y7 and ITIC-M or Y7 and $PC_{70}BM$ should be negligible in blend films. According to the above analysis, the dynamic process between the mixed acceptor alloys should be energy transfer from either ITIC-M or $PC_{70}BM$ to Y7, which may provide an additional route for improving exciton utilization of ternary OSCs. **Figure 5.5c** illustrates the working mechanism observed in PM6:Y7:$PC_{70}BM$ ternary OSC, a similar working mechanism is also shown by PM6:Y7:ITIC-M ternary OSC.

As demonstrated above that the extra addition of third components can modify the photovoltaic parameters and blend morphologies, further investigation of charge dynamics in the ternary devices, including charge separation, transport, and collection is worth studied. First, the photocurrent density (J_{ph}) versus effective voltage (V_{eff}) measurement of the studied devices were performed to gain insight into their exciton dissociation and charge collection. As shown in **Figure 5.5d**, J_{ph} for all devices became saturated in the large effective voltage regime (V_{eff} > 0.5V), suggesting that under high applied field, nearly all the excitons could separate and generated free carriers, and then collected by the contacts. The corresponding data is summarized in **Table 5.5**, including the saturated current density (J_{sat}), maximum

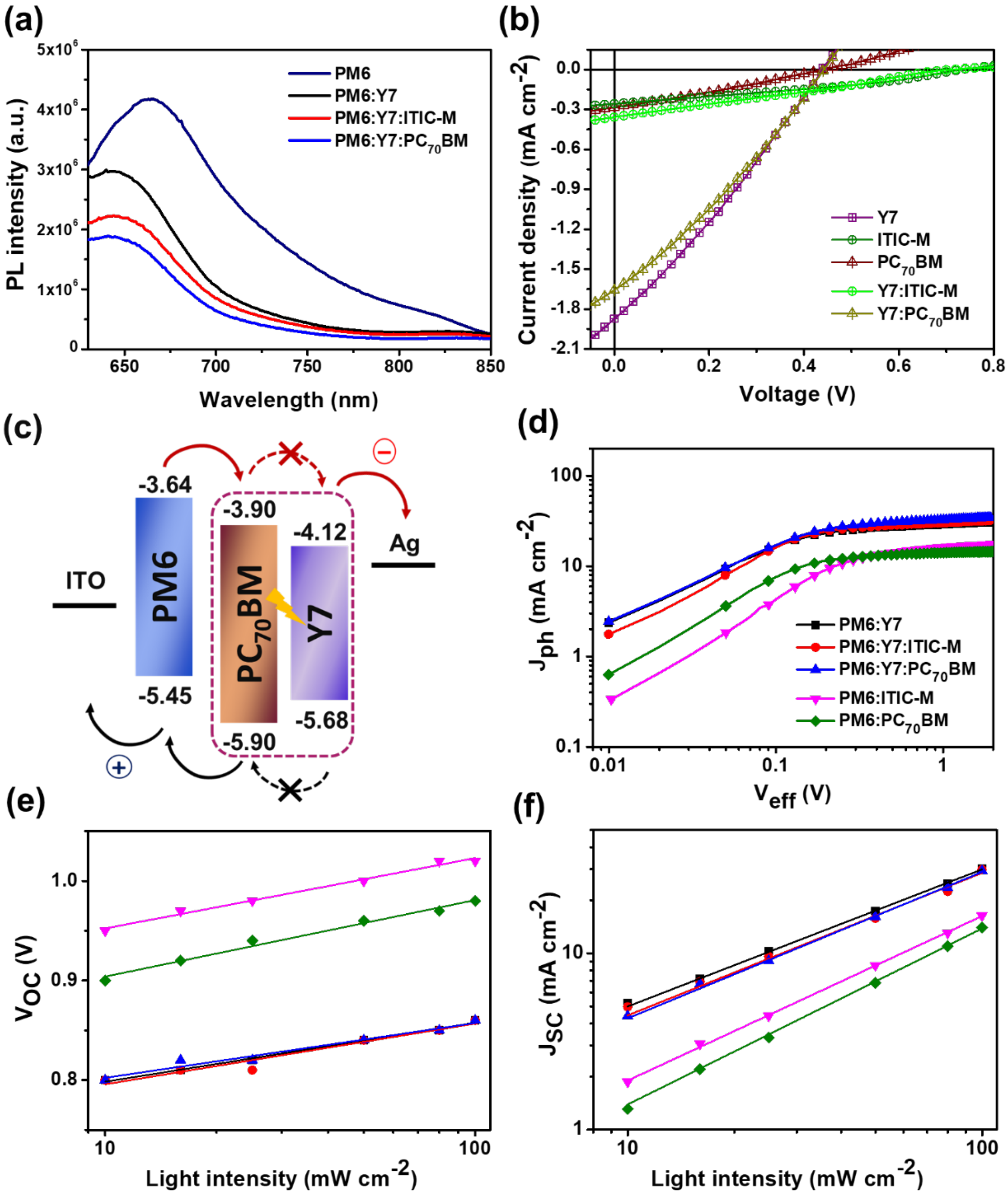

Figure 5.5 (a) PL spectra of Y7-based devices excited at 600 nm and (b) the *J-V* curves of acceptor-only devices illuminated under AM 1.5G condition; (c) Energy levels diagram illustrating a ternary working mechanism in our study; (d) J_{ph}–V_{eff} curves, (e) V_{OC} and (f) J_{SC} versus light intensity characteristics based on optimized binary and ternary OSCs.

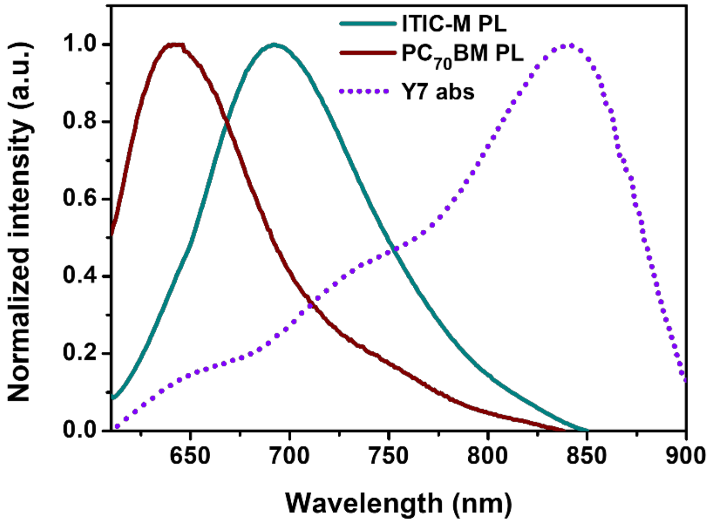

Figure 5.6 Absorption spectrum of Y7 film and emission spectra of ITIC-M and $PC_{70}BM$ films.

Table 5.5 Calculated parameters obtained from J_{ph}-V_{eff} curves.

Blend system	J_{sat} **(mA cm^{-2})**	J_{SC} **(mA cm^{-2})**	J_{MPP} **(mA cm^{-2})**	G_{max} **(m^{-3} s^{-1})**	η_{diss} **(%)**	η_{coll} **(%)**	P_{diss}	P_{coll}
Binary PM6:Y7	30.97	28.83	23.01	1.93×10^{28}	93.08	74.28	1.80×10^{30}	1.44×10^{30}
Ternary PM6:Y7:ITIC-M	31.85	30.05	23.95	1.99×10^{28}	94.36	75.19	1.88×10^{30}	1.49×10^{30}
Ternary PM6:Y7:$PC_{70}BM$	32.71	31.01	25.00	2.04×10^{28}	94.81	76.42	1.94×10^{30}	1.56×10^{30}
Binary PM6:ITIC-M	17.01	16.06	12.10	1.06×10^{28}	94.38	71.13	1.00×10^{30}	7.55×10^{29}
Binary PM6:$PC_{70}BM$	14.33	14.08	11.70	8.95×10^{27}	98.25	81.61	8.79×10^{29}	7.30×10^{29}

amounts of absorbed photons (G_{max}), exciton dissociation (η_{diss}), charge collection efficiency (η_{coll}), dissociation and collection probabilities (P_{diss} and P_{coll}) values. Binary PM6:$PC_{70}BM$ OSCs show the lowest G_{max} value of 8.95×1028 m^{-3} s^{-1}, consistent with its lowest value of J_{SC}. Higher values of G_{max} implied excellent light harvesting in the devices, which corresponding to more efficient exciton generation.

The η_{diss} and η_{coll} values as well as P_{diss} and P_{coll} for both $PC_{70}BM$- and ITIC-M-based ternary devices are higher than those of binary host PM6:Y7 OSCs, indicating that the incorporated $PC_{70}BM$ or ITIC-M has a positive effect on the exciton dissociation and charge collection processes, which could be finely associated to the increased of J_{SC} and FF values in the optimized ternary OSCs.

To investigate the influence of incorporating ITIC-M/$PC_{70}BM$ on the electron transport properties of the devices, the electron-only devices with a structure of ITO/ZnO/active layer/PDINO/Ag were fabricated. The electron (μ_e) mobilities were carefully evaluated by a space-charge-limited-current (SCLC) method following the Mott-Gurney model.[255,256] Both ternary blend films of PM6:Y7:ITIC-M and PM6:Y7:$PC_{70}BM$ show higher μ_e values of 3.91×10^{-4} and 3.67×10^{-4} $cm^2V^{-1}s^{-1}$, respectively than those of binary host device (3.04×10^{-4} $cm^2V^{-1}s^{-1}$), as depicted in **Figure 5.7a**. Moreover, as the ITIC-M or $PC_{70}BM$ increase, the μ_e values decrease, giving the PM6:ITIC-M and PM6:$PC_{70}BM$ binary blends the μ_e values of 6.62×10^{-5} and 4.21×10^{-4} $^{1}cm^2V^{-1}s^{-1}$, respectively. The enhanced electron mobility of the ternary blend should facilitate charge transport and suppress charge recombination, which contributes to the higher FF among all the devices in this work. Furthermore, we investigated the trap density (N_{trap}) of the different binary and ternary blend films using the following equation 5.2:

$$V_{TFL} = \frac{qN_{trap}L^2}{2\varepsilon_r\varepsilon_0} \tag{5.2}$$

where, V_{TFL} is the trap-filled limit voltage evaluated from SCLC measurements as illustrated in **Figure 5.7b**, in which q is the elementary charge, L is the thickness of active blend layer ε_r is the dielectric constant of the blend film, and ε_0 is the vacuum permittivity. It is worth mentioning that the values of the V_{TFL} were diminished for the ternary devices, as listed in the inset of Figure 5.7b. Moreover, it was interesting to obtain that the ternary devices showed remarkable lower N_{trap} values of 2.13×10^{15} and 1.94×10^{15} cm^{-3} for the PM6:Y7:ITIC-M and PM6:Y7:$PC_{70}BM$ devices. On the other hand, PM6:Y7, PM6:ITIC-M and PM6:PC$_{70}$BM binary devices demonstrated higher N_{trap} values of 6.20 ×10^{15}, 1.74 ×10^{16}, and 3.10 ×10^{15} cm^{-3}, respectively. Accordingly, this exhibited behavior indicates that the ternary blend passivated the trap states, providing enhanced path for effectively charge carrier transfer and collection by suppressing the defect density and the recombination mechanisms explains their superior P_{diss}, $G_{\max}$, J_{SC} along with their champion PCE more than the binary ones.

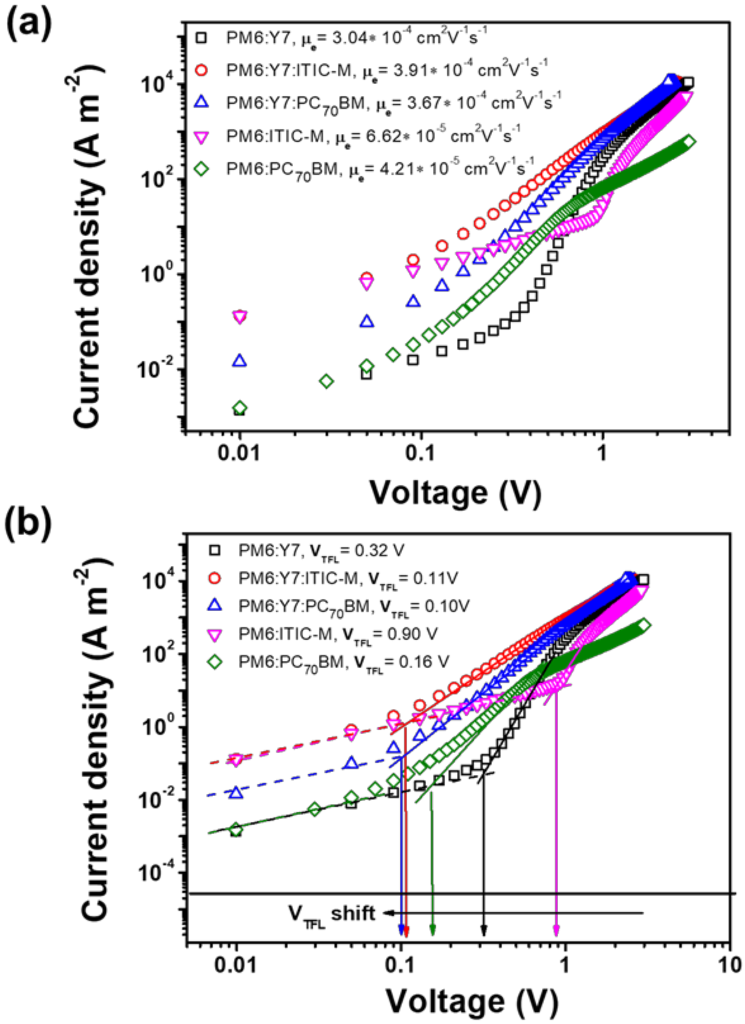

Figure 5.7 The log-log plot of dark J-V curves of the electron only devices with (a) electron mobilities and (b) V_{TFL} values of the optimized binary and ternary OSCs.

To investigate the charge recombination mechanism in the binary and ternary OSCs, the dependence of V_{OC} and J_{SC} on the various light intensities (P_{light}) were measured according to the corresponding *J-V* characteristics (see **Figure 5.5e,f** and **Table 5.6**). The degree of trap-assisted recombination in the binary and ternary OSCs can be estimated by the variation of V_{OC} as a function of P_{light} described by the relationship $V_{\mathrm{OC}} \propto (S2kT/q)\ \ln(P_{\mathrm{light}}) \propto (nkT/q)\ \ln(J_{\mathrm{SC}})$, where n stands for the recombination ideality factor of the diode ($n = S2/S1$), k is the Boltzmann constant, T is the cell temperature in Kelvin, and q is the elementary charge. Generally, the n values close to 2 reflects the presence of the traps across the active layer and/or at the BHJ/electrode interface, which leads trap-assisted recombination as the major recombination in OSCs.[175] As shown in Figure 5e and Table S5, the calculated n values are 1.280, 1.267, and 1.303 for PM6:Y7, PM6:Y7:ITIC-M, and PM6:ITIC-M devices, respectively, which indicates that the trap-assisted recombination can be restrained in the ternary devices by the addition of ITIC-M. Showing similar tendency, n values of PM6:Y7:PC$_{70}$BM and PM6:PC$_{70}$BM are 1.160 and 1.294, respectively, implying that adding PC$_{70}$BM can make trap-assisted recombination less dominant. In addition, the relationship between J_{SC} and P_{light} can be expressed by the power law, $J_{SC} \propto P_{\mathrm{light}}^{S1}$, in which *S1* is the exponential factor referring to bimolecular recombination. Bimolecular recombination can be negligible when *S1* value is close to unity. As shown in Figure 5f and Table S5, the fitting *S1* values are 0.778, 0.808, 0.830, 0.933, 0.998 for PM6:Y7, PM6:Y7:ITIC-M, PM6:Y7:PC$_{70}$BM, PM6:ITIC-M, and PM6:PC$_{70}$BM, respectively. A stronger deviation of *S1* from 1 for Y7-based devices indicates that the photo-current generation for these devices is limited by bimolecular recombination process. It is worth to note that *S1* values were closer to unity by the addition of ITIC-M or PC$_{70}$BM as third components, indicating that the guest acceptor components can effectively suppress bimolecular recombination, which is consistent with the improvement of FF of the ternary devices.

Table 5.6 The diode recombination ideality factor of the binary and ternary devices fitted from the variation of J_{SC} and V_{OC} in a function of light intensities.

Blend system	**S1**	**S2**	n_{id} **= S2/S1**
Binary PM6:Y7	0.778	1.041	1.338
Ternary PM6:Y7:ITIC-M	0.808	1.043	1.268
Ternary PM6:Y7:PC$_{70}$BM	0.830	1.066	1.284
Binary PM6:ITIC-M	0.933	1.316	1.411
Binary PM6:PC$_{70}$BM	0.998	1.291	1.372

To further evaluate the charge recombination dynamics and extraction across the binary and ternary blends in devices, charge extraction (CE), transient photovoltage (TPV), transient photocurrent (TPC) and differential capacitance (DC, combination of TPV/TPC) measurements were performed. DC method is considered as an alternative to charge extraction (CE) techniques.[76,257–259] In brief, the TPC technique measured in the short-circuit condition evaluates the charge present at the solar cell and the TPV in the open-circuit condition examines the charge recombination decay under different light biases.[76] Detail of the experimental description can be found in the Supporting Information. **Figure 5.8a** shows the charges present under illumination at different open circuit voltages for the PM6:Y7 host binary and PM6:Y7:ITIC-M and PM6:Y7:PC$_{70}$BM ternary systems. The charges measured in the solar cell were obtained by measuring the capacitance at different light biases: $C(Voc) = \frac{\Delta Q}{\Delta V}$. And finally, the integration of this capacitance gives us an estimation of the charges stored in the cell: $Q(Voc) = \int_0^{Voc} C(Voc)dVoc$. The obtained curve is mainly formed by two different regimes, first a constant part, attributed to the geometrical capacitance (Cgeo) and the chemical capacitance (the exponential part) attributed to the charges accumulated at the bulk. Therefore, in order to avoid an incorrect interpretation of the results, the linear part can be fitted and removed from the data, resulting in the solid lines at the bottom. The resulting solid lines show that the charges in the bulk are higher for the ternary systems and so, following the same trend with the corresponding device photocurrent. We can also observe that the slightly shift of voltage at 1 sun conditions agree well with the V_{OC} values obtained for these devices (see **Table 5.7**). Next, in **Figure 5.8b** and **5.8c** we analyse the ideality factors for the binary and ternary system by using TPC and TPV measurements. As in previous works reported in more detail,[252,260,261] the ideality factor (n_{id}) can be also obtained by using the following expressions:

$$n = n_0 \times \exp\left(\frac{qVoc}{n_n kT}\right) \tag{5.3}$$

$$\tau_{\Delta n} = \tau_{\Delta n_0} \times \exp\left(\frac{qVoc}{n_\tau kT}\right) \tag{5.4}$$

and where the parameters γ and β obtained from the Figures 6b and 6c are defined as $\gamma = \frac{q}{n_n kT}$ and $\beta = \frac{q}{n_\tau kT}$, respectively. Finally, the n_{id} can be calculated by using the equation $n_{id}^{-1} = n_n^{-1} + n_\tau^{-1}$. Table 5.7 shows all the parameters obtained through TPC/TPV and the comparison with the ideality factors obtained with the *J-V* characteristics. Although two different techniques were employed, the n_{id} values from *J-V* characteristics and from TPC/TPV techniques are found to be identical for our solar cells. The identical ideality factor values has been reported in our previous work and other authors with respect to the steady-state values.[252,262,263] As a result, the good agreement of steady state and transient techniques demonstrates the validity of the Shockley model to studying the recombination and diode behavior for ternary organic solar cells. In addition, the recombination kinetics were evaluated by plotting the small perturbation lifetime −obtained by TPV− as a function of charge density −obtained by DC− as shown in **Figure 5.8d**. Clearly, for the same number of charges, the binary system presents faster recombination in comparison to the ternary systems. These results imply that the third component can contribute to more effective extraction of charges and a retardation in charge recombination losses, which also implies higher *J*sc, V_{OC}, FF and thus improving the overall cell performance.[264–266]

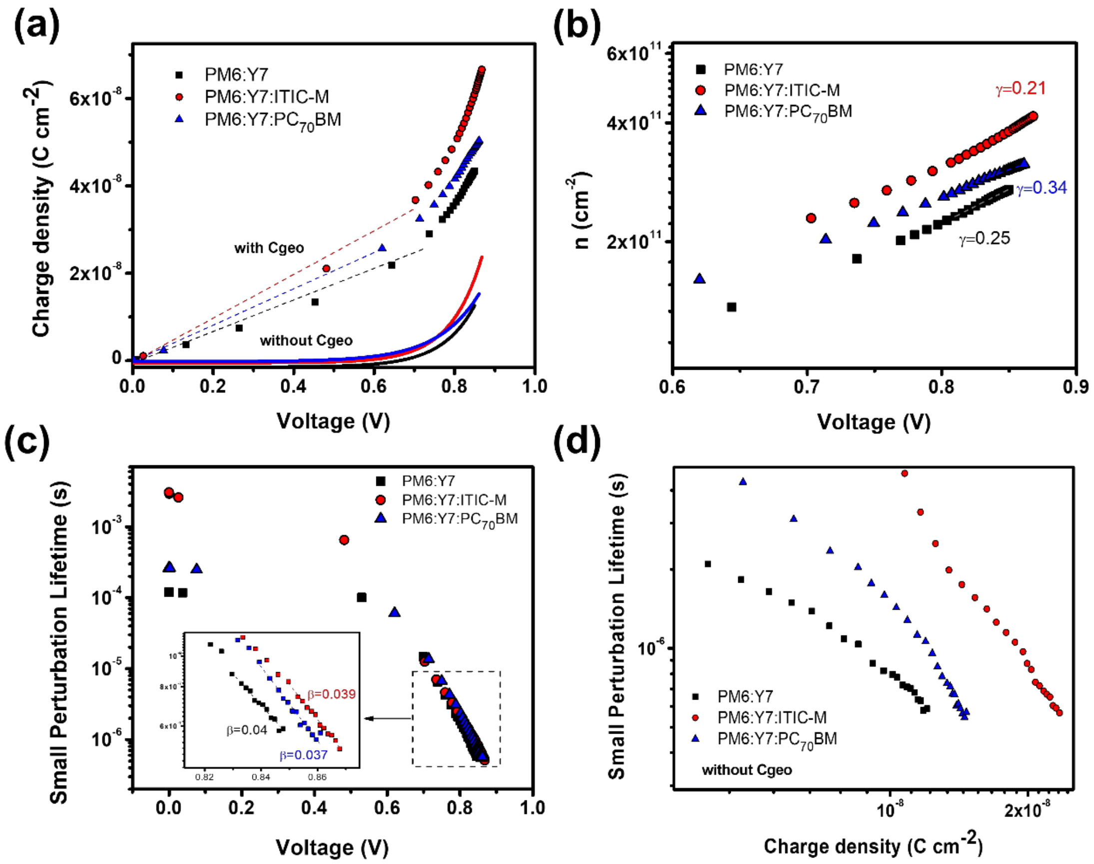

Figure 5.8 (a) Charge density as a function of V_{OC} for the binary and ternary systems; (b) Charge (n) versus voltage with the n_n fitting (γ). (c) Small perturbation lifetime versus voltage with the n_τ fitting (β). (d) Small perturbation lifetime plot as a function of charge density without the geometrical capacitance.

Table 5.7 Summary of the ideality factors obtained by TPC/TPV techniques and *J-V* characteristics.

Blend	n_n	n_τ	n_{id} (TPC/TPV)	n_{id} (*J-V*)
Binary PM6:Y7	9.76	1.54	1.34	1.34
Ternary PM6:Y7:ITIC-M	8.12	1.78	1.26	1.27
Ternary PM6:Y7:$PC_{70}BM$	13.39	1.43	1.29	1.28

To gain deeper insight into the process involved by incorporating $PC_{70}BM$/ITIC-M as third component in ternary blend devices, impedance spectroscopy (IS) was employed to measure the capacitance-frequency *(Cf)* and capacitance-voltage (*C-V*) characteristics of solar cells. In order to extract charge carrier accumulation and/or interfacial charge transfer information, the IS measurement should be carried out under open-circuit condition and equivalent circuits are often modelled to fit the experimental data.[169,170] **Figure 5.9a** and **5.9b** shows the Cole-Cole plots for binary host, ITIC-M- and $PC_{70}BM$-ternary solar cells measured at open-circuit bias voltage under constant illumination of 1 Sun with frequency ranging from 5 kHz to 10 MHz. A typical arc behavior with one semicircle is observed for all samples, indicating the presence of different RC components in the spectra. Arredondo *et al.* proposed that the low frequency arc is ascribed to the charge accumulation that cannot be extracted by the device contacts.[267] The smaller arc radius and lower impedance at low frequency observed for both ITIC-M- and $PC_{70}BM$-based ternary devices suggest that ternary strategy could suppress the charge accumulation impact that could be originated from surface morphology disorder of the blend[268]. These results are coherent with the lower RMS and low leakage current and as a sequence, better device performance of both ternary devices compares to those of binary ones. Similar behavior was obtained for the binary host and ternary devices at maximum power point voltage (V_{MPP}) and short circuit current voltage (V = 0V) bias, as shown in **Figure 5.10**.

To understand in which layer the accumulation is taking place, an equivalent circuit model comprising one series resistance (R_S) connected in series with three resistor/capacitor components (3RC) with Debye model was employed to fit the experimental Z'-Z'' data (see inset Figure 5.9a). The solid lines are the fitting curves and the fitted parameters of the 3RC+Debye equivalent circuit are listed in **Table 5.8**. R_S represents the series resistance from the metallic wires and the ohmic components such as ITO layer or Ag electrodes[269] and *L* is the added inductor to

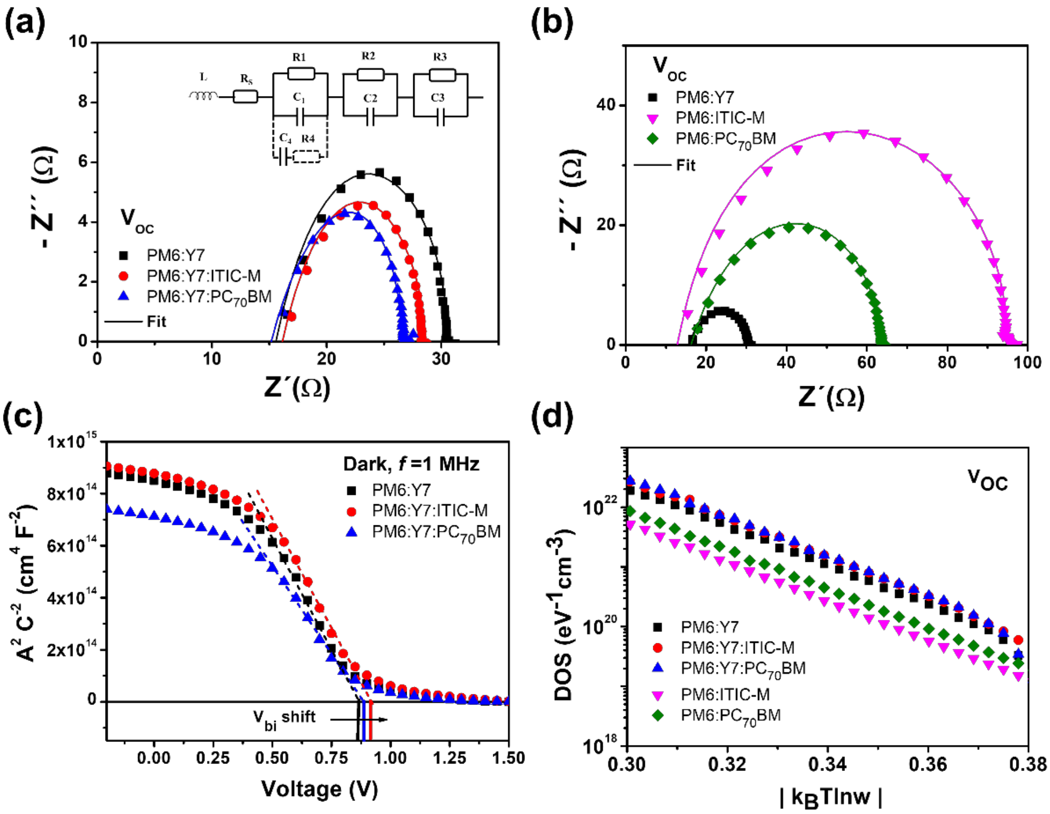

Figure 5.9 (a) Cole-Cole plot of binary host and ternary OSCs and (b) Cole-Cole plot of binary OSCs; (c) Mott-Schottky curve of at 1 MHz under dark condition; and (d) density of states (DOS) plot as a function of $|k_BT\ln\omega|$ at V_{OC} under AM 1.5G illumination for binary and ternary OSCs.

Table 5.8 The fitted parameters of binary and ternary devices according to the impedance spectroscopy at open-circuit voltage bias.

Blend system	R_S (Ω)	C_1 (nF)	R_1 (Ω)	C_2 (nF)	R_2 (Ω)	C_3 (nF)	R_3 (Ω)	R_{total} (Ω)	τ (μs)
Binary PM6:Y7	9.8	5.8	1.7	2.8	1.8	26.6	16.8	30.1	0.45
Ternary PM6:Y7:ITIC-M	9.8	5.8	1.6	2.8	1.6	26.6	15	28	0.40
Ternary PM6:Y7:$PC_{70}BM$	9.8	5.8	1.4	2.8	1	26.6	14.5	26.7	0.39
Binary PM6:ITIC-M	9.8	5.8	55	3.3	2	26.6	29	95.8	0.32
Binary PM6:$PC_{70}BM$	9.8	5.8	35	3.3	1	26.6	18	63.8	0.20

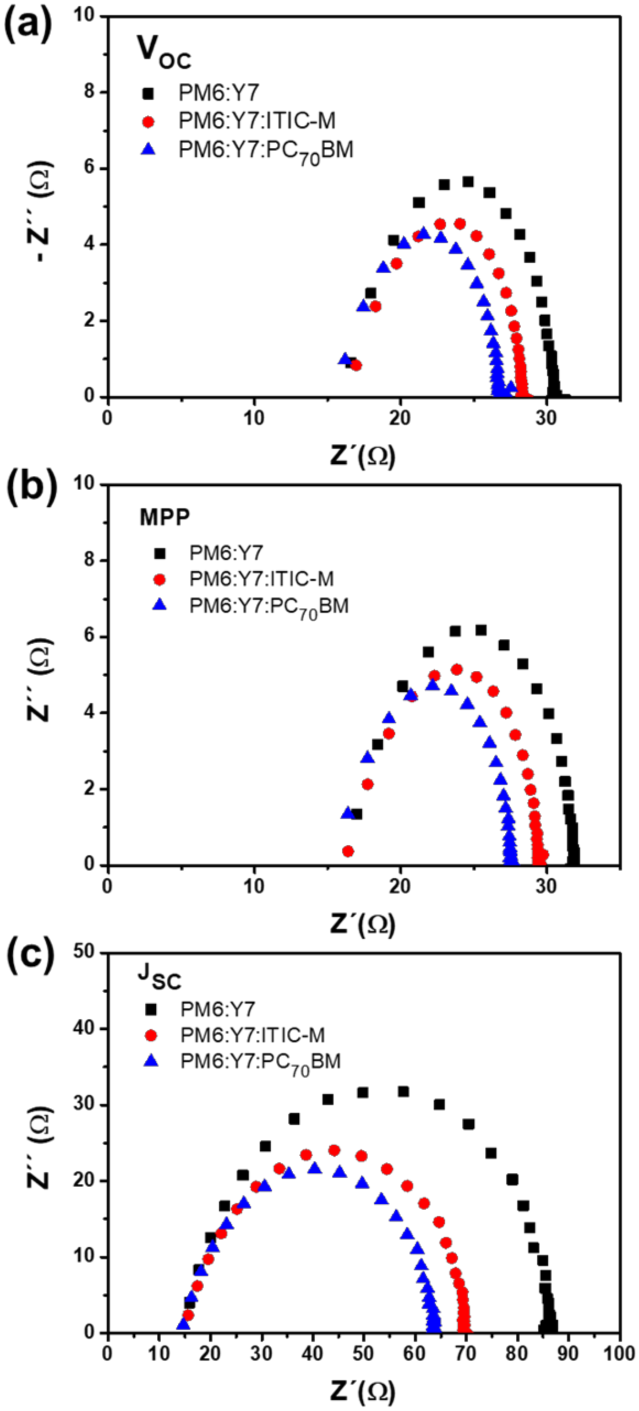

Figure 5.10 Cole-Cole plots of binary host and ternary devices at (a) open-circuit, (b) maximum power-point, and (c) short-circuit voltage bias.

Table 5.9 Dielectric constant, thickness, and calculated capacitance for each layer.

Layers	ε_{layer}*	d_{layer} (nm)	Capacitance (nF)
PEDOT:PSS	2.2	30	5.84
Bulk	3.5	100	2.79
PDINO	5.0	15	26.56

*The relative dielectric constant values for each layer were obtained from the literature.[74]

eliminate the impact of the connecting line during high-frequency scanning.[79,270] A distributed resistor (R) in 3RC elements represents the resistance of electron transport in each layer where R_1, R_2, and R_3 refers to PEDOT:PSS, blend active layer, and the PDINO layer, respectively. It is important to note that the capacitance (C) corresponds to the geometrical capacitance calculated from each layer, which can be expressed by $C_g = \frac{\varepsilon_0 \varepsilon_r}{A}$. Notably, an extra impeded R4 and C4 in series that attached in parallel with R1 and C1 is following the Debye model to explain the effect of the effect of third component introduction in ternary blends. As shown in Table S5, the values of C_1, C_2, and C_3 are constant for all devices, coherent with the theoretical values shown in **Table 5.9**. This might implied that at V_{OC}, the impedance response was controlled by the geometrical capacitances provided by the metal insulator-metal (MIM) model portraying the presence of fully depleted layers.[271] Compared to R_1 and R_2 values, the R_3 values of binary host and ternary devices are one-fold higher and contribute more to the total resistance (R_{total}) of the corresponding devices, as depicted in **Figure 5.11**. It suggests that the electrical properties of Y7-based binary and ternary devices was mainly controlled by the charge accumulation at the cathode interface (active layer/PDINO). In contrast, the total contribution of R_{total} originates from the contribution of R_2 values in binary ITIC-M and binary $PC_{70}BM$ are more pronounced by higher amount third component introduced to the system, which means that the charges cannot be easily extracted due to the higher guest components content in the active layers. This trend of the resistance obtained for the devices was confirmed by the Bode plot curves in **Figure 5.12**. It is interesting to find that the

R_1, R_2, R_3 and thus R_{total} values for ITIC-M- or $PC_{70}BM$-ternary devices are smaller than the binary devices, which can well explain the simultaneously increased J_{SC} and FF in the optimized ternary devices that agree well with *J-V* characteristic, EQE, PL, surface analysis and TPV measurements.

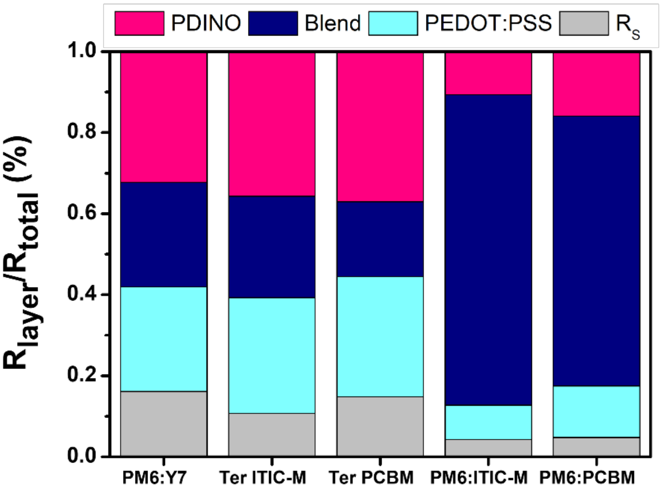

Figure 5.11 The percentage contribution of each layer resistance to the total resistance of binary and ternary devices.

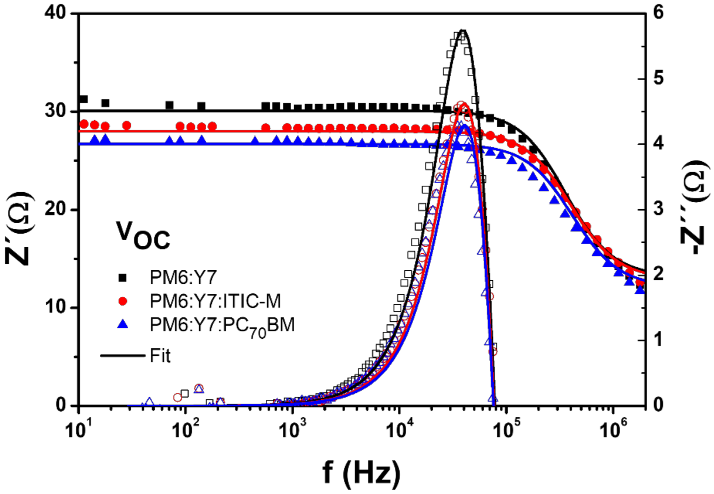

Figure 5.12 Bode plots of binary host and ternary devices with experimental (symbols) and fitted (lines) values for the real part (left axis) and the imaginary part (right axis) at V_{OC} condition.

In addition, impedance spectroscopy can be applied to investigate the effect of third component addition on the energetic disorder of transport site in ternary blends by *C-V* analysis. **Figure 5.9c** shows the Mott-Schottky plots for binary host, ITIC-M-based, and $PC_{70}BM$-based ternary OSCs from which the built-in potential (V_{bi}) can be extracted by the intercept of the curve with *x*-axis. The calculated V_{bi} from the *C-V* analysis were recorded in the dark at frequency of 1 MHz. The obtained V_{bi} values were 0.865 V, 0.915 V, and 0.885 V for binary host, ITIC-M ternary and $PC_{70}BM$ ternary OSCs, respectively. It is observed that V_{bi} values increase after the addition of the third component. The increasing V_{bi} values is also observed in binary ITIC-M and binary $PC_{70}BM$ OSCs, as shown in **Figure 5.13**. With the larger V_{bi}, a wider depletion region would be formed, resulting in improved separation of charge carriers and reduced bulk recombination.[272] As a consequence, the influence of the electric field in device with larger V_{bi} yields to the higher V_{OC} of both ternary devices.

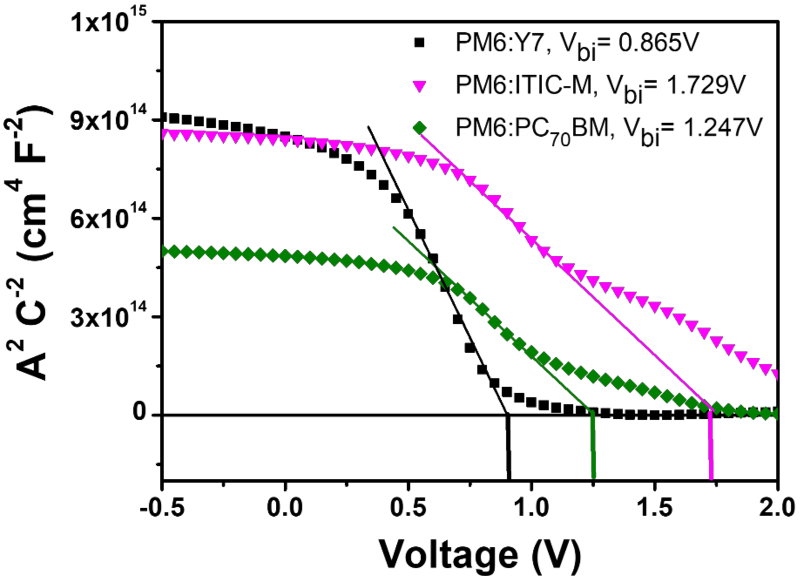

Figure 5.13 Bode plots of binary host and ternary devices with experimental (symbols) and fitted (lines) values for the real part (left axis) and the imaginary part (right axis) at V_{OC} condition.

The defects density can be evaluated from the capacitance-frequency (Cf) measurement to calculate the trap density of state (DOS) at a given energy level, E_ω, by the variation of the capacitance of the device with the frequency, as described by equation 5.5:

$$\mathrm{DOS}(E_\omega) = -\frac{V_{bi}\omega}{t\,q\,T\,k_B}\frac{\partial\,\mathrm{C}}{\partial\,\omega} \tag{5.5}$$

where C is the measured capacitance, V_{bi} is the built-in potential, ω is the angular frequency, t is the layer thickness, k_B is the Boltzmann constant, q is the electron charge and T is room temperature in Kelvin. The assumption in equation 3 is that the variations in the capacitance of the devices with frequency is correlated to the trapping and the charge release by shallow traps in the band gap near to the Fermi energy level.[82,273] To observe the relation of the trap-DOS as an energy dependent, the following equation 5.6 has been applied:

$$(E_\omega)_{traps} = k_B\,\mathrm{T}\ln\frac{2\beta\mathrm{N}}{\omega} = E_O - \mathrm{kB\;T\;ln\omega} \tag{5.6}$$

where β is the cross section and N is the effective density of state[274]. Assuming that $2\beta N$ is independent of the frequency value, the change in its value is related to the shift in the DOS values on energy scale (E_O). **Figure 5.9d** displays the calculated trap-DOS plotted as a function of energy for the fabricated devices. A single exponential trap distribution for all samples is observed with almost the same slope values, which defines the same trap activation energy and carrier response[275]. Interestingly, after the introduction of either ITIC-M or $PC_{70}BM$ into the binary host blend, a shift in E_O values was observed, showing a slight increase density of defects. As explained by equation 5.6, the higher shift of E_O or higher DOS values could be originated from the decrease in the βN value, indicating a higher obtained energy due to the less-localized shallow trap sites created by adding a small amount of the appropriate third components. In addition, **Figure 5.14** is shown to further quantify the energy shifting values of the corresponding ternary OSCs with respect to the binary host according to equation 5.6. It is noticed that the PM6:Y7 binary OSC exhibit higher trapping sites than those of ternary OSCs, confirming the higher per-

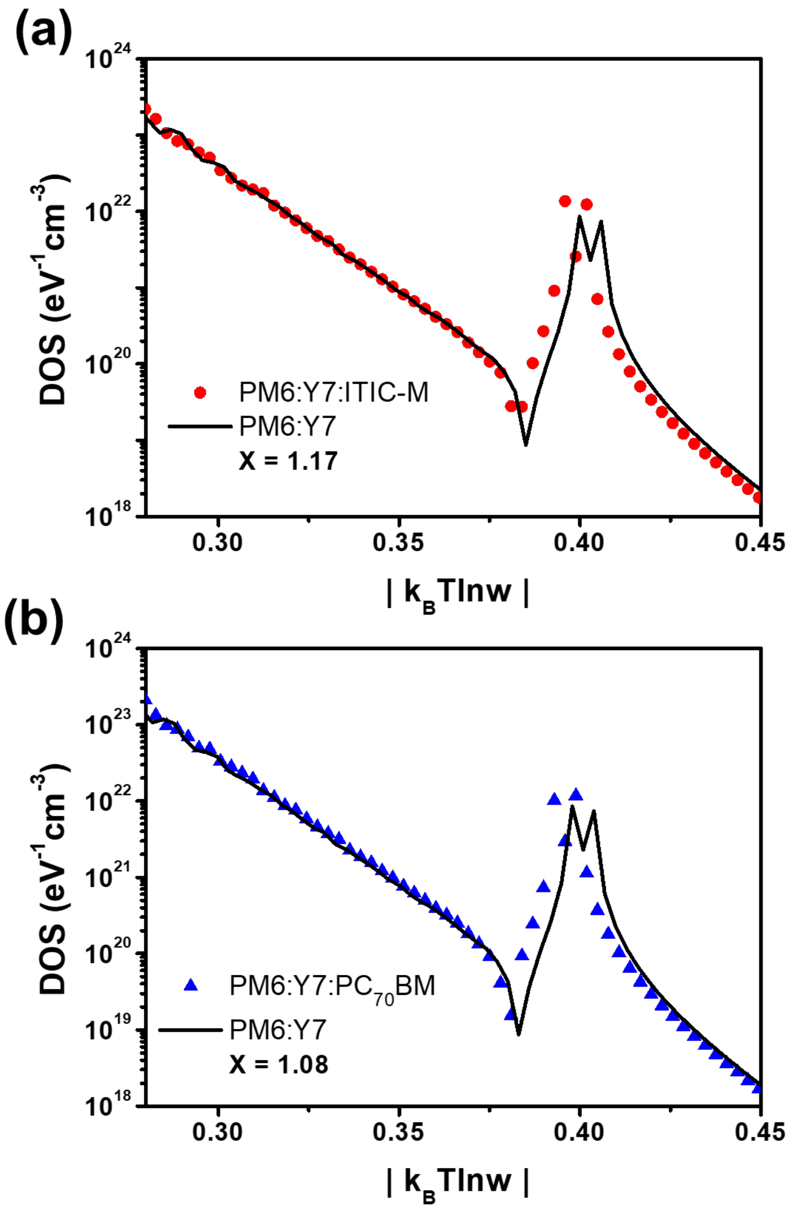

Figure 5.14 Density of states (DOS) as a function of energy with the energy shifting between (a) binary PM6:Y7 superimposed with ternary PM6:Y7:ITIC-M OSCs with the shifting value X of 1.17, and (b) binary PM6:Y7 superimposed with PM6:Y7:PC$_{70}$BM OSCs with the X value of 1.08.

formance of ternary OSCs due to the addition of ITIC-M or $PC_{70}BM$ that minimized the present of defects inside the ternary devices. It is interesting that the less-localized shallow trap sites in ternary blends is in highly accordance with the calculated Urbach energy, as shown in **Figure 5.15** and described by equation 5.7:

$$\alpha(E) = \alpha_0 e^{(E-E_g)/E_U} \tag{5.7}$$

where $\alpha(E)$ is the optical absorption coefficient, α_0 is the optical absorption coefficient at the band edge, E is the photon energy, and E_U is the Urbach's energy. The E_U represents the DOS distribution, which explains the energetic disorder in the molecular orbital. The calculated E_U were 27.99, 27.28, 25.81 meV, respectively for PM6:Y7, PM6:Y7:ITIC-M, and PM6:Y7:$PCP_{70}BM$ based OSCs, indicating the lower energetic disorder can be achieved by the introduction of higher lying LUMO energy and morphology compatible of third components in the ternary devices.

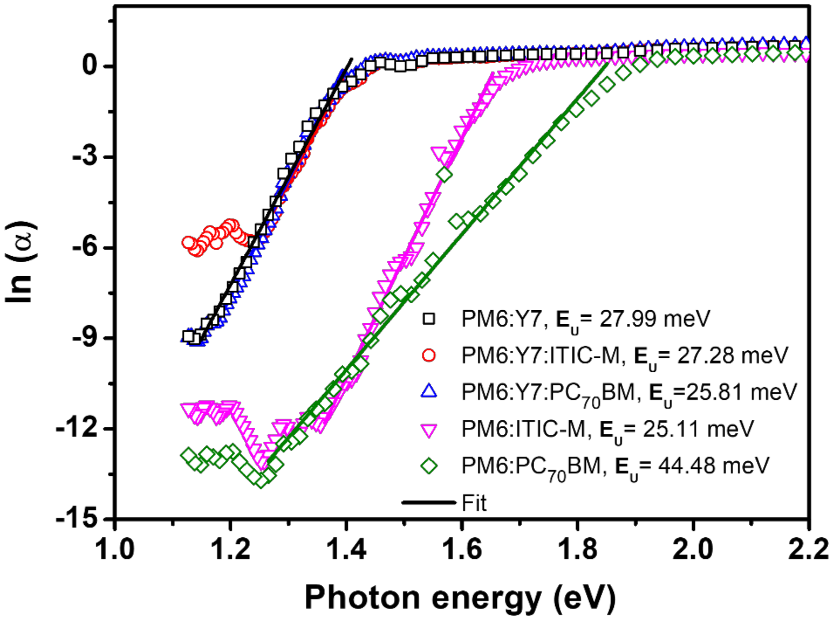

Figure 5.15 The Urbach's energy plot of the binary and ternary devices.

5.3 Conclusions

In summary, a series of OSCs were prepared with PM6 as host donor, Y7 as host acceptor, and IT-M or $PC_{70}BM$ as guest acceptors. Despite the fact that the two acceptor guests $PC_{70}BM$ and ITIC-M have completely different chemical structures, their excellent miscibility and higher LUMO energy level in comparison to the host acceptor Y7 results in a PCE boost of over 7% in the ternary devices. Compared to the optimized PM6:Y7 binary OSCs with a PCE of 16.46%, the ITIC-M-based and $PC_{70}BM$-based ternary OSCs led to a high PCE of 17.73% and 17.67%, respectively, with the same weight ratio of D1:A1:A2 = 1:1:0.1. By intensively investigating charge transport, charge extraction and charge recombination properties in ternary OSCs, we found that the ITIC-M or $PC_{70}BM$ guests exhibits an excellent compatibility with the host acceptor Y7, such that well-mixed acceptor phase are formed in the ternary blends. The higher LUMO levels of the third components helps the ternary OSCs elevates the V_{OC} by reducing energy-loss and reverse saturation current, creating less-localized shallow trap sites along with suppressing charge recombination and Urbach energy. Furthermore, photoluminescence and single material device investigations demonstrate energy transfer between the two well-mixed acceptors, contributing to the increased J_{SC}. The combination of these improvements leads in a simultaneously enhanced V_{OC}, J_{SC} and FF with respect to those of binary host. Our findings demonstrates that a good compatibility between the guest and host acceptors with suitable energy levels to achieve complementary absorption are the keys to realizing synergistically modified nanomorphology and photophysical processes toward high efficiency ternary organic solar cells.

Chapter 6

Semitransparent nonfullerene-based ternary organic solar cells

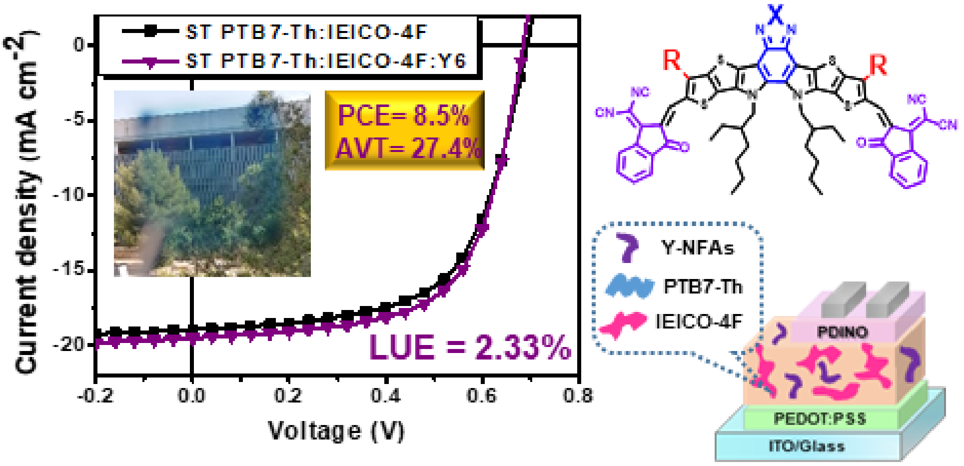

This chapter is based on to be published work: Torimtubun, A.A.A. *et al.* Enabling Efficient and Stable Semitransparent Ternary Organic Solar Cells Using Y-series Nonfullerene Acceptors as Third Components, *to be published*.

6.1 Introduction to semitransparent organic solar cells

Semitransparent organic solar cells (ST-OSCs) have gained considerable attention toward real applications in the field of photovoltaics due to their promising features, such as transparency, solution-processed, low-cost, flexible and color tunability, that could transform normal power-harvesting organic solar cell (OSC) devices into value-added technologies, such as building-integrated photovoltaics, automobile windows and agrivoltaics to generate electric power, as depicted in **Figure 6.1a**.[252,276–282] In comparison with inorganic photovoltaics with few tunabilities on optical properties, ST-OSCs that consist of organic semiconductors possesses inherently narrow absorption, which can be tailored to harvest the near-infrared (NIR) region while transmitting photons in the visible region, enabling the ST-OSCs to attain high average visible transmittance (AVT, from 370 nm to 740 nm) and a decent power conversion efficiency (PCE).[283] **Figure 6.1b** shows the AM 1.5G solar emission spectrum and its energy proportion in different regions. Typically, the main challenge toward practical applications of ST-OSCs in the niche market is the trade-off between high PCE, high AVT, and stable device in operating conditions. To date, the PCEs of ST-OSCs have arrived at 14% with AVT at around 20%.[284,285] However, depending on the applications, a high AVT exceeding 25% and high stable device in operating conditions are required to meet the criteria for solar windows.[282] Since the light absorption and transmittance appear to be contradict for photovoltaic devices, the light utilization efficiency (LUE) defined as a product of PCE and AVT has been proposed to objectively evaluate the performance of ST-OSCs.[286] Considering that an ideal ST-OSC should take full advantage of the invisible photons to achieve high LUE, the efficient narrow bandgap materials offer considerable potential for preparing high-performance ST-OSC with excellent absorbing selectivity by sufficiently exploiting NIR light and transmitting the visible ones. Thanks to the easily tailored molecular structures in organic semiconductors, the recent emergence of high-performance Y-series nonfullerene acceptors (NFAs)

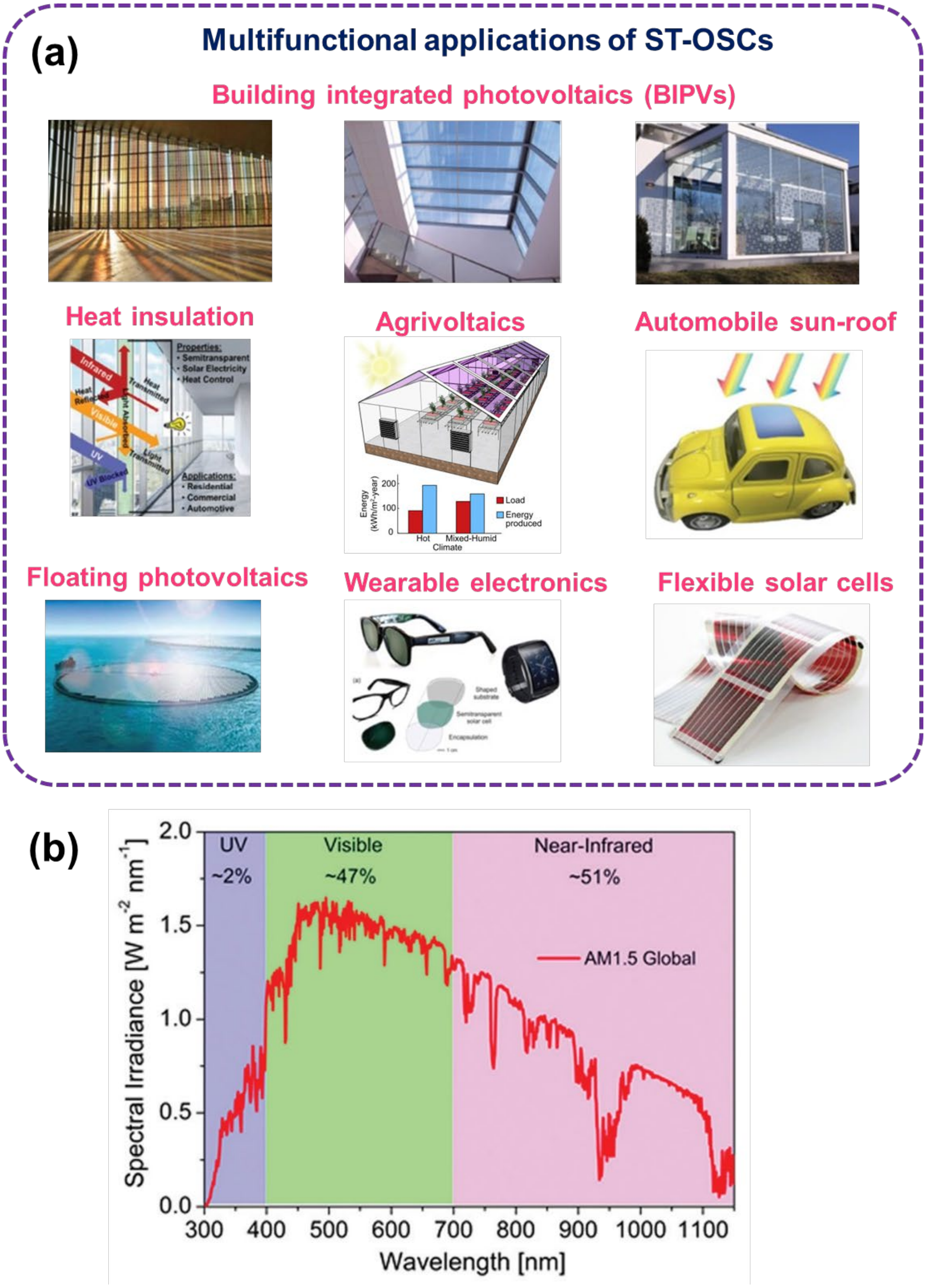

Figure 6.1 (a) Potential applications of semitransparent OSCs; (b) Solar emission spectrum and the energy fraction in the UV, visible, and infrared regions. The figures are reproduced from Ref[17,279].

with narrow bandgap and absorption profiles lying within the NIR region allows for the realization of the above-mentioned, which displays highly-tunable optoelectronic characteristics and may reach a high exciton dissociation efficiency at a relatively low voltage loss in devices.[30,287,288] According to the theoretical prediction, the ideal bandgap of ST-OSCs deviates significantly from those of the best performance in their opaque counterparts, thus making narrow to ultra-narrow bandgap photovoltaic materials highly desirable towards high-performance ST-OSCs.[285,289,290]

Aside from the benefits of narrow bandgap materials, device engineering with a simple fabrication process such as ternary strategy has been demonstrated as an effective method to further improve the PCE and AVT of ST-OSCs, especially by employing an ultra-narrow bandgap material as third component.[237,291–296] For example, Ma et al. introduced few amounts of ultra-narrow bandgap acceptor IEICO-4F into PTB7-Th:COi8DFIC binary host system to develop semitransparent ternary OSCs (ST-TOSCs) with PCE of 8.23% and AVT of 20.78%.[297] Moreover, Hu et al. also employed IEICO-4F as ultra-narrow band gap third component to construct PTB7-Th:BDTThIT-4F:IEICO-4F ST-TOSCs, which delivered PCE of 9.40% and AVT of 24.60%.[298] Besides adjusting the photon harvesting of the active layers, the third component can also play an important role in modulating the energetics and manipulating the film morphology, as demonstrated by the work of Yin et al. [284] and Liu et al.[285] in which they reported ST-TOSCs based on binary blends of D18-Cl:Y6-1O and PM6:Y6 with the addition of ultra-narrow band gap Y6 and SN, giving PCEs of 13.02% and 14.00% with similar AVTs of 20.20%, respectively. These results show an important role of the third component in ST-TOSCs in balancing the trade-off between PCE and AVT by elaborately selecting narrow or ultra-narrow bandgap materials. However, despite such advantages, the operational stability that is the most critical issue for the practical application of ST-OSCs is rarely studied in the literature. In addition, to the best of our knowledge, there have been no articles that study comparatively the use of different narrow band gap materials as the third components in ST-OSCs, especially for Y-series NFAs.

In this contribution, a series of opaque and semitransparent ternary OSCs were fabricated with narrow bandgap donor PTB7-Th and ultra-narrow bandgap acceptor IEICO-4F as host materials, while narrow to ultra-narrow bandgap Y-series NFA materials, particularly Y1, Y5, Y6 and Y7 were employed as third components to achieve good balance between PCE, AVT and operational stability of ST-OSCs. The structural differences among Y-series NFAs lie in the electron-accepting ability of central acceptor unit and the linear side chains at the thiophthene β-site of the fused rings cores (Y1 versus Y5, Y6, Y7),[30,287,299] as exhibited in **Figure 6.1a**. Moreover, the structure difference in the end groups of 1,1-dicyanomethylene-3-indanone (IC) for Y5 versus Y6 (fluorination) versus Y7 (chlorination) which provide tunable absorption light for capturing more NIR region[208,241,300,301] was also comparatively study for ST-OSCs application. When blended with PTB7-Th:IEICO-4F with the PCE of 11.86%, the PCEs of 11.32%, 11.55%, 13.02%, and 12.32% were yielded for opaque Y1, Y5, Y6, and Y7 based ternary OSCs. A series of ST-OSCs were prepared with 10 nm thickness of Ag as the electrode. The different photovoltaic performance as well as the difference in AVT values were observed using different Y-series NFA materials. The ST-TOSCs based on PTB7-Th:IEICO-4F:Y6 with a modified Ag electrode thickness of 10 nm achieve the highest LUE of 2.35% as the product of good PCE of 8.47% and high AVT of 27.77% among the other Y-series incorporated ST-TOSCs. Moreover, Y6 based ST-TOSCs exhibited good thermal and photostability under inert conditions. The presented results in this work imply that ultra-narrow band gap engineering and ternary strategy by the molecular modification for third component materials selection are one of the keys to balancing the trade-off between PCE, AVT, and operational stability of ST-OSCs.

6.2 Results and discussion

The energy levels of the used active layer materials are shown in **Figure 6.2b**. The highest occupied molecular orbital (HOMO) levels values were obtained by UV photoelectron spectroscopy (UPS) and the lowest unoccupied molecular orbital (LUMO) levels values were acquired from inverse photoelectron spectroscopy (IPES) were acquired from our previous work.[302] The cascaded energy levels observed in Y1 added component may provide more potential pathways for charge transfer in ternary active layer. Moreover, the almost identical LUMO energies of Y6 and Y7 will deliver similar open-circuit voltage (V_{OC}) to IEICO-4F, whereas the shallower LUMO level of Y5 than IEICO-4F will be beneficial for raising the V_{OC}. **Figure 6.2c** exhibits the normalized UV-vis absorption spectra of the materials in pure films. The absorption peaks of three Y-series NFAs lie between those of PTB7-Th and IEICO-4F, indicating the good complementary absorption covering the range from 300 to 1000 nm by third components. The gradually bathochromic shift of absorption peaks and onset from Y1 to Y7 can be correlated with their molecular geometry and aggregation properties, as the effect from the modification by benzothiadiazole in the core acceptor unit and fluorination or chlorination modification in end groups. The molecular modification causes additional intermolecular charge transfer effect to redshift the absorbance, which is beneficial for semitransparent applications to harvest more NIR light. Furthermore, the absorption spectra of the blend films are shown in **Figure 6.3**. Absorption peaks at 716 and 876 nm are observed in the binary films of PTB7-Th:Y6 and PTB7-Th:IEICO-4F, respectively, indicating that adding Y-series NFAs as third components can compensate the absorption for the host system.

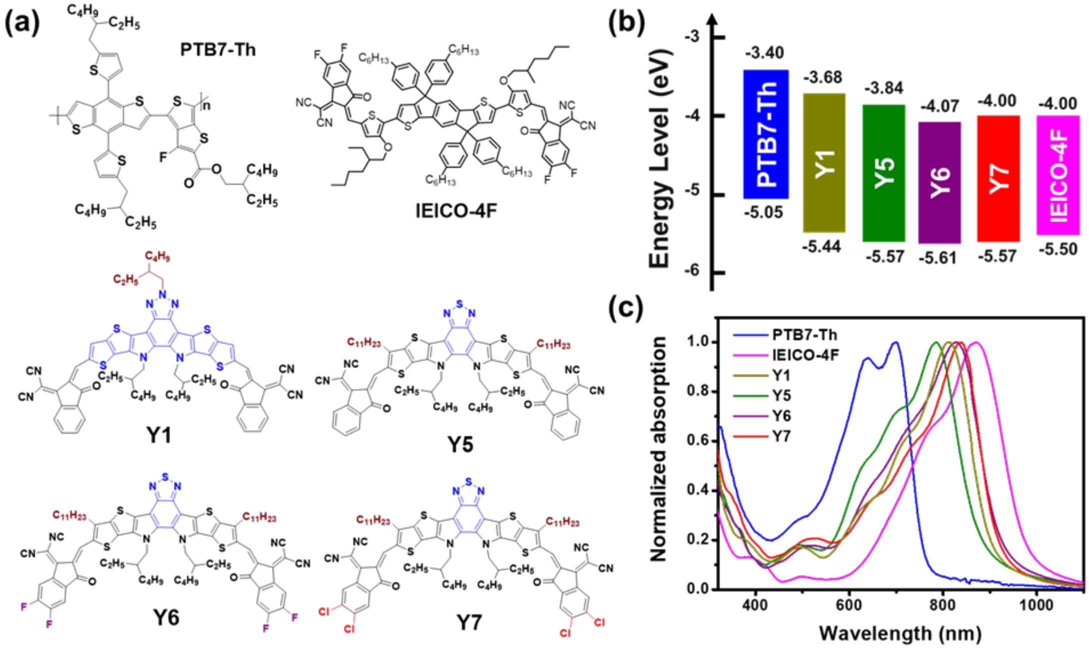

Figure 6.2 (a) Molecular structures, (b) energy level diagram, and (c) normalized absorption spectra of neat films of the used active layer materials.

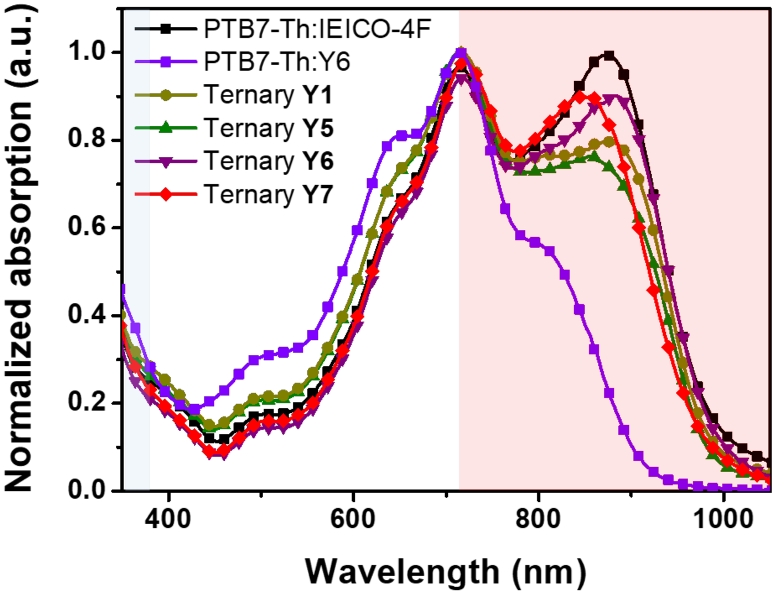

Figure 6.3 Absorption spectra of blend films. The blue area is the UV light region, the transparent area is the visible light region, and the red area is the near-infrared region.

In order to evaluate the photovoltaic performance of the binary and ternary blend systems, a series of opaque OSCs based on PTB7-Th:IEICO-4F with different Y-series NFAs (primarily Y1, Y5, Y6 and Y7) contents were fabricated with a conventional device architecture of ITO/PEDOT:PSS/active layer/PDINO/Ag, the thickness of the Ag layer was 100 nm. The total weight ratio of the donor (D) and acceptor (A) was fixed at 1:1.5, while the acceptor ratio between Y-series NFAs third components and IEICO-4F was varied to determine the optimal composition. All the active layers with a thickness of ~ 100 nm delivered the best device performance when they were spin-coated from their chlorobenzene solutions. The detailed fabrication and characterization of OSCs are described in the Supporting Information. **Figure 6.4a** depicts the current density-voltage (*J-V*) characteristics of binary and ternary opaque OSCs under simulated AM 1.5G solar irradiance with an intensity of 100 mW cm^{-1}, and **Table 6.1** summarizes the key photovoltaic performance parameters of the corresponding devices. At the same time, the photovoltaic parameters and its corresponding *J-V* curves of the binary OSCs based on PTB7-Th:Y6 and PTB7-Th:Y7 are provided in **Table 6.2** and **Figure 6.5**, respectively. The average power conversion efficiency (PCE) values are obtained from at least 20 individual cells from different fabrication batches, representing a good reproducibility of the ternary OSCs. The optimized binary OSCs based on PTB7-Th:IEICO-4F exhibited a PCE of 11.62% with a V_{OC} of 0.70 V, a short-circuit current (J_{SC}) of 25.16 mA cm^{-2}, and a fill factor (FF) of 66.39%, which is comparable to the results in the literature. Note that the PTB7-Th:IEICO-4F devices performed higher than PTB7-Th:Y6 and PTB7-Th:Y7 devices with PCEs of 9.84% and 2.70%, respectively, therefore IEICO-4F is selected as the host acceptor in the ternary devices. With a small fraction of Y6 added, the ternary device shows an improved PCE as high as 13.02%, with the concurrent increase in J_{SC} of 27.30 mA cm^{-2} and FF of 67.46% compared with the PTB7-Th:IEICO-4F binary host device. Besides, loading Y7 into PTB7-Th:IEICO-4F blend can also obtain similar effects as Y6 with an enhancement in J_{SC} of 25.97 mA cm^{-2} and FF of 67.89%, thus the PCE of the ternary Y7 based devices increased to 12.40%. It is highlighted that the J_{SC} and FF of the optimized ternary OSCs are much larger than those of three binary OSCs, indicating that end group modification strategy in Y6 and Y7 third components can simultaneously improve the photon harvesting and charge transport in the ternary active layers. In contrast to the Y6 and Y7 based ternary devices, the decreasing J_{SC} and FF with respect to those of PTB7-Th:IEICO-4F binary cell was observed in Y1 and Y5 added ternary OSCs, which eventually resulted in a slightly dropped PCEs of 11.32% and 11.55%, respectively. It is interesting to note that the V_{OC} value in Y5 ternary device is slightly increase to 10 meV and the similar V_{OC} values in Y1, Y6, and Y7 ternary devices as compared to binary devices, which verified our hypothesis.

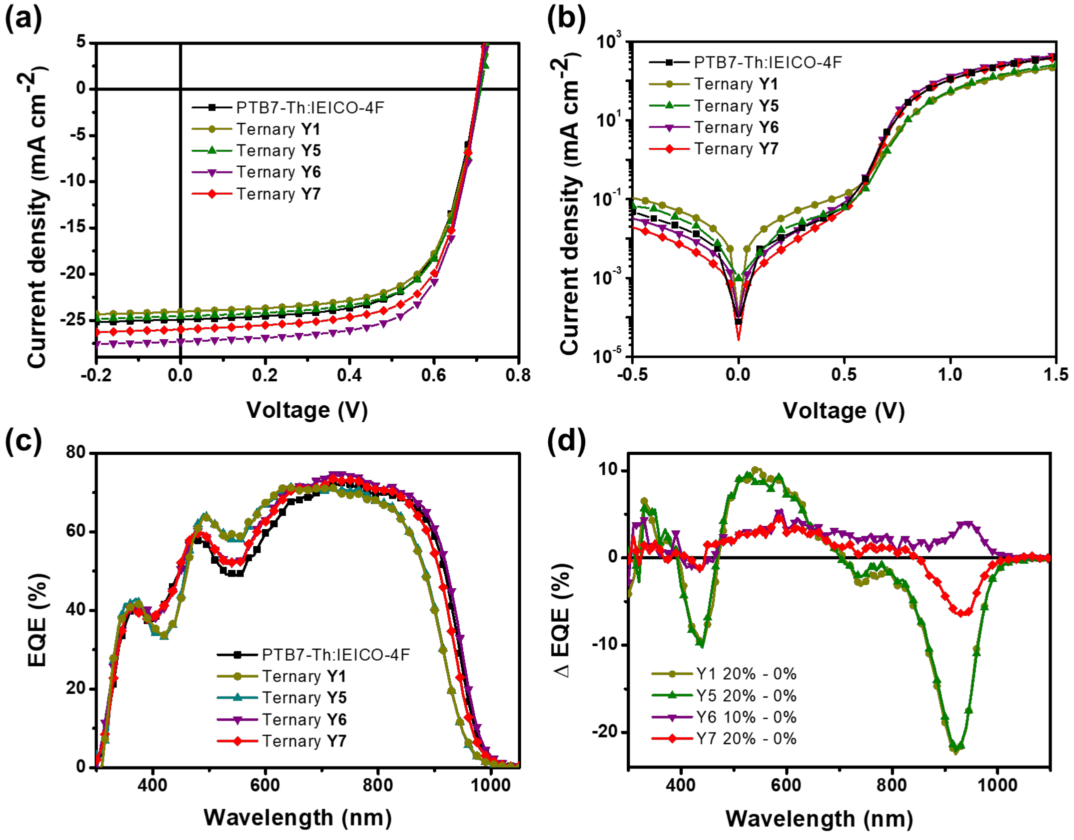

Figure 6.4 Current density-voltage (*J*-*V*) curves measured under (a) AM 1.5G illumination and (b) in dark conditions; (c) EQE curves of the corresponding OSCs, and (d) the ΔEQE values of ternary OSCs concerning the binary host device.

Table 6.1 Photovoltaic performance parameters of optimized opaque OSCs measured under AM 1.5G with 100 mW cm^{-2} intensity and AVT (370–740 nm) of corresponding blend films.

Blend	**V_{OC} (V)**	**J_{SC} (mA cm^{-2})**	**FF (%)**	**PCE [(a)] (%)**	**AVT of blend films (%)**
Binary PTB7-Th:IEICO-4F	0.70	25.16	66.39	11.62 (11.41 ± 0.22)	52.33
Ternary PTB7-Th:IEICO-4F:**Y1**	0.70	24.13	65.95	11.32 (11.19 ± 0.12)	46.51
Ternary PTB7-Th:IEICO-4F:**Y5**	0.71	24.57	66.09	11.55 (11.27 ± 0.14)	47.88
Ternary PTB7-Th:IEICO-4F:**Y6**	0.70	27.30	67.46	13.02 (12.39 ± 0.46)	52.83
Ternary PTB7-Th:IEICO-4F:**Y7**	0.70	25.97	67.89	12.40 (11.98 ± 0.36)	51.68

(a) The values in parentheses are the average and standard deviation values calculated from over 10 individual cells prepared from different batches.

Figure 6.4b shows the dark *J-V* characteristics of the corresponding opaque devices, which the information regarding shunt resistance (R_{Sh}) and series resistance (R_S) can be extracted and listed in **Table 6.3**. The drift of charge carriers is defined by R_{Sh} at reverse voltage bias without illumination ($V < 0$V) which is associated with the current loss such as leakage current. The ideal R_{Sh} should be very high, resulting in zero current flows through R_{Sh} and no leakage current in the device. It is apparent that R_{Sh} values increased with the addition of Y6 and Y7 but then decreased with the incorporation of Y1 and Y5 with respect to those of binary host device. The trend R_{Sh} with the addition of Y-NFAs in PTB7-Th:IEICO-4F blend implies that introducing the red-shifted third components can reduce leakage current and charge carrier recombination in the ternary devices. At higher voltages ($V > 1$V), the charges begin to accumulate and are restricted by R_S, which is derived from the interfacial and bulk resistance of the active layer and electrodes. The lower R_S values of Y6 and Y7 ternary OSCs in comparison with the binary host, Y1 and Y5 ternary OSCs indicates fewer defects at the Y6 and Y7 ternary blends and/or at the interfaces within the corresponding devices, which should be beneficial for an efficient charge carrier collection and better charge carrier mobility.[242,252] The opaque OSCs display higher FF with PTB7-Th:IEICO-4F:Y6 and PTB7-Th:IEICO-4F:Y7 blends, which can be well supported by the minimal R_S and maximal R_{Sh}.

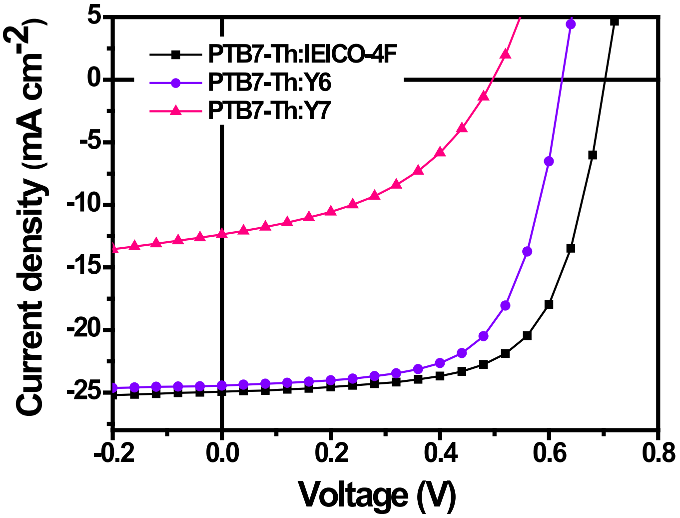

Figure 6.5 The *J-V* curves of the PTB7-Th based binary devices with different nonfullerene acceptor materials.

Table 6.2 Device performance parameters of binary PTB7-Th:IEICO-4F, PTB7-Th:Y6, and PTB7-Th:Y7 based OSCs, measured under AM 1.5G irradiation (100 mW cm^{-2}). The values in parentheses are the average and standard deviation values calculated from over 10 individual cells prepared from different batches.

Blend	**V_{OC} (V)**	**J_{SC} (mA cm^{-2})**	**FF (%)**	**PCE (%)**	**AVT of blend films (%)**
PTB7-Th:**IEICO-4F**	0.70	25.16	66.39	11.62 (11.41 ± 0.22)	52.34
PTB7-Th:**Y6**	0.63	24.44	64.35	9.84 (8.92 ± 0.72)	47.26
PTB7-Th:**Y7**	0.50	12.36	43.83	2.70 (2.55 ± 0.08)	N/A

We speculate that the improved J_{SC} of the Y6 and Y7 ternary devices is ascribed to the fact that the narrower bandgap of Y6 and Y7, allows more NIR light to be better utilized. The external quantum efficiency (EQE) spectra of opaque OSCs were measured to validate this, and the results are displayed in **Figure 6.4c**. The onset of EQE spectra of Y1 and Y5 ternary devices is 956 nm, while those of binary host, Y6 or Y7 ternary devices are 20 nm red-shifted to 976 nm, which is inconsistent with the absorption spectra. In detail, ternary Y6 and Y7 have higher EQE responses within 480 – 860 nm with maximum EQE values of 74.9% and 73.5%, higher than those of 72.9%, 71.3%, and 71.5% for binary host, Y1 and Y5 ternary devices, respectively, proving that more photons can be transformed to photocurrent especially in the NIR region, which is quite beneficial for ST-OSCs. As shown in **Figure 6.4d** by taking ΔEQE (EQE ternary – EQE binary) into consideration**,** the positive ΔEQE values observed in Y6 or Y7 ternary devices suggest good light-to-photon conversion capabilities of Y6 or Y7 as third components in the PTB7-Th:IEICO-4F blend in the long wavelength range of 300–1000 nm, particularly for Y6 added blend with ΔEQE values arrive to ~4% at 940 nm. This result implies that the better light-harvesting involving excitons generated in the acceptor phase is boosted in the ternary cell by an appropriate molecular structure modification of third components, which accounts for the higher J_{SC}.

Table 6.3 Extracted values of series resistances, shunt resistances, and leakage currents from dark J-V curves of the corresponding devices.

Blend system	R_S **(Ω cm²)**	R_{Sh} **(Ω cm²)**	$J_{leakage}$ **at -0.5V (mA cm⁻²)**
PTB7-Th:IEICO-4F	1.52	1.11×10^4	0.05
PTB7-Th:IEICO-4F:**Y1**	2.07	6.39×10^3	0.11
PTB7-Th:IEICO-4F:**Y5**	2.02	8.46×10^3	0.06
PTB7-Th:IEICO-4F:**Y6**	1.28	2.48×10^4	0.03
PTB7-Th:IEICO-4F:**Y7**	1.39	4.53×10^4	0.19

To deepen further insight into the effect of Y-NFAs addition on phase separation of ternary blends and the modified photovoltaic characteristics in the ternary devices, the morphology of blended films was characterized by using atomic force microscopy (AFM) and transmission electron microscopy (TEM) measurements. The topographic and phase AFM and TEM images are displayed in **Figure 6.6**. In the height images of AFM as shown in **Figure 6.6a**, the blend films of the PTB7-Th:IEICO-4F, ternary Y1, ternary Y5, ternary Y6, and ternary Y7 exhibit the root-mean-square (RMS) surface roughness of 4.95 nm, 5.57 nm, 4.83 nm, 1.87 nm, and 1.52 nm, respectively. The rougher surface of ternary Y1 or ternary Y5 is undesirable for charge collection by the electrodes, which well-explained the higher R_S values and the lower FF values with respect to the binary host blend. On the other hand, the smaller RMS roughness values of Y6 or Y7 ternary blend films indicate the homogeneous morphology of the optimized ternary blend films, which should be beneficial to optimize phase separation degree of blend films by the addition of Y6 or Y7. The AFM phase images of blend films (**Figure 6.6b**) exhibit the well-developed nanofibrous-like structure and relatively small phase separation degree or domain size in the Y6 and Y7 ternary blend films. No featured regions observed in TEM images of ternary Y6 or Y7 blend films (**Figure 6.6c**) further confirm the homogeneous morphology distribution with small domain size of the optimized ternary blend films. Notably, the relatively large dark and bright regions observed from TEM image of PTB7-Th:IEICO-4F:Y1 blend films may be harmful for exciton dissociation in the active layers. These results suggest that the judicious selection of ultra-narrow bandgap third component may form sufficient donor/acceptor interfaces for efficient exciton dissociation, bi-continuous charge transport networks, and charge collection.[297,303,304]

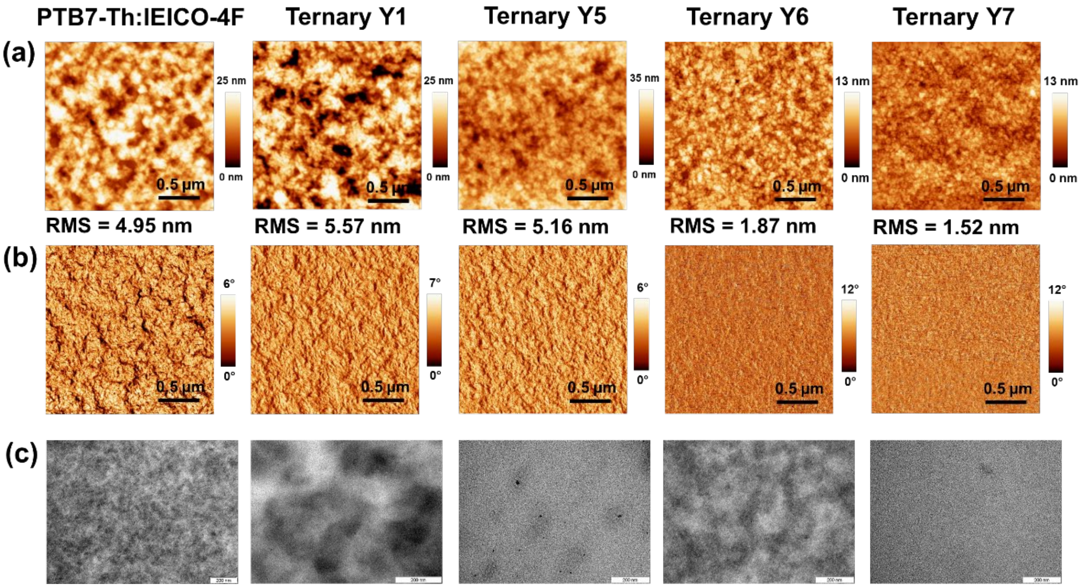

Figure 6.6 AFM (a) topographic and (b) phase images and (c) TEM images of binary and ternary blend films.

To confirm the small domain size and good compatibility of ternary system from the materials perspective, contact angle measurements of neat and binary host blend films were performed based on liquid drops of water, ethylene glycol (EG), and diiodomethane (DM), as exhibited in **Figure 6.7**. The surface tension of the materials and the interactions between them that are relevant for phase separation and morphology can be observed from contact angle measurement. The surface tension (γ) values of the materials and the corresponding interaction parameters (χ) are listed in **Table 6.4**. The surface tensions for pure films of PTB7-Th, IEICO-4F, Y1, Y5, Y6, and Y7 as well as PTB7-Th:IEICO-4F blend films are 32.0, 39.9, 49.7, 42.4, 36.4, 36.0, and 31.4 mN m^{-1}, respectively. Accordingly, the interaction parameters (χ) between each pair of materials were acquired through the Flory – Huggins model and the results show that the interaction parameter between PTB7-Th:IEICO-4F blend film with the addition of Y6 or Y7 is low, indicating remarkable miscibility between them, which is consistent with the results of the phase separation from morphology characterizations.

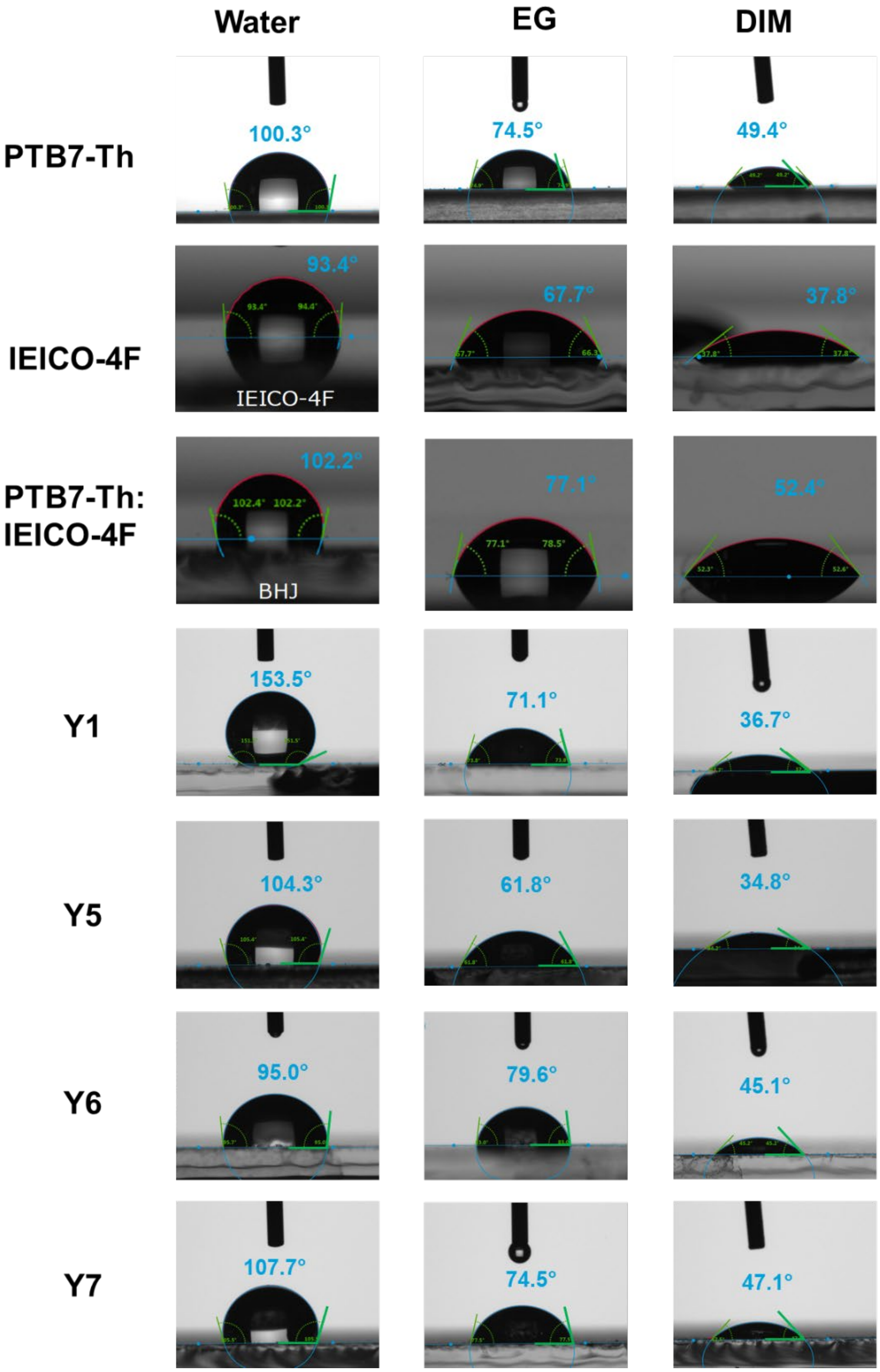

Figure 6.7 The water, ethylene glycol, and diiodo-methane droplet contact angle images of PTB7-Th, IEICO-4F, Y1, Y5, Y6, and Y7 neat films. The values of the images are the average contact angle from at least three tests of different part in the same film.

Table 6.4 Contact angles, surface tension (γ), and interaction parameters (χ)^(a).

Materials	**θ_{water} (°)**	**θ_{EG} (°)**	**θ_{DM} (°)**	**γ (mN m^{-1})**	**χ with D1**	**χ with A1**	**χ with D1:A1**
PTB7-Th	100.3	74.5	49.4	32.0	–	0.431	–
IEICO-4F	93.4	67.7	37.8	39.9	0.431	–	–
PTB7-Th:IEICO-4F	102.2	52.4	77.1	31.4	–	–	–
Y1	153.5	71.1	36.7	49.7	1.935	0.540	2.096
Y5	104.3	61.8	34.8	42.4	0.719	0.037	0.818
Y6	95.0	79.6	45.1	36.4	0.141	0.079	0.187
Y7	107.7	74.5	47.1	36.0	0.116	0.099	0.158

(a)The Flory-Huggins interaction parameter based on the surface tension data formula between the donor (D) and the acceptor (A) calculated using $\chi = (\sqrt{\gamma D} - \sqrt{\gamma A})^2$.

To gain insight into the exciton dissociation and charge collection in binary and ternary devices, we calculated the exciton dissociation efficiency (η_{dis}) and the charge collection efficiency (η_{col}) based on the relationship between the photocurrent density (J_{ph}) and the effective voltage (V_{eff}), as shown in **Figure 6.8a**. J_{ph} is defined as J_L–J_D, where J_L and J_D are photocurrent density measured under illumination and dark conditions, respectively. The V_{eff} is given by V_0–V_{bias}, in which V_0 is the voltage when $J_L = J_D$ and V_{bias} is the applied voltage. In the large effective voltage regime ($V_{eff} > 0.5$ V), J_{ph} became saturated, suggesting that all the excitons could separate and generate free carriers, and then be collected by electrodes under the assistance of applied field. The η_{dis} and η_{col} can be acquired from the ratio of J_{ph}/J_{sat} under short-circuit and maximal power point conditions, respectively, where J_{sat} is the saturation photocurrent density. The η_{dis} values are calculated to be 92.9%, 91.7%, 92.5%, 95.8%, and 93.5% for the binary, Y1, Y5, Y6, and Y7-based devices, respectively. The η_{col} values follow the same trend as η_{dis} values, implying that more effective exciton dissociation and charge extraction efficiency in Y6 and Y7 based ternary devices among the other two ternary and binary host devices, which support the trend of J_{SC} and FF of the corresponding OSCs.

Apart from exciton dissociation and charge collection, to investigate the charge recombination mechanism within ternary OSCs, the *J-V* curves under different illumination intensities (P_{light}) of the binary and ternary devices were measured. The bimolecular recombination can be described by the relationship between J_{SC} and P_{light} with a power-law formula of $J_{SC} \propto P_{light}^{\alpha}$, in which slope α is the exponential factor related to bimolecular recombination degree.[175,305] As depicted in **Figure 6.8b**, the fitting α values were 0.898, 0.878, 0.912, 0.943, and 0.940 for binary, Y1, Y5, Y6, and Y7 added ternary OSCs, respectively. After adding Y6 or Y7 into PTB7-Th:IEICO-4F, the α values were closer to unity, indicating that the addition of Y6 or Y7 can effectively suppress bimolecular recombination, which is consistent with the improvement in J_{SC} and FF of the corresponding OSCs. In addition, the degree of trap-assisted recombination in the binary and ternary devices can be evaluated by plotting the curve of V_{OC} *versus* logarithm of P_{light}. The relationship between V_{OC} and P_{light} mechanism can be described as $V_{OC} \propto \ln P_{light}$. In general, a slope of $k\mathrm{T}/q$ is expected for a device dominated by bimolecular recombination (where k is Boltzmann constant, T is temperature, and q is the elementary charge), whereas a device dominated by trap-assisted recombination has a slope of 2 $k\mathrm{T}/q$.[42,45] As depicted in **Figure 6.8c**, the PTB7-Th:IEICO-4F:Y6 or the PTB7-Th:IEICO-4F:Y7-based ternary devices show the fitted slopes of 1.18 $k\mathrm{T}/q$, which is smaller than that of the binary device (1.25 $k\mathrm{T}/q$) and ternary devices based on PTB7-Th:IEICO-4F:Y1 (1.60 $k\mathrm{T}/q$) or the PTB7-Th:IEICO-4F:Y5 (1.36 $k\mathrm{T}/q$), indicating weakened trap-assisted charge recombination in the Y6 or Y7 ternary OSCs. Simultaneously suppressed bimolecular and trap-assisted charge recombination can be obtained by the addition of the red-shifted Y6 or Y7 added ternary OSCs, which can well explain the J_{SC} and FF improvement.

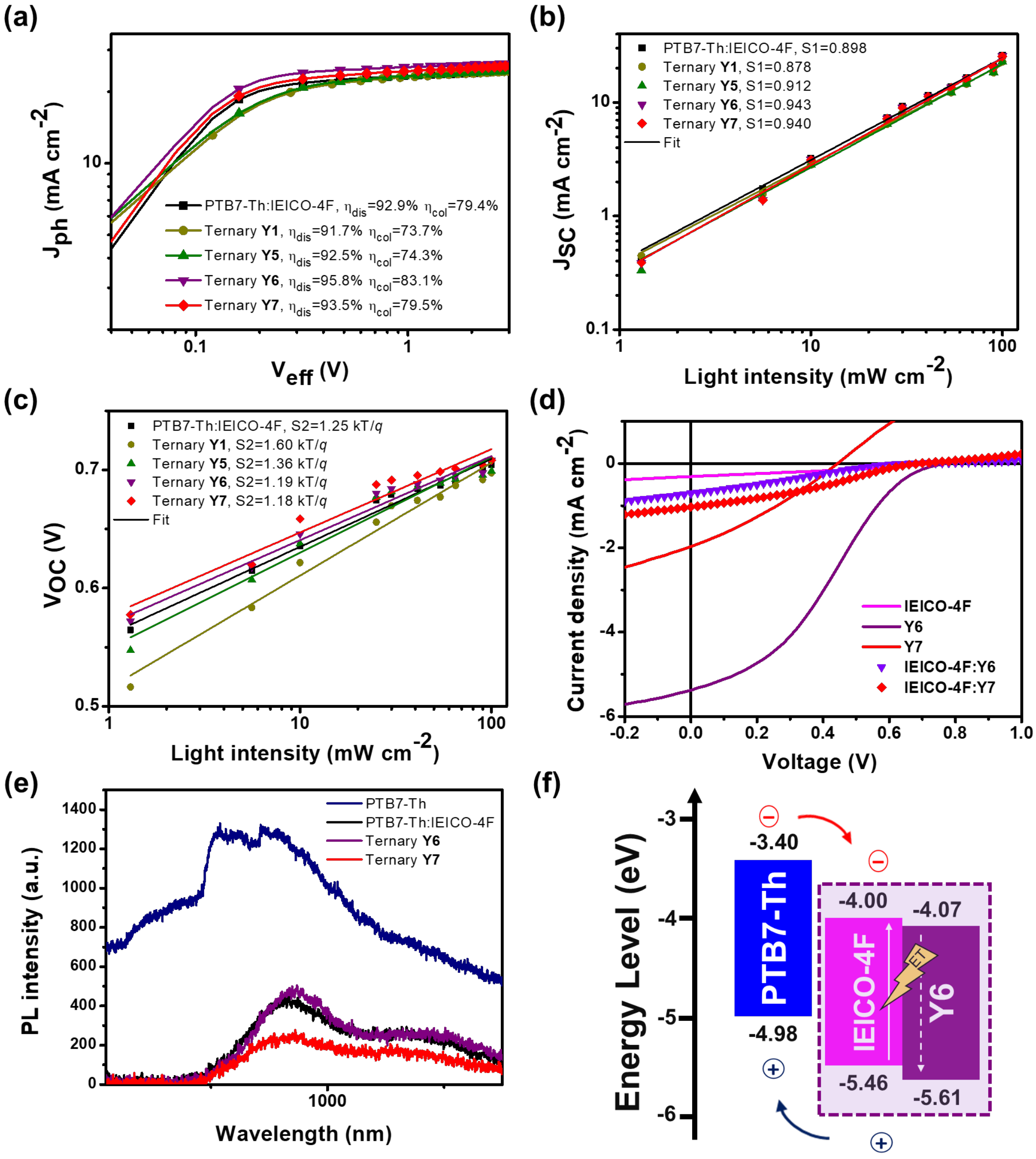

Figure 6.8 (a) J_{ph}–V_{eff} curves of the optimized binary and ternary OSCs; (b) V_{OC} and (c) J_{SC} versus light intensity characteristics; (d) *J-V* curves of acceptor-only devices illuminated under AM 1.5G condition; (e) photoluminescence spectra of PTB7-Th neat film and the corresponding ternary blends; and (f) working mechanism in ternary PTB7-Th:IEICO-4F:Y6 blend.

The recombination of OSCs is also influenced by an energetic disorder of photoactive layer. An Urbach tail energy model is leveraged to quantify the degree of energetic disorder, in which generally disordered organic semiconductors tend to absorb the light at photon energies below the bandgap (sub-bandgap absorption). From this region, we could calculate the Urbach energy from the tail states of EQE spectra, as shown in **Figure 6.9** and described by equation 5.7. Since the E_U is determined by the width of the localized tail state on the edge of the optical band gap, the smaller E_U represents a smaller degree of energy disorder in the molecular orbital and sharpened band edge with reduced tail states.[40,41] The calculated E_U was 26.67, 31.08, 30.92, 26.08, and 26.72 meV, respectively for host binary device and ternary devices based on Y1, Y5, Y6, and Y7, respectively. Relative to the host binary device and the other Y-NFAs ternary devices, the lower Urbach energy of Y6 based ternary device can be attributed to the lower degree of charge recombination in ternary cells and better molecular orientation in the ternary blends.[42] This result implies that the lower energetic disorder can be achieved by introducing an appropriate third component in the ternary devices.

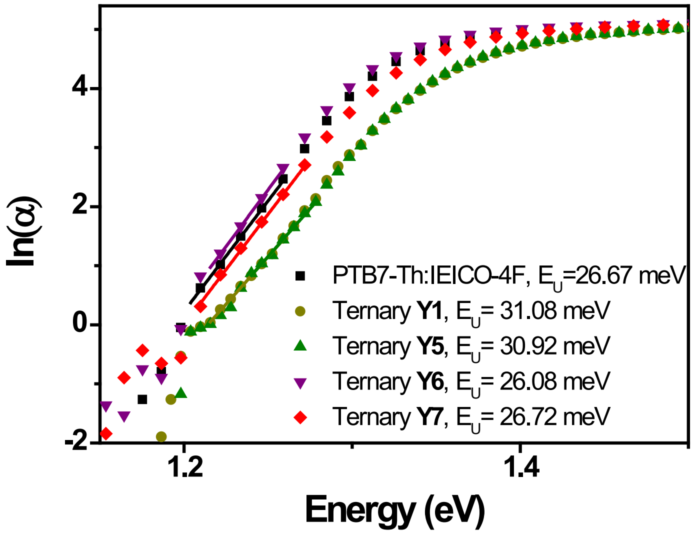

Figure 6.9 The Urbach's energy plots of the binary and ternary based PTB7-Th:IEICO-4F devices.

Among the Y-NFAs introduced ternary blend, ternary blends with the addition of Y6 and Y7 showed better performance and reasonable charge dynamics. Thus, to give more solid experimental evidence on the intermolecular dynamic process between IEICO-4F and Y6 or Y7, a series of cells without donor were fabricated with IEICO-4F, Y6, Y7, IEICO-4F:Y6, and IEICO-4F:Y7 as active layers. The corresponding *J-V* curves of cells were measured under AM 1.5G illumination with a light intensity of 100 mW cm-2 and are depicted in **Figure 6.8d**. The J_{SC} of IEICO-4F:Y6 and IEICO-4F:Y7 based cells is in between that of IEICO-4F, Y6, and Y7 based cells, suggesting that the charge transfer between the corresponding Y-NFAs with host acceptor IEICO-4F should be negligible in blend films. Therefore, it is very likely that an acceptor alloy-composite could be the additional pathway in ternary blends for charge transfer and dissociation by the addition of Y6 and Y7. From thermodynamic point of view by measuring the interaction parameter of host acceptor IEICO-4F and guest acceptor Y6 and Y7 (see Table 6.4), it is revealed that Y6 and Y7 show lower χ values with IEICO-4F and exhibit higher χ values with PTB7-Th, suggesting excellent intermixing of Y6 or Y7 with IEICO-4F which can form an acceptor alloy-composite like. To verify this, a series of photoluminescence (PL) quenching experiments based on PTB7-Th neat film, binary and Y6- or Y7-based ternary blends were carried out. As shown in **Figure 6.8e**, the PL of PTB7-Th from excitation upon a 650 nm laser was more efficiently quenched in ternary Y7 blend than in the binary and ternary Y6 blend indicating that the addition of Y7 clearly promote electron transfer from PTB7-Th to the mixed acceptor phase. Interestingly, ternary Y6 blend shows slightly higher emission spectra than binary blend, which may indicate the presence of energy transfer from Y7 to binary PTB7-Th:IEICO-4F, however it seems not a significantly important mechanism as compared to the alloy-like formation between Y6 and IEICO-4F, as shown in **Figure 6.8f**.

Considering the PCE improvement of ternary devices which is mainly attributed to the formation of alloy-like composite to enhance photon harvesting in long wavelength by employing Y6 and Y7 as third component, it is expected to develop their ST-OSCs to achieve well-balanced between high PCE, high AVT values, and stable devices for real applications. Replacing 100 nm Ag by 10 nm Ag as electrode, semitransparent OSCs were prepared with the structure of ITO/PEDOT:PSS/active layers/PDINO/10 nm Ag. Here, the *J-V* curves of the semitransparent OSCs with 10 nm of Ag as the electrodes were measured under the simulated AM 1.5G illumination with light intensity of 100 mW cm^{-2} and are shown in **Figure 6.10a**. The corresponding photovoltaic parameters of semitransparent OSCs are summarized in **Table 6.5**. The semitransparent binary OSCs exhibit PCE of 8.11%, AVT of 26.48%, with LUE value of 2.15%. The PCE and AVT of semitransparent OSCs can be simultaneously improved by incorporating Y6 and Y7. The increased PCE of 8.51% with higher AVT of 27.35%, resulting in higher LUE value of 2.33% is obtained by the addition of Y6 in ternary device. The PCE and AVT of semitransparent ternary OSCs with Y7 in the alloyed acceptor are increased to 8.20% and 27.34%, respectively. The V_{OC} and FF values of semitransparent OSCs are slightly lower than those of opaque OSCs, mainly resulting from the relatively low conductivity of semitransparent Ag electrode. It is apparent that J_{SC} values of semitransparent OSCs are much lower than those of opaque OSCs due to the photon loss from the semitransparent Ag electrode.

The transmittance spectra of binary and ternary blend films and the corresponding semitransparent OSCs with 10 nm of Ag as the electrode was measured and shown in **Figure 6.10b**. The active layer exhibit relatively high transmittance in the short wavelength range, which is in good accord with the absorption spectra of blended films. The transmittance of semitransparent OSCs is markedly decreased compared with that of active layers, which should be attributed mainly to the enhanced light reflection of the Ag electrode. This phenomenon can be

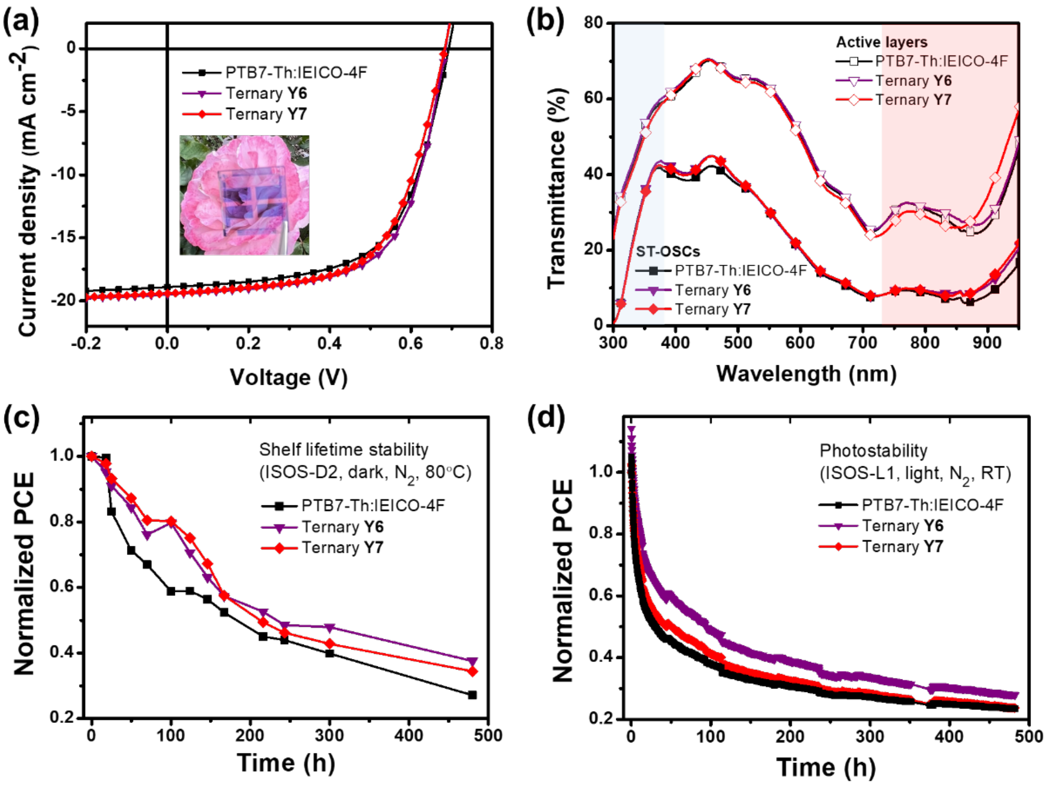

Figure 6.10 (a) *J–V* light curves, (b) transmission spectra of the active layers and the corresponding semitransparent OSCs with 10 nm Ag thickness as the electrode, (c) thermal stability, and (d) photostability test of the corresponding ST-OSCs.

Table 6.5 Summarized device performance parameters, AVT, and LUE of semitransparent binary and ternary devices with different Ag thickness, measured under AM 1.5G with 100 mW cm^{-2} intensity.

Blend	**V_{OC} (V)**	**J_{SC} (mA cm^{-2})**	**FF (%)**	**PCE $^{(a)}$ (%)**	**AVT (%)**	**LUE (%)**
PTB7-Th:IEICO-4F	0.69	18.91	61.90	8.11 (7.84 ± 0.16)	26.48	2.15
PTB7-Th:IEICO-4F:**Y6**	0.68	19.51	63.65	8.51 (8.36 ± 0.31)	27.35	2.33
PTB7-Th:IEICO-4F:**Y7**	0.68	19.48	61.77	8.20 (8.00 ± 0.16)	27.34	2.24

$^{(a)}$ The values in parentheses are the average and standard deviation values calculated with 6 individual cells prepared from different batches.

further confirmed from the transmission spectra of semitransparent OSCs with 10 nm thickness of Ag as electrode. **Figure 6.10c** and **6.10d** shows the thermal and photostability test for the corresponding ST-OSCs. It is observed that Y6 added ternary device shows high stability compared to the binary devices and Y7 ternary device. Interestingly, similar degradation behaviours were observed in ST devices and corresponding opaque ones, indicating that thinner metal electrode would not degrade the device lifetime. It should be emphasized that the difference between ST-OSCs and opaque ones lies on the top electrodes only, which means that the stability issues related to the active layers of ST-OSCs should be similar to those of opaque ones. This observation is in accordance with the work of Romero-Gomez and co-workers.[306]

6.3 Conclusions

In conclusion, a series of ternary organic solar cells (OSCs) with near-infrared Y-series nonfullerene acceptors (NFAs; mainly Y1, Y5, Y6, and Y7) were comparatively studied as third components in semitransparent PTB7-Th:IEICO-4F binary blend to balance the trade-off between the power conversion efficiency (PCE), average visible transmittance (AVT), and operational stability for the practical applications of ST-OSCs. The photovoltaic, transmittance, and stability behaviors of the resultant ternary OSCs differ significantly by introducing different Y-series NFAs materials. When blended with PTB7-Th:IEICO-4F with the PCE of 11.86%, the PCEs of 11.32%, 11.55%, 13.02%, and 12.32% were yielded for opaque Y1, Y5, Y6, and Y7 based ternary OSCs. A series of ST-OSCs were prepared with 10 nm thickness of Ag as the electrode. The different photovoltaic performance as well as the difference in AVT values were observed using different Y-series NFA materials. The ST-TOSCs based on PTB7-Th:IEICO-4F:Y6 with a modified Ag electrode thickness of 10 nm achieve the highest LUE of 2.35% as the product of good PCE of 8.47% and high AVT of 27.77% among the other Y-series incorporated

ST-TOSCs. Moreover, Y6 based ST-TOSCs exhibited good thermal and photo stability under inert condition. Our findings indicate that without optical manipulation, ternary strategy with a proper selection of ultra-narrow band gap third components materials should provide great potential toward well-balanced PCE, AVT, and operational stability of ST-OSCs.

Chapter 7

Shelf lifetime analysis of organic solar cells combining frequency and time resolved techniques

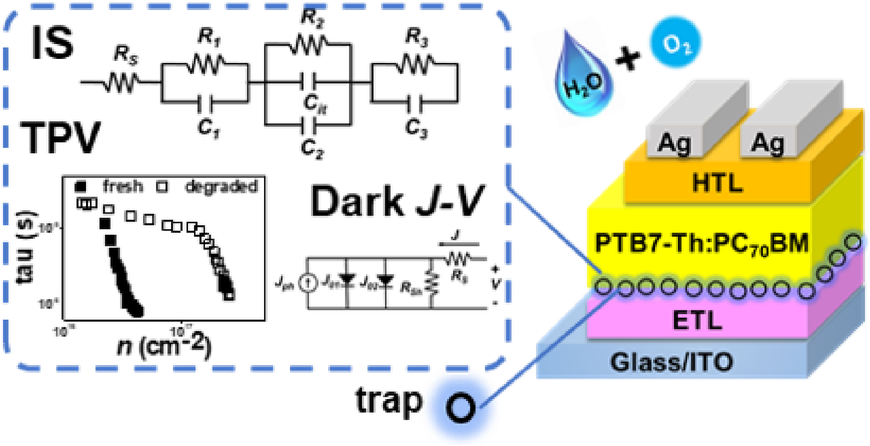

This chapter is based on the published work: Torimtubun, A.A.A. *et al.* Shelf Lifetime Analysis of Organic Solar Cells Combining Frequency and Time Resolved Techniques *Sustain. Energy Fuels*, **2021**, *5*, 6498-6508.

7.1 Introduction and the aim of the work

Emerging photovoltaic technologies such as dye sensitized solar cells, perovskite, and organic solar cells have established their significant as a sustainable solar to energy devices. OSCs, in contrast to current perovskite solar cells, are lead-free, low-cost with a short energy payback time, and can be solution-processed on light-weight, semitransparent, flexible substrate over large areas by roll-to-roll technique.[292,307–310] Along with these appealing properties, in recent years, a rapid improvement in PCE of up to over 18% in single-junction OSC may bring OSC an opportunity into the market.[311–313] However, high efficiency and low cost are not only the requirements to scale up the OSC device into the market. Device operational stability is also one of the key criteria to make large-scale production of OSC commercially more feasible. Up to now, the silicon-based PVs companies guarantee their products for 25 years of operational stability.[121] For OSC, a lifetime of over 20 years is estimated to be financially competitive,[314] giving space for further stability improvement.

A huge effort is being made to understand the degradation mechanisms and strategies to make the OSC lifetime longer. For instance, modifying the chemical structure of the active layer materials, employing ternary strategy in the active layer, using a compatibilizer to reduce the interfacial tension, inverting the OSC device polarity, optimizing buffer layers, using stable electrodes, eliminating photo-dimerization of fullerene, and increasing the material crystallinity of nonfullerene materials are known degradation mechanisms to minimize the intrinsic degradation. [120,237,315–317] Meanwhile, a proper encapsulation is widely used to prevent the interaction of oxygen and moisture from the atmosphere into the OSC devices. This method can lead to suppressing the device extrinsic degradation. Nevertheless, the production cost, weight, and device flexibility are the important concerns from industrial engineering perspective when the devices need to be encapsulated. It is hence highly desirable to improve the intrinsic stability and minimize the encapsulation.

Some studies on polymer:fullerene OSC showed that the inverted structure and the choice of metal oxide, stable metal or electron transport polymer for the cathode material have a key contribution to improve the air stability of the device.[82,119,122,318] In iOSC, the hygroscopic and acidic poly(3,4-ethylenedioxythiophene):poly(styrene sulfonic acid) (PEDOT:PSS) can be avoided and the low work function aluminium electrode that causes the degradation can be replaced by a high work function metal electrode such as silver or gold.[123] The electron transport layer (ETL) is a key component in acquiring high performance and stable iOSC. The ETL has a role in modifying the alignment between the work function of the transparent conductive ITO cathode and the Fermi level of the semiconductor, promoting the electron transfer and the carrier extraction process.[319,320] To improve the stability, the ETL may act as a scavenging layer to protect the active layer from oxygen and moisture.[119] Transition metal oxides as ETL, such as titanium dioxide (TiO_x) and zinc oxide (ZnO), and water-soluble organic ETL, poly [(9,9-bis(3'-(N,N-dimethylamino)propyl)-2,7-fluorene)-alt-2,7-(9,9–dioctylfluorene)] (PFN), are the most commonly ETLs used in iOSC. These ETL materials exhibit high electron conductivity, an excellent optical transmittance, low work function, high refractive index, good chemical stability, non-toxicity, and an ability to improve charge carrier extraction.[138,175,321,322]

It is apparent that the interlayer engineering and its optimization are the crucial factors to be considered to fabricate high performance and air-stable devices. To gain further insight into the physical mechanisms governing the device operation, optoelectronic characterization techniques are widely employed. Small-perturbation time- and frequency-domain measurements such as transient photovoltage/photocurrent (TPV/TPC) spectroscopy, charge extraction, and impedance spectroscopy (IS) have been widely employed to study relaxation processes in the field of dye-sensitized solar cells (DSSC),[323,324] OSCs,[325,326] and perovskite solar cells[327] but fewer studies arise from the combination of both techniques. Electronic transitions can be studied with TPV/TPC at a very fast time scale (higher frequency) while the electronic and ionic conduction can be observed by IS at lower time scales (lower frequency).[79] Nevertheless, the same information and comparable results can be obtained from TPV/TPC or EIS. The combined TPV and IS techniques have been already used by Pockett *et al.* to study the effect of degradation on the active layer and interlayer in OSC.[328] However, in-depth discussion of the device lifetime analysis according to ISOS protocol using combined TPV and IS techniques remains unclear. In the meantime, ISOS protocols play an important role in the advancement of OSC's research and future industrial manufacture.

In this study, we perform IS and TPV/TPC measurements on the inverted PTB7-Th:$PC_{70}BM$-based device with different ETL materials to investigate the effect of ETL on the stability of nonencapsulated iOSC. The standard procedure of ISOS D-1 protocol (under dark, and ambient condition) was used for an accurate lifetime determination.[137] Three different ETLs were investigated, one water-soluble organic-based (PFN) and two metal oxides-based (TiOx and ZnO). We demonstrate that TPV/TPC combined with IS can be employed to gain a deeper insight into the behavior and degradation mechanisms of iOSC concerning the cathode interlayer used. The TPV measurements are useful in observing the degradation of the active layer as a result of trap formation, while IS measurements give more detail information about the interfacial density of states across the interlayer. We found that using an appropriate ETL, it can significantly improve the stability of iOSC. Under nonencapsulated ambient condition, metal oxides show more stable ETL while organic interlayers are more susceptible to the oxygen and moisture ingress.

7.2 Photovoltaic characteristics by *J-V* measurement

In this study, the BHJ device were fabricated with inverted configuration ITO/ETL/PTB7-Th:$PC_{70}BM/V_2O_5$/Ag as schematically illustrated in **Figure 7.1a** by using different ETL materials. An inverted structure is chosen to minimize any degradation originating from the metal electrode oxidation and the acidic interfacial layer.[329] The selected interlayers studied here represent the most common organic and inorganic materials employed as ETL in iOSC. The as-fabricated device namely "fresh device" was characterized immediately after the fabrication process. The nonencapsulated fresh devices then were kept under ambient environment (room temperature (RT) of 23°–27°C and controlled relative humidity (RH) of 35–50%) in open circuit condition with no illumination, following the ISOS-D1 protocol.[137] The devices were only exposed to the light during device characterization and returned to the dark shelf chamber.

Figure 7.1b shows the current density to voltage (*J-V*) characteristics of these fresh and degraded cells measured under simulated AM 1.5G illumination (100 mW cm^{-2}) at RT. The corresponding devices parameters are summarized in **Table 7.1**. In addition, **Figure 7.2a-c** shows the initial transient of the illuminated *J-V* measurements. For the performance of the fresh device, ZnO-iOSC shows the lowest J_{SC}, the lowest shunt resistance (R_{Sh}), thus the lowest PCE_{max} of 9.79%. TiOx-iOSC exhibits the highest J_{SC}, the lowest FF and the highest series resistance (R_S), resulting in PCE_{max} of 9.99%. Meanwhile, PFN-iOSC can improve the device performance, showing the highest V_{OC}, FF and R_{Sh}, which leads to the highest PCE_{max} of 10.35%. From the degradation perspective, degraded (526 h) devices show a prominent reduction in the device performance for all ETLs compared to fresh (0 h) devices. J_{SC} of PFN-, TiOx-, and ZnO-iOSCs fell 13%, 9% and 7% after 526 h. The J_{SC} reduction in all degraded cells is coherent with the reduction of calculated J_{SC} values obtained from external quantum efficiency when compared to those of fresh devices, as shown in **Figure 7.1c**. On the other hand, V_{OC} decreases slightly after degradation, fell 10% for PFN-iOSC and fell 4% for each TiOx- and ZnO-iOSC. In addition, a significant decrease in FF after 526 h degradation is observed; FF fell by 33%, 17% and 16% for PFN-, TiOx- and ZnO-iOSC, respectively. A significance FF reduction may arise from a gradual increase of R_S and a drop of R_{Sh} observed for degraded devices as a result of the parasitic resistance effect. It leads to a considerably lower PCE, in which PCE of PFN-iOSC drop to almost 50% of its initial value while TiOx- and ZnO-iOSCs drop to 26% and 24% from their initial value. In general, the devices using PFN as cathode interlayer in iOSC suffer from the worst stability while the devices using ZnO as ETL resulted in the most stable devices. Since the device architecture and fabrication process are identical, the difference in device parameter stability observed may be attributed to the different ETL materials used.

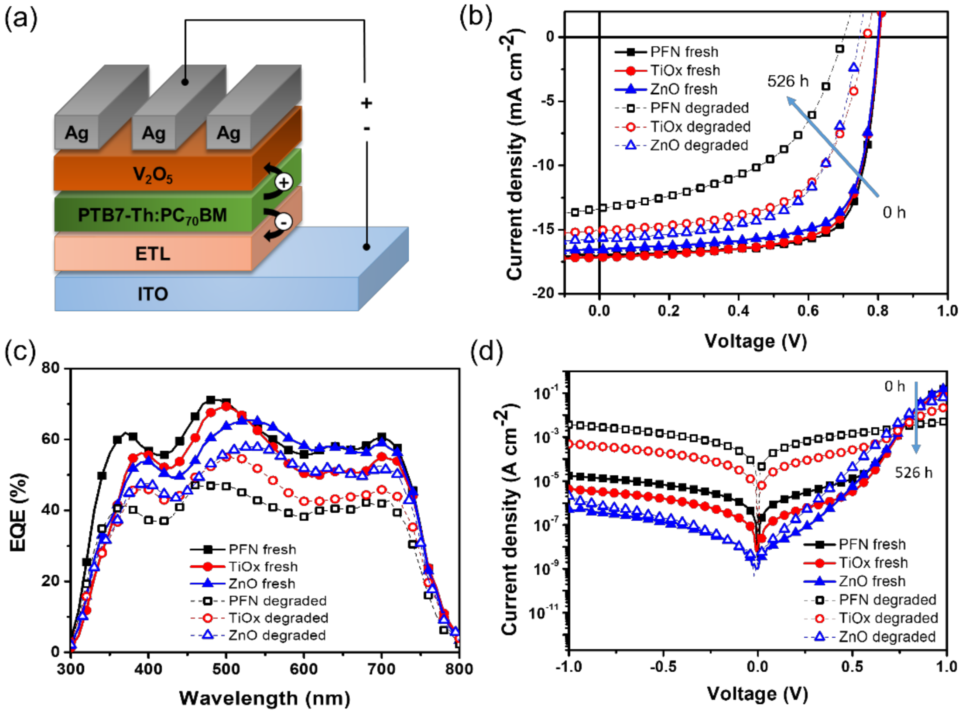

Figure 7.1 (a) Schematic illustration of the inverted device architecture, (b) *J–V* characteristics under illumination, (c) EQE spectra, and (d) dark *J–V* characteristics of fresh and 526 h degraded PTB7-Th:PC_{70}BM-based devices with different ETLs (PFN, TiO_x, and ZnO).

Table 7.1 Device performance parameters for different ETLs (PFN, TiO_x and ZnO), measured under AM 1.5G with 100 mW cm^{-2} intensity. Nonencapsulated devices were degraded after 526 h under ambient condition (RT, % RH = 35 – 50%).

ETL		J_{SC} / J_{calc} ^{a} **(mA cm^{-2})**	V_{OC} **(V)**	**FF (%)**	**PCE / PCE$_{max}$ (%)**	R_s **(Ω cm^2)**	R_{sh} **(kΩ cm^2)**
PFN	fresh	16.83 ±0.37 / 15.98	0.80 ±0.006	74.40 ±0.52	10.0 ±0.20 / 10.35	0.95 ±0.06	1618 ±542
	aged	14.69 ±0.93 / 14.04	0.72 ±0.018	50.21 ±1.22	5.31 ±0.36 / 5.89	7.94 ±1.08	242 ±23
TiO_x	fresh	17.19 ±0.17 / 16.71	0.79 ±0.005	71.40 ±1.12	9.73 ±0.18 / 9.99	1.69 ±0.08	1044 ±315
	aged	15.71 ±0.39 / 15.01	0.76 ±0.004	59.43 ±1.62	7.11 ±0.32 / 7.39	5.16 ±2.04	543 ±63
ZnO	fresh	16.70 ±0.20 / 15.43	0.79 ±0.005	72.45 ±0.61	9.60 ±0.14 / 9.79	0.94 ±0.07	858 ±424
	aged	15.53 ±0.32 / 14.47	0.76 ±0.017	61.17 ±1.86	7.21 ±0.25 / 7.41	2.78 ±1.27	531 ±132

*The performance parameters of devices were obtained from over 4 devices.

Figure 7.1d further compares the dark *J-V* characteristics for all devices before and after 526 hours of degradation. **Table 7.2** summarizes the experimental and modeled device performance parameters from dark *J-V* curves. The fitting values are obtained using a two-diode equivalent model where the detail fitting calculation can be found elsewhere.[160] In addition, **Figure 7.2d-f** shows the initial transient of the dark *J-V* measurements and **Figure 7.3** displays the fitting for the fresh and degraded devices. All fresh devices shows an ideal exponential region with an ideality factor in the range of 1.05 to 1.11, combined with the R_S at medium-high voltage bias and a leakage current at low bias, which can be linked to the manufacturing imperfections.[330] The leakage current depends on the ETL and can be ascribed as the combination of a R_{Sh} and a second non-ideal exponential region with an ideality factor larger than 2. A high leakage current is probably caused by lower contact selectivity within the cell and increase surface wetting condition when exposed under ambient degradation.[331,332] After 526 h degradation, all devices show a reduction in the current density in forward and reverse bias due to the loss in diode and resistance properties. The observed R_S increment in all degraded devices can be ascribed to several factors such as a creation of deep and shallow traps due to the interaction of oxygen and water with the polymer reducing charge carrier mobility, a loss of injection efficiency from electrode contacts into the active layer due to increasing barrier for charge injection or a creation of isolation layer between the bulk active

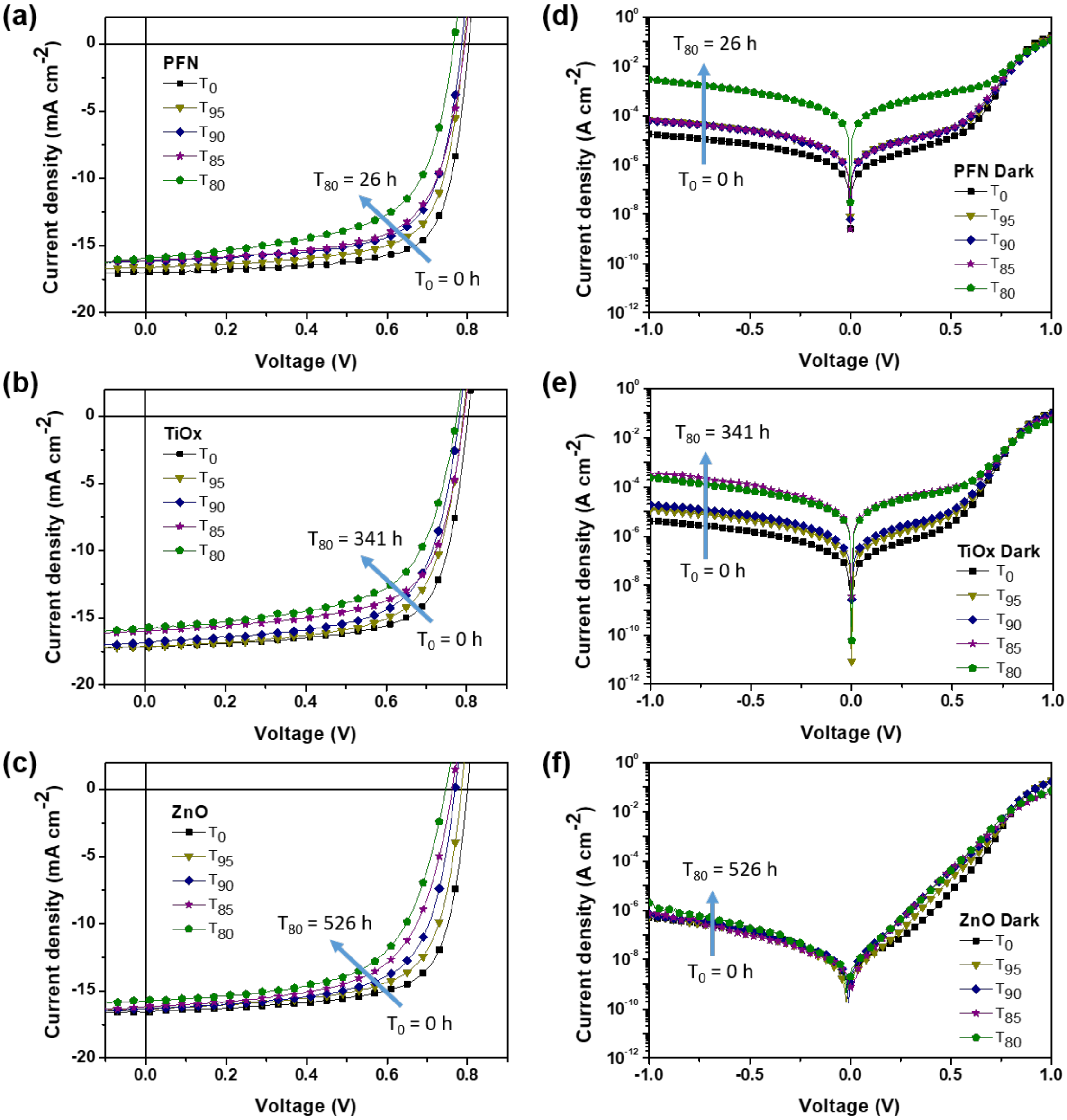

Figure 7.2 (a–c) Light illumination and (d–f) dark *J*-*V* characteristic of PTB7-Th:PC$_{70}$BM-based device with different ETLs: (a,d) PFN, (b,e) TiO$_x$, and (c,f) ZnO exposed to ambient conditions over storage time. T_0 is the initial time for the initial testing measurement of the fresh device and T_{80} is the time the devices took to decay 20% from its initial measurement.

layer and contact hindering the charge carrier collection.[333] In addition, the ideality factor values of degraded devices in the first exponential region change to 1.59 – 1.91 and the leakage current strongly increases due to the reduction of R_{Sh} values and the worsening of the second exponential region, with the ideality factors much larger than 2. Therefore, the lower PCE observed in PFN-iOSC and TiOx-iOSC than those of ZnO-iOSC could be limited by a lower charge extraction and higher leakage current. These two effects are in good agreement with the higher trap defects due to the degradation process as described later in this work.

Table 7.2 Extracted series resistance and shunt resistance values from experimental and modeled data from dark *J-V* curves Figure 7.1d for fresh and degraded devices after 526 h exposure time.

Device Parameters	**PFN Fresh**	**PFN Deg**	**TiO_x Fresh**	**TiO_x Deg**	**ZnO Fresh**	**ZnO Deg**
R_S^{exp} (Ω cm^2)	11.92	204	19.22	67.50	11.71	28.96
R_S^{fit} (Ω)	0.62	69	1.24	7	0.64	2
R_{Sh}^{exp} (Ω cm^2)	9.24×10^4	4.30×10^2	5.16×10^5	3.16×10^3	9.09×10^6	8.16×10^6
R_{Sh}^{fit} (Ω)	9.22×10^4	4.00×10^2	5.35×10^5	3.15×10^3	7.45×10^6	9.36×10^6
J_{01}^{fit} (A cm^{-2})	8.42×10^{-15}	4.67×10^{-9}	5.95×10^{-15}	1.84×10^{-12}	1.88×10^{-15}	1.42×10^{-11}
n_1	1.11	1.91	1.09	1.37	1.05	1.50
J_{02}^{fit} (A cm^{-2})	2.28×10^{-8}	4.10×10^{-5}	1.58×10^{-9}	7.30×10^{-7}	3.68×10^{-10}	4.34×10^{-9}
n_2	3.35	6.4	2.64	4.12	2.00	2.12

To get a further insight into the degradation trend behavior of iOSC with different ETLs over shelf lifetime under ambient environment, the normalized device performance parameters (V_{OC}, J_{SC}, FF and PCE) are presented in **Figure 7.4** Corresponding to ISOS-D1 protocol, the operating shelf lifetime of each studied cells is summarized in **Table 7.3**. The term E_0 is the initial testing measurement of fresh devices at 0 h (T_0) while E_{80} is the testing measurement of degraded devices under dark ambient condition after the PCE decay 20% from its initial value at time T_{80}.[137] **Figure 7.4a** shows the PCE decay behavior for all devices. It is worth noting that the

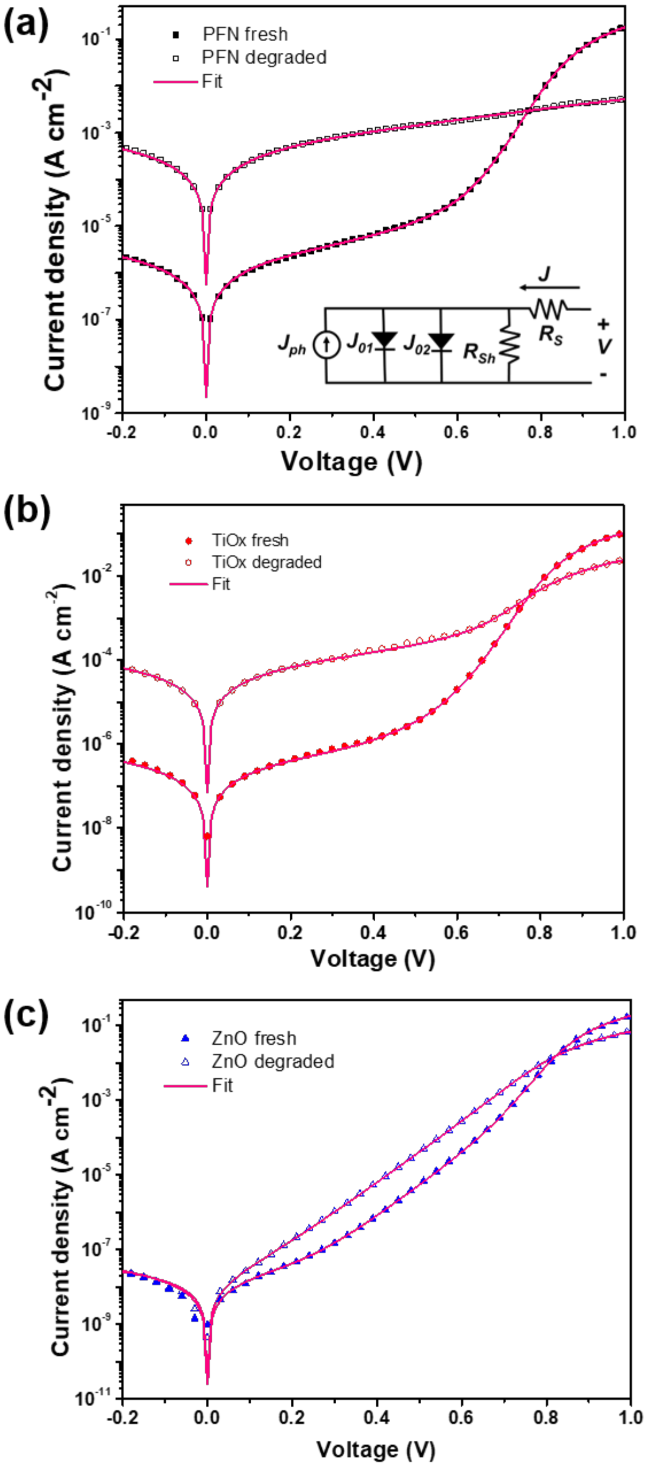

Figure 7.3 Fitting dark *J-V* curves of fresh and degraded cells at 526 h for (a) PFN-, (b) TiOx-, (c) ZnO-iOSCs using two-diode electrical circuit model.

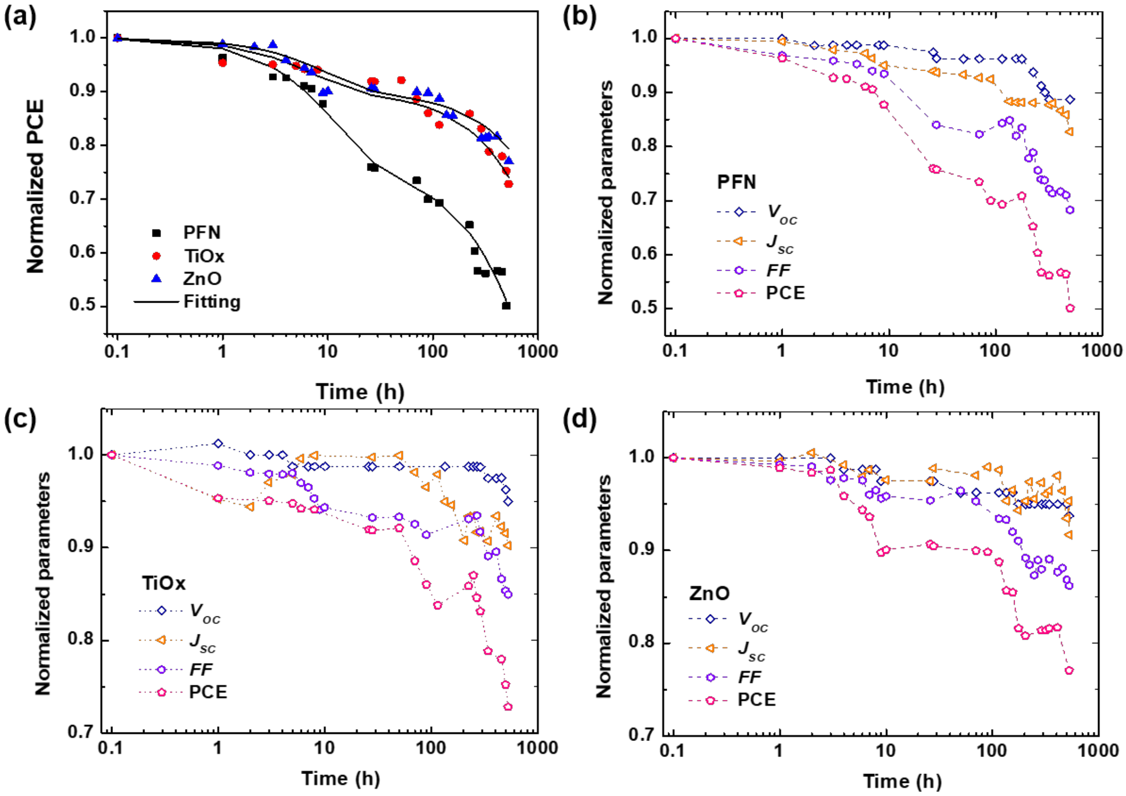

Figure 7.4 (a) Fitting of the normalized PCE over the storage time using eqn (1) for all devices. (b) – (d) Normalized device performance parameters of each inverted PTB7-Th:$PC_{70}BM$-based device with different ETLs: (b) PFN, (c) TiO_x, and (d) ZnO. The symbols are the experimental data, the solid lines are the fitting curves, and the dashed lines are guide to the eyes. The samples were degraded in dark ambient environment and all measurements were carried out under AM 1.5G illumination.

rapid PCE decay in the first few hours are observed in all devices. It is known as "burn-in loss" degradation loss mechanism due to the photochemical reaction within the device layers.[130,334] It can be seen that PFN-iOSC reached to decay its 20% (T_{80}) performance after only 26 h, faster than its TiOx- and ZnO-iOSC counterparts that took 341 h (2 weeks) and 526 h (3 weeks) to reach T_{80}, suggesting the poor stability of the PFN as ETL in nonencapsulated iOSC. It is because their performance parameter decreases rapidly in a short exposure time, as shown in **Figure 7.4b** and Table 7.3. V_{OC}, J_{SC}, FF of PFN-iOSC at T_{80} are reduced down to 4%, 6% and 16%, while those of TiOx-iOSC at T_{80} are fell to 3%, 7%, 11% (**Figure 7.4c**) and those of ZnO-iOSC at T_{80} are decreased down to 5%, 8%, 14% (**Figure 7.4d**), respectively. The evolution of illuminated and dark *J-V* characteristics over the device lifetimes are shown in Figure 7.2. In general, compared to the other device parameters, V_{OC} seems to be the least affected by the degradation in PTB7-Th:PC$_{70}$BM-based iOSC, while J_{SC} and FF appear to suffer more by the degradation. It suggests that the performance deterioration is probably more associated with the charge extraction and leakage current-dominated photogeneration, which is correlated with the interlayer quality of the devices.

Table 7.3 The summary shelf lifetime data for all the nonencapsulated devices under ambient condition (RT, %RH= 35 – 50%). The data given are in hours

Standard lifetime	PFN	TiOx	ZnO
E_0, T_0 (PCE, %)	10.35	9.99	9.79
T_{95}	3	8	7
T_{90}	9	70	115
T_{85}	12	224	224
T_{80}	26	341	526

As displayed in Figure 7.4a, the degradation of all devices displays an exponential decay. A fast initial decay followed by a slow decay can be fitted by the superposition of two exponential function with different time constants, as previously reported by [122,335]:

$$\frac{PCE(t)}{PCE(0)} = A1 \times \exp\left(\frac{-t}{T1}\right) + A2 \times \exp\left(\frac{-t}{T2}\right) \tag{7.1}$$

where PCE (0) is the relative initial power conversion efficiency at t = 0 h. The time constants (T1, T2) and the degradation power factors of the individual exponential functions (A1, A2) are obtained via a least-squares fit. The two exponential functions of the measured and modeled curves for each ETLs using equation 1 can be observed clearly in **Figure 7.5** and **Table 7.4** summarized the values extracted from equation 1 for all devices. It is observed that metal oxide ETLs-based device (ZnO-iOSC and

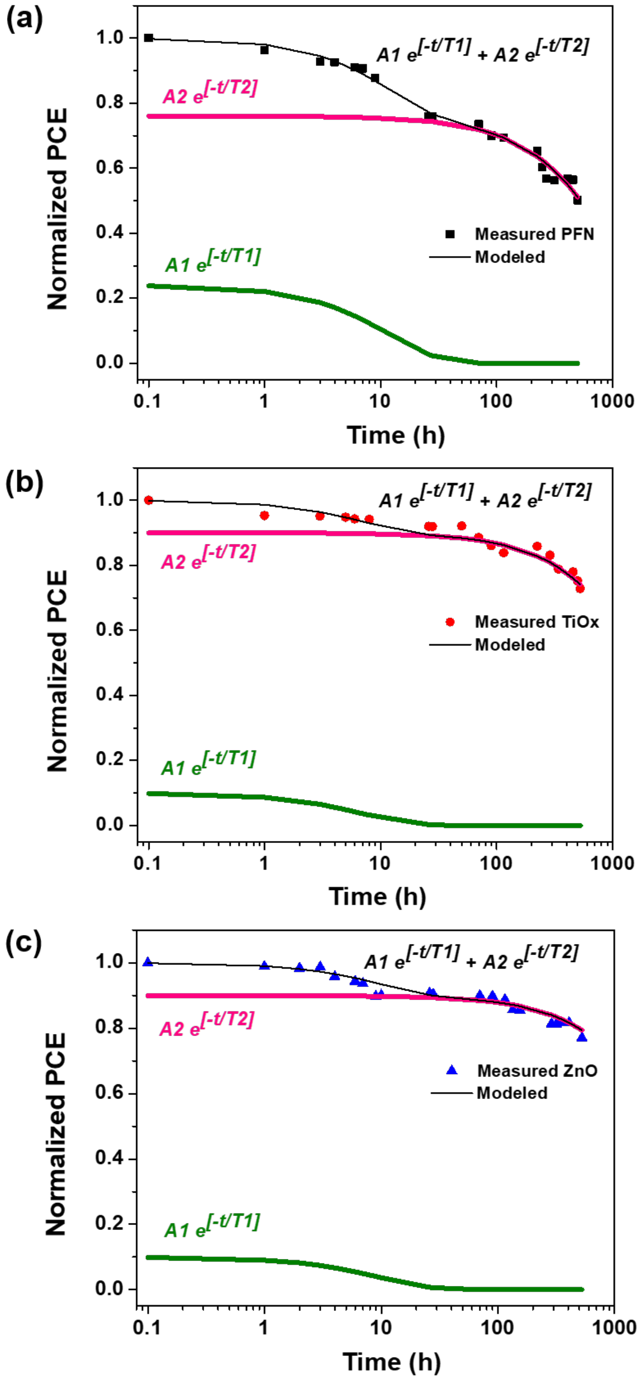

Figure 7.5 The modeled normalized PCE of a, PFN-, b, TiO_x- and c, ZnO-ETLs iOSCs over storage time using Eq. (1). The filled symbols are the experimental data and the lines are the fitting curves. The green line represents the fast initial decay and the pink line shows the slow decay, the black line is the total decay observed.

TiOx-iOSC) have similar two-stage degradation, a fast decay followed by slow degradation behavior while PFN-iOSC shows more rapid PCE deterioration. The degradation mechanism of the first fast decay regarding T1 is mainly caused by water and the second slow decay of T2 is related to oxygen ingress in the device, as was observed similarly with Yang *et al*. work[335] The smaller values of T1 for all devices than T2 indicate that water diffusion is being more detrimental in this degradation process. The time constant T2 of PFN-iOSC (1260 h) shows the lowest value among the studied ETLs, suggesting PFN-iOSC is suffered more by the presence of oxygen than the metal oxide ETLs-based iOSC. On the other hand, the highest time constant T2 (4000 h) is observed in ZnO-iOSC and the second highest T2 (2526 h) is acquired by TiOx-iOSC. This result suggests that the use of metal oxide, especially for ZnO as ETL in nonencapsulated iOSC may be favorable to obtain the more stable device performance parameters. The calculated parameter r defined as A1/A2 follows a behavior $r < 1$ for all nonencapsulated devices, showing a reliable measurement in the same condition: dark ambient environment exposure.

Table 7.4 Parameters obtained from fit the normalized PCE by eqn (7.1) with different ETLs. T1 and T2 are the time constants, A1 and A2 are the degradation power factors and r is the ratio of A1/A2.

ETL	**A1 (%/%)**	**A2 (%/%)**	**T1 (h)**	**T2 (h)**	r **= A1/A2**
PFN	0.24	0.76	12	1260	0.32 ($r<1$)
TiOx	0.06	0.92	6	2526	0.07 ($r<1$)
ZnO	0.11	0.89	9	4000	0.12 ($r<1$)

Figure 7.6 presents the behavior of series and shunt resistances over shelf lifetime. As shown in **Figure 7.6a**, the R_S of nonencapsulated iOSC with different ETLs increases after 526 h exposure to ambient conditions in which similar behavior observed to the PCE decay. R_S values remain constant regarding its initial time and start to increase to 3 h (T_{95}), 70 h (T_{90}), and 115 h (T_{90}) for PFN-, TiOx- and ZnO-

iOSC, respectively. Afterwards, R_S values rise abruptly for PFN-, increase gradually for TiOx- and increase steadily for ZnO-iOSC until 526 h. Interestingly, in **Figure 7.6b**, it is shown that R_{Sh} of ZnO-iOSC was stable for 526 h while those of PFN- and TiOx- showed a rapid decrease during 26 h (T_{80}) and 70 h (T_{90}), respectively, following the PCE decay behavior. The most stable and the lowest R_S combined with the highest R_{Sh} values belongs to ZnO-iOSC which is coherent with FF and PCE decay behavior (see Figure 7.4, Table 7.4). As the increase of R_S and decrease of R_{Sh} are followed by the FF and PCE decay, it is reasonable to suppose that the stability of studied iOSCs exposed to ambient conditions relates to the interface degradation, as observed in similar work.[336,337] This is in good agreement with the AFM measurement of each ETLs fresh and degraded films, as shown in **Figure 7.7**. The difference between the root-mean-square (RMS) roughness of fresh and degraded for ZnO film is very small (ΔRMS = 0.01 nm) compared to the PFN film (ΔRMS = 1.31 nm), which explain an effective interfacial area between the ZnO layer and the active layer. The smoother ETL film, the smaller ETL/active layer interfacial area, the less interface traps, leading to suppress undesired charge recombination and leakage current in which reduce the FF.[143,338] This can be attributed to the function of ZnO layer as scavenging layer to prevent the diffusion of oxygen and water molecules ingress to the active layer.[119] Moreover, the better quality ZnO film than the other ETLs can help to passivate the blend/ETL interface layer from the interface defect due to the chemisorption of oxygen as trap states causing the concentration of free electron to decrease.[339,340] Nevertheless, it is important to note that due to the complexity of the degradation mechanisms of each layer within the device, the information extracted solely from the *J-V* characteristics do not provide conclusive evidence to understand the dominating mechanism of performance deterioration. Therefore, a combined technique of time and frequency domain to study the shelf-lifetime degradation analysis is discussed more in detail in the following section.

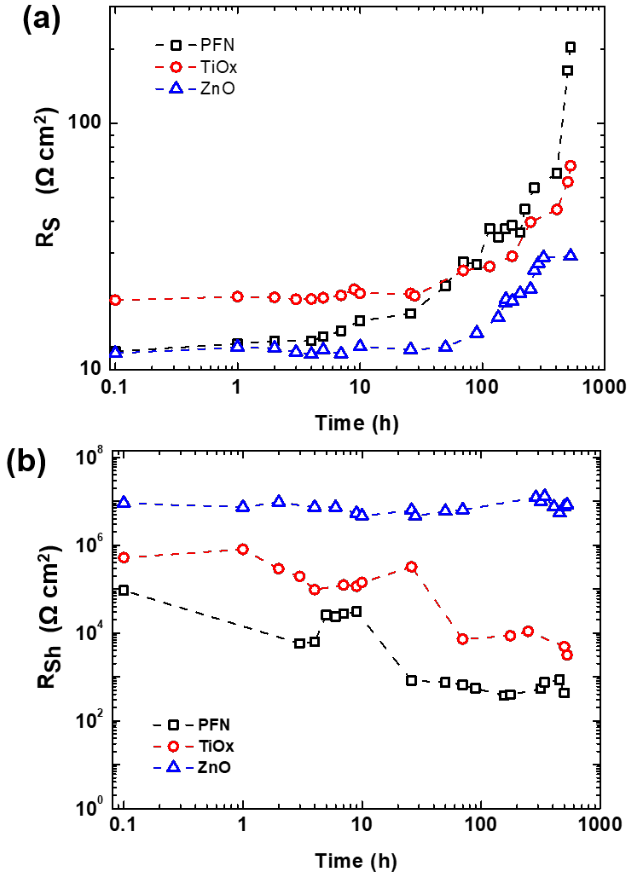

Figure 7.6 (a) Series and (b) shunt resistances of the inverted PTB7-Th:$PC_{70}BM$-based device over shelf lifetime with different ETLs (PFN, TiO_x, and ZnO) extracted from dark $J - V$ measurements.

7.3 Transient photovoltage / photocurrent analysis

To investigate the different ETL on charge kinetics and recombination, fresh and degraded nonencapsulated iOSC were measured under operando conditions by using charge extraction (CE) and transient photovoltage (TPV)/photocurrent (TPC) techniques. These techniques have been frequently employed to analyze the carrier losses and the carrier recombination in dye-sensitized solar cells and OSC,[139,341,342] and more recently in perovskite solar cells.[77,257,343] Understanding the carrier loss mechanisms is key to increase solar cell efficiency. Therefore, we consider analyzing

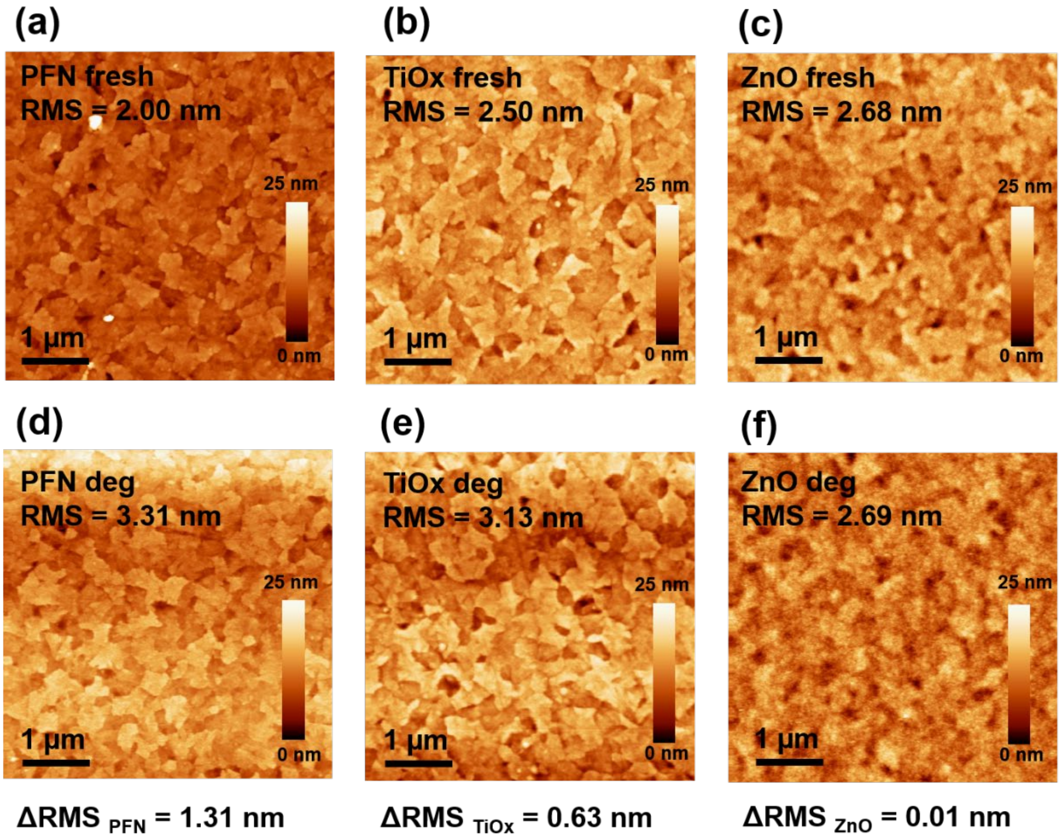

Figure 7.7 AFM height images of (a-c) fresh and (d-f) degraded ETL films. The ETLs used are (a,d) PFN, (b,e) TiO_x, and (c,f) ZnO. The delta root-mean-square (ΔRMS = RMS degraded – RMS fresh) roughness values are extracted.

the fresh and degraded devices as an important way to elucidate the different mechanisms in the device interfaces. While a brief description of the experimental procedure can be found in the *Device Characterization* section, the technique is described in detail elsewhere.[76]

In general, the CE technique allows the measurement of the accumulated charges and the TPV permits to register the carrier recombination decay under different light bias (solar cell voltage as a result of light irradiation). In most kind of solar cells, such as the full-organic or dye-sensitized solar cells, the photo-generated carriers are extracted before they recombine. In other words, the CE decay is always much faster than the TPV at the same light bias, as we can observe from our devices (see **Figure 7.8**). Nevertheless, the combination of TPV/TPC allows to obtain the Differential Capacitance (DC) as an alternative technique to CE.[344] Here we used both CE and DC techniques to accurately analyse the charge density of the devices (see an example in **Figure 7.9**).

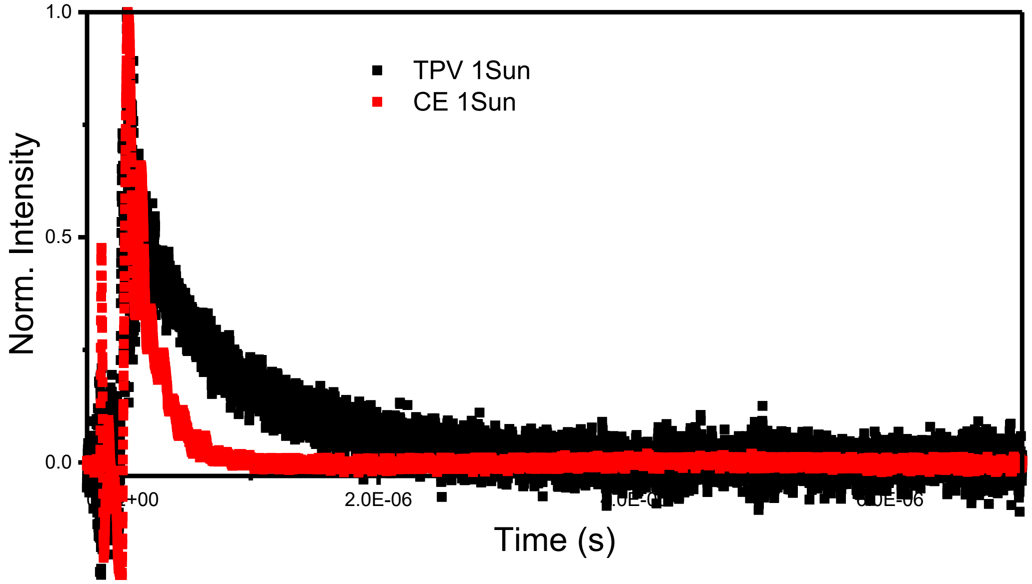

Figure 7.8 The CE and TPV decays under 1 Sun illumination conditions for OSC using TiO_x as ETL.

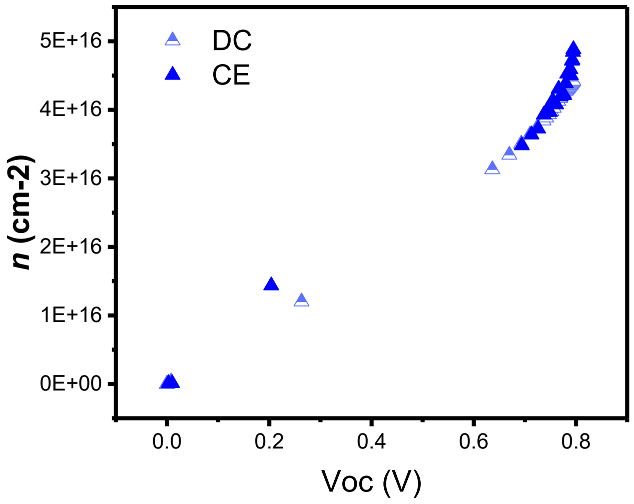

Figure 7.9 Comparison between the charge density measured by using charge extraction (CE) and differential capacitance (DC) techniques for a device using ZnO as ETL.

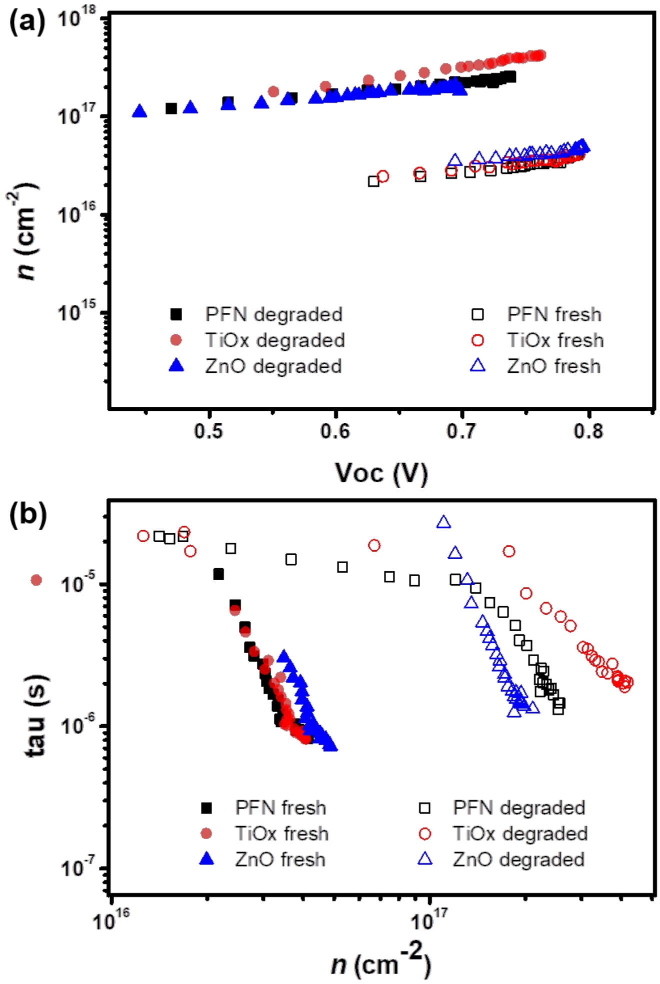

Figure 7.10 (a) The charge density versus V_{OC} and (b) the charge lifetime versus charge density for fresh and degraded devices.

For a comparison between iOSC with different ETL, we made sure that the film thicknesses are equal in all devices within measurement error, *i.e.* ETL thicknesses close to 20 nm. **Figure 7.10a** shows photo-generated charges stored in the fresh and degraded cells at equilibrium at different V_{OC} values, achieved by tuning the background illumination from dark to 1 Sun equivalent. At first sight, degraded samples showed higher charge density values for a given V_{OC}. In agreement with similar works recently reported,[328] this, can be attributed to chemical reactions as a result of the interlayer degradation originated near the interface. Meanwhile, the charge density for fresh devices is very similar for the different ETL and consistent with the observed V_{OC} (~0.8 V), the increase in charge density upon degradation is different for each ETL and so, less consistent with the V_{OC}. Charge density usually exhibited a linear and exponential part, attributed to the charges accumulated at the interfaces –known as geometrical capacitance– and within the bulk –chemical capacitance–, as depicted in **Figure 7.11**. By analyzing both separately, we obtained more information about how the degradation process is affecting the charge extraction of the devices depending on the ETL used. **Figure 7.11b** shows that TiOx in degraded cells presents slightly higher charge density.

A change in recombination kinetics can be observed by looking at the charge density dependence of the carrier lifetime. Therefore, the carrier lifetimes (τ) obtained from TPV decays of fresh and degraded devices are plotted as a function of charge density in **Figure 7.10b**. There is a lengthening of the carrier lifetime in the degraded devices, approximately 3 times longer than the fresh devices at a charge density of 2.5×10^{16} cm^{-2}.

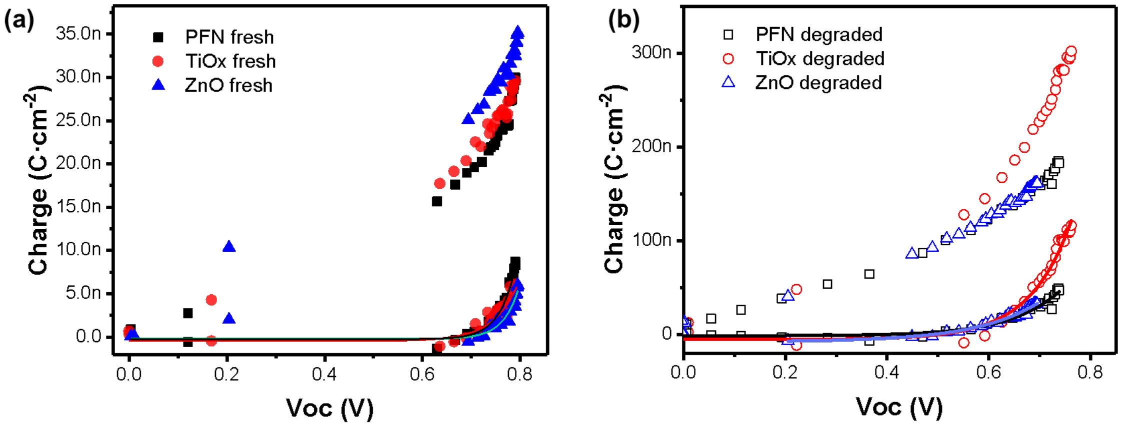

Figure 7.11 Charge measured at different light bias for OSCs with different ETL. The solid lines at the graph bottom represents only the exponential part of the fits: $y=Be^{Cx}$ (chemical capacitance) for (a) fresh and (b) degraded devices.

These results are consistent with the increase in trap formation upon degradation (mainly due to oxygen and water penetration) as carrier lifetimes are shown to increase for given carrier densities. Due to the presence of traps, charges may spend a certain amount of time in these traps, before being released and so being recombined. We have seen that the increased carrier lifetime does not causes higher V_{OC} values for those degraded devices because to reach the same Fermi-level splitting, much higher charge density would now be needed comparing to the fresh devices. We can also notice that in general, lifetimes are similar for all devices, especially near to 1 Sun intensity, which indicates that the ETL properties do not have a significant influence on recombination kinetics.

Therefore, we can conclude from this section that, as we have not observed significant changes in recombination behavior and in the device ideality factor from light intensity dependency measurement (see **Figure 7.12**), the observed performance degradation is improbable to come from energy level changes, or specifically. In this case, we can confirm that the degradation does not induce significant increases in trap-assisted recombination which may be one potential source of performance loss.

7.4 Impedance spectroscopy analysis

To obtain a deeper understanding of the degradation mechanism associated with the interfaces, we performed IS measurements on the same devices investigated by TPV/TPC. IS measure the phase shift and the amplitude of the current response obtained upon applying an AC voltage to the device at a given frequency. The frequency dependent measurements aid to explain the several mechanisms occurring at several interfaces.[345] Thus, the interface state will be distinguished more easily by IS than TPV in which all charges are forced to recombine.

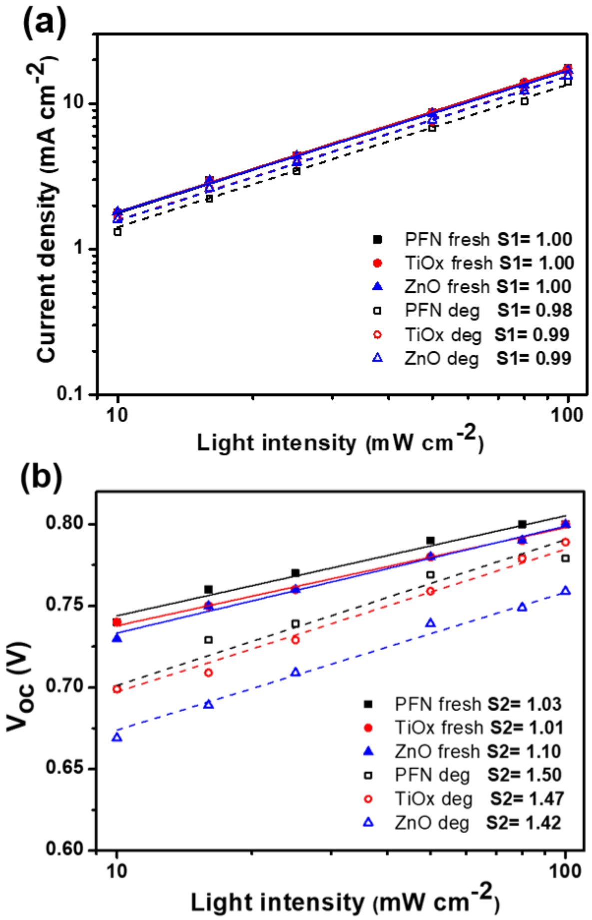

Figure 7.12 (a-c) J_{SC} and (d-f) V_{OC} dependence on light intensity over storage time of PTB7-Th:PC$_{70}$BM–based OSCs with different ETLs: (a,d) PFN, (b,e) TiO$_x$, and (c,f) ZnO. It is worth noting that the ideality factor values, n ($n = S2/S1$) of this measurement is in good agreement with the n_1 values obtained from the dark J-V fitting parameters in Table 7.2.

The first approach to fit the experimental IS data of all fresh samples is to use an equivalent circuit model composing one series resistance connected in series with three resistor/capacitor components (3RC). The 3RC equivalent circuit model can be employed to get information about each layer within the devices.[170,346] To properly fit the impedance data at higher frequencies (HF), i.e. $f > 0.1$ MHz, for all fresh samples, the main effect to overcome is the reduction of the phase values. From the circuital point of view, a reduction of the -Z” experimental value in negative x-axis can only be explained by the presence of series inductance (L). The physical origin of the *L* term could be related to wiring, despite a compensation was done before the measurement. An alternative origin could be the typical equivalent circuit of a capacitor at HF. A series resistance element (R_S) takes into consideration the ITO sheet resistance and three RC elements are corresponding to the capacitance and resistance of the ETL, the bulk active layer, and the hole transport layer (HTL). The geometrical capacitance (C_{geo}) values of each layer are listed in Table 3.7. These values depend on the dielectric permittivity and the thickness of the layer, as expressed by Equation S1. The comparison of the different C_{geo} values of each layer and the fitting values enable us to predict the correlation between each RC components.

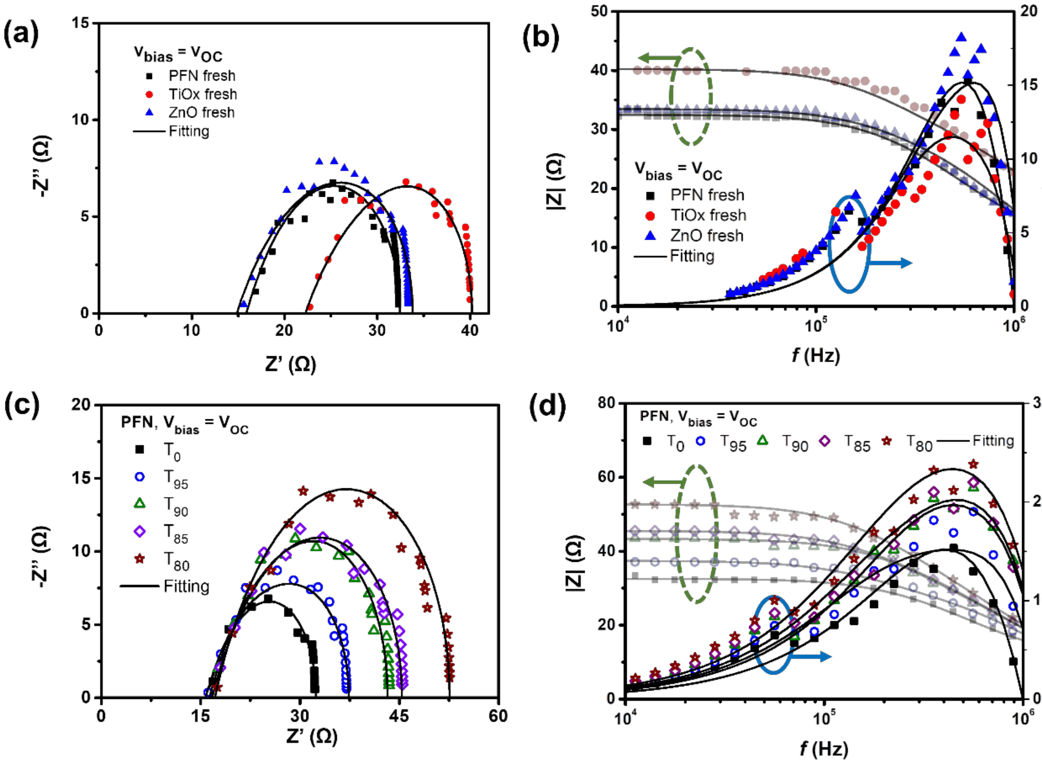

Figure 7.13 (a) and (c) Cole – Cole plot and (b) and (d) Bode plot (modulus green-dashed arrow and phase blue-solid arrow) for (a) and (b) fresh devices using three different ETLs and (c) and (d) degraded PFN-based non-encapsulated devices over degradation time (T_0, T_{95}, T_{90}, T_{85}, and T_{80}) measured under open-circuit conditions. The experimental results were fitted using a RC circuit model (solid lines) shown in Figure 3.10.

The typical arc behavior with a single semi-circle is observed in the Cole-Cole plots (**Figure 7.13a**) with one peak in the phase angle of Bode plots (**Figure 7.13b**), suggesting the presence of RC components. **Table 7.5** summarizes the extracted capacitance and resistance values from fitting the impedance spectra of all devices using 3RC equivalent circuit model at open-circuit condition. It is noticed that ITO sheet resistances depend on the ETL used, where a R_S value in the range of 10 Ω was expected. Among the fresh samples, at a given frequency, PFN-iOSCs demonstrate the lowest impedance value in the flat region of $|Z|$ vs f compares to the metal oxide-ETLs counterparts. These results corroborate with the highest device performance obtained using PFN–ETL as fresh device. It is worth noting that the fitted equivalent capacitance values (C_{fit}) of the bulk are higher than C_{geo} of the blend ≈ 3 nF. From the circuital point of view, an increase of C_{fit} over C_{geo} can only be explained by the presence of a parallel capacitance. Figure 3.10 shows the equivalent circuit model used to fit the impedance spectra, allowing the interfacial density of states (D_{it}) of the blend and the traps created during the degradation process to be observed. This estimation is based on polymer metal-insulator-semiconductor (MIS) capacitors work.[347,348] The interface states are represented by an interface trap capacitance (C_{it}) in parallel with the capacitance of the semiconductor. C_{it} can be obtained by subtracting C_{geo} to C_{fit} ($C_{it} = C_{fit} - C_{geo}$), so the interface density of states $D_{it} = C_{it}/qA$ can be calculated as 4–6 $\times 10^{11}$ $cm^{-2}eV^{-1}$ for PTB7-Th at open-circuit condition, see **Table 7.6**. These values are within the range of values obtained for the interface density of states in P3HT.[42,349]

After degradation, as shown in **Figure 7.13c**, a single semicircle behavior is still observed with the increased average diameter of the arcs over storage time for PFN-iOSCs at open-circuit condition. A similar trend is observed for the other studied ETLs. The time degradation impedance characteristics have been examined by fitting these with equivalent circuit model. The other common characteristic for PFN-, TiO_x- and ZnO-iOSCs is that the diameter of arcs decreases with increasing

Table 7.5 Capacitance and resistance values of each layer for different ETLs used under AM 1.5G for fresh (*T_0*) and *T_{80}* degraded devices. For PFN devices, the values for 526h are also shown (in parenthesis). The values were extracted by using the circuit model shown in Figure 3.10 at open-circuit voltage.

ETLs	**Layers**	**Capacitance (nF)**		**Resistance (Ω)**	
		Fresh	**Degraded**	**Fresh**	**Degraded**
PFN	R_s	-	-	7	10 (53)
	PFN	28	28 (28)	11	17 (54)
	Bulk	10	11 (14)	7	13 (23)
	V_2O_5	78	78 (78)	7	12 (13)
TiO_x	R_s	-	-	14	21
	TiO_x	200	200	3	17
	Bulk	9	12	15	32
	V_2O_5	78	78	9	13
ZnO	R_s	-	-	6	12
	ZnO	21	21	4	25
	Bulk	12	13	15	18
	V_2O_5	78	78	8	17

Table 7.6 Interface trap density (*D_{it}*) of all devices before and after degradation under open-circuit conditions

ETL	**$C_{it} = C_{fit} - C_{geo}$ (nF)**		**$D_{it} = C_{it}/Qa$ ($cm^{-2}eV^{-1}$)**		**ΔD_{it}**
	Fresh	**Degraded**	**Fresh**	**Degraded**	
PFN	7	11	4.86×10^{11}	7.64×10^{11}	57%
TiOx	6	9	4.17×10^{11}	6.25×10^{11}	50%
ZnO	9	10	6.25×10^{11}	6.94×10^{11}	11%

applied bias voltage, which can be related to the efficient charge extraction.[170] **Figure 7.13d** exhibits the |Z|-*f* relation of PFN-iOSC over degradation time in which the impedance values increase as the degradation time increase and the difference is more prominent in the lower frequencies (LF) region, suggesting the LF feature becomes evident in the degraded cells. As compared to C_{geo} values, the fitted capacitance values of charge transport layers (ETL and HTL) appear to be the same and remain constant over degradation, see Table 7.5. However, the fitted capacitance values of the blend in all samples are higher than those of geometrical values and their values increase over the degradation time. As shown in Table 7.6, the interface density of states values after degradation time of 526 hours increase 57%, 50% and 11% for PFN-, TiO_x- and ZnO-iOSCs, respectively, in good agreement with the increase of the dark leakage current-voltage characteristic on the degraded devices. The highest degradation of the PFN iOSC correlates with the largest increase of the interface density of states values for this sample. Thus, we can assume that the traps created by water and oxygen will modify only the bulk interface with ETL and HTL, whereas ETL and HTL are fully depleted layers.

7.5 Combined steady-state and transient techniques

To obtain an excellent agreement within the steady-state and transient techniques, we both compare the ideality factors obtained from dark *J-V* modelling results with TPV/TPC studies. As shown in **Figure 7.14**, charge carrier density and charge carrier lifetime both exponentially depend on V_{OC}, following the equations 7.2 and 7.3:

$$n = n_0 \times \exp\left(\frac{qV_{OC}}{n_n kT}\right) \tag{7.2}$$

$$\tau_{\Delta n} = \tau_{\Delta n_0} \times \exp\left(\frac{qV_{OC}}{n_\tau kT}\right) \tag{7.3}$$

where $n_n$and n_τ defined as the ideality factors correspond to carrier density and carrier lifetime, respectively.[350] In previous works, the slopes in the semilogarithmic plots of Fig. 6 were described by the parameters $\gamma = q/n_n kT$ and $\beta = q/n_\tau kT$.[260] All the n_n and $n_\tau$ideality factors obtained from **Figure 7.14a** are summarized in **Table 7.7**. It is important to notice that fresh devices but not after degradation, shows an exponential fitting with two different regions. One region at higher voltages (0.75-0.79 V) which can be attributed to bulk dynamics, and another region (0.63-0.75 V) attributed to the capacitive contribution.

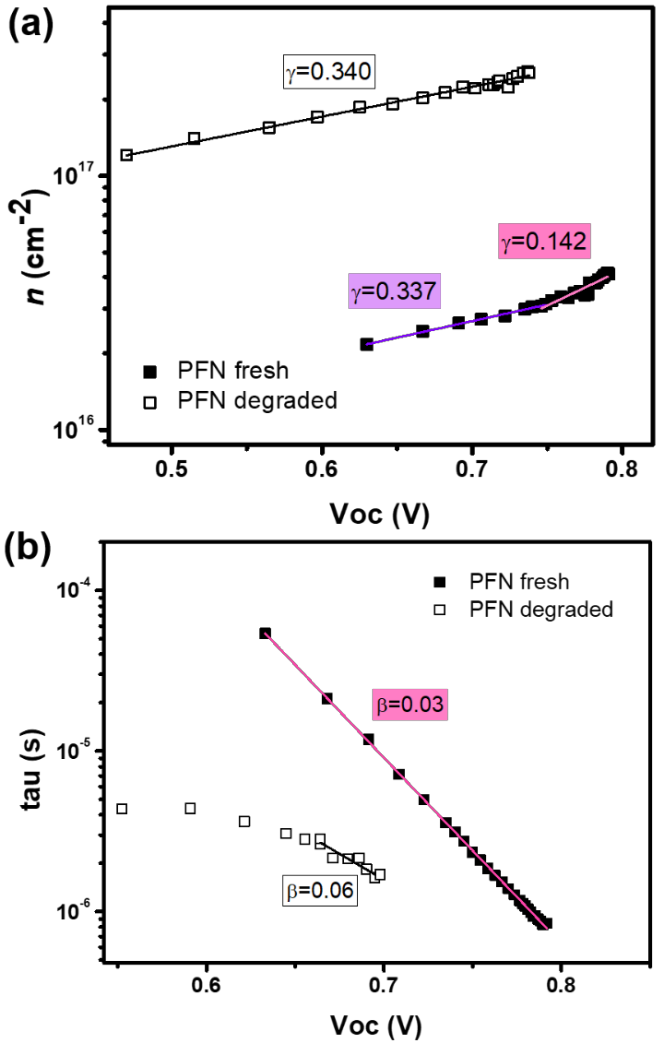

Figure 7.14 The fitted data of (a) charge carrier density and (b) charge carrier lifetime *versus* open circuit voltage from CE and TPV measurements using eqn (2) and (3) for the fresh and degraded PFN-iOSCs.

Table 7.7 Summary of ideality factors determined by transient (CE and TPV) techniques and *J-V* characteristics

	n_n	n_τ	n_{id} (CEn_n/TPVn_τ)	n_{id} (*J-V*)
PFN fresh	5.48 ($V_{OC} > 0.75$)	1.42	1.12	1.11
	13.01($V_{OC} < 0,75$)	-	-	
PFN deg.	13.13	2.31	1.96	1.91

Charge extraction and transient photovoltage techniques can be used to determine charge carrier densities and carrier recombination but also steady-state parameters like the ideality factor n_{id}. The diode ideality factor is correlated with n_n (at higher V$_{OC}$ voltages, i.e. 0.75 – 0.79V) and n_τ by following the equation 7.4:

$$n_{id}^{-1} = n_n^{-1} + n_\tau^{-1} \tag{7.4}$$

Although the ideality factors were determined in two different ways –from *J-V* characteristics and from CE and TPV techniques– both n_{id} found to be identical for our solar cells. These n_{id} has already been compared by other authors[350–352] where they obtained identical ideality factors as in our case, very close values or slightly underestimated compared to the steady-state values. Therefore, the good agreement of steady-state and transient techniques demonstrates the validity of the Shockley model for this kind of solar cells.

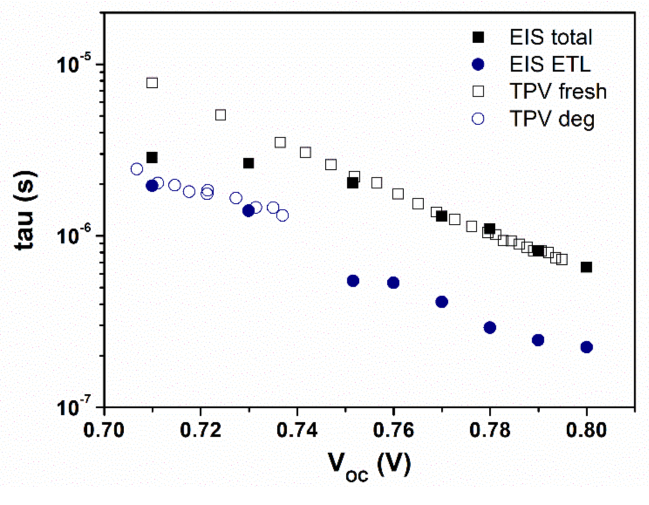

Figure 7.15 IS time constant under open-circuit conditions compared to the carrier lifetimes extracted from TPV measurements for the fresh and degraded PFN-iOSCs.

To validate the aforementioned assumption and the proposed model of D$_{it}$, we checked the time constant obtained from the IS and TPV measurements. The similar carrier lifetime values between the two techniques should correlate each other when the recombination took place. The characteristic time constant from RC circuit of IS data at open-circuit condition is given by τ = R×C. The time constants measured from both techniques for PFN-iOSCs are shown in **Figure 7.15**. On one side, each V_{OC} bias point from IS data corresponds to a different degradation time with the same illumination, whereas on the other side those of TPV data correspond to the same degradation time with different illumination. A good agreement is observed between total τ of IS in the V_{OC} range from 0.8 V (fresh sample) to 0.74 V (degraded sample 176 h) and the total τ of TPV fresh PFN-iOSCs data from 0.8 V (the highest light intensity) to 0.74 V (lower light intensity). The time constant obtained from IS in the V_{OC} range from 0.74 V to 0.70 V (degraded 526 h) begin to outward the pattern of TPV fresh and follow the pattern of TPV degraded data. To find out which layer is the main effect of degradation, we analyze the contribution of each layer. We found that by fitting ETL time constant, $\tau_{ETL} = R_{ETL} \times C_{ETL}$, it follows the trend of τ extracted from TPV for degraded devices at 267 h and 526 h. The relative τ contribution of each layer to the total τ is shown in **Figure 7.16**. In fresh devices, almost 30% contribution of τ values is due to the HTL, whereas in the degraded devices, almost 70% contribution of τ values is due to the ETL. This result is in good agreement with the generation of interfacial trap in the degradation process. It suggests that the interfacial defect, which demonstrated by the presence of interface states effect, D_{it}, can be the main cause of degradation.

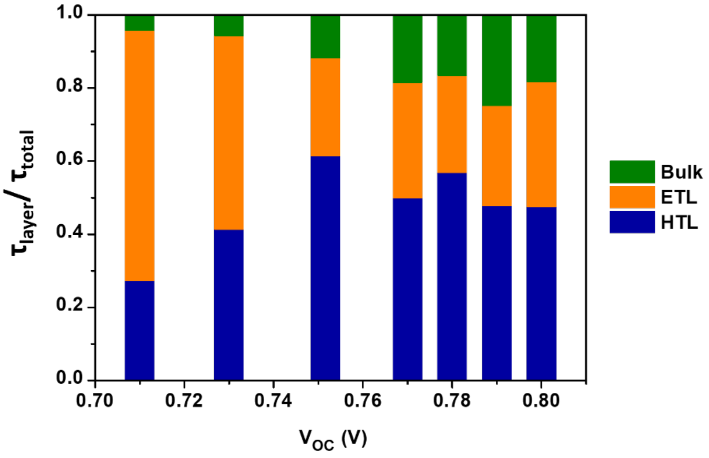

Figure 7.16 The relative contribution of each layer to the total τ value at different degradation time.

7.6 Conclusions

In summary, we performed both frequency and time-domain characterization techniques to investigate the shelf-life degradation of ITO/ETL/PTB7-Th:$PC_{70}BM/V_2O_5$/Ag using three different ETLs, one organic-based ETL (PFN) and two metal oxide-based ETLs (TiOx and ZnO), following ISOS-D1 protocol. Both techniques can provide real information on how different ETL were degraded and affecting the stability of the active layer over storage time. We have found that the main cause of degradation is due to the formation of interface traps under dark and upon air exposure. TPV measurements, it gives an insight into the interfacial recombination processes, particularly it shows an increase of trap density in the active layer due to the degradation. From the IS data, it is possible not only to determine the relative contribution of each layer to the total time constant but also estimate the increase of the interface density of states values due to the degradation process. Modelling dark current-voltage (*J-V*) characteristic and atomic force microscopy (AFM) measurement further confirms the presence of traps on the degraded devices.

Chapter 8

Summary and outlook

8.1 Summary

In conclusion, the work done in this thesis has successfully developed interfacial engineering and ternary strategies to simultaneously improve the efficiency and stability of OSCs for versatile applications. Encouraged by the PCE milestone of OSCs by nearly 20% and even higher based on the theoretical simulation, the motivation for undertaking this challenging task is based on the optimistic view of together contributing to the progress of OSCs to bring it in the PV market in the near future. First, we have investigated the performance and photostability of binary fullerene-based OSCs using an interface engineering strategy under 1 sun condition and under indoor LED illumination. Then, for traditional outdoor application, we have employed the ternary strategy by adding the novel fluorinated metallophthalocyanines $MPcF_{48}$ and commercial ITIC-M or $PC_{70}BM$ as third components in binary fullerene-based and binary nonfullerene-based blends, respectively, to improve the device efficiency and stability. Yet, the ternary strategy can be applied to the semitransparent nonfullerene-based OSCs by adding state-of-the-art Y-series nonfullerene acceptors. As last, we have introduced combined frequency and time-resolved techniques to study in-depth the shelf lifetime degradation of OSCs in accordance with the ISOS-D1 protocol.

In **Chapter 3**, the device performance and stability of fullerene-based binary OSCs under outdoor (1 Sun condition) and indoor (2700 K LED) illumination were comparatively investigated. A cathode interface engineering using three different ETL materials has been demonstrated to significantly affect the indoor OSCs performance, especially the leakage-current, trap-assisted recombination, and charge collection efficiency. It was found that choosing the proper properties of ETLs such as metal oxide ETLs TiOx and ZnO could improve the parasitic resistance effect in indoor OSCs, thus their indoor efficiency was increased by almost two-folds, whereas organic ETL such as PFN suffered more with the higher leakage-current, showing a slightly increase in the indoor efficiency. In addition, we analysed the photostability study and degradation mechanism of highly efficient indoor OSCs along with the photoaged OSC under AM1.5 G illumination to further accelerate the commercialization of OSC on the Internet of Things (IoT) market.

In **Chapter 4**, we synthesized fluorinated zinc and copper metallophthalocyanines $MPcF_{48}$ and incorporated them as third components in fullerene-based binary PTB7-Th:$PC_{70}BM$ blend to construct an efficient ternary BHJ OSCs. The effect of different central metal atoms from $MPcF_{48}$ small molecules as third component on the performance of ternary OSCs has been investigated. Employing copper as metal atom substitution in the third component of TOSCs enhanced J_{SC} as a result of complementary absorption spectra in the near-infrared region. In combination with J_{SC} enhancement, suppressed charge recombination, improved exciton dissociation, and charge carrier collection efficiency, and better morphology led to a slightly improved FF, resulting in a 7% enhancement of PCE than those of binary OSCs. In addition to the increased PCE, the photostability of TOSCs has also been improved by the appropriate addition of $CuPcF_{48}$. Detailed studies implied that metal atom substitution in phthalocyanines is an effective way to improve J_{SC}, FF, and thus the performance and photostability of TOSCs.

In **Chapter 5**, nonfullerene acceptor ITIC-M and fullerene acceptor $PC_{70}BM$ which have higher lowest unoccupied molecular orbital (LUMO) and good miscibility with nonfullerene acceptor Y7 were incorporated as third components in the state-of-the-art of PM6:Y7 binary blend. Over 7% enhancement in PCE for both ternary OSCs was achieved, from 16.46% for binary host OSCs to 17.73% and 17.67% for ITIC-M-based and $PC_{70}BM$-based ternary OSCs, respectively. The higher LUMO of the third component could play multiple roles in elevating the open-circuit voltage (V_{OC}) such as reducing energy-loss and reverse saturation current, creating less-localized shallow trap sites along with suppressing charge recombination and Urbach energy. Moreover, the good miscibility facilitates an alloy-like phase in acceptors domain for efficient exciton dissociation and carrier transport, which leads to improved short-circuit current density (J_{SC}) and fill factor (FF) in ternary devices. Our results provide a promising approach to realizing high performance of ternary OSCs by synergizing compatible third component with a host acceptor.

In **Chapter 6**, we investigated the semitransparent properties, device performance, and the operational stability (thermal- and photo-stability) of PTB7-Th:IEICO-4F OSCs by adding Y-series nonfullerene acceptors as ternary components. A series of ternary OSCs with near-infrared Y-series nonfullerene acceptors (mainly Y1, Y5, Y6 and Y7) were comparatively studied as third components in semitransparent PTB7-Th:IEICO-4F binary blend to balance the trade-off between the PCE, AVT, and operational stability for the practical applications of ST-OSCs. The photovoltaic, transmittance and stability behaviors of the resultant ternary OSCs differ significantly by introducing different Y-series NFAs materials. When blended with PTB7-Th:IEICO-4F with the PCE of 11.86%, the PCEs of 11.32%, 11.55%, 13.02%, and 12.32% were yielded for opaque Y1, Y5, Y6, and Y7 based ternary OSCs. Then, a series of ST-OSCs were prepared with 10 nm Ag as the electrode. The different photovoltaic performance as well as the difference in AVT values were observed using different Y-series NFA materials. The ST-TOSCs based on PTB7-Th:IEICO-4F:Y6 with a modified Ag electrode thickness of 10 nm achieve the highest LUE of 2.35% as the product of good PCE of 8.47% and high AVT of 27.77% among the other Y-series incorporated ST-TOSCs with an alloy-like dominant mechanism. Moreover, Y6 based ST-TOSCs exhibited good thermal and photostability under inert conditions. Our findings indicate that ternary strategy with a proper selection of ultra-narrow band gap third components materials should provide great potential toward well-balanced PCE, AVT, and operational stability of ST-OSCs.

In **Chapter 7**, the stability study of organic solar cells specifically on the shelf lifetime analysis of PTB7-Th:$PC_{70}BM$-based OSC using combined frequency and time-resolved techniques was discussed. In accordance with the ISOS-D1 protocol, we observed the whole degradation process of each layer with the aid of advanced photophysics techniques: IS and TPV/TPC. The increase of trap density in the active layer was revealed by TPV/TPC measurement, while the change in interface trap density due to the interfacial defect upon degradation was further confirmed by IS.

8.2 Outlook

Ternary organic solar cells along with an interface engineering strategy have shown promising approaches to realize high-performance and stable devices for versatile applications such as indoor OSCs and semitransparent OSCs. **Figure 8.1** depicts a schematic diagram of the key factors to design high-performance and stable OSCs for near-future application using interface engineering and ternary strategies.

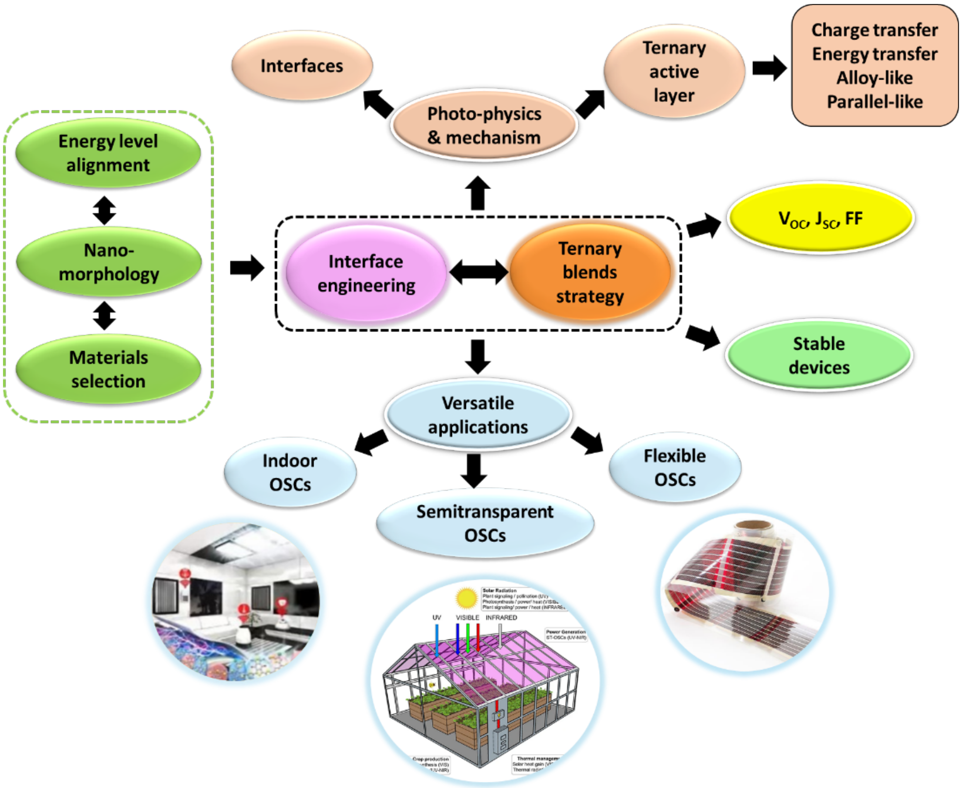

Figure 8.1 Outlook for high performance and stable organic solar cells by synergizing interface engineering and ternary blend strategies.

Bibliography

1. Cleland, J. World Population Growth; Past, Present and Future. *Environ. Resour. Econ.* **55**, 543–554 (2013).
2. Cozzi, L. (International E. A. & Gould, T. (International E. A. World Energy Outlook 2021. 1–386 (2021).
3. Adrian, G. Key World Energy Statistics 2021. 1–82 (2015).
4. BP Energy outlook. Statistical Review of World Energy globally consistent data on world energy markets . and authoritative publications in the field of energy. *BP Energy Outlook 2021* **70**, 8–20 (2021).
5. Grätzel, M. Recent Advances in Sensitized Mesoscopic Solar Cells. *Acc. Chem. Res.* **42**, 1788–1798 (2009).
6. Becquerel, E. Report on the electrical effects produced under the influence of solar rays. *Comptes rendus l'Académie des Sci.* **IX**, 561–567 (1839).
7. G A, B. W. V. The action of light on selenium. *Proc. R. Soc. London* **25**, 113–117 (1877).
8. Fritts, C. E. On a new form of selenium cell, and some electrical discoveries made by its use. *Am. J. Sci.* **23–26**, 465–472 (1883).
9. Fraas, L. M. Chapter 1: History of Solar Cell Development. in *Low-Cost Solar Electric Power* 1–12 (Springer International Publishing, 2014).
10. Laboratory, N. R. E. Best Research-Cell Efficiency Chart | Photovoltaic Research | NREL. https://www.nrel.gov/pv/cell-efficiency.html (2022).
11. Kaltenbrunner, M. *et al.* Ultrathin and lightweight organic solar cells with high flexibility. *Nat. Commun.* **3**, 1–7 (2012).
12. Li, X. *et al.* Review and perspective of materials for flexible solar cells. *Mater. Reports Energy* **1**, 100001 (2021).
13. Yin, H. *et al.* Highly-Transparent and True-Colored Semitransparent Indoor Photovoltaic Cells. *Small Methods* **4**, 1–8 (2020).
14. Wang, W. *et al.* Controlling Molecular Mass of Low-Band-Gap Polymer Acceptors for High-Performance All-Polymer Solar Cells. *Joule* **4**, 1070–1086 (2020).
15. Funde, A. & Shah, A. *Solar Cells and Modules*. (Springer Nature Switzerland AG 2020, 2020).
16. Cutting, C. L., Bag, M. & Venkataraman, D. Indoor light recycling: A new home for organic photovoltaics. *J. Mater. Chem. C* **4**, 10367–10370 (2016).
17. Kini, G. P., Jeon, S. J. & Moon, D. K. Latest Progress on Photoabsorbent Materials for Multifunctional Semitransparent Organic Solar Cells. *Adv. Funct. Mater.* **31**, 1–32 (2021).
18. Kaltenbrunner, M. *et al.* Flexible high power-per-weight perovskite solar cells with chromium oxide–metal contacts for improved stability in air. *Nat. Mater.* **14**, 1032–1039 (2015).
19. Zhang, J. *et al.* Highly Efficient Semitransparent Organic Solar Cells with Color Rendering Index Approaching 100. *Adv. Mater.* **31**, 1–9 (2019).

20. Shirakawa, H., Louis, E. J., MacDiarmid, A. G., Chiang, C. K. & Heeger, A. J. Synthesis of electrically conducting organic polymers: Halogen derivatives of polyacetylene, (CH)x. *J. Chem. Soc. Chem. Commun.* 578–580 (1977).
21. Tang, C. W. Two-layer organic photovoltaic cell. *Appl. Phys. Lett.* **48**, 183–185 (1986).
22. Kymissis, I. The physics of organic semiconductors. in *Organic Field Effect Transistors Theory, Fabrication and Characterization* 5–16 (Springer, Boston, MA, 2009).
23. Dappe, Y. J. Encapsulation of organic molecules in carbon nanotubes: role of the van der Waals interactions. *J. Phys. D. Appl. Phys.* **47**, 083001 (2014).
24. Käfer, D., El Helou, M., Gemel, C. & Witte, G. Packing of planar organic molecules: Interplay of van der waals and electrostatic interaction. *Cryst. Growth Des.* **8**, 3053–3057 (2008).
25. Wu, J. *et al.* A Comparison of Charge Carrier Dynamics in Organic and Perovskite Solar Cells. *Adv. Mater.* **34**, 1–24 (2022).
26. Zhan, C.-G., Nichols, J. A. & Dixon, D. A. Ionization Potential, Electron Affinity, Electronegativity, Hardness, and Electron Excitation Energy: Molecular Properties from Density Functional Theory Orbital Energies. *J. Phys. Chem. A* **107**, 4184–4195 (2003).
27. Torabi, S. *et al.* Strategy for Enhancing the Dielectric Constant of Organic Semiconductors Without Sacrificing Charge Carrier Mobility and Solubility. *Adv. Funct. Mater.* **25**, 150–157 (2015).
28. Poelking, C. & Andrienko, D. Design Rules for Organic Donor–Acceptor Heterojunctions: Pathway for Charge Splitting and Detrapping. *J. Am. Chem. Soc.* **137**, 6320–6326 (2015).
29. Hoppe, H. & Sariciftci, N. S. Organic solar cells: An overview. *J. Mater. Res.* **19**, 1924–1945 (2004).
30. Lu, B. *et al.* Recent progress of Y-series electron acceptors for organic solar cells. *Nano Sel.* **2**, 2029–2039 (2021).
31. Ameri, T., Dennler, G., Lungenschmied, C. & Brabec, C. J. Organic tandem solar cells: A review. *Energy Environ. Sci.* **2**, 347–363 (2009).
32. Köhler, A. & Bässler, H. *Electronic processes in organic semiconductors: An introduction*. *Wiley-VCH* (Wiley-VCH Verlag, 2015). doi:10.1002/9783527685172.
33. Classen, A. *et al.* The role of exciton lifetime for charge generation in organic solar cells at negligible energy-level offsets. *Nat. Energy* **5**, 711–719 (2020).
34. Firdaus, Y. *et al.* Long-range exciton diffusion in molecular non-fullerene acceptors. *Nat. Commun. 2020 111* **11**, 1–10 (2020).
35. A Lin, J. D. *et al.* Systematic study of exciton diffusion length in organic semiconductors by six experimental methods. *Mater. Horizons* **1**, 280–285 (2014).
36. Yu, G., Gao, J., Hummelen, J. C., Wudl, F. & Heeger, A. J. Polymer Photovoltaic Cells: Enhanced Efficiencies via a Network of Internal Donor-Acceptor Heterojunctions. *Science (80-.).* **270**, 1789–1791 (1995).
37. Kaake, L. G. *et al.* Photoinduced Charge Generation in a Molecular Bulk Heterojunction Material. *J. Am. Chem. Soc.* **134**, 19828–19838 (2012).
38. Brédas, J.-L., Brédas, B., Norton, J. E., Cornil, J. & Coropceanu, V. Molecular Understanding of Organic Solar Cells: The Challenges. *Acc. Chem. Res.* **42**, 1691–1699 (2009).

39. Colladet, K. *et al.* Low band gap donor-acceptor conjugated polymers toward organic solar cells applications. *Macromolecules* **40**, 65–72 (2007).
40. Deibel, C. *et al.* Role of the Charge Transfer State in Organic Donor-Acceptor Solar Cells. *Adv. Mater.* **22**, 40907–4111 (2010).
41. Han, G. & Yi, Y. Origin of Photocurrent and Voltage Losses in Organic Solar Cells. *Adv. Theory Simulations* **2**, (2019).
42. Proctor, C. M., Kim, C., Neher, D. & Nguyen, T. Q. Nongeminate recombination and charge transport limitations in diketopyrrolopyrrole-based solution-processed small molecule solar cells. *Adv. Funct. Mater.* **23**, 3584–3594 (2013).
43. Proctor, C. M., Kuik, M. & Nguyen, T. Q. Charge carrier recombination in organic solar cells. *Progress in Polymer Science* vol. 38 1941–1960 (2013).
44. Proctor, C. M. & Nguyen, T. Q. Effect of leakage current and shunt resistance on the light intensity dependence of organic solar cells. *Appl. Phys. Lett.* **106**, (2015).
45. Koster, L. J. A., Mihailetchi, V. D., Ramaker, R. & Blom, P. W. M. Light intensity dependence of open-circuit voltage of polymer:fullerene solar cells. *Appl. Phys. Lett.* **86**, 123509 (2005).
46. Samuel Balderrama, V. *et al.* Organic Solar Cells Toward the Fabrication Under Air Environment; Organic Solar Cells Toward the Fabrication Under Air Environment. *IEEE J. Photovoltaics* **6**, 491 (2016).
47. Laboratory, N. R. E. Reference Air Mass 1.5 Spectra | Grid Modernization | NREL. *National Renewable Energy Laboratory* https://www.nrel.gov/grid/solar-resource/spectra-am1.5.html (2022).
48. Elumalai, N. K. & Uddin, A. Open circuit voltage of organic solar cells: an in-depth review. *Energy Environ. Sci.* **9**, 391–410 (2016).
49. Qi, B. & Wang, J. Fill factor in organic solar cells. *Phys. Chem. Chem. Phys* **15**, 8972–8982 (2013).
50. Waldauf, C., Scharber, M. C. & Schilinsky, P. Physics of organic bulk heterojunction devices for photovoltaic applications. *J. Appl. Phys* **99**, 104503 (2006).
51. Servaites, J. D., Ratner, M. A. & Marks, T. J. Organic solar cells: A new look at traditional models. *Energy Environ. Sci.* **4**, 4410–4422 (2011).
52. Zheng, Z. *et al.* Tandem Organic Solar Cell with 20.2% Efficiency. *Joule* **6**, 171–184 (2022).
53. Zhang, Y. & Li, G. Functional Third Components in Nonfullerene Acceptor-Based Ternary Organic Solar Cells. *Accounts Mater. Res.* **1**, 158–171 (2020).
54. Fan, B. *et al.* Improved Performance of Ternary Polymer Solar Cells Based on A Nonfullerene Electron Cascade Acceptor. *Adv. Energy Mater.* **7**, 1602127 (2017).
55. Koppe, M. *et al.* Near IR Sensitization of Organic Bulk Heterojunction Solar Cells: Towards Optimization of the Spectral Response of Organic Solar Cells. *Adv. Funct. Mater.* **20**, 338–346 (2010).
56. An, Q. *et al.* Simultaneous improvement in short circuit current, open circuit voltage, and fill factor of polymer solar cells through ternary strategy. *ACS Appl. Mater. Interfaces* **7**, 3691–3698 (2015).
57. Zhou, D. *et al.* Recent progress in ternary organic solar cells based on solution-processed non-fullerene acceptors. *J. Mater. Chem. A* **8**, 23096–23122 (2020).
58. Ma, R. *et al.* Adding a Third Component with Reduced Miscibility and Higher LUMO Level Enables Efficient Ternary Organic Solar Cells. *ACS Energy Lett.* **5**,

2711–2720 (2020).

59. Yang, L., Zhou, H., Price, S. C. & You, W. Parallel-like bulk heterojunction polymer solar cells. *J. Am. Chem. Soc.* **134**, 5432–5435 (2012).
60. Zhang, W. *et al.* Phthalimide Polymer Donor Guests Enable over 17% Efficient Organic Solar Cells via Parallel-Like Ternary and Quaternary Strategies. *Adv. Energy Mater.* **10**, 2001436 (2020).
61. Khlyabich, P. P., Burkhart, B. & Thompson, B. C. Compositional dependence of the open-circuit voltage in ternary blend bulk heterojunction solar cells based on two donor polymers. *J. Am. Chem. Soc.* **134**, 9074–9077 (2012).
62. Zhan, L. *et al.* Over 17% efficiency ternary organic solar cells enabled by two non-fullerene acceptors working in an alloy-like model. *Energy Environ. Sci.* **13**, 635–645 (2020).
63. Liu, S. *et al.* Enhanced efficiency of polymer solar cells by adding a high-mobility conjugated polymer. *Energy Environ. Sci.* **8**, 1463–1470 (2015).
64. Jia, Z. *et al.* Understanding of the Nearly Linear Tunable Open-Circuit Voltages in Ternary Organic Solar Cells Based on Two Non-fullerene Acceptors. *J. Phys. Chem. Lett.* **12**, 151–156 (2021).
65. Liu, Z. & Wang, N. Small energy loss in ternary organic solar cells with a blend of cascade energy levels: two fullerene-free acceptors as the electron acceptor. *J. Mater. Chem. C* **7**, 10039 (2019).
66. Peters, C. H. *et al.* The mechanism of burn-in loss in a high efficiency polymer solar cell. *Adv. Mater.* **24**, 663–668 (2012).
67. Gasparini, N., Salleo, A., Mcculloch, I. & Baran, D. The role of the third component in ternary organic solar cells. *Nat. Rev. Mater.* **4**, 229–242 (2019).
68. Baran, D. *et al.* Robust nonfullerene solar cells approaching unity external quantum efficiency enabled by suppression of geminate recombination. *Nat. Commun.* **9**, 2059 (2018).
69. Doumon, N. Y., Yang, L. & Rosei, F. Ternary organic solar cells: A review of the role of the third element. *Nano Energy* **94**, 106915 (2022).
70. Birnie, D. P. Spin Coating Technique. in *Sol-Gel Technologies for Glass Producers and Users* 49–55 (Springer, Boston, MA, 2004).
71. Forrest, S. R. The path to ubiquitous and low-cost organic electronic appliances on plastic. *Nature* **428**, 911–918 (2004).
72. Mihailetchi, V. D., Koster, L. J. A., Hummelen, J. C. & Blom, P. W. M. Photocurrent generation in polymer-fullerene bulk heterojunctions. *Phys. Rev. Lett.* **93**, (2004).
73. Schauer, F. Space-charge-limited currents for organic solar cells optimisation. *Sol. Energy Mater. Sol. Cells* **87**, 235–250 (2005).
74. Tokmoldin, N. *et al.* Extraordinarily long diffusion length in PM6:Y6 organic solar cells. *J. Mater. Chem. A* **8**, 7854–7860 (2020).
75. Li, Y. Molecular design of photovoltaic materials for polymer solar cells: Toward suitable electronic energy levels and broad absorption. *Acc. Chem. Res.* **45**, 723–733 (2012).
76. Palomares, E. *et al.* Photovoltage/photocurrent transient techniques. in *Characterization Techniques for Perovskite Solar Cell Materials* 161–180 (Elsevier, 2019).
77. Nia, N. Y., Méndez, M., Di Carlo, A. & Palomares, E. Energetic disorder in

perovskite/polymer solar cells and its relationship with the interfacial carrier losses. *Philos. Trans. R. Soc. A Math. Phys. Eng. Sci.* **377**, (2019).

78. Arredondo, B. *et al.* Impedance spectroscopy analysis of small molecule solution processed organic solar cell. *Sol. Energy Mater. Sol. Cells* **128**, 351–356 (2014).
79. Von Hauff, E. Impedance Spectroscopy for Emerging Photovoltaics. *J. Phys. Chem. C* **123**, 11329–11346 (2019).
80. Ripolles-Sanchis, T., Guerrero, A., Bisquert, J. & Garcia-Belmonte, G. Diffusion-Recombination Determines Collected Current and Voltage in Polymer:Fullerene Solar Cells. *J. Phys. Chem. C* **116**, 16925–16933 (2012).
81. Von Hauff, E. & Klotz, D. Impedance spectroscopy for perovskite solar cells: characterisation, analysis, and diagnosis. *J. Mater. Chem. C* **10**, 742–761 (2022).
82. Ecker, B. *et al.* Degradation effects related to the hole transport layer in organic solar cells. *Adv. Funct. Mater.* **21**, 2705–2711 (2011).
83. Xu, L., Wang, J. & Hsu, J. W. P. Transport Effects on Capacitance-Frequency Analysis for Defect Characterization in Organic Photovoltaic Devices. *Phys. Rev. Appl.* **6**, 1–10 (2016).
84. Huhtamäki, T., Tian, X., Korhonen, J. T. & Ras, R. H. A. Surface-wetting characterization using contact-angle measurements. *Nat. Protoc.* **13**, 1521–1538 (2018).
85. Wu, S. Calculation of interfacial tension in polymer systems. *J. Polym. Sci. Part C Polym. Symp.* **34**, 19–30 (1971).
86. Cui, Y. *et al.* Wide-gap non-fullerene acceptor enabling high-performance organic photovoltaic cells for indoor applications Wide-gap. *Nat. Energy* **4**, 768–775 (2019).
87. Ka, H. *et al.* Outstanding Indoor Performance of Perovskite Photovoltaic Cells – Effect of Device Architectures and Interlayers. *Sol. RRL* **1800207**, 1–7 (2018).
88. Yin, H. *et al.* Designing a ternary photovoltaic cell for indoor light harvesting with a power conversion efficiency exceeding 20%. *J. Mater. Chem. A* **6**, 8579–8585 (2018).
89. Khan, J. A., Qureshi, H. K., Iqbal, A. & Lacatus, C. Energy management in Wireless Sensor Networks: A survey. *Comput. Electr. Eng.* **41**, 159–176 (2015).
90. Al-Fuqaha, A., Guizani, M., Mohammadi, M., Aledhari, M. & Ayyash, M. Internet of Things: A Survey on Enabling Technologies, Protocols, and Applications. *IEEE Commun. Surv. Tutorials* **17**, 2347–2376 (2015).
91. Lee, H. K. H. *et al.* Organic photovoltaic cells-promising indoor light harvesters for self-sustainable electronics. *J. Mater. Chem. A* **6**, 5618–5626 (2018).
92. Yang, S.-S., Hsieh, Z.-C., Keshtov, M. L., Sharma, G. D. & Chen, F.-C. Toward High-Performance Polymer Photovoltaic Devices for Low-Power Indoor Applications. *Sol. RRL* **1**, 1770143 (2017).
93. Gubbi, J., Buyya, R., Marusic, S. & Palaniswami, M. Internet of Things (IoT): A vision, architectural elements, and future directions. *Futur. Gener. Comput. Syst.* **29**, 1645–1660 (2013).
94. Ng, I. C. L. & Wakenshaw, S. Y. L. The Internet-of-Things: Review and research directions. *Int. J. Res. Mark.* **34**, 3–21 (2017).
95. Lee, H. K. H., Li, Z., Durrant, J. R. & Tsoi, W. C. Is organic photovoltaics promising for indoor applications? *Appl. Phys. Lett.* **108**, 253301 (2016).
96. Müller, M. F., Freunek, M. & Reindl, L. M. Maximum efficiencies of indoor

photovoltaic devices. *IEEE J. Photovoltaics* **3**, 59–64 (2013).

97. Torimtubun, A. A. A., Pallarès, J. & Marsal, L. F. Analysing the Efficiency Enhancement of Indoor Organic Photovoltaic using Impedance Spectroscopy Technique. in *2021 IEEE Latin America Electron Devices Conference (LAEDC)* 1–4 (2021). doi:10.1109/LAEDC51812.2021.9437965.
98. Torimtubun, A. A. A., Sánchez, J. G., Pallarès, J. & Marsal, L. F. High-Performance Organic Photovoltaic Cells for Indoor Light Energy Harvesting. in *Imagine Nano 2020 Online* vol. 107 1 (2020).
99. Lechêne, B. P. *et al.* Organic solar cells and fully printed super-capacitors optimized for indoor light energy harvesting. *Nano Energy* **26**, 631–640 (2016).
100. Vincent, P. *et al.* Indoor-type photovoltaics with organic solar cells through optimal design. *Dye. Pigment.* **159**, 306–313 (2018).
101. Freitag, M. *et al.* Dye-sensitized solar cells for efficient power generation under ambient lighting. *Nat. Photonics* **11**, 372–378 (2017).
102. Minnaert, B. & Veelaert, P. Efficiency simulations of thin film chalcogenide photovoltaic cells for different indoor lighting conditions. *Thin Solid Films* **519**, 7537–7540 (2011).
103. Mori, S. *et al.* Investigation of the organic solar cell characteristics for indoor LED light applications. *Jpn. J. Appl. Phys.* **54**, 071602 (2015).
104. Chen, C. Y. *et al.* Perovskite Photovoltaics for Dim-Light Applications. *Adv. Funct. Mater.* **25**, 7064–7070 (2015).
105. De Rossi, F., Pontecorvo, T. & Brown, T. M. Characterization of photovoltaic devices for indoor light harvesting and customization of flexible dye solar cells to deliver superior efficiency under artificial lighting. *Appl. Energy* **156**, 413–422 (2015).
106. Xiao, B., Wu, H. & Cao, Y. Solution-processed cathode interfacial layer materials for high-efficiency polymer solar cells. *Mater. Today* **18**, 385–394 (2015).
107. Li, M. *et al.* Interface Modification by Ionic Liquid: A Promising Candidate for Indoor Light Harvesting and Stability Improvement of Planar Perovskite Solar Cells. *Adv. Energy Mater.* **8**, 1–8 (2018).
108. Aoki, Y. Photovoltaic performance of Organic Photovoltaics for indoor energy harvester. *Org. Electron. physics, Mater. Appl.* **48**, 194–197 (2017).
109. Minnaert, B. & Veelaert, P. A proposal for typical artificial light sources for the characterization of indoor photovoltaic applications. *Energies* **7**, 1500–1516 (2014).
110. Kim, S., Jahandar, M., Jeong, J. H. & Lim, D. C. Recent progress in solar cell technology for low-light indoor applications. *Curr. Altern. Energy* **2**, 1–15 (2018).
111. Gupta, V. *et al.* Barium: An efficient cathode layer for bulk-heterojunction solar cells. *Sci. Rep.* **3**, 6–11 (2013).
112. Zhang, H. *et al.* Fullerene-free polymer solar cell based on a polythiophene derivative with an unprecedented energy loss of less than 0.5 eV. *J. Mater. Chem. A* **4**, 18043–18049 (2016).
113. Zhang, J., Tan, H. S., Guo, X., Facchetti, A. & Yan, H. Material insights and challenges for non-fullerene organic solar cells based on small molecular acceptors. *Nat. Energy* **3**, 720–731 (2018).
114. Nam, M. *et al.* Ternary Organic Blend Approaches for High Photovoltaic Performance in Versatile Applications. *Adv. Energy Mater.* **1901856**, 1901856 (2019).

115. Goo, J. S., Shin, S. C., You, Y. J. & Shim, J. W. Polymer surface modification to optimize inverted organic photovoltaic devices under indoor light conditions. *Sol. Energy Mater. Sol. Cells* **184**, 31–37 (2018).
116. Shin, S.-C., You, Y.-J., Goo, J. S. & Shim, J. W. In-depth interfacial engineering for efficient indoor organic photovoltaics. *Appl. Surf. Sci.* **495**, 143556 (2019).
117. Jørgensen, M., Norrman, K. & Krebs, F. C. Stability/degradation of polymer solar cells. *Sol. Energy Mater. Sol. Cells* **92**, 686–714 (2008).
118. Gevorgyan, S. A. *et al.* Lifetime of organic photovoltaics: Status and predictions. *Adv. Energy Mater.* **6**, 1–17 (2016).
119. Sánchez, J. G. *et al.* Stability study of high efficiency polymer solar cells using TiOx as electron transport layer. *Sol. Energy* **150**, 147–155 (2017).
120. Duan, L. & Uddin, A. Progress in Stability of Organic Solar Cells. *Adv. Sci.* **1903259**, 1–39 (2020).
121. Mateker, W. R. & McGehee, M. D. Progress in Understanding Degradation Mechanisms and Improving Stability in Organic Photovoltaics. *Adv. Mater.* **29**, (2017).
122. Balderrama, V. S. *et al.* Degradation of electrical properties of PTB1:PCBM solar cells under different environments. *Sol. Energy Mater. Sol. Cells* **125**, 155–163 (2014).
123. Jeon, I. I. & Matsuo, Y. Vertical phase separation and light-soaking effect improvements by photoactive layer spin coating initiation time control in air-processed inverted organic solar cells. *Sol. Energy Mater. Sol. Cells* **140**, 335–343 (2015).
124. Uddin, A., Upama, M. B., Yi, H. & Duan, L. Encapsulation of organic and perovskite solar cells: A review. *Coatings* **9**, 1–17 (2019).
125. Inasaridze, L. N. *et al.* Light-induced generation of free radicals by fullerene derivatives: An important degradation pathway in organic photovoltaics? *J. Mater. Chem. A* **5**, 8044–8050 (2017).
126. Doumon, N. Y., Wang, G., Chiechi, R. C. & Koster, L. J. A. Relating polymer chemical structure to the stability of polymer:fullerene solar cells. *J. Mater. Chem. C* **5**, 6611–6619 (2017).
127. Williams, G. & Aziz, H. Implications of the device structure on the photo-stability of organic solar cells. *Sol. Energy Mater. Sol. Cells* **128**, 320–329 (2014).
128. Gasparini, N. *et al.* Exploiting Ternary Blends for Improved Photostability in High-Efficiency Organic Solar Cells. *ACS Energy Lett.* **5**, 1371−1379 (2020).
129. Duan, L. *et al.* Comparative analysis of burn-in photo-degradation in non-fullerene COi8DFIC acceptor based high-efficiency ternary organic solar cells. *Mater. Chem. Front.* **3**, 1085–1096 (2019).
130. Kong, J. *et al.* Long-term stable polymer solar cells with significantly reduced burn-in loss. *Nat. Commun.* **5**, 1–8 (2014).
131. He, Z. *et al.* Enhanced power-conversion efficiency in polymer solar cells using an inverted device structure. *Nat. Photonics* **6**, 591–595 (2012).
132. Cui, Y. *et al.* 1 cm 2 Organic Photovoltaic Cells for Indoor Application with over 20% Efficiency . *Adv. Mater.* **1904512**, 1904512 (2019).
133. Jagadamma, L. K., Sajjad, M. T., Savikhin, V., Toney, M. F. & Samuel, I. D. W. Correlating photovoltaic properties of a PTB7-Th:PC71BM blend to photophysics and microstructure as a function of thermal annealing. *J. Mater. Chem. A* **5**, 14646–

14657 (2017).
134. Jain, N. *et al.* Interfacial disorder in efficient polymer solar cells: The impact of donor molecular structure and solvent additives. *J. Mater. Chem. A* **5**, 24749–24757 (2017).
135. Pearson, A. J. *et al.* Critical light instability in CB/DIO processed PBDTTT-EFT:PC71BM organic photovoltaic devices. *Org. Electron.* **30**, 225–236 (2016).
136. Liu, Q. *et al.* Circumventing UV Light Induced Nanomorphology Disorder to Achieve Long Lifetime PTB7-Th:PCBM Based Solar Cells. *Adv. Energy Mater.* **7**, 1–9 (2017).
137. Reese, M. O. *et al.* Consensus stability testing protocols for organic photovoltaic materials and devices. *Sol. Energy Mater. Sol. Cells* **95**, 1253–1267 (2011).
138. Yang, D. *et al.* High efficiency inverted polymer solar cells with room-temperature titanium oxide/polyethylenimine films as electron transport layers. *J. Mater. Chem. A* **2**, 17281–17285 (2014).
139. Balderrama, V. S. *et al.* High-efficiency organic solar cells based on a halide salt and polyfluorene polymer with a high alignment-level of the cathode selective contact. *J. Mater. Chem. A* **6**, 22534–22544 (2018).
140. Seki, K., Furube, A. & Yoshida, Y. Detailed balance limit of power conversion efficiency for organic photovoltaics. *Appl. Phys. Lett.* **103**, 253904 (2013).
141. Scharber, M. C. *et al.* Design rules for donors in bulk-heterojunction solar cells - Towards 10 % energy-conversion efficiency. *Adv. Mater.* **18**, 789–794 (2006).
142. Brabec, C. J. Organic photovoltaics: Technology and market. *Sol. Energy Mater. Sol. Cells* **83**, 273–292 (2004).
143. Qi, B. & Wang, J. Fill factor in organic solar cells. *Phys. Chem. Chem. Phys.* **15**, 8972–8982 (2013).
144. Steim, R. *et al.* Solar Energy Materials & Solar Cells Organic photovoltaics for low light applications. *Sol. Energy Mater. Sol. Cells* **95**, 3256–3261 (2011).
145. One-Material. PCE-10 from 1-mat. http://www.1-material.com/wp-content/uploads/2013/12/1M_From-PTB7-to-PCE-10_Confidential.pdf (2013).
146. Zhang, S. *et al.* Side chain selection for designing highly efficient photovoltaic polymers with 2D-conjugated structure. *Macromolecules* **47**, 4653–4659 (2014).
147. Wan, Q. *et al.* 10 . 8 % Effi ciency Polymer Solar Cells Based on PTB7-Th and PC 71 BM via Binary Solvent Additives Treatment. *Adv. Funct. Mater.* **26**, 6635–6640 (2016).
148. Wang, D. *et al.* Tuning nanoscale morphology using mixed solvents and solvent vapor treatment for high performance polymer solar cells. *RSC Adv.* **4**, 48724–48733 (2014).
149. Yan, H. *et al.* Increasing Polymer Solar Cell Fill Factor by Trap-Filling with F4-TCNQ at Parts Per Thousand Concentration. *Adv. Mater.* **28**, 6491–6496 (2016).
150. Fan, R. *et al.* Enhanced performance of polymer solar cells based on PTB7-Th:PC71BM by doping with 1-bromo-4-nitrobenzene. *J. Mater. Chem. C* **5**, 10985–10990 (2017).
151. Huang, W. *et al.* Unraveling the morphology of high efficiency polymer solar cells based on the donor polymer PBDTTT-EFT. *Adv. Energy Mater.* **5**, 1–11 (2015).
152. He, Z. *et al.* Single-junction polymer solar cells with high efficiency and photovoltage. *Nat. Photonics* **9**, 174–179 (2015).
153. Liu, Q., Mantilla-Perez, P., Montes Bajo, M., Romero-Gomez, P. & Martorell, J.

UV-Induced Oxygen Removal for Photostable, High-Efficiency PTB7-Th:PC71BM Photovoltaic Cells. *ACS Appl. Mater. Interfaces* **8**, 28750–28756 (2016).

154. Huang, W. *et al.* A facile approach to alleviate photochemical degradation in high efficiency polymer solar cells. *J. Mater. Chem. A* **3**, 16313–16319 (2015).
155. Yuan, T., Zhu, X., Zhou, L., Zhang, J. & Tu, G. Efficient inverted polymer solar cells based on conjugated polyelectrolyte and zinc oxide modified ITO electrode. *Appl. Phys. Lett.* **106**, 083302 (2015).
156. Chen, J. De *et al.* Single-junction polymer solar cells exceeding 10% power conversion effi ciency. *Adv. Mater.* **27**, 1035–1041 (2015).
157. Nian, L. *et al.* Photoconductive Cathode Interlayer for Highly Efficient Inverted Polymer Solar Cells. *J. Am. Chem. Soc.* **137**, 6995–6998 (2015).
158. Liao, S. H., Jhuo, H. J., Cheng, Y. S. & Chen, S. A. Fullerene derivative-doped zinc oxide nanofilm as the cathode of inverted polymer solar cells with low-bandgap polymer (PTB7-Th) for high performance. *Adv. Mater.* **25**, 4766–4771 (2013).
159. Huang, J. *et al.* Highly Efficient Organic Solar Cells with Improved Vertical Donor-Acceptor Compositional Gradient Via an Inverted Off-Center Spinning Method. *Adv. Mater.* **28**, 967–974 (2016).
160. Pallarès, J., Cabré, R., Marsal, L. F. & Schropp, R. E. I. A compact equivalent circuit for the dark current-voltage characteristics of nonideal solar cells. *J. Appl. Phys.* **100**, 2–7 (2006).
161. Lucarelli, G., Di Giacomo, F., Zardetto, V., Creatore, M. & Brown, T. M. Efficient light harvesting from flexible perovskite solar cells under indoor white light-emitting diode illumination. *Nano Res.* **10**, 2130–2145 (2017).
162. Goo, J. S., Lee, J. H., Shin, S. C., Park, J. S. & Shim, J. W. Undoped ZnO electrodes for low-cost indoor organic photovoltaics. *J. Mater. Chem. A* **6**, 23464–23472 (2018).
163. Sánchez, J. G. *et al.* Impact of inkjet printed ZnO electron transport layer on the characteristics of polymer solar cells. *RSC Adv.* **8**, 13094–13102 (2018).
164. Proctor, C. M. & Nguyen, T. Q. Effect of leakage current and shunt resistance on the light intensity dependence of organic solar cells. *Appl. Phys. Lett.* **106**, 083301 (2015).
165. Kim, J. *et al.* Light-soaking issue in polymer solar cells: Photoinduced energy level alignment at the sol-gel processed metal oxide and indium tin oxide interface. *J. Appl. Phys.* **111**, 114511 (2012).
166. Noh, Y. J., Na, S. I. & Kim, S. S. Inverted polymer solar cells including ZnO electron transport layer fabricated by facile spray pyrolysis. *Sol. Energy Mater. Sol. Cells* **117**, 139–144 (2013).
167. Zhang, H., Zhou, W., Yu, C., Guo, J. & Li, F. Revealing working mechanisms of PFN as a cathode interlayer in conventional and inverted polymer solar cells. *Phys. Chem. Chem. Phys.* **21**, 20065–20072 (2019).
168. Trost, S. *et al.* Tin Oxide (SnOx) as Universal 'light-Soaking' Free Electron Extraction Material for Organic Solar Cells. *Adv. Energy Mater.* **5**, 1–4 (2015).
169. Von Hauff, E. Impedance Spectroscopy for Emerging Photovoltaics. *J. Phys. Chem. C* **123**, 11329–11346 (2019).
170. Osorio, E. *et al.* Degradation Analysis of Encapsulated and Nonencapsulated TiO2/PTB7:PC70BM/V2O5 Solar Cells under Ambient Conditions via Impedance

Spectroscopy. *ACS Omega* **2**, 3091–3097 (2017).

171. Pockett, A., Lee, H. K. H., Coles, B. L., Tsoi, W. C. & Carnie, M. J. A combined transient photovoltage and impedance spectroscopy approach for a comprehensive study of interlayer degradation in non-fullerene acceptor organic solar cells. *Nanoscale* **11**, 10872–10883 (2019).
172. Thiagarajan, S., Thaiyan, M. & Ganesan, R. Physical property exploration of highly oriented V2O5 thin films prepared by electron beam evaporation. *New J. Chem.* **39**, 9471–9479 (2015).
173. Peng, Z. *et al.* One-step coating inverted polymer solar cells using a conjugated polymer as an electron extraction additive. *J. Mater. Chem. A* **3**, 20500–20507 (2015).
174. Contreras-Bernal, L. *et al.* Impedance analysis of perovskite solar cells: A case study. *J. Mater. Chem. A* **7**, 12191–12200 (2019).
175. Torimtubun, A. A. A., Sánchez, J. G., Pallarès, J. & Marsal, L. F. A cathode interface engineering approach for the comprehensive study of indoor performance enhancement in organic photovoltaics. *Sustain. Energy Fuels* **4**, 3378–3387 (2020).
176. Sacramento, A. *et al.* Degradation Study of Inverted Polymer Solar Cells Using Inkjet Printed ZnO Electron Transport Layer. *Lat. Am. Electron Devices Conf. LAEDC 2019* (2019) doi:10.1109/LAED.2019.8714734.
177. Gasparini, N. *et al.* Burn-in Free Nonfullerene-Based Organic Solar Cells. *Adv. Energy Mater.* **7**, 1–7 (2017).
178. Doumon, N. Y. *et al.* 1,8-diiodooctane acts as a photo-acid in organic solar cells. *Sci. Rep.* **9**, 1–14 (2019).
179. Sundqvist, A., Sandberg, O. J., Nyman, M., Smått, J. H. & Österbacka, R. Origin of the S-Shaped JV Curve and the Light-Soaking Issue in Inverted Organic Solar Cells. *Adv. Energy Mater.* **6**, 1–7 (2016).
180. Ecker, B., Egelhaaf, H. J., Steim, R., Parisi, J. & Von Hauff, E. Understanding S-shaped current-voltage characteristics in organic solar cells containing a TiO x interlayer with impedance spectroscopy and equivalent circuit analysis. *J. Phys. Chem. C* **116**, 16333–16337 (2012).
181. Koster, L. J. A., Mihailetchi, V. D., Ramaker, R., Xie, H. & Blom, P. W. Light intensity dependence of open-circuit voltage and short-circuit current of polymer/fullerene solar cells. *Org. Optoelectron. Photonics II* **6192**, 61922G (2006).
182. Hartnagel, P. & Kirchartz, T. Understanding the Light-Intensity Dependence of the Short-Circuit Current of Organic Solar Cells. *Adv. Theory Simulations* **2000116**, 1–11 (2020).
183. Chegaar, M. *et al.* Effect of illumination intensity on solar cells parameters. *Energy Procedia* **36**, 722–729 (2013).
184. Razzell-Hollis, J. *et al.* Photochemical stability of high efficiency PTB7:PC70BM solar cell blends. *J. Mater. Chem. A* **2**, 20189–20195 (2014).
185. He, Z. *et al.* Single-junction polymer solar cells with high efficiency and photovoltage. *Nat. Photonics* **9**, 174–179 (2015).
186. Shen, P. *et al.* High-efficiency polymer solar cells with low temperature solution-processed SnO2/PFN as a dual-function electron transporting layer. *J. Mater. Chem. A* **6**, 17401–17408 (2018).
187. Zhao, B. *et al.* Flexible polymer solar cells with power conversion efficiency of

8.7%. *J. Mater. Chem. C* **2**, 5077–5082 (2014).

188. Bihar, E. *et al.* Fully Inkjet-Printed, Ultrathin and Conformable Organic Photovoltaics as Power Source Based on Cross-Linked PEDOT:PSS Electrodes. *Adv. Mater. Technol.* **5**, 1–7 (2020).
189. Liu, Y. *et al.* Highly Flexible and Lightweight Organic Solar Cells on Biocompatible Silk Fibroin. *ACS Appl. Mater. Interfaces* **6**, 20670–20675 (2014).
190. Liu, Q. *et al.* 18% Efficiency organic solar cells. *Sci. Bull.* **65**, 272–275 (2020).
191. Meng, L. *et al.* Organic and solution-processed tandem solar cells with 17.3% efficiency. *Science (80-.).* **361**, 1094–1098 (2018).
192. Jiang, W. *et al.* Ternary Nonfullerene Polymer Solar Cells with 12.16% Efficiency by Introducing One Acceptor with Cascading Energy Level and Complementary Absorption. *Adv. Mater.* **30**, 1–7 (2018).
193. Salim, M. B., Nekovei, R. & Jeyakumar, R. Organic tandem solar cells with 18.6% efficiency. *Sol. Energy* **198**, 160–166 (2020).
194. Firdaus, Y. *et al.* Novel wide-bandgap non-fullerene acceptors for efficient tandem organic solar cells. *J. Mater. Chem. A* **8**, 1164–1175 (2020).
195. Shi, Z., Bai, Y., Chen, X., Zeng, R. & Tan, Z. Tandem structure: a breakthrough in power conversion efficiency for highly efficient polymer solar cells. *Sustain. Energy Fuels* **3**, 910–934 (2019).
196. Weng, K. *et al.* Ternary organic solar cells based on two compatible PDI-based acceptors with an enhanced power conversion efficiency. *J. Mater. Chem. A* **7**, 3552–3557 (2019).
197. An, Q. *et al.* Versatile ternary organic solar cells : a critical review Energy & Environmental Science a critical review. *Energy Environ. Sci.* **9**, 281–322 (2016).
198. Bi, P. & Hao, X. Versatile Ternary Approach for Novel Organic Solar Cells : A Review. *Sol. RRL* **1800263**, 1–34 (2019).
199. Liu, X., Yan, Y., Yao, Y. & Liang, Z. Ternary Blend Strategy for Achieving High-Efficiency Organic Solar Cells with Nonfullerene Acceptors Involved. *Adv. Funct. Mater.* **28**, 1–20 (2018).
200. Lakhotiya, G., Belsare, N., Arbuj, S., Kale, B. & Rana, A. Enhanced performance of PTB7-Th : PCBM based active layers in ternary organic solar cells. *RSC Adv.* **9**, 7457–7463 (2019).
201. Zhan, L. *et al.* Over 17% efficiency ternary organic solar cells enabled by two non-fullerene acceptors working in an alloy-like model. *Energy Environ. Sci.* **13**, 635–645 (2020).
202. Torimtubun, A. A. A., Follana-Berná, J., Sastre-Santos, Á., Pallarès, J. & Marsal, L. F. Effect of thermal annealing on the performance of PTB7-Th:PC<inf>70</inf>BM-based ternary organic solar cells; Effect of thermal annealing on the performance of PTB7-Th:PC<inf>70</inf>BM-based ternary organic solar cells. in *2021 13th Spanish Conference on Electron Devices (CDE)* 45–48 (2021). doi:10.1109/CDE52135.2021.9455729.
203. Cheng, P. *et al.* Unique Energy Alignments of a Ternary Material System toward High-Performance Organic Photovoltaics. *Adv. Mater.* **30**, 1–8 (2018).
204. Lin, Y. C. *et al.* Molecular engineering of side chain architecture of conjugated polymers enhances performance of photovoltaics by tuning ternary blend structures. *Nano Energy* **43**, 138–148 (2018).
205. Cheng, H.-W. *et al.* Realizing Efficient Charge/Energy Transfer and Charge

Extraction in Fullerene-Free Organic Photovoltaics via a Versatile Third Component. *Nano Lett.* **19**, 5053–5061 (2019).

206. Yang, C. *et al.* Nonfullerene Ternary Organic Solar Cell with Effective Charge Transfer between Two Acceptors. *J. Phys. Chem. Lett.* **11**, 927–934 (2020).
207. Xiao, L. *et al.* Multiple Roles of a Non-fullerene Acceptor Contribute Synergistically for High-Efficiency Ternary Organic Photovoltaics Multiple Roles of a Non-fullerene Acceptor Contribute Synergistically for High-Efficiency Ternary Organic Photovoltaics. *Joule* **2**, 2154–2166 (2018).
208. Cui, Y. *et al.* Over 16% efficiency organic photovoltaic cells enabled by a chlorinated acceptor with increased open-circuit voltages. *Nat. Commun.* **10**, 1–8 (2019).
209. Stenta, C. *et al.* Diphenylphenoxy-thiophene-PDI dimers as acceptors for OPV applications with open circuit voltage approaching 1 volt. *Nanomaterials* **8**, 1–16 (2018).
210. Sanchez, J. G. *et al.* Effects of Annealing Temperature on the Performance of Organic Solar Cells Based on Polymer: Non-Fullerene Using V2O5 as HTL. *IEEE J. Electron Devices Soc.* **8**, 421–428 (2020).
211. Martín-Gomis, L., Fernández-Lázaro, F. & Sastre-Santos, Á. Advances in phthalocyanine-sensitized solar cells (PcSSCs). *J. Mater. Chem. A* **2**, 15672–15682 (2014).
212. Urbani, M., De La Torre, G., Nazeeruddin, M. K. & Torres, T. Phthalocyanines and porphyrinoid analogues as hole-and electron-transporting materials for perovskite solar cells. *Chem. Soc. Rev.* **48**, 2738–2766 (2019).
213. Urbani, M., Ragoussi, M. E., Nazeeruddin, M. K. & Torres, T. Phthalocyanines for dye-sensitized solar cells. *Coord. Chem. Rev.* **381**, 1–64 (2019).
214. Molina, D., Guerrero, A., Garcia-Belmonte, G., Fernández-Lázaro, F. & Sastre-Santos, Á. Synthesis of a fully conjugated phthalocyanine-diketopyrrolopyrrole-phthalocyanine triad as low band gap donor in small molecule bulk heterojunction solar cells. *European J. Org. Chem.* **2014**, 4585–4591 (2014).
215. Wang, Y., Zhuang, C., Fang, Y., Yu, H. & Wang, B. Various roles of dye molecules in organic ternary blend solar cells. *Dye. Pigment.* **176**, 108231 (2020).
216. Faure, M. D. M. ., Grant, T. M. . & Lessard, B. H. Silicon phthalocyanines as acceptor candidates in mixed solution/evaporation processed planar heterojunction organic photovoltaic devices. *Coatings* **9**, 1–13 (2019).
217. Honda, S., Nogami, T., Ohkita, H., Benten, H. & Ito, S. Improvement of the light-harvesting efficiency in polymer/fullerene bulk heterojunction solar cells by interfacial dye modification. *ACS Appl. Mater. Interfaces* **1**, 804–810 (2009).
218. Honda, S., Yokoya, S., Ohkita, H., Benten, H. & Ito, S. Light-harvesting mechanism in polymer/fullerene/dye ternary blends studied by transient absorption spectroscopy. *J. Phys. Chem. C* **115**, 11306–11317 (2011).
219. Xu, H., Ohkita, H., Tamai, Y., Benten, H. & Ito, S. Interface Engineering for Ternary Blend Polymer Solar Cells with a Heterostructured Near-IR Dye. *Adv. Mater.* **27**, 5868–5874 (2015).
220. Ke, L. *et al.* A Series of Pyrene-Substituted Silicon Phthalocyanines as Near-IR Sensitizers in Organic Ternary Solar Cells. *Adv. Energy Mater.* **6**, 1–13 (2016).
221. Vebber, M. C., Grant, T. M., Brusso, J. L. & Lessard, B. H. Bis(trialkylsilyl oxide) Silicon Phthalocyanines: Understanding the Role of Solubility in Device

Performance as Ternary Additives in Organic Photovoltaics. *Langmuir* **36**, 2612–2621 (2020).

222. Xu, Z. X., Roy, V. A. L., Low, K. H. & Che, C. M. Bulk heterojunction photovoltaic cells based on tetra-methyl substituted copper(ii) phthalocyanine:P3HT:PCBM composite. *Chem. Commun.* **47**, 9654–9656 (2011).
223. Stylianakis, M. M. *et al.* Ternary organic solar cells incorporating zinc phthalocyanine with improved performance exceeding 8.5%. *Dye. Pigment.* **146**, 408–413 (2017).
224. Huang, H. *et al.* Enhanced performance of ternary organic solar cells with a wide bandgap acceptor as the third component. *J. Mater. Chem. A* **7**, 27423–27431 (2019).
225. Bi, P. *et al.* Dual Forster resonance energy transfer effects in non-fullerene ternary organic solar cells with the third component embedded in the donor and acceptor. *J. Mater. Chem. A* **5**, 12120–12130 (2017).
226. Yang, C. *et al.* Effects of energy-level offset between a donor and acceptor on the photovoltaic performance of non-fullerene organic solar cells. *J. Mater. Chem. A* **7**, 18889–18897 (2019).
227. Lessard, B. H. . *et al.* Bis(tri-n-hexylsilyl oxide) Silicon Phthalocyanine: A Unique Additive in Ternary Bulk Heterojunction Organic Photovoltaic Devices. *ACS Appl. Mater. Interfaces* **6**, 15040−15051 (2014).
228. Koster, L. J. A., Kemerink, M., Wienk, M. M., Maturová, K. & Janssen, R. A. J. Quantifying bimolecular recombination losses in organic bulk heterojunction solar cells. *Adv. Mater.* **23**, 1670–1674 (2011).
229. Lakhwani, G., Rao, A. & Friend, R. H. Bimolecular Recombination in Organic Photovoltaics. *Annu. Rev. Phys. Chem.* **65**, 557–581 (2014).
230. Ito, M. *et al.* Characterization of the organic thin film solar cells with active layers of PTB7/PC71BM prepared by using solvent mixtures with different additives. *Int. J. Photoenergy* **2014**, 1–8 (2014).
231. Doumon, N. Y. *et al.* Improved photostability in ternary blend organic solar cells: The role of [70]PCBM. *J. Mater. Chem. C* **7**, 5104–5111 (2019).
232. Zhang, K. N. *et al.* High-Performance Ternary Organic Solar Cells with Morphology-Modulated Hole Transfer and Improved Ultraviolet Photostability. *Sol. RRL* **2000165**, 1–10 (2020).
233. Cui, Y. *et al.* Single-Junction Organic Photovoltaic Cell with 19% Efficiency. *Adv. Mater.* **33**, (2021).
234. Yu, K. *et al.* Achieving 18.14% Efficiency of Ternary Organic Solar Cells with Alloyed Nonfullerene Acceptor. *Small Struct.* **2**, 2100099 (2021).
235. Chen, X. *et al.* 18.02% Efficiency ternary organic solar cells with a small-molecular donor third component. *Chem. Eng. J.* **424**, 130397 (2021).
236. Liu, Q. *et al.* 18% Efficiency organic solar cells. *Sci. Bull.* **65**, 272–275 (2020).
237. Torimtubun, A. A. A. *et al.* Fluorinated Zinc and Copper Phthalocyanines as Efficient Third Components in Ternary Bulk Heterojunction Solar Cells. *ACS Appl. Energy Mater.* **4**, 5201–5211 (2021).
238. Zhao, C. *et al.* Recent advances, challenges and prospects in ternary organic solar cells. *Nanoscale* vol. 13 2181–2208 (2021).
239. An, Q. *et al.* Versatile ternary organic solar cells: A critical review. *Energy and Environmental Science* vol. 9 281–322 (2016).

240. Gasparini, N., Salleo, A., McCulloch, I. & Baran, D. The role of the third component in ternary organic solar cells. *Nature Reviews Materials* vol. 4 229–242 (2019).
241. Moustafa, E., Torimtubun, A. A. A., Pallarès, J. & Marsal, L. F. Effect of Additives and Annealing on the Performance of Nonfullerene-Based Binary and Ternary Organic Photovoltaics. *Sol. RRL* **2100480**, 1–16 (2021).
242. Jiang, B.-H. *et al.* Improved Blend Film Morphology and Free Carrier Generation Provide a High-Performance Ternary Polymer Solar Cell. *ACS Appl. Mater. Interfaces* **13**, 1076−1085 (2021).
243. Torimtubun, A. A. A., Sanchez, J. G., Ferre-Borrull, J. & Marsal, L. F. (Invited) High Performance Ternary Organic Solar Cells Based on Non-Fullerene Acceptors. *ECS Meet. Abstr.* **MA2021-01**, 1049 (2021).
244. An, Q. *et al.* Alloy-like ternary polymer solar cells with over 17.2% efficiency. *Sci. Bull.* **65**, 538–545 (2020).
245. Pan, M. A. *et al.* 16.7%-efficiency ternary blended organic photovoltaic cells with PCBM as the acceptor additive to increase the open-circuit voltage and phase purity. *J. Mater. Chem. A* **7**, 20713–20722 (2019).
246. Dong, Y. *et al.* Ternary Polymer Solar Cells Facilitating Improved Efficiency and Stability. *Adv. Mater.* **31**, 1904601 (2019).
247. Zhang, K. N. *et al.* Suppressing Kinetic Aggregation of Non-Fullerene Acceptor via Versatile Alloy States Enables High-Efficiency and Stable Ternary Polymer Solar Cells. *Advanced Functional Materials* vol. 31 (2021).
248. Zhan, L. *et al.* Over 17% efficiency ternary organic solar cells enabled by two non-fullerene acceptors working in an alloy-like model. *Energy Environ. Sci.* **13**, 635–645 (2020).
249. Wang, X. *et al.* High-Efficiency (16.93%) Pseudo-Planar Heterojunction Organic Solar Cells Enabled by Binary Additives Strategy. *Adv. Funct. Mater.* **31**, 2102291 (2021).
250. Tambasco, M., Lipson, J. E. G. & Higgins, J. S. Blend Miscibility and the Flory−Huggins Interaction Parameter: A Critical Examination. *Macromolecules* **39**, 4860–4868 (2006).
251. Yan, C. *et al.* Reducing V OC loss via structure compatible and high lowest unoccupied molecular orbital nonfullerene acceptors for over 17%-efficiency ternary organic photovoltaics . *EcoMat* **2**, (2020).
252. Torimtubun, A. A. A. *et al.* Shelf lifetime analysis of organic solar cells combining frequency and time resolved techniques. *Sustain. Energy Fuels* **5**, 6498–6508 (2021).
253. Ma, X. *et al.* Achieving 17.4% Efficiency of Ternary Organic Photovoltaics with Two Well-Compatible Nonfullerene Acceptors for Minimizing Energy Loss. *Adv. Energy Mater.* **10**, 2001404 (2020).
254. Chang, Y. *et al.* Achieving Efficient Ternary Organic Solar Cells Using Structurally Similar Non-Fullerene Acceptors with Varying Flanking Side Chains. *Advanced Energy Materials* vol. 11 (2021).
255. Röhr, J. A., Moia, D., Haque, S. A., Kirchartz, T. & Nelson, J. Exploring the validity and limitations of the Mott-Gurney law for charge-carrier mobility determination of semiconducting thin-films. *J. Phys. Condens. Matter* **30**, 105901 (2018).

256. Moiz, S. A., Khan, I. A., Younis, W. A. & Karimov, K. S. Space Charge–Limited Current Model for Polymers. in *Conducting Polymers* (2016).
257. Rodríguez-Seco, C. *et al.* Minimization of Carrier Losses for Efficient Perovskite Solar Cells through Structural Modification of Triphenylamine Derivatives. *Angew. Chemie - Int. Ed.* 1–6 (2020) doi:10.1002/anie.201915022.
258. Montcada, N. F., Méndez, M., Cho, K. T., Nazeeruddin, M. K. & Palomares, E. Photo-induced dynamic processes in perovskite solar cells: The influence of perovskite composition in the charge extraction and the carrier recombination. *Nanoscale* **10**, 6155–6158 (2018).
259. Ryan, J. W., Palomares, E., Ryan, J. W. & Palomares, E. Photo-Induced Charge Carrier Recombination Kinetics in Small Molecule Organic Solar Cells and the Influence of Film Nanomorphology. *Adv. Energy Mater.* **7**, 1601509 (2017).
260. Shuttle, C. G. *et al.* Experimental determination of the rate law for charge carrier decay in a polythiophene: Fullerene solar cell. *Appl. Phys. Lett.* **92**, 1–4 (2008).
261. Kirchartz, T. & Nelson, J. Meaning of reaction orders in polymer:fullerene solar cells. *Phys. Rev. B - Condens. Matter Mater. Phys.* **86**, (2012).
262. Kiermasch, D. *et al.* Unravelling steady-state bulk recombination dynamics in thick efficient vacuum-deposited perovskite solar cells by transient methods. *J. Mater. Chem. A* **7**, 14712–14722 (2019).
263. Kiermasch, D., Baumann, A., Fischer, M., Dyakonov, V. & Tvingstedt, K. Revisiting lifetimes from transient electrical characterization of thin film solar cells; A capacitive concern evaluated for silicon, organic and perovskite devices. *Energy Environ. Sci.* **11**, 629–640 (2018).
264. Yin, A. *et al.* Mediated Non-geminate Recombination in Ternary Organic Solar Cells Through a Liquid Crystal Guest Donor. *Front. Chem.* **8**, 21 (2020).
265. Privado, M. *et al.* Highly efficient ternary polymer solar cell with two non-fullerene acceptors. *Sol. Energy* **199**, 530–537 (2020).
266. Sharma, R. *et al.* Performance enhancement of conjugated polymer-small molecule-non fullerene ternary organic solar cells by tuning recombination kinetics and molecular ordering. *Sol. Energy* **201**, 499–507 (2020).
267. Arredondo, B. *et al.* Monitoring degradation mechanisms in PTB7:PC71BM photovoltaic cells by means of impedance spectroscopy. *Sol. Energy Mater. Sol. Cells* **144**, 422–428 (2016).
268. Upama, M. B. *et al.* Effect of annealing dependent blend morphology and dielectric properties on the performance and stability of non-fullerene organic solar cells. *Sol. Energy Mater. Sol. Cells* **176**, 109–118 (2018).
269. Moustafa, E., Sánchez, J. G., Marsal, L. F. & Pallarès, J. Stability Enhancement of High-Performance Inverted Polymer Solar Cells Using ZnO Electron Interfacial Layer Deposited by Intermittent Spray Pyrolysis Approach. *ACS Appl. Energy Mater.* **4**, 4099–4111 (2021).
270. Gao, J. *et al.* Over 17.7% efficiency ternary-blend organic solar cells with low energy-loss and good thickness-tolerance. *Chem. Eng. J.* **428**, (2022).
271. Schroeder, H. Poole-Frenkel-effect as dominating current mechanism in thin oxide films - An illusion?! *J. Appl. Phys.* **117**, 215103 (2015).
272. Zhu, Y., Song, T., Zhang, F., Lee, S. T. & Sun, B. Efficient organic-inorganic hybrid Schottky solar cell: The role of built-in potential. *Appl. Phys. Lett.* **102**, 113504 (2013).

273. Haneef, H. F., Zeidell, A. M. & Jurchescu, O. D. Charge carrier traps in organic semiconductors: A review on the underlying physics and impact on electronic devices. *Journal of Materials Chemistry C* vol. 8 759–787 (2020).
274. Walter, T., Herberholz, R., Müller, C. & Schock, H. W. Determination of defect distributions from admittance measurements and application to Cu(In,Ga)Se2 based heterojunctions. *J. Appl. Phys.* **80**, 4411–4420 (1996).
275. Garcia-Belmonte, G. *et al.* Charge carrier mobility and lifetime of organic bulk heterojunctions analyzed by impedance spectroscopy. *Org. Electron.* **9**, 847–851 (2008).
276. Ravishankar, E. *et al.* Achieving Net Zero Energy Greenhouses by Integrating Semitransparent Organic Solar Cells. *Joule* **4**, 490–506 (2020).
277. Pascual-San-José, E. *et al.* Towards photovoltaic windows: scalable fabrication of semitransparent modules based on non-fullerene acceptors via laser-patterning. *J. Mater. Chem. A* **8**, 9882–9895 (2020).
278. Shin, D. H. & Choi, S. H. Recent studies of semitransparent solar cells. *Coatings* vol. 8 (2018).
279. Khandelwal, K., Biswas, S., Mishra, A. & Sharma, G. D. Semitransparent organic solar cells: From molecular design to structure-performance relationships. *J. Mater. Chem. C* **10**, 13–43 (2022).
280. Tai, Q. & Yan, F. Emerging Semitransparent Solar Cells: Materials and Device Design. *Adv. Mater.* **29**, 1–37 (2017).
281. Landerer, D. *et al.* Solar Glasses: A Case Study on Semitransparent Organic Solar Cells for Self-Powered, Smart, Wearable Devices. *Energy Technol.* **5**, 1936–1945 (2017).
282. Corzo, D., Bihar, E., Alexandre, E. B., Rosas-Villalva, D. & Baran, D. Ink Engineering of Transport Layers for 9.5% Efficient All-Printed Semitransparent Nonfullerene Solar Cells. *Adv. Funct. Mater.* **31**, (2021).
283. Bai, Y. *et al.* Interfacial engineering and optical coupling for multicolored semitransparent inverted organic photovoltaics with a record efficiency of over 12%. *J. Mater. Chem. A* **7**, 15887–15894 (2019).
284. Yin, P., Yin, Z., Ma, Y. & Zheng, Q. Improving the charge transport of the ternary blend active layer for efficient semitransparent organic solar cells. *Energy Environ. Sci.* **13**, 5177–5185 (2020).
285. Liu, W. *et al.* Design of Near-Infrared Nonfullerene Acceptor with Ultralow Nonradiative Voltage Loss for High-Performance Semitransparent Ternary Organic Solar Cells. *Angew. Chemie - Int. Ed.* **100190**, (2021).
286. Yao, N. *et al.* Solution-Processed Highly Efficient Semitransparent Organic Solar Cells with Low Donor Contents. *ACS Appl. Energy Mater.* **4**, 14335–14341 (2021).
287. Yang, Y. The Original Design Principles of the Y-Series Nonfullerene Acceptors, from Y1 to Y6. *ACS Nano* **15**, 18679–18682 (2021).
288. Li, S., Li, C.-Z., Shi, M. & Chen, H. New Phase for Organic Solar Cell Research: Emergence of Y-Series Electron Acceptors and Their Perspectives. *ACS Energy Lett.* **5**, 1554−1567 (2020).
289. Li, Y. *et al.* High-Performance Semi-Transparent Organic Photovoltaic Devices via Improving Absorbing Selectivity. *Adv. Energy Mater.* **11**, (2021).
290. Song, X. *et al.* Controlling Blend Morphology for Ultrahigh Current Density in Nonfullerene Acceptor-Based Organic Solar Cells. *ACS Energy Lett.* **3**, 669–676

(2018).

291. Xie, Y. *et al.* High-Performance Semitransparent Ternary Organic Solar Cells. *Adv. Funct. Mater.* **28**, 1–7 (2018).
292. Hu, Z. *et al.* Semitransparent organic solar cells exhibiting 13.02% efficiency and 20.2% average visible transmittance. *J. Mater. Chem. A* **9**, 6797–6804 (2021).
293. Sano, T., Inaba, S. & Vohra, V. Ternary Active Layers for Neutral Color Semitransparent Organic Solar Cells with PCEs over 4%. *ACS Appl. Energy Mater.* **2**, 2534–2540 (2019).
294. Zhu, C. *et al.* Spin-coated 10.46% and blade-coated 9.52% of ternary semitransparent organic solar cells with 26.56% average visible transmittance. *Sol. Energy* **204**, 660–666 (2020).
295. Cui, Y. *et al.* Efficient Semitransparent Organic Solar Cells with Tunable Color enabled by an Ultralow-Bandgap Nonfullerene Acceptor Organic Solar Cells. *Adv. Mater* **29**, 1703080 (2017).
296. Gasparini, N. *et al.* Exploiting Ternary Blends for Improved Photostability in High-Efficiency Organic Solar Cells. *ACS Energy Lett.* **5**, 1371–1379 (2020).
297. Ma, X. *et al.* Simultaneously improved efficiency and average visible transmittance of semitransparent polymer solar cells with two ultra-narrow bandgap nonfullerene acceptors. *J. Mater. Chem. A* **6**, 21485–21492 (2018).
298. Hu, Z. *et al.* Semitransparent ternary nonfullerene polymer solar cells exhibiting 9.40% efficiency and 24.6% average visible transmittance. *Nano Energy* **55**, 424–432 (2019).
299. Cheng, H. W. *et al.* Realizing Efficient Charge/Energy Transfer and Charge Extraction in Fullerene-Free Organic Photovoltaics via a Versatile Third Component. *Nano Lett.* **19**, 5053–5061 (2019).
300. Huang, J., Tang, H., Yan, C. & Li, G. 1,1-Dicyanomethylene-3-Indanone End-Cap Engineering for Fused-Ring Electron Acceptor-Based High-Performance Organic Photovoltaics. *Cell Reports Phys. Sci.* **2**, 100292 (2021).
301. Zhong, S., Yap, B. K., Zhong, Z. & Ying, L. Review on Y6-Based Semiconductor Materials and Their Future Development via Machine Learning. *Crystals* **12**, (2022).
302. Song, X. *et al.* Dual Sensitizer and Processing-Aid Behavior of Donor Enables Efficient Ternary Organic Solar Cells. *Joule* **3**, 846–857 (2019).
303. Song, J. *et al.* Ternary Organic Solar Cells with Efficiency >16.5% Based on Two Compatible Nonfullerene Acceptors. *Adv. Mater.* **31**, 1–9 (2019).
304. An, Q. *et al.* Two compatible polymer donors contribute synergistically for ternary organic solar cells with 17.53% efficiency. *Energy Environ. Sci.* **13**, 5039–5047 (2020).
305. Hartnagel, P. & Kirchartz, T. Understanding the Light-Intensity Dependence of the Short-Circuit Current of Organic Solar Cells. *Adv. Theory Simulations* **3**, (2020).
306. Romero-Gomez, P. *et al.* Enhanced stability in semi-transparent PTB7/PC71BM photovoltaic cells. *Sol. Energy Mater. Sol. Cells* **137**, 44–49 (2015).
307. Zhao, B. *et al.* Flexible polymer solar cells with power conversion efficiency of 8.7%. *J. Mater. Chem. C* **2**, 5077–5082 (2014).
308. Gusain, A., Faria, R. M. & Miranda, P. B. Polymer solar cells-interfacial processes related to performance issues. *Front. Chem.* **7**, 1–25 (2019).
309. Madogni, V. I. *et al.* Comparison of degradation mechanisms in organic

photovoltaic devices upon exposure to a temperate and a subequatorial climate. *Chem. Phys. Lett.* **640**, 201–214 (2015).

310. Wang, Y. *et al.* Organic photovoltaics with 300 nm thick ternary active layers exhibiting 15.6% efficiency. *J. Mater. Chem. C* **9**, 9892–9898 (2021).

311. Lin, Y. *et al.* 17% Efficient Organic Solar Cells Based on Liquid Exfoliated WS 2 as a Replacement for PEDOT:PSS. *Adv. Mater.* **1902965**, 1–9 (2019).

312. Lin, Y. *et al.* 17.1% Efficient Single-Junction Organic Solar Cells Enabled by n-Type Doping of the Bulk-Heterojunction. *Adv. Sci.* **1903419**, 1–9 (2020).

313. Liu, Q. *et al.* 18 % Efficiency organic solar cells. *Sci. Bull.* **65**, 272–275 (2020).

314. Xu, X. *et al.* Interface-enhanced organic solar cells with extrapolated T80 lifetimes of over 20 years. *Sci. Bull.* **65**, 208–216 (2020).

315. Newman, M. J. *et al.* Photo-stability study of a solution-processed small molecule solar cell system : correlation between molecular conformation and degradation. *Sci. Technol. Adv. Mater.* **6996**, 1–9 (2018).

316. Cheng, P. & Zhan, X. Stability of organic solar cells: Challenges and strategies. *Chem. Soc. Rev.* **45**, 2544–2582 (2016).

317. An, Q. *et al.* High-efficiency and air stable fullerene-free ternary organic solar cells. *Nano Energy* **45**, 177–183 (2018).

318. Torimtubun, A. A. A., Sanchez, J. G., Pallares, J. & Marsal, L. F. Study of the Degradation of PTB7-Th:PC70BM-based Solar Cells using TiOx as Electron Transport Layers under Ambient Environment. *LAEDC 2020 - Lat. Am. Electron Devices Conf.* 22–25 (2020) doi:10.1109/LAEDC49063.2020.9073326.

319. Wang, Y., Cong, H., Yu, B., Zhang, Z. & Zhan, X. Efficient Inverted Organic Solar Cells Based on a Fullerene Derivative-Modified Transparent Cathode. *Materials (Basel).* **10**, 1064 (2017).

320. Torimtubun, A. A. A., Sanchez, J. G., Pallarés, J. & Marsal, L. F. . Study of the Degradation of PTB7-Th:PC70BM- based Solar Cells using TiOx as Electron Transport Layers under Ambient Environment. in *2020 IEEE Latin America Electron Devices Conference (LAEDC)* 1–4 (2020).

321. Prosa, M. *et al.* Enhanced Ultraviolet Stability of Air-Processed Polymer Solar Cells by Al Doping of the ZnO Interlayer. *ACS Appl. Mater. Interfaces* **8**, 1635–1643 (2016).

322. Xie, F. X. *et al.* Enhanced charge extraction in organic solar cells through electron accumulation effects induced by metal nanoparticles. *Energy Environ. Sci.* **6**, 3372–3379 (2013).

323. Sacco, A. Electrochemical impedance spectroscopy: Fundamentals and application in dye-sensitized solar cells. *Renew. Sustain. Energy Rev.* **79**, 814–829 (2017).

324. Yan, W., Huo, M. M., Hu, R. & Wang, Y. Working area effects on the energetic distribution of trap states and charge dynamics of dye-sensitized solar cells. *RSC Adv.* **9**, 1734–1740 (2019).

325. Jiang, M. *et al.* Two-Pronged Effect of Warm Solution and Solvent-Vapor Annealing for Efficient and Stable All-Small-Molecule Organic Solar Cells. *ACS Energy Lett.* **6**, 2898–2906 (2021).

326. Jiang, M. *et al.* Rational compatibility in a ternary matrix enables all-small-molecule organic solar cells with over 16% efficiency. *Energy Environ. Sci.* **14**, 3945–3953 (2021).

327. Jiménez-López, J. & Palomares, E. Interfacial recombination kinetics in aged

perovskite solar cells measured using transient photovoltage techniques. *Nanoscale* **11**, 20024–20029 (2019).

328. Pockett, A., Lee, H. K. H., Coles, B. L., Tsoi, W. C. & Carnie, M. J. A combined transient photovoltage and impedance spectroscopy approach for a comprehensive study of interlayer degradation in non-fullerene acceptor organic solar cells. *Nanoscale* **11**, 10872–10883 (2019).
329. Chaturvedi, N., Kumar Swami, S., Kumar, A. & Dutta, V. Role of ZnO nanostructured layer spray deposited under an electric field in stability of inverted organic solar cells. *Sol. Energy Mater. Sol. Cells* **126**, 74–82 (2014).
330. Grossiord, N., Kroon, J. M., Andriessen, R. & Blom, P. W. M. Degradation mechanisms in organic photovoltaic devices. *Org. Electron.* **13**, 432–456 (2012).
331. Guerrero, A. *et al.* Charge carrier transport and contact selectivity limit the active layer thickness. *J. Mater. Chem. A* **1**, 12345–12354 (2013).
332. Islam, M. A., Hasanuzzaman, M. & Rahim, N. A. Effect of Different Factors on the Leakage Current Behavior of Silicon Photovoltaic Modules at High Voltage Stress. *IEEE J. Photovoltaics* **8**, 1259–1265 (2018).
333. Kawano, K. *et al.* Degradation of organic solar cells due to air exposure. *Sol. Energy Mater. Sol. Cells* **90**, 3520–3530 (2006).
334. Sacramento, A., Balderrama, V. S., Ramírez-como, M., Marsal, L. F. & Estrada, M. Degradation study under air environment of inverted polymer solar cells using poly fl uorene and halide salt as electron transport layers. *Sol. Energy* **198**, 419–426 (2020).
335. Yang, H. Bin, Song, Q. L., Gong, C. & Li, C. M. The degradation of indium tin oxide/pentacene/fullerene/tris-8-hydroxy-quinolinato aluminum/aluminum heterojunction organic solar cells: By oxygen or moisture? *Sol. Energy Mater. Sol. Cells* **94**, 846–849 (2010).
336. Norrman, K., Madsen, M. V., Gevorgyan, S. A. & Krebs, F. C. Degradation patterns in water and oxygen of an inverted polymer solar cell. *J. Am. Chem. Soc.* **132**, 16883–16892 (2010).
337. Guerrero, A. *et al.* Nanoscale mapping by electron energy-loss spectroscopy reveals evolution of organic solar cell contact selectivity. *Org. Electron.* **16**, 227–233 (2015).
338. Ma, Z. *et al.* Influences of Surface Roughness of ZnO Electron Transport Layer on the Photovoltaic Performance of Organic Inverted Solar Cells. *J. Phys. Chem. C* **116**, 24462−24468 (2012).
339. Lilliedal, M. R., Medford, A. J., Madsen, M. V., Norrman, K. & Krebs, F. C. The effect of post-processing treatments on inflection points in currentvoltage curves of roll-to-roll processed polymer photovoltaics. *Sol. Energy Mater. Sol. Cells* **94**, 2018–2031 (2010).
340. Ramírez-Como, M. *et al.* Small molecule organic solar cells toward improved stability and performance for Indoor Light Harvesting Application. *Sol. Energy Mater. Sol. Cells* **230**, 111265 (2021).
341. Xu, L. *et al.* Increasing the Efficiency of Organic Dye-Sensitized Solar Cells over 10 . 3 % Using Locally Ordered Inverse Opal Nanostructures in the Photoelectrode. **1706291**, 1–12 (2018).
342. Tuladhar, S. M. *et al.* Low Open-Circuit Voltage Loss in Solution- Processed Small-Molecule Organic Solar Cells. *ACS Energy Lett.* **1**, 302–308 (2016).

343. Montcada, N. F., Méndez, M., Cho, K. T., Nazeeruddin, M. K. & Palomares, E. Photo-induced dynamic processes in perovskite solar cells: The influence of perovskite composition in the charge extraction and the carrier recombination. *Nanoscale* **10**, 6155–6158 (2018).
344. Maurano, A. *et al.* Transient optoelectronic analysis of charge carrier losses in a selenophene/fullerene blend solar cell. *J. Phys. Chem. C* **115**, 5947–5957 (2011).
345. Gupta, S. K., Pali, L. S. & Garg, A. Impedance spectroscopy on degradation analysis of polymer/fullerene solar cells. *Sol. Energy* **178**, 133–141 (2019).
346. Torimtubun, A. A. A., Sanchez, J. G., Pallares, J. & Marsal, L. F. Photostability Study of Inverted Polymer Solar Cells under AM 1.5G and LED Illumination via Impedance Spectroscopy. *IEEE J. Electron Devices Soc.* **9**, 484–491 (2021).
347. Torres, I. & Taylor, D. M. Interface states in polymer metal-insulator-semiconductor devices. *J. Appl. Phys.* **98**, (2005).
348. Hirwa, H., Pittner, S. & Wagner, V. Interfaces analysis by impedance spectroscopy and transient current spectroscopy on semiconducting polymers based metal – insulator – semiconductor capacitors. *Org. Electron.* **24**, 303–314 (2015).
349. Foertig, A. *et al.* Nongeminate and geminate recombination in PTB7:PCBM Solar Cells. *Adv. Funct. Mater.* **24**, 1306–1311 (2014).
350. Foertig, A., Rauh, J., Dyakonov, V. & Deibel, C. Shockley equation parameters of P3HT:PCBM solar cells determined by transient techniques. *Phys. Rev. B - Condens. Matter Mater. Phys.* **86**, 1–7 (2012).
351. Kiermasch, D. *et al.* Unravelling steady-state bulk recombination dynamics in thick efficient vacuum-deposited perovskite solar cells by transient methods. *J. Mater. Chem. A* **7**, 14712–14722 (2019).
352. Kirchartz, T., Pieters, B. E., Kirkpatrick, J., Rau, U. & Nelson, J. Recombination via tail states in polythiophene:fullerene solar cells. *Phys. Rev. B - Condens. Matter Mater. Phys.* **83**, 1–13 (2011).

Appendices

APPENDIX 1. Supporting Figures

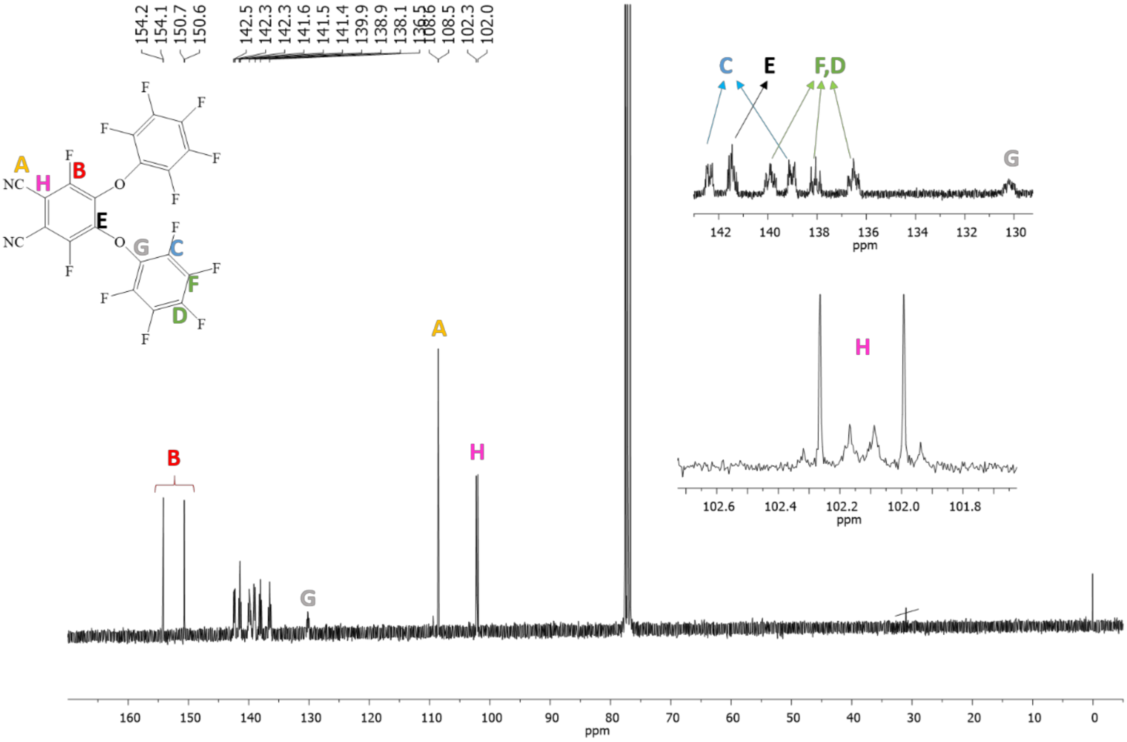

Figure A.1 ^{13}C NMR spectrum of phthalonitrile **1** in $CDCl_3$.

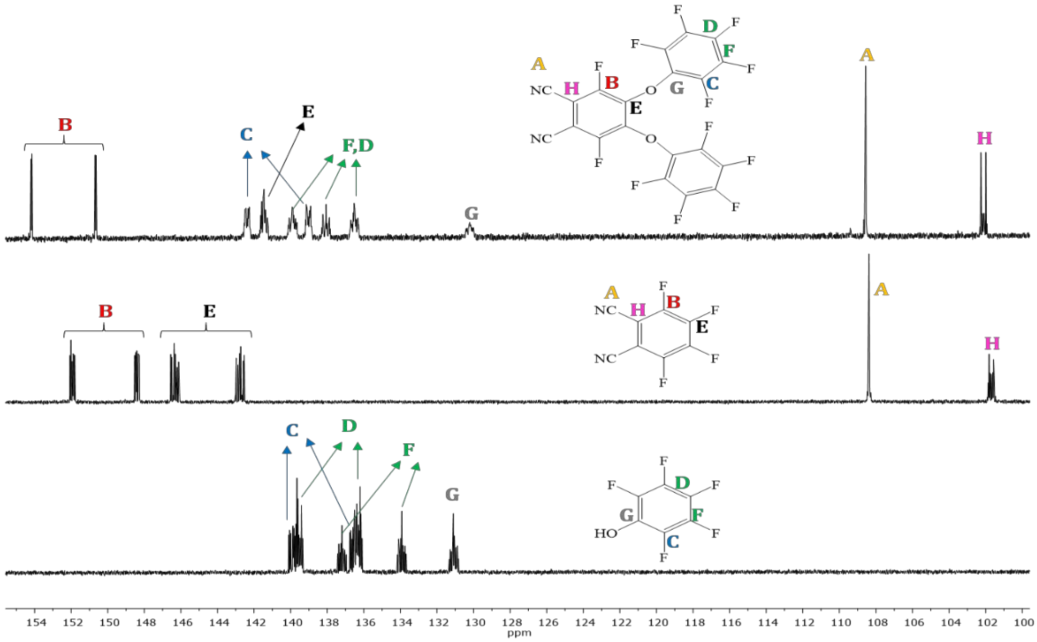

Figure A.2 ^{13}C NMR comparison between phthalonitrile **1**, pentafluorophthalonitrile and pentafluorophenol in $CDCl_3$.

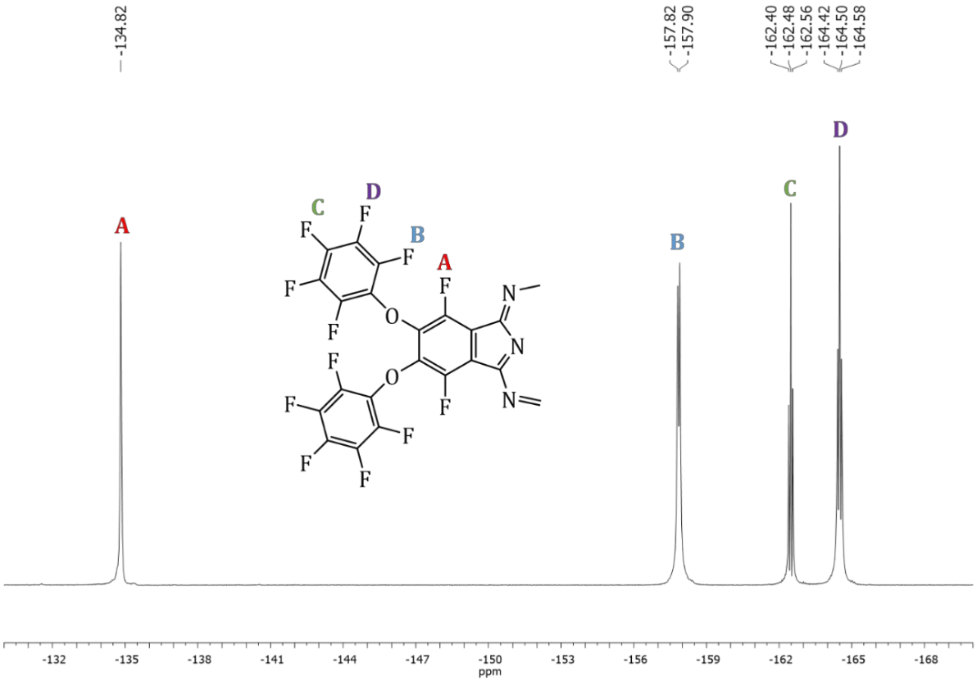

Figure A.3 ^{19}F NMR spectrum of **ZnPcF$_{48}$** in THF-d_8.

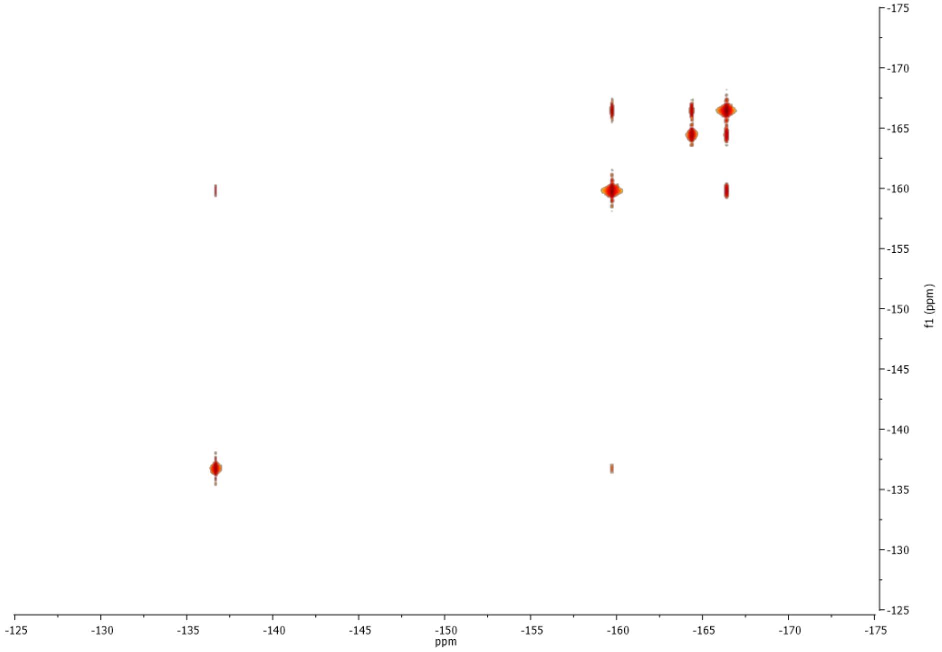

Figure A.4 ^{19}F-^{19}F 2D NMR spectrum of **ZnPcF$_{48}$** in THF-d_8.

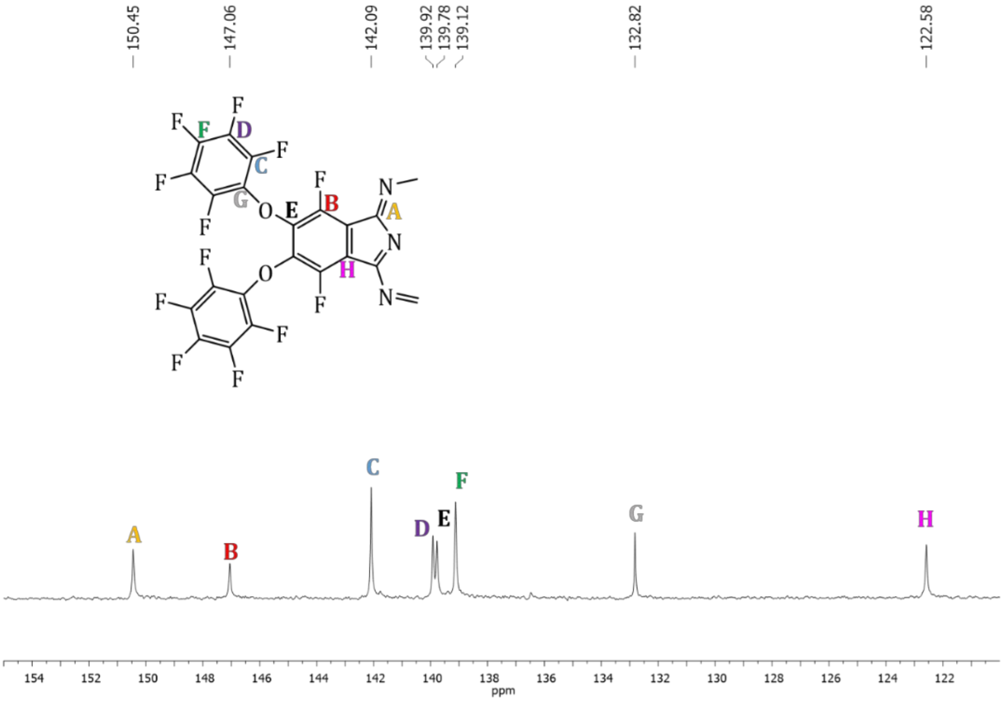

Figure A.5 ^{13}C{^{19}F}NMR spectrum of **ZnPcF$_{48}$** in THF-d_8.

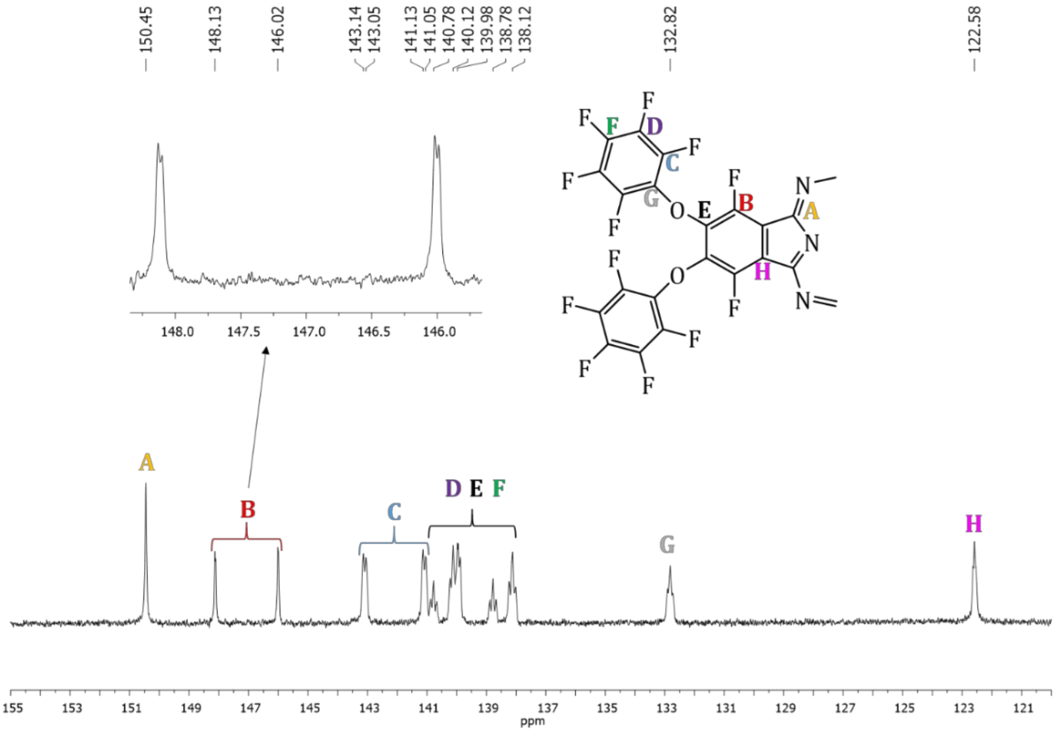

Figure A.6 ^{13}C NMR spectrum of **ZnPcF$_{48}$** in THF-d_8.

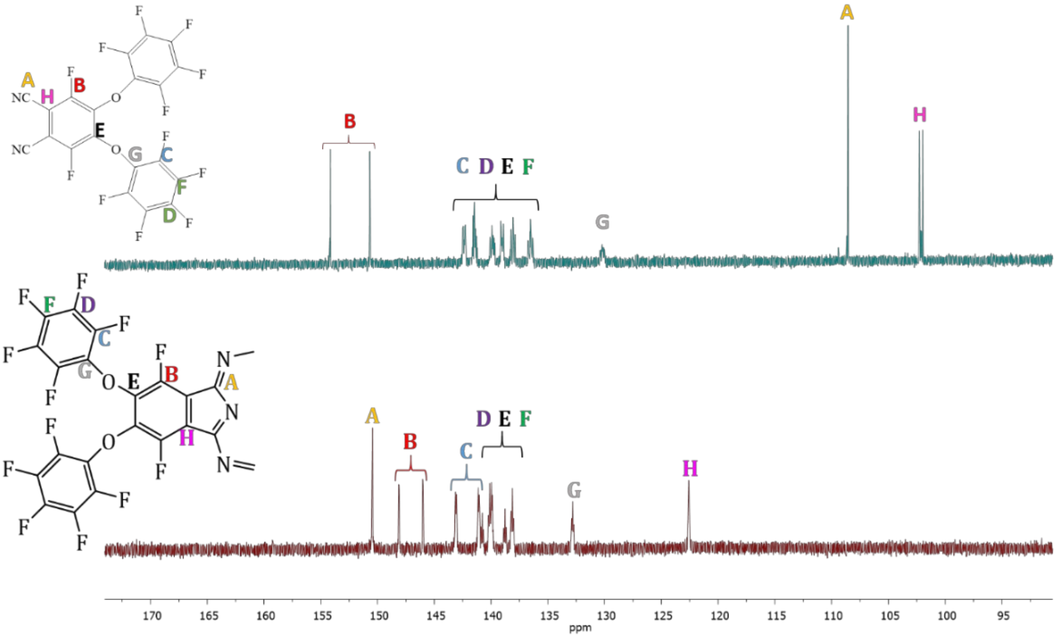

Figure A.7 ^{13}C NMR comparison between phthalonitrile **1** and **ZnPcF$_{48}$**.

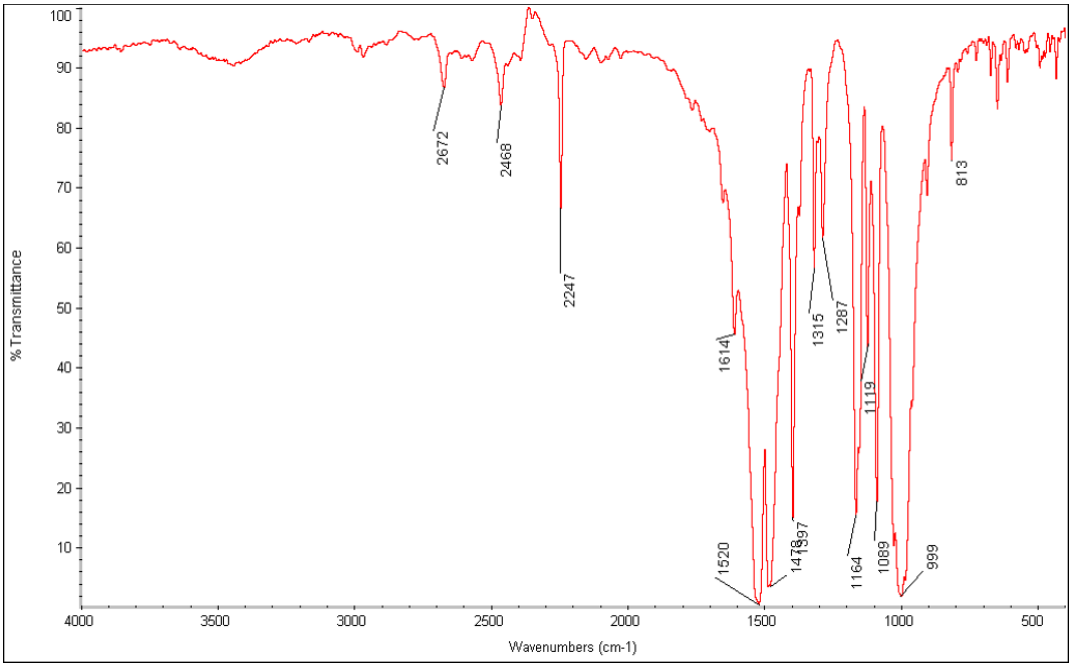

Figure A.8 FT-IR spectrum of phthalonitrile **1**.

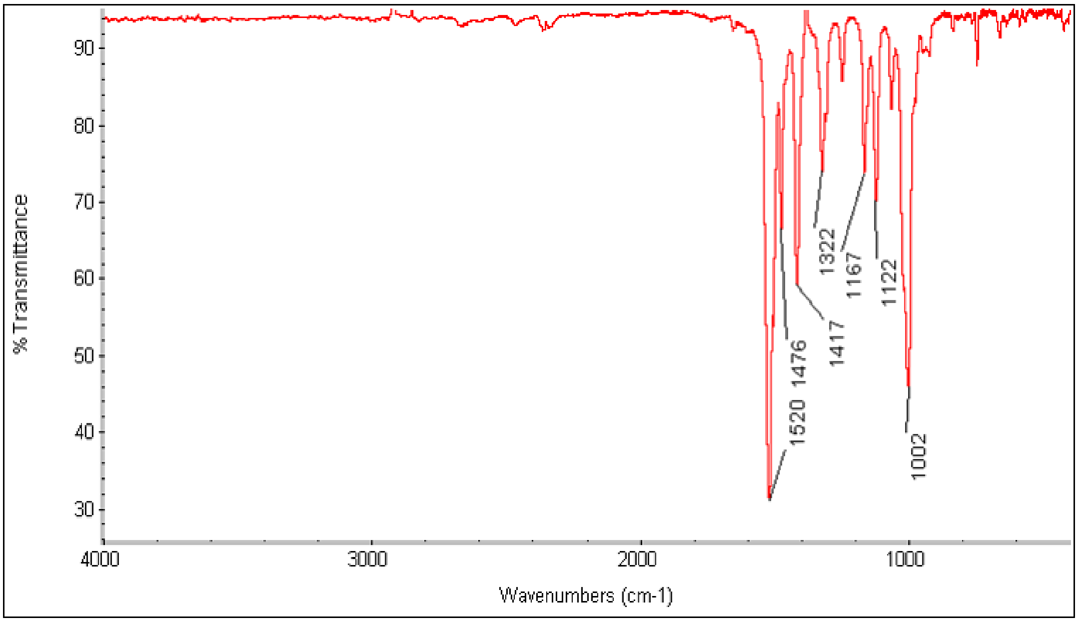

Figure A.9 FT-IR spectrum of **ZnPcF$_{48}$**.

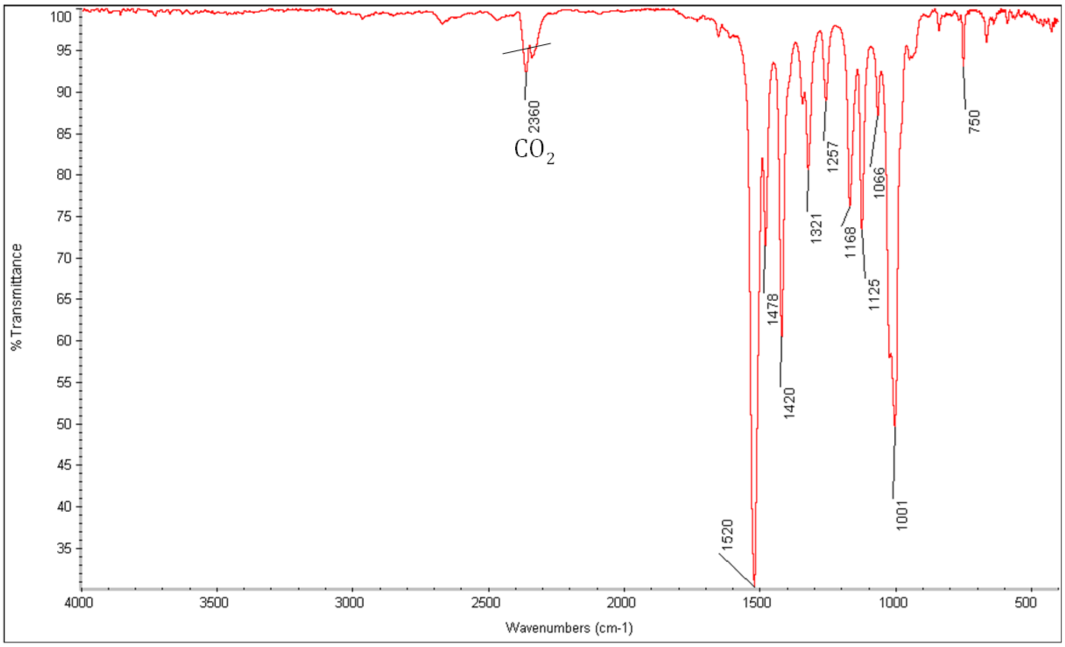

Figure A.10 FT-IR spectrum of **CuPcF$_{48}$**.

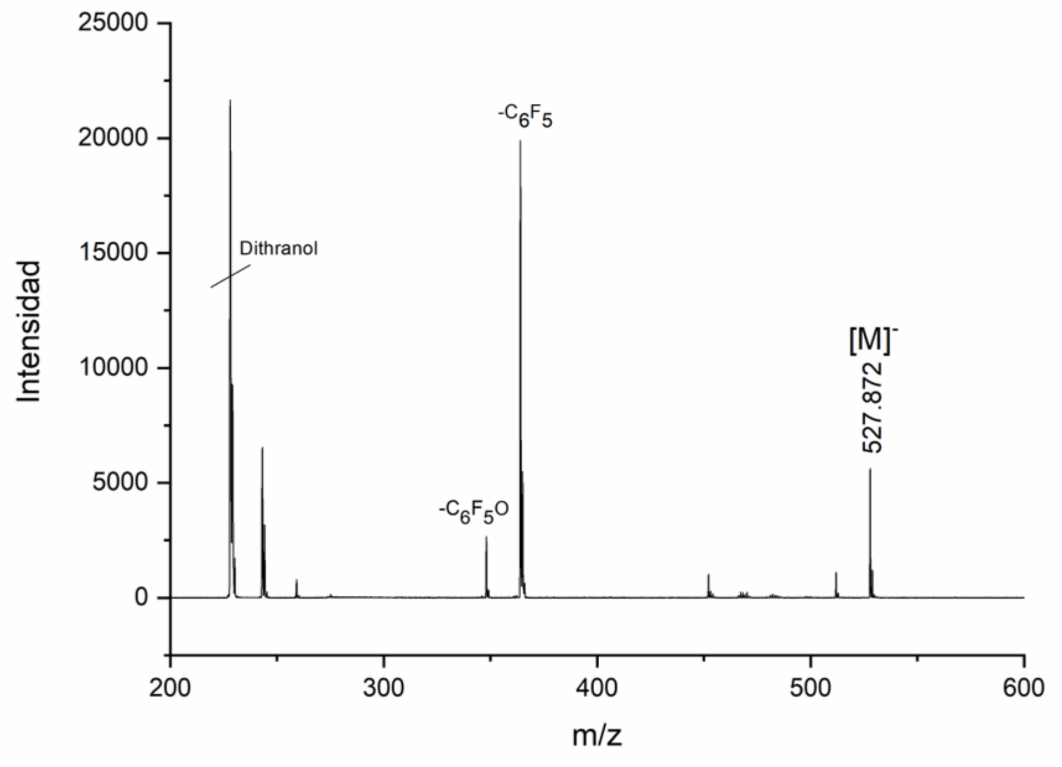

Figure A.11 MS-MALDI-TOF of phthalonitrile **1**.

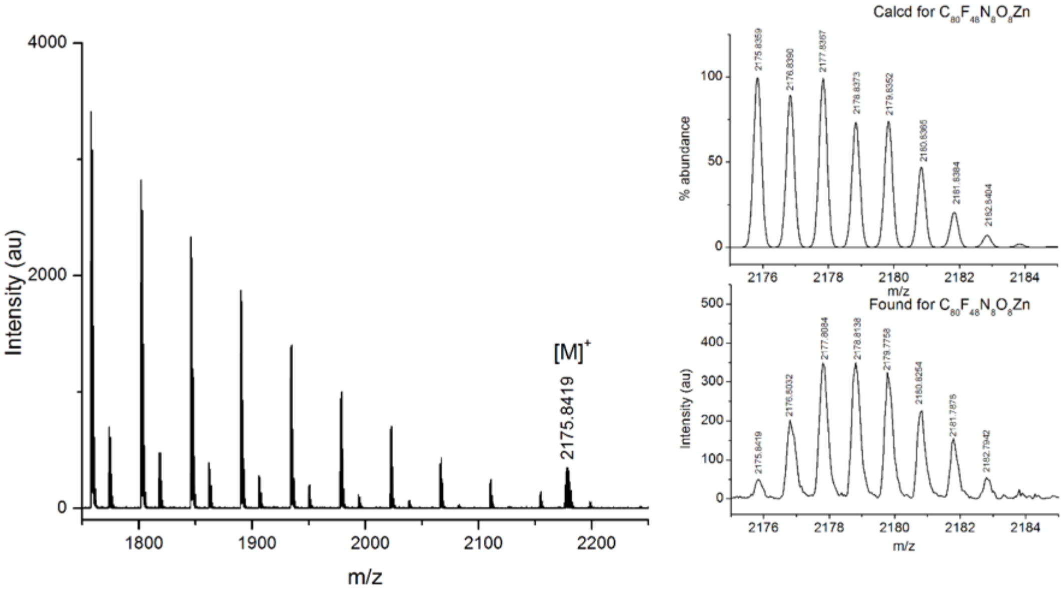

Figure A.12 HR-MALDI-TOF of **ZnPcF$_{48}$**.

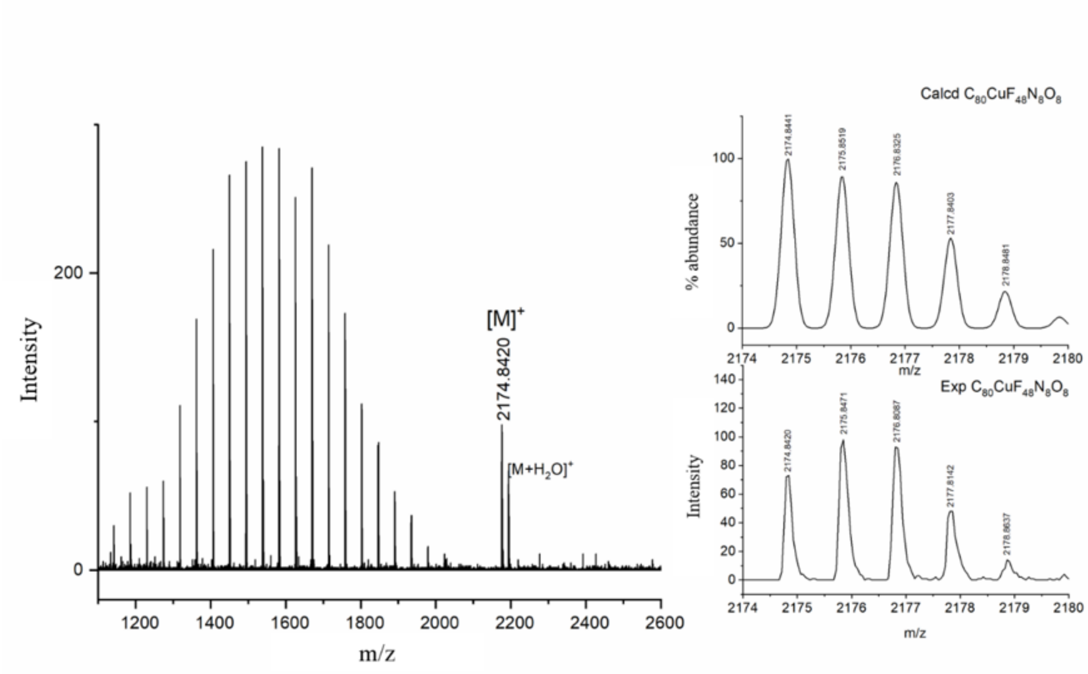

Figure A.13 HR-MALDI-TOF of **CuPcF$_{48}$**.

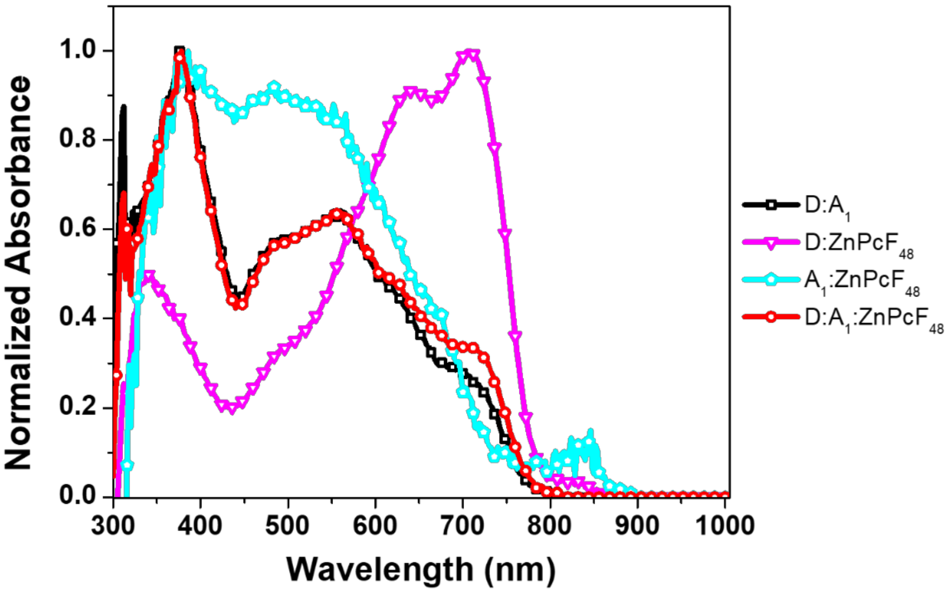

Figure A.14 Normalized absorption spectra of reference blend, binary and ternary blend based on **ZnPcF$_{48}$** in thin film.

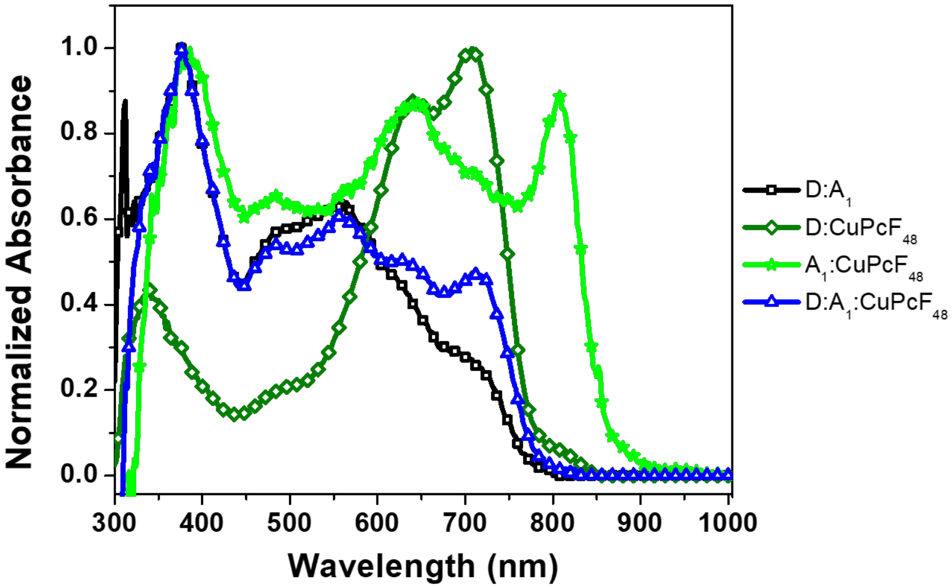

Figure A.15 Normalized absorption spectra of reference blend, binary and ternary blend films based on **CuPcF$_{48}$** in thin film.

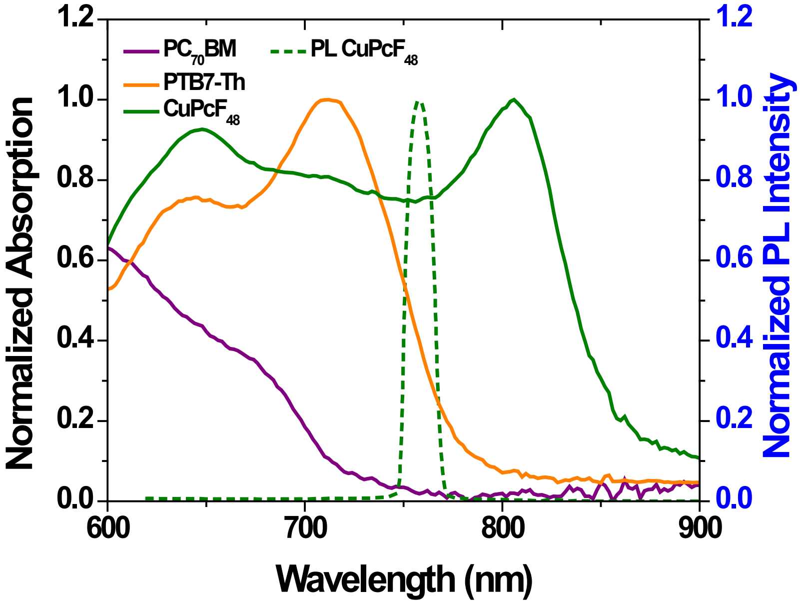

Figure A.16 Normalized absorption spectra (left black y-axis, solid lines) of $PC_{70}BM$, PTB7-Th and **$CuPcF_{48}$** individual thin films, and photoluminescence spectra (right blue y-axis, dash line) of **$CuPcF_{48}$**. The excited wavelength for PL spectra is at 610 nm. The yellow area is the overlapping area of **$CuPcF_{48}$** emission spectrum vs PTB7-Th and $PC_{70}BM$.

APPENDIX 2. Supporting Tables

Table A.1 Optimization of D:A_1:A_2 weight ratio and solvent vapour annealing (SVA) treatment for PTB7-Th:$PC_{70}BM$:**$CuPcF_{48}$** in inverted solar cells. Average values were obtained from over 10 devices for weight ratio optimization and over 3 devices for SVA treatment.

D:A_1:A_2 [%w/w]	**SVA**	**J_{SC} [mA·cm^{-2}]**	**V_{OC} [V]**	**FF [%]**	**PCE [%]**
1:1.5:0	-	16.82	0.78	68.22	9.01
	SVA	14.77	0.80	65.47	7.78
1:1.47:0.03	-	17.90	0.78	68.54	9.57
	SVA	16.18	0.79	64.86	8.37
1:1.44:0.06	-	14.08	0.77	71.18	7.69
	SVA	14.32	0.78	63.81	7.10
1:1.4:0.1	-	15.63	0.73	64.70	7.37
1:1.38:0.12	-	13.24	0.76	58.07	5.81
	SVA	11.79	0.33	28.30	1.12
1:0:1	-	0.06	0.32	0.24	0.01

Table A.2 Optimization of electron transport layer for PTB7-Th:$PC_{70}BM$:**$ZnPcF_{48}$** in inverted solar cells. Average values were obtained from over 3 devices.

D:A_1:A_2 [%w/w]	**ETL**	**J_{SC} [mA·cm^{-2}]**	**V_{OC} [V]**	**FF [%]**	**PCE [%]**
1:1.5:0	PFN	16.82	0.78	68.22	9.01
	TiOx	10.76	0.78	71.18	5.92
1:1.4:0.1	PFN	14.25	0.78	64.47	7.12
	TiOx	11.87	0.70	58.84	4.88

Table A.3 Optimization of D:A_1:A_2 weight ratio for PTB7-Th:$PC_{70}BM$:**$ZnPcF_{48}$** in inverted solar cells. Average values were obtained from over 10 devices.

D:A_1:A_2 [%w/w]	**J_{SC}** [mA·cm^{-2}]	**V_{OC}** [V]	**FF** [%]	**PCE** [%]
1:1.5:0	16.82	0.78	68.22	9.01
1:1.47:0.03	14.25	0.78	64.47	7.12
1:1.4:0.1	14.25	0.78	64.47	7.12
1:0:1	0.29	0.33	0.50	0.03

UNIVERSITAT
ROVIRA i VIRGILI

ICIQ
Institute of Chemical
Research of Catalonia

UNIVERSITAS
Miguel
Hernández

جامعة الملك عبدالله
للعلوم والتقنية
King Abdullah University of
Science and Technology